



HAL
open science

Estimation et contrôle d'un moteur diesel HCCI. Estimation des systèmes périodiques.

Jonathan Chauvin

► **To cite this version:**

Jonathan Chauvin. Estimation et contrôle d'un moteur diesel HCCI. Estimation des systèmes périodiques.. Mathematics [math]. École Nationale Supérieure des Mines de Paris, 2006. English. NNT : . pastel-00002804

HAL Id: pastel-00002804

<https://pastel.hal.science/pastel-00002804>

Submitted on 30 Jul 2007

HAL is a multi-disciplinary open access archive for the deposit and dissemination of scientific research documents, whether they are published or not. The documents may come from teaching and research institutions in France or abroad, or from public or private research centers.

L'archive ouverte pluridisciplinaire **HAL**, est destinée au dépôt et à la diffusion de documents scientifiques de niveau recherche, publiés ou non, émanant des établissements d'enseignement et de recherche français ou étrangers, des laboratoires publics ou privés.

THÈSE

PRÉSENTÉE À
L'ÉCOLE NATIONALE SUPÉRIEURE DES MINES DE PARIS
PAR

JONATHAN CHAUVIN

EN VUE DE L'OBTENTION DU TITRE DE

DOCTEUR DE L'ÉCOLE DES MINES DE PARIS

SPÉCIALITÉ: MATHÉMATIQUES ET AUTOMATIQUE

SUJET DE LA THÈSE:

**ESTIMATION ET CONTRÔLE D'UN MOTEUR
DIESEL HCCI. ESTIMATION DES SYSTÈMES
PÉRIODIQUES.**

SOUTENUE LE 29 SEPTEMBRE 2006 DEVANT LE JURY COMPOSÉ DE

MM. CARLOS CANUDAS-DE-WIT	RAPPORTEUR
LINO GUZZELLA	RAPPORTEUR
GILLES CORDE	EXAMINATEUR
NICOLAS PETIT	EXAMINATEUR
PIERRE ROUCHON	EXAMINATEUR
MICHEL SORINE	EXAMINATEUR

JONATHAN CHAUVIN

**ESTIMATION AND CONTROL OF
A DIESEL HCCI ENGINE.
ESTIMATION FOR TIME PERIODIC
SYSTEMS**

JONATHAN CHAUVIN

École Nationale Supérieure des Mines de Paris, Centre Automatique et Systèmes,
60, Bd. Saint-Michel, 75272 Paris Cedex 06, France.

Institut Français du Pétrole, 1 et 4 avenue du Bois Préau, 92852 Rueil-Malmaison,
France.

E-mail : jonathan.chauvin@ensmp.fr, jonathan.chauvin@ifp.fr

Url : www.cas.ensmp.fr/~chauvin

Key words and phrases. — Engine control, HCCI, air path control, cylinder balancing, motion planning, dynamic inversion, periodic systems, periodic observers, Kalman filter.

Mots Clés. — Contrôle moteur, HCCI contrôle de la boucle d'air, équilibrage cylindre à cylindre, génération de trajectoire, inversion de dynamique, systèmes périodiques, observateurs périodiques, filtre de Kalman.

15th September 2006

Aux Miens.

**ESTIMATION AND CONTROL OF A DIESEL
HCCI ENGINE. ESTIMATION FOR TIME
PERIODIC SYSTEMS**

JONATHAN CHAUVIN

Résumé. — La combustion homogène Diesel (HCCI: Homogeneous Combustion Compression Ignition) est caractérisée par un très haut taux de recirculation de gaz brûlés (EGR: Exhaust Gas Recirculation). Cette technique de combustion permet d'augmenter la qualité de mélange et la dilution dans le cylindre, tout en réduisant la formation des polluants. Malheureusement, ce procédé nuit à la stabilité de la combustion. Un compromis est nécessaire entre la stabilité de combustion et les performances du moteur, quantifiées en terme de couple produit et d'émissions polluantes. C'est là le rôle du contrôle moteur. À fins d'implémentation de stratégie de contrôle, il est nécessaire d'estimer en temps réel l'évolution des paramètres de combustion qui ne sont pas directement mesurés par des capteurs.

Cette thèse, réalisée en collaboration avec l'IFP (Institut Français du Pétrole), propose des algorithmes de contrôle qui ont été validés expérimentalement sur un moteur HCCI quatre cylindres développé par l'IFP.

Nous décomposons le problème en trois parties et proposons des solutions, validées sur banc moteur, pour les deux premières.

La première étape consiste à réaliser le *contrôle de la boucle d'air*. Le but est d'estimer et de contrôler les masses aspirées par les cylindres (air frais et gaz brûlés). Ces masses s'expriment directement en fonction de la pression, la composition et les débits du collecteur d'admission. Des observateurs non linéaires permettent d'estimer ces variables, en n'utilisant que les capteurs présents sur les véhicules de série. La construction de ces observateurs ainsi que leurs preuves de convergence utilisent la méthode dite "d'injection de sortie" ainsi que la théorie de stabilité de Lyapunov. Une technique de génération de trajectoires est utilisée pour définir des consignes de débits (air frais et EGR). Cette loi de commande boucle ouverte prend explicitement en compte les contraintes physiques. Enfin, des contrôleurs de type proportionnel intégral (PI) sont utilisés pour garantir le suivi des consignes prescrites. Nous décrivons les résultats expérimentaux obtenus dans différents cas de figures, tels que des transitoires de charge et le cycle de référence européen.

La deuxième étape est l'*équibrage cylindre à cylindre*. Le but est d'estimer les paramètres de combustion de chacun des cylindres afin de garantir que les cylindres ont la même combustion en dépit de la variabilité des éléments techniques les constituant. Pour cela, nous créons un observateur de couple instantané et un observateur de richesse cylindre à cylindre à partir de capteurs présents sur les véhicules de série. Nous exploitons l'information haute fréquence contenue dans les signaux mesurés (échantillonnage aux 6 degré vilebrequin). Ces observateur sont validés expérimentalement. Leur conception est nouvelle. Il s'agit d'un nouveau type d'observateurs asymptotiques reconstituant un nombre arbitraire de fréquences d'un signal périodique inconnu entrant dans un système linéaire périodique. Ces observateurs surpassent (à performances comparables) les filtres de Kalman en terme de temps de calculs. Ils sont inspirés des techniques de moyennisation. Une méthodologie de réglage automatique est proposée et justifiée par l'extension à un nombre infini de fréquences.

La troisième étape est le *contrôle de la boucle de fuel*. Durant des transitoires de couple, la boucle de carburant doit suivre la dynamique plus lente de la boucle d'air (qui est typiquement 10 fois plus lente). Nous décrivons cette problématique et expliquons les principales difficultés.

Abstract. — Homogeneous Combustion Compression Ignition (HCCI) combustion is characterized by a very high rate of Exhaust Gas Recirculation (EGR). This improves mixing and dilution in the cylinders, reduces pollutant formation at the expense of combustion stability. Thus HCCI engines requires real-time control to ensure a good trade-off between performance (in terms of torque production and low pollutant emissions) and combustion stability. Such closed-loop control are based on estimation of combustion parameters that are not directly measured.

This thesis, supported by IFP (Institut Français du Pétrole), proposes some control algorithms that have been tested experimentally on a 4-cylinders HCCI engine developed by IFP.

We decompose the control synthesis in three steps. We propose solutions with experimental validations for the first two steps.

The first step is *air path control*. The goal is to estimate and to control the masses entering in the cylinders (fresh air and burned gas). These masses are directly related to collector pressure, compositions and flow-rates. These variables are estimated via nonlinear observers using commercial cars sensors. Design and theoretical convergence proof follow linearization via output injection and Lyapunov argument. Feedforward control based on motion planning for differentially flat systems are used to derive the flow-rate set points (fresh air and EGR). This feedforward control takes explicitly physical input constraints into account. Finally, fast Proportional Integral (PI) controller are designed to track these step points using as measured values the above estimations. We describe experimental results for large torque transient and also for driving phases of the eurocycle.

The second step is *cylinder balancing*. The goal is to estimate and control the combustion parameters in order to guarantee that all the cylinders have the same combustion in any steady-state regime. For that, we design instantaneous torque and cylinder individual air/fuel ratio (AFR) observers using commercial car sensors. We exploit here the high-frequency information contained in the measured signals (sampling of 6 degree crank angle). Experimental results are reported. These results are based on a new class on asymptotic observers of an arbitrary numbers of Fourier modes associated to an unknown periodic input entering a linear time-periodic system. These observers outperform Kalman filters in terms of computation burden. Design and convergence proof are based on averaging techniques. A gain design methodology is proposed and justified for large numbers of modes via extension to infinite dimension of the finite-dimensional convergence analysis.

The third step is *fuel path control*. During large transient, the fuel path must follow the slower air path transient. We describe this still open problematic and point out its main difficulties.

INTRODUCTION GÉNÉRALE

Les contraintes croissantes des normes environnementales ont placé le contrôle moteur au cœur de nombreuses préoccupations des constructeurs automobiles. L'objectif du contrôle moteur est la gestion en temps réel de l'alimentation en air et en carburant du moteur pour le pilotage actif de la combustion dans les cylindres. En pratique, on peut contrôler le circuit d'air et le système d'injection, en jouant sur les quantités admises ainsi que sur les lois horaires et leur synchronisation. Une volonté persistante de diminuer les polluants et d'augmenter la performance du moteur a suscité la recherche de techniques de contrôle et de combustion de plus en plus sophistiquées. Récemment, le mode de combustion homogène – incluant la combustion HCCI (Homogeneous Charge Compression Ignition) – est apparue comme une des solutions les plus avancées. Cette combustion nécessite l'utilisation par recirculation de forts taux de gaz brûlés (EGR Exhaust Gas Recirculation). Elle permet d'avoir une combustion homogène dans tout le cylindre. L'EGR augmente la dilution du mélange et permet une diminution du bruit et des émissions polluantes. Cependant, l'augmentation de la recirculation d'EGR tend à déstabiliser la combustion. Un compromis entre performance (en terme de faibles émissions polluantes) et stabilité est donc nécessaire. Un contrôle précis du mélange dans le cylindre est nécessaire. Pour contrôler précisément la combustion, nous devons tenir compte des différentes échelles de temps des boucles de la dynamique moteur.

1. La plus rapide (environ 2kHz) est lié au processus de combustion. La combustion dans la chambre dure un temps correspondant à quelques degrés vilebrequin ($500\mu s$ pour 6° vilebrequin à 2000 tr/min). D'un point de vue contrôle, cette fréquence est considérée comme une haute fréquence.
2. L'échelle de temps intermédiaire (environ 50Hz) correspond à la production de couple sur un cycle moteur (ce qui correspond à 60ms à 2000 tr/min). Cela correspond à l'ensemble du phénomène de combustion. C'est l'échelle de temps de la boucle de fuel: on est capable de changer les paramètres d'injection d'un cycle à l'autre.

3. La boucle la plus lente (environ 1Hz) est liée à la boucle d'air.

La thèse se divise en trois parties

- Partie I: Le moteur HCCI et les problèmes de contrôle associés.
- Partie II: Le contrôle de la boucle d'air et le contrôle cylindre à cylindre.
- Partie III: L'estimation de systèmes linéaires périodiques.

Partie I. — Cette partie décrit les différentes étapes de la combustion et les variables qui jouent sur le processus de combustion. Pour contrôler le processus de combustion, nous cherchons à connaître précisément la masse totale, la composition et la température de ce qui est aspiré dans le cylindre et déterminons quand et comment injecter le carburant.

Le chapitre 1 est dédié à la description d'un moteur Diesel, nous présentons les différentes étapes du processus de combustion.

Dans le chapitre 2, nous décrivons la structure de contrôle pour moteur Diesel développé à l'IFP. Nous examinons l'impact de chaque actionneur sur le processus de combustion. Nous donnons une interprétation de l'évolution des caractéristiques du mélange aspiré dans le cylindre (masse totale, composition et température), lorsque les consignes des actionneurs varient. En résumé, nous étudions les effets des commandes sur le processus de combustion et sur les performances du moteur. Ces performances sont exprimées en terme de bruit, de couple fourni et d'émissions polluantes. Enfin, nous nous intéressons à la gestion de l'injection. Ce problème se résume en deux questions : "quel est le moment le plus opportun pour injecter le carburant dans le cylindre?" et "quelle quantité doit-on en injecter?".

Dans le chapitre 3, nous proposons de séquencer le problème général du contrôle de la combustion en trois sous problèmes.

- Le contrôle de la boucle d'air: dans un premier temps, nous cherchons contrôler les masses aspirées dans le cylindre (air frais et gaz brûlés).
- Le contrôle cylindre à cylindre: il s'agit du problème d'équilibrage entre les cylindres en dépit de la variabilité des éléments techniques constitutifs (notamment les injecteurs). En effet, alors que chaque injecteur reçoit la même consigne, on observe que tous les cylindres n'ont pas le même comportement.
- Le contrôle de la boucle de fuel: pour garantir les caractéristiques du mélange dans le cylindre il est nécessaire de ralentir la dynamique de la boucle de fuel pour l'adapter à celle de la boucle d'air, typiquement dix fois plus lente.

Comme nous le montrons expérimentalement sur un moteur HCCI, les deux premiers problèmes sont essentiels au fonctionnement du moteur. Le troisième n'est pas primordial. En revanche ne pas le résoudre revient à accepter un niveau élevé de bruit et d'émission de polluants en transitoire. Ce qui est en contradiction avec une utilisation sur véhicule série.

Partie II. — Cette partie présente des solutions aux deux premiers problèmes présentés dans la Partie I.

Dans le chapitre 4, nous nous plaçons dans le cas d'une modification de la demande en couple. Nous avons montré que pour garantir une combustion performante pendant le transitoire il était nécessaire de contrôler la boucle d'air. Grâce à une relation statique établie expérimentalement, nous traduisons l'évolution de la demande en couple en consigne sur les caractéristiques du mélange aspiré dans le cylindre. Pour cela, nous proposons une structure de contrôle à deux niveaux. Tout d'abord nous générons une trajectoire admissible pour le système. Ensuite, nous développons un observateur/contrôleur qui réalise le suivi des variables commandées autour de la trajectoire planifiée. Des résultats expérimentaux sont présentés.

Dans le chapitre 5, nous considérons le problème de l'estimation et du contrôle de la richesse cylindre à cylindre. Les déséquilibres de richesse cylindre à cylindre reflètent les différences entre la combustion de chacun des cylindres. Ces différences peuvent être mesurées par le capteur placé derrière la turbine. Nous présentons deux stratégies dont nous comparons les efficacités et présentons des résultats en boucle fermée.

Dans le chapitre 6, nous considérons le problème de l'estimation du couple de combustion. Le couple de combustion caractérise les performances du moteur. Il dépend de diverses entrées comme le temps d'injection, le taux d'EGR. . . Nous n'avons pas de mesure directe de ce couple mais nous mesurons la vitesse instantanée de l'arbre vilebrequin au bout de la transmission. Nous développons des observateurs haute fréquence pour estimer ce couple. Nous prouvons la convergence des observateurs considérés et présentons des résultats expérimentaux.

Partie III. — Comme vu au chapitre 6, l'estimation des systèmes périodiques excités par une perturbation périodique inconnue est très utile dans les problèmes d'observateurs dans le domaine du contrôle moteur. Comme décrit dans 6.3.4, les filtres de Kalman donnent une estimation de cette excitation au prix d'un temps de calcul très élevé. C'est

pourquoi, nous proposons des observateurs linéaires périodiques pour résoudre ce problème.

Dans le Chapitre 7, nous considérons le système $\dot{x} = A(t)x + A_0(t)w(t)$, $y = C(t)x$, $x \in \mathbb{R}^n$, $w \in \mathbb{R}^m$, $y \in \mathbb{R}^p$, ($m \leq p \leq n$) où $A(t)$, $A_0(t)$, et $C(t)$ sont des matrices T_0 -périodiques. Le signal d'entrée inconnu $w(t)$ est T_0 -périodique mais nous supposons qu'il admet une décomposition de Fourier ayant un nombre fini d'harmoniques. Nous proposons une technique, reposant sur les principes de moyennisation [53], pour estimer w à partir de la mesure y . Dans les cas d'une mesure partielle ou totale, nous proposons un observateur pour les coefficients de Fourier de la décomposition de $w(t)$.

Dans le chapitre précédent, nous avons regardé les filtres de dimension finie pour les systèmes linéaires périodiques excités par une entrée périodique inconnue. Dans le chapitre 8, nous regardons son extension naturelle: les filtres de dimension infinies. L'extension de la théorie aux filtres de dimension infinies permet d'obtenir une formule asymptotique qui, une fois tronquée, sert de méthodologie de réglage. Nous expliquons sous quelles conditions un choix approprié de gains garantit la convergence dans l'espace des fonctions de Sobolev de type H^1 .

GENERAL INTRODUCTION

Performance and environmental requirements of Diesel engines have steadily increased over the last thirty years, which in turn has required an increase in the sophistication of employed control strategies. Advances in combustion strategies over this period have been one of the keys in meeting the demands. Lately, the Highly Premixed Combustion mode (HPC) – including Homogeneous Charge Compression Ignition (HCCI) – has become of major interest. It requires the use of high Exhaust Gas Recirculation (EGR) rates. Simultaneous ignition in the whole combustion chamber is performed and controlled. EGR improves mixing and dilution in the cylinders, and, eventually, reduces pollutant formation. However, increasing the EGR rate tends at destabilizing the combustion. A trade-off must be found between performance (in terms of low pollutant emissions) and combustion stability. The precise control of the mixture entering in the cylinder is needed.

We consider here three different time-scales.

1. The fastest ones (around 2kHz) are related to combustion. The ignition in the combustion chamber last for few crank angle degrees (which corresponds at $500\mu\text{s}$ for 6° crank angle at 2000 rpm). In the context of real time control, this frequency range (more than 2 kHz) is considered as high frequency.
2. The intermediate one (around 50Hz) corresponds to the engine torque productions scale and the engine cycle (corresponding to 60 ms at 2000 rpm). It corresponds to the overall combustion process. This is also the timescale of the fuel path: the injection parameters are updated from one cycle to another one.
3. The slow one (around 1 Hz) is relative to the air path dynamics (around 0.5 s for low load operating point or a high operating point when the turbocharger dynamics is the limiting factor).

The thesis is divided into three parts

- Part I: HCCI dynamics and control problems.
- Part II: Air path control and cylinder balancing.
- Part III: Estimation for linear-time periodic systems.

Part I. — In this part, we detail the several steps of engine combustion. This description points out the main variables affecting the combustion. To control the combustion, it appears desirable to know what is aspirated in the cylinder (i.e. the total mass of gas and its composition) and how much and when fuel is injected. In this part, we present a physics-based description of the engine dynamics and stress the main relationship between actuators and combustion variables.

Chapter 1 is dedicated to the description of the Diesel engine. We present the several steps of the combustion and stress the main variables impacting on the combustion process.

Chapter 2 describes the main effects of each actuator on the combustion process. We investigate the impact of air path actuators (EGR valve and turbocharger) and fuel path actuators (injection timing and quantity) on the cylinder pressure and the engine performance in terms of noise, torque production and pollutant emissions.

Chapter 3 presents several control issues to be solved in order to run the engine over an usual operating range including steady-states and transients. Three main problems are defined.

1. Air path control: The goal is to estimate and to control the masses entering in the cylinders (fresh air and burned gas).
2. Cylinder balancing: The goal is estimate and control the combustion parameter in order to guarantee that all the cylinders have the same combustion in any steady-state regime.
3. Fuel path control: During large transient, the fuel path (50hz) must follow the slower air path transient (1Hz).

Solving the first two problems is a requirement to run the engine. If the last problem is ignored, unacceptable noise and pollutant emissions in transient will prevent from reaching commercial specifications.

Part II. — This part contains solutions to the first two control problems presented in Chapter 3 of Part I.

In Chapter 4, we present a control scheme for the air path. The objective is to control the masses aspirated by the cylinder ($M_{asp,air}$ and $M_{asp,bg}$) with the two air path actuators (EGR valve and the Variable Geometry Turbocharger). In practical applications, the considered masses can not be measured. Yet, equivalent variables can be considered. Controlling those two masses is equivalent to controlling the intake pressure P_{int} (being an image

of $M_{asp,air} + M_{asp,bg}$) and the burned gas rate F_{int} (representing to ratio $\frac{M_{asp,bg}}{M_{asp,air} + M_{asp,bg}}$). In this study, experimental results are reported on a 4 cylinder HCCI engine. We expose results for torque transient and also during driving phases of the eurocycle. This work has been published in [31, 27].

In Chapter 5, we address the cylinder individual Air Fuel Ratio estimation and control problems. The AFR is a representation of the composition of the gas in the cylinder at the end of the combustion. Cylinder individual AFR unbalances reflect a variability in the combustion. This variability can be measured on the single sensor located behind the turbine. Comparisons and experimental results are reported. Some closed loop results are exposed. This work appears in [32, 34, 37, 33, 93].

In Chapter 6, we address the combustion torque estimation problem. The combustion torque characterizes the performance of the engine. We do not have a direct measurement of this torque but of the instantaneous engine speed located at the end of the transmission. The instantaneous engine speed is the output of a cascade consisting of a first periodic linear system (crankshaft-connecting rod) and a second linear system (transmission dynamics) fed by a periodic combustion torque. High frequency observers are designed and validated experimentally. This work appears in [22, 23, 24, 21].

Part III. — As seen in the previous part, estimation of periodic systems driven by periodic unknown inputs is very useful in automotive engine estimation problems. Kalman filters provide an estimation of this excitation but at the expense of a high computation burden. As an alternative, we propose linear periodic observers based on averaging techniques.

In Chapter 7, we consider $\dot{x} = A(t)x + A_0(t)w(t)$, $y = C(t)x$, $x \in \mathbb{R}^n$, $w \in \mathbb{R}^m$, $y \in \mathbb{R}^p$, ($m \leq p \leq n$) where $A(t)$, $A_0(t)$, and $C(t)$ are T_0 -periodic matrices. T_0 is assumed to be known and the T_0 -periodic input signal $w(t)$ is unknown but is assumed to admit a finite dimensional Fourier decomposition. We propose a technique to estimate w from the measurements y . In both full state and partial state measurement cases, we propose an asymptotic observer for the coefficients of the Fourier decomposition of $w(t)$. In this situation, standard estimation techniques based on Kalman filters are sometimes discarded because of their relative high computational burden. By contrast, the proposed technique is well suited to such real-time system requirements. This work appears in [30, 29].

In Chapter 8, we address the case of an infinite number of harmonics (w is a series) in the case $n = p$. Convergence is guaranteed under some hypothesis. The extension of the theory to the infinite dimensional case provides a simple asymptotic gain design that, when truncated, can successfully serve as a tuning methodology. We explain why such gain design guarantees convergence in Sobolev functional space of H^1 type.

NOTATIONS AND ACRONYMS

Acronyms

AFR	Air-Fuel Ratio
BGR	Burned Gas Rate
CI	Compression Ignition
CHRR	Combustion Heat Release Rate
DI	Direct Injection
ECU	Electronic Control Unit
EGR	Exhaust Gas Recirculation
HCCI	Homogeneous Compression Compression Ignition
HPC	Highly Premixed Combustion
IVC	Intake Valve Closing
IMEP	Indicated Mean Effective Pressure
LNT	Lean NO _x Trap
rpm	Revolutions per Minute
SI	Spark Ignition
TDC	Top Dead Centre
TWC	Three Way Catalytic converter
UEGO	Universal Exhaust Gas Oxygen sensor
VGT	Variable Geometry Turbocharger
VVA	Variable Valve Activation

Engine notations

Symb.	Quantity	Unit
D	Flow	kg.s ⁻¹
F	Burned gas fraction	-
J	Inertia	kg.m ⁻²
M	Mass	kg
n	Number	-
N	Speed	rad.s ⁻¹
O	Normalized opening valve lift	
P	Pressure	Pa
\mathcal{P}	Power	W
Q	CHRR	
R	Ideal gas constant	J.(kgK) ⁻¹
S	Normalized effective area	
t	time	s
T	Temperature	K
V	Volume	m ³
α	Crank angle	rad
γ	Specific heats ratio	-
τ	Delay	s
λ	Normalized AFR	-
ϕ	Equivalent ratio	-
η_{vol}	Volumetric efficiency	-

Subscripts applied to D, M, P, T, V

asp	aspirated into the cylinders at IVC
air	fresh air
ai	auto ignition
amb	ambient
bg	burned gas
comp	compressor
cyl	cylinder
e	engine
egr	exhaust gas recirculation
exh	exhaust manifold
i	coming from cylinder i
inj	injected
int	intake manifold
post	after the turbine
sp	set point
turb	turbine
vg	variable geometry turbocharger

Control notations

Fields of Numbers

\mathbb{C}	complex numbers
i	the imaginary unit, i.e. $i^2 = -1$
\mathbb{N}	integer numbers
\mathbb{R}	real numbers
\mathbb{R}^+	strictly positive real numbers

Functional spaces

ℓ_n^j	$\{\{x_k\}_{k \in \mathbb{Z}} \in (\mathbb{R}^n)^{\mathbb{Z}} / \sum_{k \in \mathbb{Z}} \ x_k\ _n^j < +\infty\}$
H_n^1	$\{\{x_k\}_{k \in \mathbb{Z}} \in (\mathbb{R}^n)^{\mathbb{Z}} / \sum_{k \in \mathbb{Z}} (k^2 + 1) \ x_k\ _n^2 < +\infty\}$
Ω	$\mathbb{R}^n \times H_m^1$
L_n^2	$\{t \mapsto x(t) \in \mathcal{C}^0([0, +\infty[, \mathbb{R}) / \int_0^{+\infty} \ x(t)\ _n^2 dt < +\infty\}$
$L_{n, \text{Loc}}^2([t - T_0, t])$	$\{t \mapsto x(t) \in \mathcal{C}^0([t - T_0, t], \mathbb{R}) / \int_{t-T_0}^t \ x(s)\ _n^2 ds < +\infty\}$

CONTENTS

Introduction Générale	ix
General Introduction	xiii
Notations and Acronyms	xvii
Acronyms	xvii
Engine notations	xviii
Control notations	xix
Part I. HCCI dynamics and control problems	1
Présentation de la Partie I	3
Presentation of Part I	5
1. From conventional Diesel to HCCI engine	7
1.1. Introduction	7
1.2. Diesel engine	8
1.3. Why HCCI combustion?	18
1.4. HCCI combustion properties	20
2. Diesel engine control basics	25
2.1. Introduction	26
2.2. Torque control structure	26
2.3. Air path actuators impact on the combustion	28
2.4. Fuel path actuators impact on the combustion	33
3. Control problems	37
3.1. Introduction	38

3.2. Air path control issues	39
3.3. Cylinder balancing issues	42
3.4. Fuel path control issues	47
Part II. Air path control and cylinder balancing	51
Présentation de la Partie II	53
Presentation of Part II	55
4. Air path control	57
4.1. Introduction	58
4.2. Control problem	60
4.3. Intake manifold modelling	60
4.4. System properties	63
4.5. Air path observer	68
4.6. Air path feedforward control	79
4.7. Air Path Control Feedback	87
4.8. Experimental results	89
4.9. Conclusions and Future work	95
5. Cylinder individual Air/Fuel Ratio estimation	97
5.1. Introduction	97
5.2. Modelling	99
5.3. Cylinder-individual AFR nonlinear observer	103
5.4. Cylinder-individual AFR Kalman filter	105
5.5. Experimental Results	109
5.6. Observers implementation	110
5.7. Robustness toward parametric errors	115
5.8. Experimental closed-loop validation	117
6. Indicated torque estimation	119
6.1. Introduction	119
6.2. Transmission Dynamics inversion	121
6.3. Indicated torque estimation	124
6.4. Conclusions	131
Part III. Estimation for linear-time periodic systems	133
Présentation de la Partie III	135
Presentation of Part III	137

7. Periodic input estimation for linear periodic systems	139
7.1. Introduction	140
7.2. Problem statement and observer design	141
7.3. Convergence results in the case of full state measurement	144
7.4. Convergence results in the case of time invariant partial state measurement ..	145
7.5. Convergence results in the case of time periodic partial state measurement ..	148
7.6. Other applications	153
8. H^1 periodic input estimation for linear bounded systems with full measurement	159
8.1. Introduction	159
8.2. Problem statement and observer design	160
8.3. Convergence proof	162
A. Personal Publications and Patents	167
B. Experimental setup	171
B.1. NADI TM engine configuration	171
B.2. Experimental set up	172
C. From simulation to control	175
C.1. Engine Simulator Design	175
C.2. From Reference Simulator to Real Time Simulator	179
D. Convergence of the periodic Kalman filter	183
D.1. Combustion Torque estimation using Kalman filtering	183
D.2. Individual AFR estimation convergence proof	188
Bibliography	193

PART I

HCCI DYNAMICS AND CONTROL PROBLEMS

PRÉSENTATION DE LA PARTIE I

Cette partie décrit les principaux éléments constitutifs du moteur et de sa dynamique. Nous détaillons les variables qui jouent un rôle important dans le processus de combustion. Comme nous le rappelons, la combustion Diesel se décompose en plusieurs séquences. Tout d'abord, les gaz, l'air et les gaz brûlés, sont aspirés dans le cylindre. Ensuite, la compression fait augmenter la température et la pression dans le cylindre. Le carburant est injecté et enfin, après un retard d'auto-inflammation, la combustion se produit. Pour contrôler le processus de combustion, nous cherchons à connaître précisément la masse totale, la composition et la température de ce qui est aspiré dans le cylindre et déterminons quand et comment injecter le carburant.

Le chapitre 1 est dédié à la description d'un moteur Diesel. Nous présentons les différentes étapes du processus de combustion. Un modèle de dégagement de chaleur est proposé, dans lequel apparaissent les variables principales intervenant au cours de la combustion. Ensuite, nous expliquons les problèmes induits par le mode de combustion Diesel, principalement en terme d'émissions polluantes. Nous détaillons pourquoi il est nécessaire de recourir à la combustion dite homogène (HCCI Homogeneous Charge Compression Ignition) qui permet de limiter les émissions polluantes. Une grande partie des éléments de ce chapitre a été publié dans [58].

Dans le chapitre 2, nous décrivons la structure de contrôle pour moteur Diesel développé à l'IFP. Nous examinons l'impact de chaque actionneur sur le processus de combustion. La structure de commande dite, "en couple", visant à contrôler le couple fourni par le moteur, est étudiée. Nous détaillons les étapes qui permettent de calculer les consignes des actionneurs, étant donnée une demande en couple du conducteur fixée. Ensuite,

nous donnons une interprétation de l'évolution des caractéristiques du mélange aspiré dans le cylindre (masse totale, composition et température), lorsque les consignes des actionneurs varient. En résumé, nous étudions les effets des commandes sur le processus de combustion et sur les performances du moteur. Ces performances sont exprimées en terme de bruit, de couple fourni et d'émissions polluantes. Enfin, nous nous intéressons à la gestion de l'injection. Le problème considéré se résume à deux questions : "quel est le moment le plus opportun pour injecter le carburant dans le cylindre?" et "quelle quantité doit-on en injecter?" En particulier, nous expliquons comment améliorer les performances du moteur. Moduler le temps d'injection et utiliser l'avance à l'injection permettent de réduire le bruit et les émissions polluantes tout en fournissant le couple demandé. Nous présentons des résultats de simulations obtenus avec le logiciel AMESim [63], qui illustrent les effets des variables de contrôle sur le processus de combustion.

Le contrôle de la combustion en mode HCCI est complexe. De petites différences entre le mélange dans le cylindre (air- gaz brûlés - carburant) et le mélange de référence peuvent avoir des conséquences sérieuses: bruits, augmentation des émissions de polluants et même extinctions d'un ou plusieurs cylindres. Dans le chapitre 3, nous proposons de séquencer le problème général du contrôle de la combustion en trois sous problèmes.

Le contrôle de la boucle d'air : Dans un premier temps, nous cherchons à contrôler les masses aspirées dans le cylindre (air frais et gaz brûlés).

Le contrôle cylindre à cylindre : Il s'agit du problème d'équilibrage entre les cylindres en dépit de la variabilité des éléments techniques constitutifs (notamment les injecteurs). En effet, alors que chaque injecteur reçoit la même consigne, on constate que tous les cylindres n'ont pas le même comportement.

Le contrôle de la boucle de fuel : Enfin, pour garantir les caractéristiques du mélange dans le cylindre il est nécessaire de ralentir la dynamique de la boucle de fuel pour l'adapter à celle de la boucle d'air (typiquement dix fois plus lente).

Comme nous le montrons expérimentalement sur un moteur HCCI, les deux premiers problèmes sont essentiels au fonctionnement du moteur. Le troisième n'est pas primordial. En revanche ne pas le résoudre revient à accepter un niveau élevé de bruit et d'émission de polluants en transitoire. Ce qui est en contradiction avec une utilisation industrielle. C'est la prochaine étape de notre travail.

PRESENTATION OF PART I

This part describe the main engine dynamics and the key variables influencing the combustion process. The Diesel engine combustion consists of several steps. First of all, gas (air and burned gas) are aspirated into the cylinder. Then, the compression increases the temperature and the pressure in the cylinder. Fuel is injected and finally, after the auto-ignition delay, combustion occurs. This simplified description points out the main variables affecting the combustion. To control the combustion, it is desired to know what is aspirated into the cylinder (i.e. the total mass of gas and its composition) and how much and when fuel should be injected. Most of the material contained in this part can be found in the classic reference [58].

Chapter 1 is dedicated to the description of the Diesel engine. Step by step, the combustion process is presented. A model of heat release is proposed, stressing the main variables impacting on the combustion process. Then, we expose the limitations of the “classic” Diesel combustion in terms of pollutant emissions. These are inconsistent with future pollutant emissions (such as Euro V). Naturally, this point justifies efforts towards realizing a cleaner combustion. We explain the role of the Exhaust Gas Recirculation (EGR) in the context of the HCCI combustion (Homogeneous Charge Compression Ignition). EGR allows a better mixing and dilution in the cylinders and leads to a combustion with less pollutant formation.

Chapter 2 describes the main effects of each actuator on the combustion process. We expose the torque control structure usually found in commercial-line engine. More precisely, we explain the several steps to turn the driver’s torque demand into actuator set points. The impact of the air path actuators (EGR valve and turbocharger) on

the gas aspirated into the cylinder (total mass aspirated, composition, temperature) is investigated. We detail their effects on the cylinder pressure and the engine performance in terms of noise, torque production, and, pollutant emissions. Finally, we describe the injection system and explain how sophisticated injection timing can produce lower NO_x . Also, we explain the impact of the injection timing and quantity on combustion in terms of noise, torque production, and pollutant emissions.

Chapter 3 presents several control issues to be solved in order to run the engine over an usual operating range including steady-states and transients. Three main problems are defined. The first problem is the air path control. Here, it is desired to control the masses (fresh air and burned gas) in the cylinders. We describe the particularities of this nonlinear, coupled, and non minimum phase dynamics. The second problem is cylinder balancing. The goal is to guarantee that all the cylinders have the same combustion. Even with identical actuator set points, the cylinders do not exactly have the same combustion. This unbalance leads to a lower overall efficiency and also increases higher pollutant emissions. Such unbalance is mainly seen at low load operating points where we are running with high burned gas rate and low fuel injection quantity. These conditions precisely correspond to the HCCI combustion mode and lead to malicious noise and possible stall. Finally, the last problem we consider is the fuel path control and its adaption to slower air path dynamics.

CHAPTER 1

FROM CONVENTIONAL DIESEL TO HCCI ENGINE

Chapitre 1. — D'un moteur Diesel vers un moteur HCCI

Dans ce chapitre, nous décrivons les différents éléments d'un moteur Diesel. Nous présentons les différentes étapes du processus de combustion. Un modèle de dégagement de chaleur est proposé. Dans ce modèle apparaissent les variables principales intervenant sur la combustion. Ensuite, nous expliquons les problèmes induits par le mode de combustion Diesel, principalement en terme d'émissions polluantes. Nous détaillons pourquoi il est nécessaire de recourir à la combustion dite homogène (HCCI Homogeneous Charge Compression Ignition) qui permet de limiter les émissions polluantes. Une grande partie des éléments de ce chapitre a été publiée dans [58].

1.1. Introduction

After carbon dioxide (CO_2) was identified as a greenhouse gas contributing to global warming, Diesel engines have emerged as an alternative to gasoline engines due to their low fuel consumption and low CO_2 emission. While carbon monoxide (CO) emissions are negligible in CI engines due to lean operation and emissions of unburnt hydrocarbons (HC) that can be handled with oxidation catalysts, the emissions of oxides of nitrogen (NO_x) and particulate matter (PM) are a main concern.

First of all, we present a “conventional” Diesel engine. A scheme of a 4-cylinder engine is presented in Figure 1.1. We describe the various parameters influencing the combustion and the different components of the engine (turbocharger, injection system, . . .). Then, we explain the limitation of Diesel combustion concerning pollutant reduction and the need

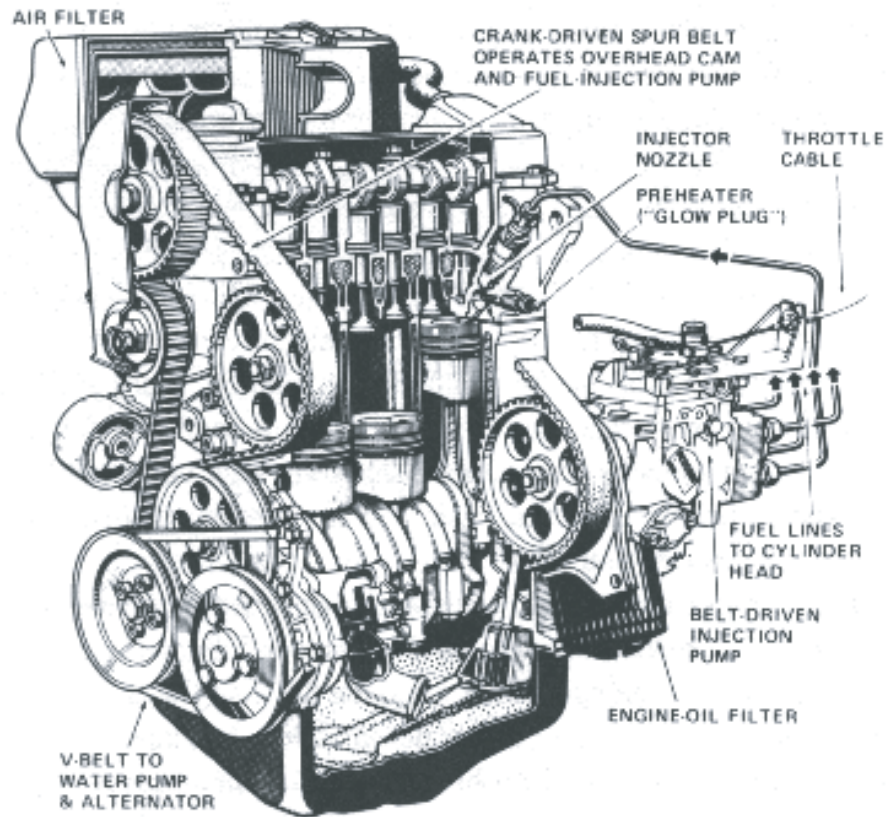


FIGURE 1.1. 4-cylinder Diesel engine scheme.

for a cleaner combustion. We explain the role of the exhaust gas recirculation (EGR) on the combustion and detail how the homogeneous combustion (HCCI combustion) limits the pollutant emissions. Most of the material contained in this chapter can be found in the classic reference [58].

1.2. Diesel engine

1.2.1. Diesel engine combustion. — The combustion process is divided into a pre-mixed phase and a diffusion phase. During the pre-mixed phase, the fuel is injected and mixed. After a small time delay, the mixture ignites and burns under premixed conditions. During the diffusion phase, the remaining part of the fuel that is injected burns at a rate

controlled by the mixing of the fuel with the surrounding air. To ensure good mixing with the air, the injected fuel spray has to break up in small droplets. This is achieved by high injection pressures (ranging from 1000 to 2000 bar, depending on the injection system) and small orifices in the injector nozzle. The power output is controlled by regulating the fuel flow while the air flow is un-throttled, resulting in a varying air-fuel ratio. The power output limit is determined by the smoke limit. At this limit, there is too much fuel to properly mix with the available air, so the fuel is only partially burned, resulting in a large amounts of soot emissions or smoke. Power is also limited by the amount of air aspirated by the engine because combustion is lean. Therefore, Diesel engines are often supercharged. In more details, the Diesel combustion process from start of injection to the end of combustion can be divided into several steps as explained in [58]. We now detail these phases.

1.2.1.1. Steps of the combustion process. — These steps are represented in Figure 1.2.

1.2.1.1.1. Initial conditions. — During the intake, gas from the intake manifold (fresh air and burned gas) are aspirated and mixed with the residual gas still present in the cylinder. Compression increases the cylinder pressure and temperature.

1.2.1.1.2. Fuel Injection. — First, fuel is injected by the injection system into the cylinder at the end of the compression stroke, right before the desired start of combustion. The liquid fuel, usually injected at high velocity by the high pressure common rail injection system, atomizes into small drops and penetrates into the combustion chamber.

1.2.1.1.3. Vaporization and mixing. — Then, the fuel vaporizes and partially mixes with the gas previously trapped into the cylinder (these gas are at high temperature and high pressure due to the compression phase). The mixing rate depends on both the turbulence in the combustion chamber and on the air entrainment into the spray. Turbulence is caused by the instability of the shear layer and the high velocity of the fuel. Since mixing limits the combustion rate, the maximum speed is limited by the mixing rate.

1.2.1.1.4. Auto ignition delay. — The ignition delay is the time between the start of injection and the start of ignition. The magnitude of this delay is determined by the time needed for evaporation and mixing of the fuel and air. This delay is characterized by the chemical delay time, τ_{ai} , which depends on the intake pressure and temperature. The combustion occurs when the integration of the delay (1.1) reaches the value 1:

$$\int_0^{\tau_{ai}} AP_{cyl}^{-n} e^{\frac{T_{act}}{T_{cyl}}} = 1 \quad (1.1)$$

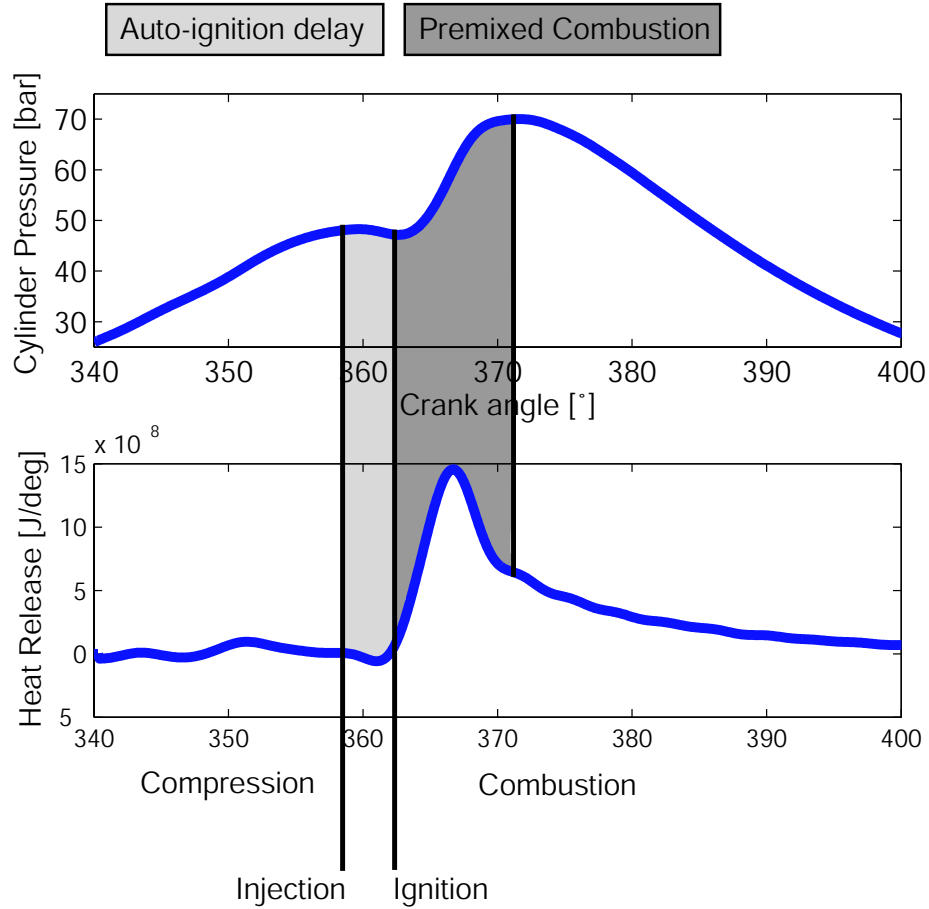


FIGURE 1.2. Experimental conventional Diesel combustion with the several steps of the combustion process. Top: Cylinder pressure. Bottom: Heat release.

where A and n are the parameters of the auto-ignition delay, T_{act} is the activation temperature defined for the auto ignition. T_{cyl} and P_{cyl} are respectively the average temperature and pressure in the combustion chamber.

1.2.1.1.5. Ignition and combustion. — Finally, since air temperature and pressure are above the fuel ignition point, spontaneous ignition of portions of the already-mixed fuel and air occurs after the auto ignition delay. The combustion starts with a premixed-type combustion. This premixed combustion is characterized by a strong heat release. It is due to the whole combustion of this mixing formed during the delay. Ignition continues until the desired amount of fuel has entered the cylinder. Atomization, vaporization, and fuel-air

mixing continue until all fuel has passed through each process. In addition, mixing of the air remaining in the cylinder with burning and already burned gas continues throughout the combustion and expansion process.

Combustion is a complex phenomena. Nevertheless, a lot of effort was done on the modelling. This provides guidelines and physical understanding on what is happening in the cylinder. In the next subsection, we describe a modelling approach of the combustion stressing out the main variables influencing the combustion.

1.2.1.2. Combustion modelling. — For conventional CI combustion mode, the injection rate is the main parameter which controls the turbulent scale and energy level in the chamber. It mainly controls the combustion process. In system simulation modelling [40, 41, 10, 6], the conventional CI combustion can be defined using a simple diffusion flame and because the injection occurs near the combustion TDC, the auto-ignition delay is short and can be neglected [41]. This type of model is suitable for single injection, but, in the case of multi-injections, the introduction of an auto-ignition model becomes important [10]. Moreover, compared with the conventional CI combustion mode, the pre-mixed part of the combustion can not be neglected any more and when the EGR rate increases, a cold flame phenomenon also appears [40, 10, 102, 97]. A representation of this cold flame on an experimental HCCI combustion is represented in Figure 1.3.

As presented below, for the Diesel conventional CI combustion mode, many studies [40, 10, 61] have shown that the diffusion combustion is the main physical phenomenon in the combustion process. This model is based on the works of Chmela [40, 41] and Jaine [64]. In this approach, the Combustion Heat Release Rate (CHRR) is related to the available vapor fuel mass in the chamber M_f . This quantity can be computed as the difference between the evaporated fuel mass $M_{f,v}$ and the burned fuel mass. A second assumption is that the local density of the turbulent kinetic energy determines the rate of mixing of the fuel vapor and fresh air and thus the CHRR. In conventional Diesel engines, the essential source of turbulent kinetic energy is the kinetic energy introduced by the fuel injection due to sprays. Using these assumptions, the CHRR Q is calculated using 2 functions f_1 and f_2 , as presented in Equation (1.2)

$$\frac{dQ}{d\alpha} = C_{mode} f_1(M_f, Q) f_2(k, V) \quad (1.2)$$

where M_f is the available vapor fuel mass, Q is the CHRR, k is the turbulent kinetic energy and V is the combustion chamber volume. The functions f_1 and f_2 are

$$f_1(M_f, Q) = M_k - \frac{Q}{LCV} \quad \text{and} \quad f_2(k, V) = e^{C_{rate} \frac{\sqrt{k}}{\sqrt{V^3}}} \quad (1.3)$$

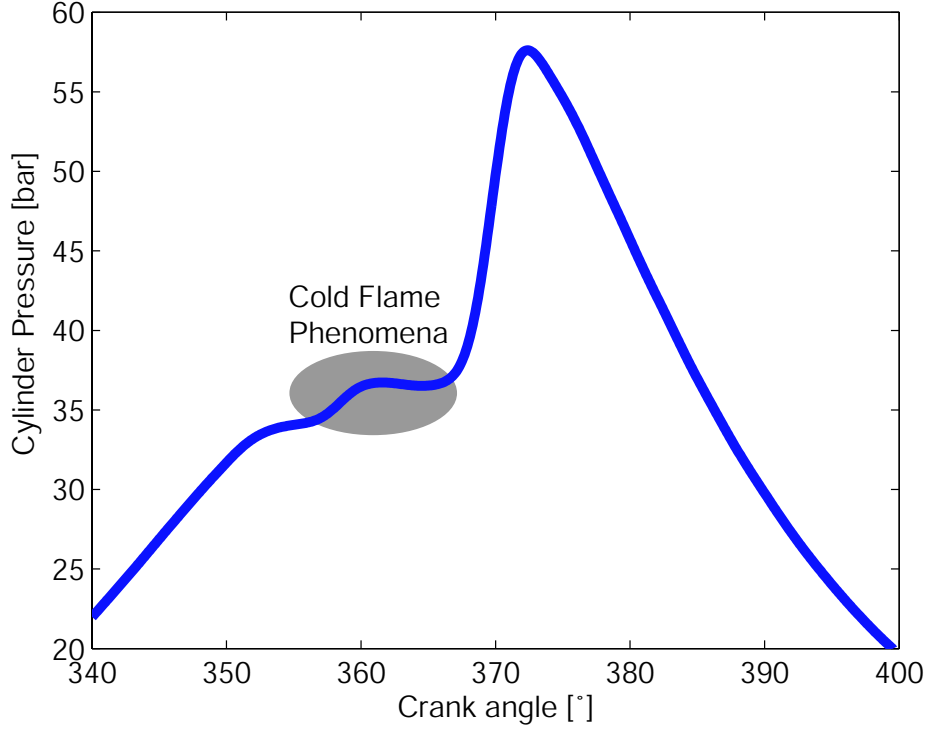


FIGURE 1.3. Experimental HCCI Diesel combustion. Cylinder pressure trace with the cold flame phenomena.

with LCV the lower calorific value, C_{mode} and C_{rate} are the model parameters to fix the effect of turbulence on the combustion process. To introduce the effects of the EGR rate on the combustion process, Equation (1.2) is modified as

$$\frac{dQ}{d\alpha} = C_{mode}(1 - X_{bg})^{\beta} f_1(M_f, Q) f_2(k, V) \quad (1.4)$$

where X_{bg} is the molar fraction of burned gas. Because increasing the EGR rate decreases CHRR, β must have a positive value.

The physical factors that affect the development of the fuel vaporization and the air charge state impact on the combustion by modifying torque production, noise, pollutant production, and ignition delay. The air charge depends on the quantity of gas entering into the cylinder during the compression ($M_{asp,air}$ and $M_{asp,bg}$) and their temperature ($T_{asp,gas}$), the fuel vaporization depends on the injection timing and quantity (t_{inj} and M_{inj}). The air charge is provided by the air path of the system (turbocharger and EGR pipe). These

elements are detailed in subsection 1.2.2. The injection system controlling the fuel path is explained in subsection 1.2.3.

1.2.2. Air path elements. — The air loop circuit has to be suitable for both running conditions at full load and at partial load. Because air capacity is an important constraint on the amount of fuel that can be burned in the Diesel engine, and therefore on the engine power, turbocharging is used extensively. The air path system consists of two parts: the turbocharger and the Exhaust Gas recirculation (EGR).

The turbocharger is a turbine driven by the exhaust gas and connected via a common shaft to the compressor, which compresses the air in the intake. Figure 1.4 represent a

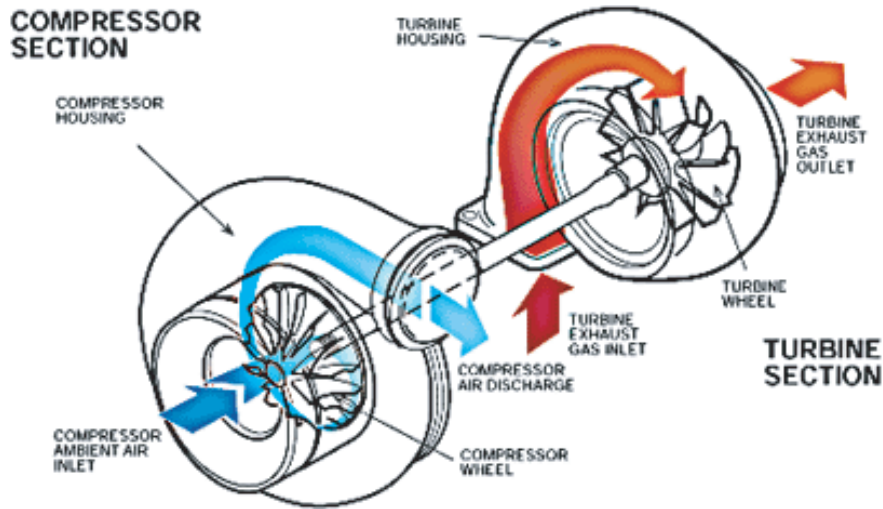


FIGURE 1.4. Turbocharger scheme from [45].

scheme of a turbocharger. The rotational speed of the turbocharger shaft N_{turb} can be derived from a power balance between the turbine \mathcal{P}_{turb} and the compressor side \mathcal{P}_{comp}

$$\frac{d}{dt}\left(\frac{1}{2}J_{turb}N_{turb}^2\right) = \mathcal{P}_{turb} - \mathcal{P}_{comp}$$

where J_{turb} is the inertia of the turbocharger.

1.2.2.1. Compressor. — In order to derive an equation for the compressor power, the first law of thermodynamics is applied. It states that (neglecting heat losses) the compressor power is related to the mass flow through the compressor D_{air} and the total change of

enthalpy by

$$\mathcal{P}_{comp} = D_{air}(h_{comp} - h_{amb}) = D_{air}c_p(T_{comp} - T_{amb})$$

where T_{amb} and T_{comp} are the ambient and the compressor temperature respectively. The second equality assumes constant specific heats. Assuming that the compression process is isentropic, the compressor power reads

$$\mathcal{P}_{comp} = D_{air}c_pT_{amb}\frac{1}{\eta_{comp}}\left(\left(\frac{P_{comp}}{P_{amb}}\right)^{\frac{\gamma-1}{\gamma}} - 1\right)$$

where η_{comp} is the compressor efficiency, P_{amb} and P_{comp} are the ambient and compressor pressure and γ the specific heat ratio. In order to calculate the compressor power, the compressor efficiency and mass flow have to be known. These variables are highly nonlinear functions of the pressure ratio across the compressor and the turbocharger shaft speed. Those variables are represented in Figures 1.5 and 1.6.

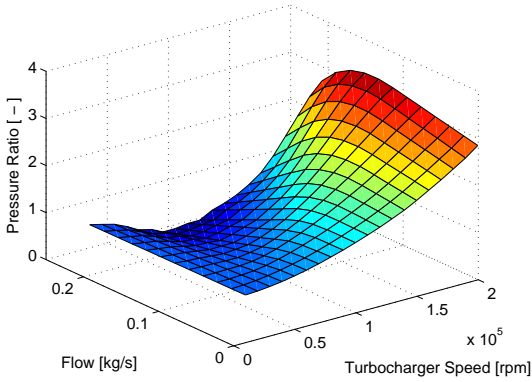


FIGURE 1.5. Compressor map. Pressure ratio at the compressor w.r.t. the flow through the compressor D_{air} and the turbine crankshaft speed N_{turb} .

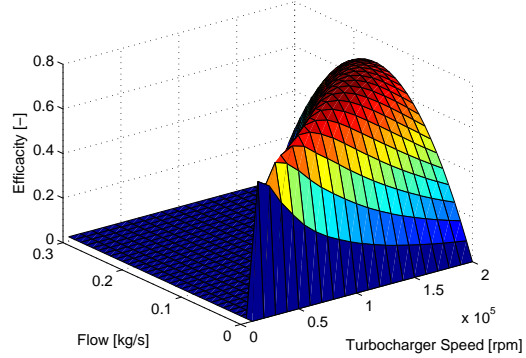


FIGURE 1.6. Compressor map. Efficiency η_{comp} at the compressor w.r.t. the flow through the compressor D_{air} and the turbine crankshaft speed N_{turb} .

1.2.2.2. Turbine. — Similarly, the turbocharger power is related to the mass flow through the turbine D_{turb} and the total change of enthalpy. This results in

$$\mathcal{P}_{turb} = D_{turb}c_pT_{post}\eta_{turb}\left(1 - \left(\frac{P_{post}}{P_{exh}}\right)^{\frac{1-\gamma}{\gamma}}\right)$$

where η_{turb} is the turbine efficiency, T_{post} and P_{post} are the temperature and pressure after the turbine, P_{exh} the exhaust manifold pressure and γ the specific heat ratio. Again, the turbine flow D_{turb} and isentropic efficiency η_{turb} are mapped versus the pressure ratio across the turbine and the turbocharger shaft speed. However, these variables also depend on the geometry of the turbocharger. They replace the conventional waste gate in order to avoid overspeeding at high engine loads without sacrificing the low load performance. Very large amount of data are needed to obtain reasonably accurate fit. Those variables are represented in Figures 1.7 and 1.8. We control the geometry of the turbine (VGT) and its

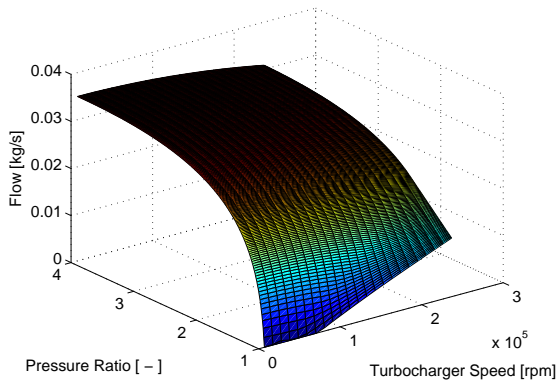


FIGURE 1.7. Turbine map. Flow through the compressor D_{exh} w.r.t. the pressure ratio $\frac{P_{exh}}{P_{post}}$ and the turbine crankshaft speed N_{turb} .

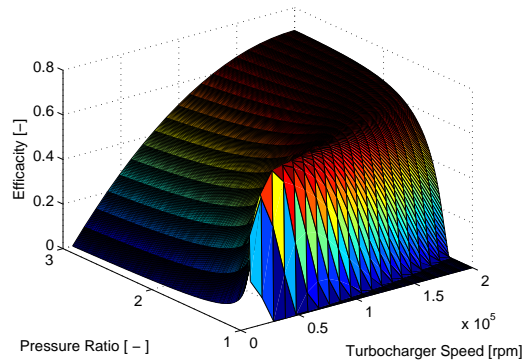


FIGURE 1.8. Turbine map. Efficiency η_{turb} at the compressor w.r.t. the pressure ratio $\frac{P_{exh}}{P_{post}}$ and the turbine crankshaft speed N_{turb} .

discharge with a waste-gate. This leads to a control of the turbocharger crankshaft speed control and then the intake air flow control.

1.2.2.3. Exhaust Gas Recirculation. — The Exhaust Gas Recirculation (EGR) allows to recirculate gas from the exhaust manifold to the intake manifold. The recirculation of exhaust gas through an EGR valve into the intake manifold where it dilutes the incoming fresh air is a well established and efficient means of reducing in-cylinder NO_x emissions (The effects of EGR on the combustion is detailed in subsection 1.4.1). The flow through the EGR pipe, D_{egr} , is driven by the pressure ratio between the exhaust manifold pressure, P_{exh} , and the intake manifold pressure P_{int} and controlled by an EGR valve. Assuming that no mass is accumulated in the EGR system, it can be modelled with static equations rather than with differential equations. The flow through the EGR valve is determined by

the standard orifice flow equation [58]

$$D_{egr} = S_{egr} \frac{P_{exh}}{\sqrt{RT_{exh}}} \sqrt{\frac{2\gamma}{\gamma-1} \left(p_r^{\frac{2}{\gamma}} - p_r^{\frac{\gamma+1}{\gamma}} \right)}$$

with the pressure ratio $p_r = \max\left\{\frac{P_{int}}{P_{exh}}, \left(\frac{2}{\gamma+1}\right)^{\frac{\gamma}{\gamma-1}}\right\}$ in order to describe subsonic as well as choked EGR flow. The effective area S_{egr} is identified as a quadratic polynomial of the normalized valve lift O_{egr} . As described in 1.4.1, the recirculation of exhaust gas raises

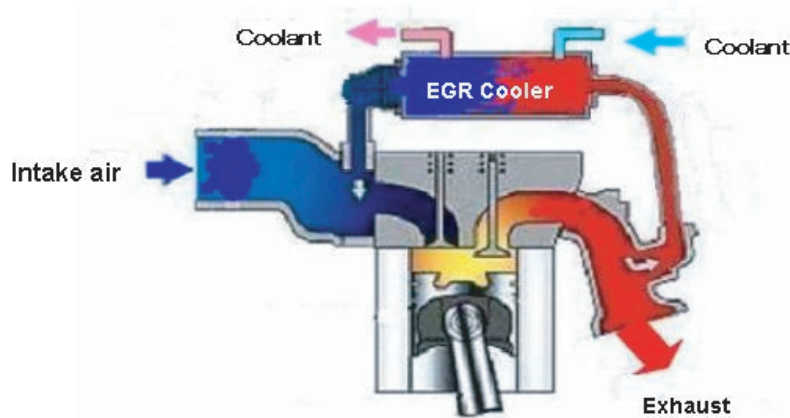


FIGURE 1.9. EGR high pressure scheme.

the temperature of the inlet charge and, consequently, leads to a higher flame temperature resulting in higher NO_x emissions which is the opposite of the initial goal of the EGR. In order to minimise the inlet charge temperature effect, the recycled exhaust gas need to be cooled. The EGR pipe is equipped with a cooler in order to reduce the temperature of the gas coming from the EGR as represented in Figure 1.9.

1.2.3. Fuel path elements. — The Common Rail fuel injection system is widely used nowadays in modern Diesel engines. The main benefits of the system is that it allows to inject the fuel in the cylinder at a very high pressure which implies a better vaporization and mixing, and then a better combustion. Moreover, contrary to pump-injectors, it decouples the pressure generation from the injection timing and duration. These processes

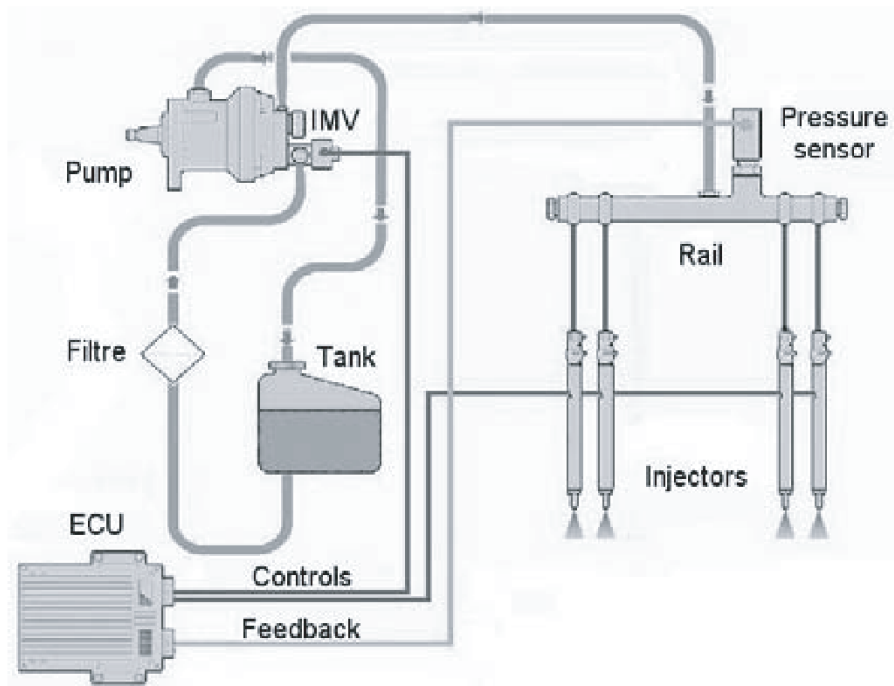


FIGURE 1.10. Scheme of the Common Rail Injection system from [44].

are independent of each other and adjustable over a wide range of operating conditions. The large amount of freedom of injection parameters has opened new opportunities to improve combustion characteristics. The Common Rail Diesel Injection System (see Figure 1.10) is an accumulator injection system. It provides more flexibility than any previous injection system, but it also needs to handle much higher pressure. The high pressure circuit contains a high-pressure pump, a pressure-control valve, a high pressure accumulator (the rail) with a rail-pressure sensor, high pressure connection lines and the injectors (see Figure 1.10). The high-pressure pump forces the fuel into the rail and generates a maximum pressure of nearly 2000 bar. There is one injector for each cylinder and the injectors contain a solenoid or piezo valve which receives a current signal from the ECU to control its position (open or closed). Every time an injection occurs, fuel is aspirated from the rail. This technology enables very short injection, i.e. it is possible to do several injections for the same combustion. We will see in section 2.4 that this possibility enables significant pollutant emission reduction. The pressure control valve attempts to keep the pressure

at the desired level. This control is based on measurements from the rail pressure sensor. With the common rail, one can control the injection timing and the start of injection of fuel in all the cylinders.

1.3. Why HCCI combustion?

From its principle, the Diesel engine is placed at the first rank of the converters of energy at low fuel consumption and minimal carbon dioxide discharge. Until now, these advantages were counterbalanced by emissions of oxides of nitrogen high, a disadvantage difficult to surmount because subordinate to the same principles of Diesel combustion, which are precisely favorable to the output. Facing the pollutant norms, Diesel engine has to evolve to face the new pollutant norms.

1.3.1. Pollutant norms. — Increasingly stringent pollution standards norms have spurred a broad interest in the reduction of global engine emissions as we can see in Table 1.1. Emissions of nitrogen oxides (NO_x) and particulate matter (PM) from Diesel

Passager Cars	PM (mg/km)		NO _x (g/km)		HC (g/km)		HC+NO _x	
	Diesel	Petrol	Diesel	Petrol	Diesel	Petrol	Diesel	Petrol
EURO I (1992-93)	140	-	-	-	-	-	.97	.97
EURO II (1996)	80	-	-	-	-	-	.7	.5
EURO III (2000)	50	-	.5	.15	-	.2	.56	-
EURO IV (2005)	25	25	.25	.08	-	.1	.3	-
EURO V-(2008)	2.5	2.5	.08	.08	.05	.05	-	-

TABLE 1.1. EU emission standards for passenger car including proposal for 2008.

Source: ACID NEWS N^o 3, September 2004.

vehicles are higher than for petrol vehicles. New findings about the harmful health effects of particulates have called for significant reductions in emission limits from Diesel vehicles. The draft Euro V limits would reduce emissions of particulates from diesel cars by 80% compared to Euro IV. Achieving high reduction of NO_x /PM for “classical” CI engine, without increasing too much CO_2 emission seems impossible. Lately, two strategies have emerged to face this problem: post-treatment and direct combustion emissions reduction.

The three way catalytic converter (TWC) removes CO and HC efficiently at lean air fuel ratios, but has a low removal efficiency for nitrogen oxides (NO_x) which must be reduced.

Research has focused on the catalytic decomposition of NO_x , but, up to now, a suitable catalyst with a significant activity in real exhaust gas has not been identified. A promising technique under investigation for NO_x removal is a LNT (Lean NO_x Trap) located after the TWC in the exhaust system. Under lean operating conditions, the NO_x is accumulated or “trapped” in the LNT. The trapped NO_x is periodically released or “purged” by operating at a stoichiometric or rich air fuel ratio. The released NO_x is reduced to N_2 by CO and H_2 already present in the exhaust gas. By the same way, a particulate filter is used to “trap” the particulates. For Diesel engines, equipments required by post-treatment and implementation issues usually carry high cost premiums. An alternative is to use a cleaner combustion mode. Therefore, the Highly Premixed Combustion mode (HPC), including Homogeneous Charge Compression Ignition (HCCI), has become of major interest in recent years. This combustion principle consists in preparing a highly diluted by burned gas air/fuel mixture, in achieving its simultaneous ignition, and in precisely controlling the combustion for the best performance in terms of efficiency and pollutant emissions. HCCI or HPC combustion takes place in a more or less homogeneous way throughout the bulk of the mixture, where thermal NO_x formation and soot production are known to be much lower than with typical conventional Diesel combustion diffusion flame.

1.3.2. Toward HCCI combustion. — In order to get good performances in terms of torque production, consumption and pollutant emission, it is important to properly mix fuel and air before starting combustion. Historically, the first development axis was to use the common rail for increasing the combustion period. Multi-injections are used to expand the combustion in order to decrease the peak pressure and temperature. While the aimed low temperature combustion allows to reduce drastically the NO_x formation, and, in some cases PM formation, this technique is seriously flawed. In particular,

- It is necessary to avoid wall impingement and promote fuel vaporisation and Air/Fuel mixing to limit PM and HC emissions while preventing oil dilution.
- Stability at high load is problematic: operating conditions at high Fuel/Air equivalence ratio are limited by combustion stability, excessive heat release, knock and noise.
- Stability at low load is also problematic: operating conditions at high BGR are limited by combustion stability, cylinder to cylinder combustion variability and stall.

To summarize, the HCCI combustion mode permits to have very low NO_x and PM emissions but it favors HC and CO emissions and increases noise level and combustion instability.

1.4. HCCI combustion properties

The defining characteristic of HCCI is that the ignition occurs at several places at a time which makes the fuel/air mixture burn nearly simultaneously. There is no direct initiator of combustion. To obtain an homogeneous mixture, the main characteristic is to dilute the air charge with a very large amount of Exhaust Gas Rate (EGR) in the combustion chamber. Recirculating burned gas can be achieved in several ways. The first one is to use Variable Valve Activation (VVA) leading to internal EGR. The second possibility is to use EGR pipes, taking gas from the exhaust line into the intake line.

In this section, we describe the effect of exhaust gas recirculation on the pollutant formation and noise reduction. Then, we present the impact on the architecture of the engine.

1.4.1. On the use of high Exhaust Gas Recirculation. — The recirculation of exhaust gas through an EGR valve into the intake manifold (where it dilutes the incoming fresh air) is a well established and efficient means of reducing in-cylinder NO_x emissions. On the other hand, the reduction of NO_x occurs at the expense of higher PM emissions (due to lower thermal efficiency). In [82, 101, 83, 84, 86, 85] separated several possible effects of EGR on the in-cylinder NO_x production are presented.

1.4.1.1. Effect on the dilution. — The change of in-cylinder oxygen by exhaust gas reduces the availability of oxygen during the combustion. This lowers the temperature of the whole combustion process in the premixed burn as well as in the diffusion flame, where most of the NO_x are created. In fact, the combustion still occurs in a region where the ratio of fuel and oxygen is close to the stoichiometric ratio but now with exhaust gas acting as a diluent. Notice that the dilution effect is the most influential parameter in the NO_x reduction by exhaust gas recirculation. While the dilution of the inlet charge has only a minor effect on the thermal efficiency of the engine, particulate emissions increase significantly while decreasing inlet charge oxygen.

1.4.1.2. Effect on the inlet charge temperature. — The recirculation of exhaust gas raises the temperature of the inlet charge and consequently leads to a higher flame temperature resulting in higher NO_x emissions (although less significantly than the dilution effect). This is a EGR drawback. Moreover, it is observed that an increase in inlet temperature results in substantially higher PM emissions (especially soot). In order to minimise the inlet temperature, the recycled exhaust gas are cooled. The EGR pipe is equipped with a cooler in order to reduce the temperature of the gas coming from the EGR. High cooling

of the EGR allows to extend the HCCI operating range. Nevertheless, when high EGR cooling is applied, condensation in the EGR pipe can appear which limit the temperature of the EGR.

1.4.1.3. Effect on the ignition delay. — While the increase of the inlet charge temperature shortens the ignition delay, the lower oxygen availability increases it. The net effect of EGR is an increase of the ignition delay. This increase potentially affects the combustion by boosting the fuel fraction burnt during the premixed burn and by shifting the auto-ignition towards the combustion chamber wall, however, the lower oxygen availability due to the dilution effect actually reduces the peak rate of premixed burning. This reduced burning rate and the delay of the combustion towards the expansion stroke reduces peak temperatures and pressures and the time the combustion gas spend under these conditions. Thereby, NO_x emissions are reduced (although significantly less than the dilution effect) at the expense of PM emissions and thermal efficiency. Obviously, the ignition delay effect can be compensated (partially) by adjusting the injection timing.

1.4.2. Impact on the EGR on the engine architecture. — The main drawback of Diesel engine is the low power density (since the mixture is always lean, less fuel can be induced in a given cylinder, at atmospheric conditions; in addition, engine top-speeds are lower due to mechanical limitations). This can quite easily be eliminated by supercharging the engines (forcing more air into the cylinder and thus allowing more fuel to be burned in the same volume). At full load, the output torque and power specifications fixe the upper limit of the air mass flow required by the engine according to the geometric compression ratio. The turbocharger choice is defined by the power specification.

When engine load increases in the HPC combustion mode, EGR and fresh air mass flow increase requires high intake pressure which can make the compressor operate near the limit operating range at low engine speed (EGR act as a discharge for the turbocharger). Small compressor size has then to be preferred. But, future target standards for the maximum output power impose an adapted air flow leading to larger compressor size. So, the compressor has to be compatible with both high and low engine speeds. Compressor choice is quite guided by turbocharger development progress which leads to enlarged the compressor operating range. On the other hand, the weak exhaust gas energy available for the turbine at low engine speed, which is further reduced by a high EGR rate, makes turbine efficiency a key parameter to consider for the choice of a turbocharger.

There are different ways to increase the required compressor work. A two stage turbocharger can be used to obtain a higher compression ratio, which allows more air to be

introduced in the engine for a given burned gas mass flow. A variable geometry compressor is also an interesting way to develop by tuning continuously the compressor map to the engine running point. E-boosts and turbocharger electrical assistance are other solutions to compensate the lack of exhaust energy when gas temperature is low. Two means to fulfil the air loop specifications are now described. They are "Conventional air loop circuit" or "High Pressure EGR" and "Modified air loop circuit" or "Low Pressure EGR". Due to the high burned gas mass flows required by engines running in the HPC mode, the EGR circuit has to be designed in both cases to allow a high EGR rate while maintaining low pressure losses which increase fuel consumption. A scheme of the location of the High Pressure EGR and Low Pressure EGR is presented in Figure 1.11.

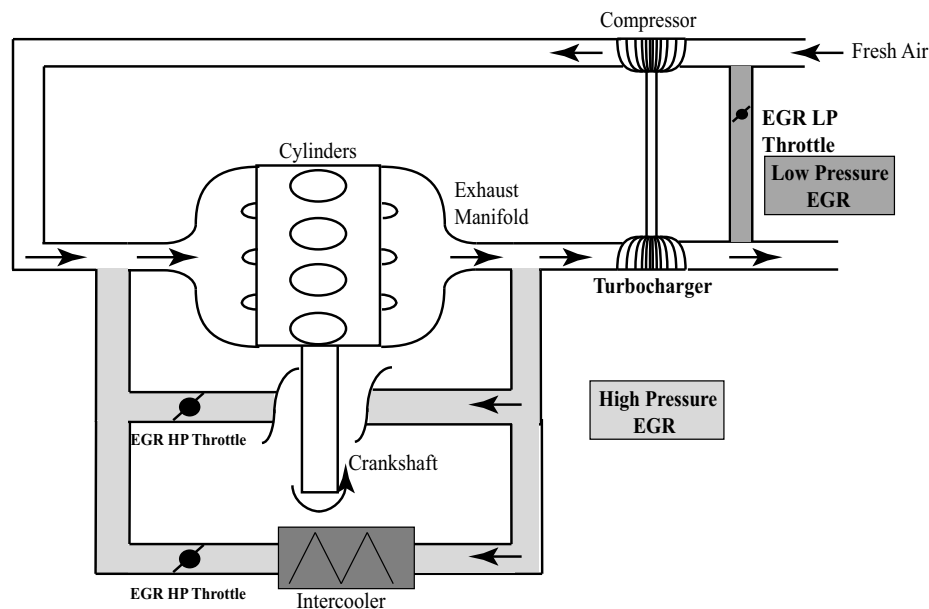


FIGURE 1.11. Schematic view of the High Pressure EGR and Low Pressure EGR on a Diesel engine.

1.4.2.1. High Pressure EGR. — In this EGR circuit layout, burned gas are picked up upstream of the turbine and mixed to fresh air downstream of the compressor. So, only fresh air passes through the compressor. In that case, EGR acts as discharge for the turbocharger. Because the EGR rate used in highly premixed combustion is significantly higher than usually considered in conventional combustion, advanced development of a specific cooler and valve are required both for the permeability aspect and for the fouling

resistance. EGR cooler effectiveness is also an important parameter to be considered because of the large amount of hot burned gas mass flow used.

As described in subsection 1.2.1, we stress out the role of the in-cylinder mixture composition and temperature on the combustion process. Two HP EGR circuit (with and without an intercooler) lead to variable temperature of burned gas. By-passing the EGR cooler is in fact a simple way to vary the burned gas temperature (it is already used on production engines). Notice that by-passing the EGR cooler decrease the delay to go to the intake manifold.s Finally, the EGR rate target has to be reached as closely as possible when the engine runs in transient operations to avoid any combustion noise or uncontrolled smoke peaks. So the short circuit allowed by High Pressure EGR layout is favorable to reduced EGR circuit response time.

1.4.2.2. Low Pressure EGR. — In this EGR circuit layout, burned gas are picked up downstream of the turbine, after the particulate filter and mixed with fresh air upstream of the compressor. Fresh air and burned gas thus pass through the compressor and the turbine. The turbocharger is then used on operating point with better output. Indeed, compressor working points go away from the compressor surge line by increasing gas mass flow. They also are located in an improved compressor efficiency zone. The same positive effect appears in the turbine located across the whole gas mass flow. This turbine operates in a better efficiency zone. Yet, very low pressure difference between the downstream particulate filter and the upstream compressor requires the inlet or exhaust line to be partially closed in order to increase the burned gas mass flow. At this stage of development, the exhaust solution seems to be the best one as it leads to a larger fuel saving. Because burned gas are picked up downstream of the particulate filter, this filter sees the whole gas flow. Its fouling is then faster than in conventional EGR circuit. This must be taken into account for the particulate filter specification. Regarding burned gas cooling, there are greater possibilities than in High Pressure EGR layout because burned gas, which are picked up downstream of the particulate filter, are cleaned. On the other hand, the burned gas to be cooled have lower temperature because there is quite a long distance between the engine exhaust manifold and the particulate filter. Condensation of exhaust gas generates variably corrosive water drops depending on the fuel sulphur content. This EGR configuration also requires an advanced EGR cooler, especially in terms of permeability to save fuel by reducing pumping losses. Because combustion is controlled by in-cylinder burned gas in the HPC combustion mode, BGR has to be the same in each cylinder. As burned gas are mixed with fresh air upstream of the compressor in Low Pressure EGR layout, the relative long distance between the compressor and the inlet manifold significantly helps

obtaining an optimal homogeneous mixture in the engine inlet manifold. This quite long distance leads to higher EGR circuit response time. This can make Low Pressure EGR layout harder to manage in transient operations. Finally, EGR circuit durability in terms of EGR cooler and valve fouling is clearly improved by the use of cleaned burned gas picked up downstream of the particulate filter.

CHAPTER 2

DIESEL ENGINE CONTROL BASICS

Chapitre 2. — Contrôle d'un moteur Diesel

L'objectif du contrôle d'un moteur Diesel est de fournir le couple demandé par l'utilisateur tout en minimisant les émissions polluantes ainsi que le bruit. L'idée de la structure de contrôle développée à l'IFP est de décomposer ce problème en deux sous-problèmes. Une boucle bas-niveau, la boucle d'air, permet d'agir sur le processus de combustion et donc de moduler les performances du moteur en terme de bruit et d'émission polluantes. Les consignes correspondant à cette régulation sont fournies par l'inversion d'une cartographie réalisée expérimentalement.

Ainsi, dans la Section 2.2 nous détaillons les principes de cette inversion, appelée "commande en couple". En particulier nous décrivons les étapes qui permettent de calculer les consignes de la boucle d'air. Ensuite dans la Section 2.3, nous montrons comment les actionneurs de la boucle d'air peuvent influencer sur les caractéristiques du mélange aspiré dans le cylindre. Ces actionneurs permettent par exemple de modifier la teneur en air, la température ou la masse totale des gaz pénétrant le cylindre. Nous expliquons ainsi comment le contrôle de la boucle d'air permet d'agir sur le processus de combustion et d'augmenter les performances du moteur. Il est en effet possible de réduire le bruit et les émissions de polluants. L'influence des variables de contrôle sur le processus de combustion est présentée et illustrée de résultats de simulations réalisées avec le logiciel AMESim [63] (pour plus de détails sur ce logiciel voir l'appendice C).

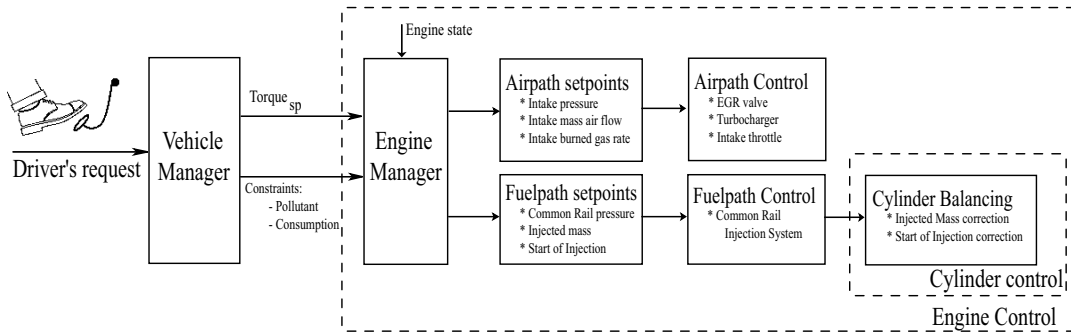


FIGURE 2.1. Hierarchical structure of the torque control for a Diesel engine.

2.1. Introduction

In this chapter, we describe the control structure of a Diesel engine developed at IFP and the impact of each actuators on the combustion process. First of all, we look at the torque control structure in Section 2.2. We describe the several steps of the transformation of the driver's torque into actuator set points. Then, in Section 2.3, we describe the impact of the air path actuators on the gas aspirated into the cylinder (total mass aspirated, composition, temperature). Moreover, we show the effects on the cylinder pressure and the engine performance in terms of noise, torque production, ... Finally, we describe the injection management in Section 2.4. In addition, we detail the impact of the injection timing and quantity onto the combustion in terms of noise, torque production and, pollutant emissions. The impact of the control variables on the combustion pressure is reported through simulation results coming from AMESim [63] (more details on the simulation software is presented in Appendix C).

2.2. Torque control structure

The driver's request considered here is the accelerator position. First, taking into account the gear box configuration, this request is turned into a torque control objective under the form of an IMEP (Indicated Mean Effective Pressure) set point. Then, the set points for the air path and the fuel path are inversely given by experimentally calibrated static maps on the $(IMEP^{sp}, N_e)$ operating range. For a fixed operating point, the calibration of the actuators set points is obtained experimentally to maximize the engine

performance. This trade-off usually includes consumption, pollutants, and noise reduction. Until the last decade, the control was only feedforward on the actuators based on the experimental.

With an increasing quantity of actuators, this “one-level” torque control (set point to actuator position) strategy is tedious to calibrate experimentally. Moreover, this structure consider transients as a series of equilibrium points. Moreover, no dynamics is considered which imply lack of performance and do not guarantee robustness.

For all that reasons, we developed a hierarchical torque control structure as described in Figure 2.1. For that, instead of actuator set points the torque structure derives air path and fuel path set points (intake pressure and burned gas rate for the air path, fuel injection quantity and timing for the fuel path). Then, the air path control is designed to reach its set points (intake pressure, burned gas rate, intake air mass flow, ...) with the air path actuators (EGR valve, turbocharger, intake throttle, ...). The fuel path control is divided into two parts. The first part addresses the determination of the injection timing and duration to fit the driver’s torque request. The second part corrects the injection duration and timing to balance the cylinders. This structure derives state variables that are independent of the actuators technologies and engine architecture (since the set points are the in-cylinder mixture composition for the air path and the injection management for the fuel path). Finally, this allow to take transient into account and develop multi variable strategies for the coupled air path problem.

One should notice the several timescales of the presented dynamics. The fastest dynamics is the combustion. The ignition in the combustion chamber last for few crank angle degree (which corresponds at $500\mu\text{s}$ for 6° crank angle at 2000 rpm). For control purpose, this kind of frequency (more than 2 kHz) is considered as high frequency. The time scale of the engine torque production is the engine cycle (corresponding to 60 ms at 2000 rpm), this corresponds to the overall combustion process. This is the timescale of the fuel path: we are able to change the injection parameter from one cycle to another one. The slowest timescale is the air path dynamics (around .5 s for large transients). A lot of engine cycles are needed to go from a low load operating point to a high operating point due to the turbocharger dynamics. In this thesis, we develop the air path control in Chapter 4 corresponding to the slowest dynamics. We design high frequency observer for cylinder balancing in Chapters 5 and 6 dealing with the high frequency combustion phenomena. Moreover, we present the difficulty of the high frequency fuel control in Chapter 3.4.

In this chapter, we consider only steady-states impact of the actuators on the combustion. It shows the degrees of freedom for the control. Section 2.3 describe the impact of the

air path actuators on the combustion (EGR valve and turbocharger). Section 2.4 exposes the impact of the fuel path actuators on the combustion (injection timing and quantity).

2.3. Air path actuators impact on the combustion

The air feedback loop purpose is to control the air and burned gas masses in the cylinder. In practical applications, those variables can not be measured. Yet, equivalent variables can be considered. We can consider the intake pressure P_{int} , the intake temperature T_{int} , the fresh air mass flow D_{air} , and the burned gas rate in the intake manifold F_{int} . The control actuators are the EGR valve and the turbocharger.

2.3.1. Influence on the air path. —

2.3.1.1. Influence of the EGR valve actuator. — The EGR valve controls the quantity of gas coming from the exhaust manifold to the intake manifold. Opening the EGR valve increase the BGR F_{int} and decreases both the intake pressure P_{int} and the fresh air mass flow D_{air} . The Influence of the EGR valve on the air path at fixed operating conditions is represented in Figure 2.2. A summary of the impact of the EGR valve on the gas aspirated into the cylinder is reported in Table 2.1.

Variable	$M_{asp,air}$	$M_{asp,bg}$	M_{asp}	$\frac{M_{asp,bg}}{M_{asp}}$	$T_{asp,gas}$
EGR valve opening	↓	↑	↓	↑	↑

TABLE 2.1. Summary of the impact of the EGR valve at fixed operating conditions. ↑ increase, ↓ decrease, * minor effect.

2.3.1.2. Influence of the turbocharger actuator. — For constant fuelling rate and engine speed, opening the turbocharger leads to a decrease of the turbocharger crankshaft speed and slow down the compression. It causes reduction in the intake manifold pressure. Hence, the turbocharger can act as a discharge and prevent overboosting the engine at high fuelling rates. Closing the turbocharger for low fuelling rates helps to maintain a larger pressure ratio across the EGR valve. The effect of the turbocharger on steady state values of D_{air} is not monotonic when the EGR valve is wide open: when VGT is almost closed, an increase in turbocharge causes D_{air} to increase while when VGT is almost completely open an increase in VGT causes D_{air} to decrease. Figure 2.3 show these two cases (EGR closed

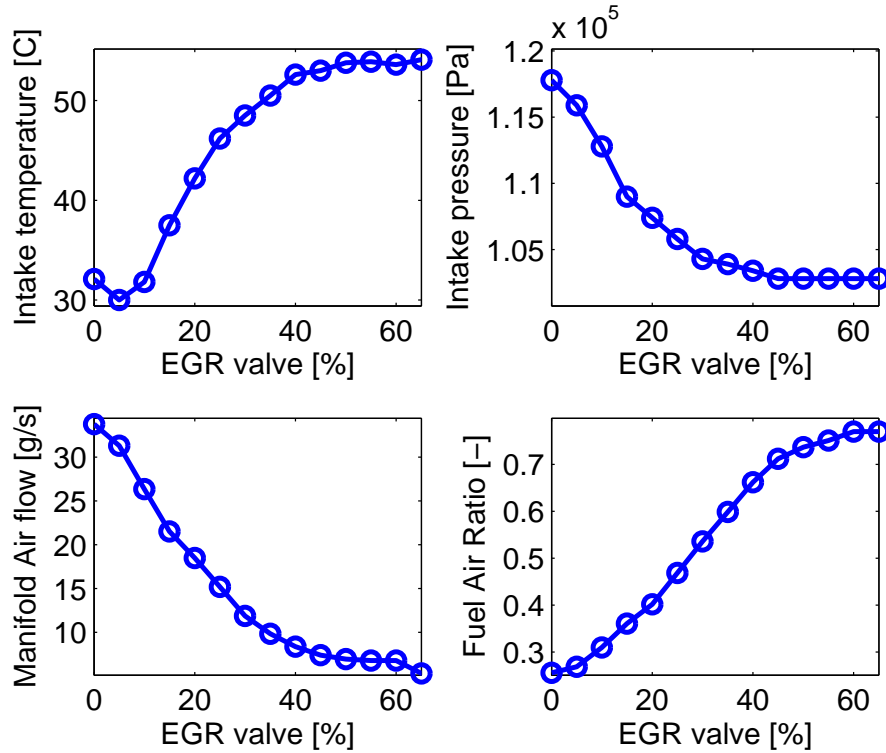


FIGURE 2.2. Experimental variation of the EGR valve at fixed operating conditions in the HCCI combustion mode ($VGT = 20\%$, $N_e = 1500$ rpm and $M_{fuel} = 0.15$ mg/st): Effect on the air path.

and EGR wide open) at fixed operating condition. A summary of the impact of the VGT on the gas aspirated into the cylinder is reported in Table 2.2.

Variable	$M_{asp,air}$	$M_{asp,bg}$	M_{asp}	$\frac{M_{asp,bg}}{M_{asp}}$	$T_{asp,gas}$
Turbocharger opening, low EGR	↓	↑	↓	↑	↑
Turbocharger opening, high EGR	↑	↓	*	↓	*

TABLE 2.2. Summary of the impact of the turbocharger at fixed operating conditions. ↑ increase, ↓ decrease, * minor effect.

2.3.2. Influence of the air path on the combustion. — In the previous subsection, we described the impact of the actuators on the air path variables (intake pressure, intake

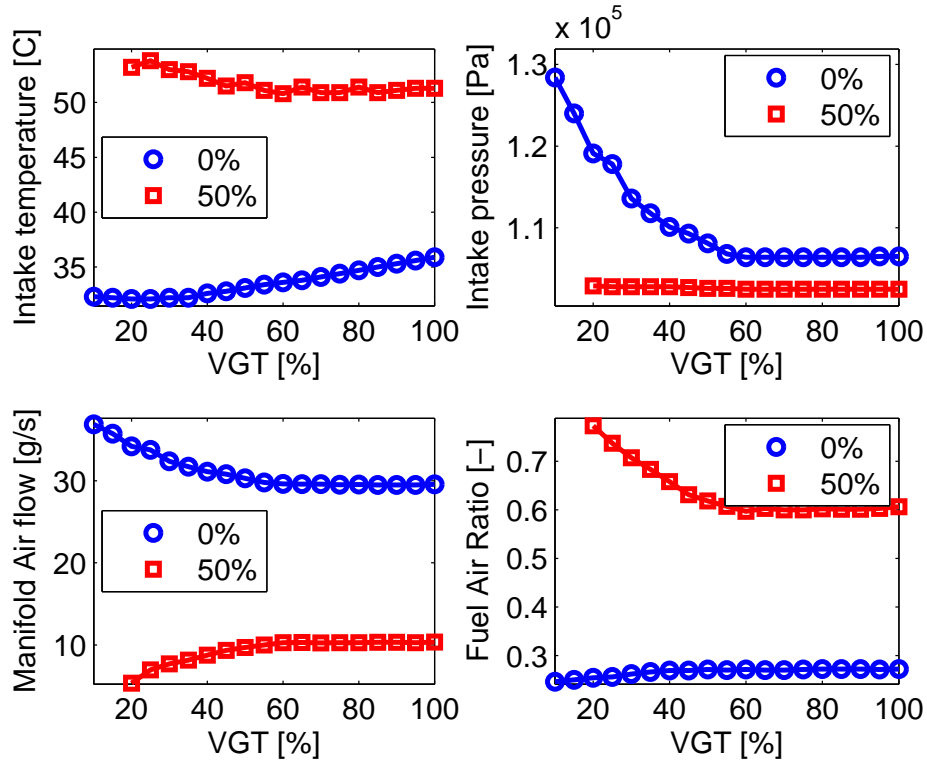


FIGURE 2.3. Experimental variation of the VGT at fixed operating conditions in the HCCI combustion mode ($EGR_{valve} = 0\%$ and $EGR_{valve} = 50\%$, $N_e = 1500$ rpm and $M_{fuel} = 0.15$ mg/st): Effect on the air path.

temperature, ...). Now, we comment the impact on the combustion through the pressure curve. For that, we look at several combustion parameter:

- $P_{cyl,max}$: the maximum cylinder pressure during the combustion.
- CA_{50} : Crank Angle when 50% of the fuel has been burnt.
- τ_{ai} : auto-ignition delay.
- Noise: Noise produced during the combustion (correlated to the maximum of pressure gradient).
- IMEP: Torque produced by the combustion.

As described in 1.2.1, the main impact of BGR is to dilute the mixture in the combustion chamber which increases the auto-ignition delay and limit the temperature peak due to combustion and finally, the pollutant production. Note that it is the total burned gas

fraction in the unburned mixture in the cylinder that acts as a diluent. These burned gas are comprised of both residual gas from the previous cycle and exhaust gas cooled by the EGR cooler and recycled to the intake. Since the burned gas dilute the unburned mixture, the absolute temperature reached after the combustion varies inversely with the burned gas mass fraction. The effect of a variation of burned gas rate on a fixed operating condition is reported in Figures 2.4 and 2.5 in both HCCI and conventional combustion mode respectively.

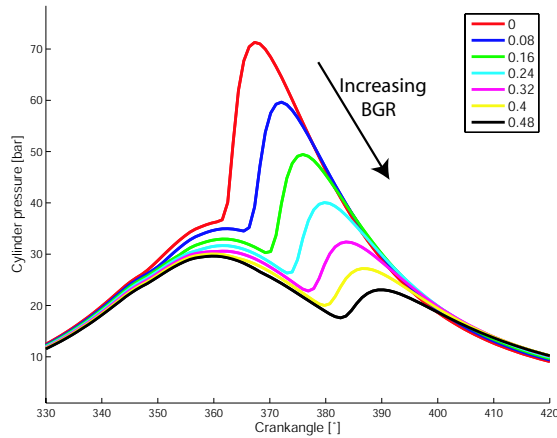


FIGURE 2.4. AMESim simulation. Variation on the burned gas rate on a fixed operating point in the HCCI combustion mode (2000 rpm, $M_{fuel} = 12.8$ mg/st, and $P_{int} = 1.08$ bar): Effect on the cylinder pressure. F_{int} from 0% to 48%.

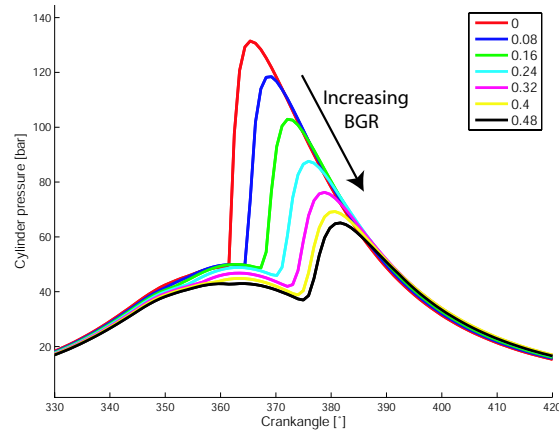


FIGURE 2.5. AMESim simulation. Variation on the burned gas rate on a fixed operating point in the conventional combustion mode (2000 rpm, $M_{fuel} = 16.8$ mg/st, and $P_{int} = 1.67$ bar): Effect on the cylinder pressure. F_{int} from 0% to 48%.

Increasing the intake pressure boost the total mass of gas aspirated into the cylinder. This leads to a lower torque production and a higher noise. But it allows to reach higher load set point by increasing the fuel quantity injection. The effect of a variation of intake pressure on a fixed operating condition is reported in Figures 2.6 and 2.7 in both HCCI and conventional combustion mode respectively.

Increasing the intake temperature raises the temperature of gas aspirated into the cylinder. Then, the auto-ignition delay is shorter leading to a higher noise for the same torque production. The effect of a variation of intake pressure on a fixed operating condition is

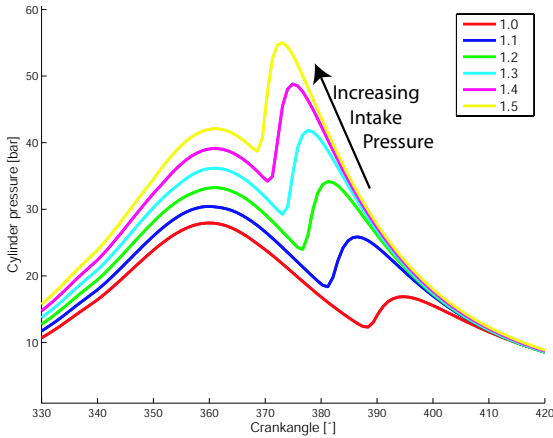


FIGURE 2.6. AMESim simulation. Variation on the intake pressure (bar) on a fixed operating point in the HCCI combustion mode (2500 rpm, $M_{fuel} = 10.95$ mg/st, and $BGR = 37\%$): Effect on the cylinder pressure. P_{int} from 1.0 bar to 1.5 bar.

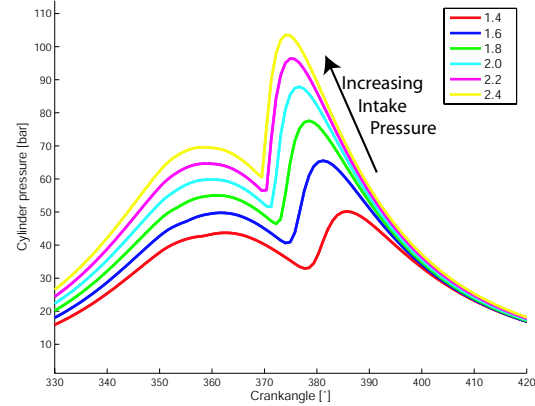


FIGURE 2.7. AMESim simulation. Variation on the intake pressure (bar) on a fixed operating point in the conventional combustion mode (2500 rpm, $M_{fuel} = 23.44$ mg/st, and $BGR = 7\%$): Effect on the cylinder pressure. P_{int} from 1.4 bar to 2.4 bar.

reported in Figures 2.8 and 2.9 in both HCCI and conventional combustion mode respectively.

A summary of the impact of the air path variables is reported in Table 2.3.

Variable	$P_{cyl,max}$	CA_{50}	τ_{AI}	Noise	IMEP
Increase F_{int}	↓	↑	↑	↓	↓
Increase P_{int}	↓	↓	↓	↑	↓
Increase T_{int}	*	↓	↓	↑	*

TABLE 2.3. Summary of the impact of the air path elements. ↑ increase, ↓ decrease, * minor effect.

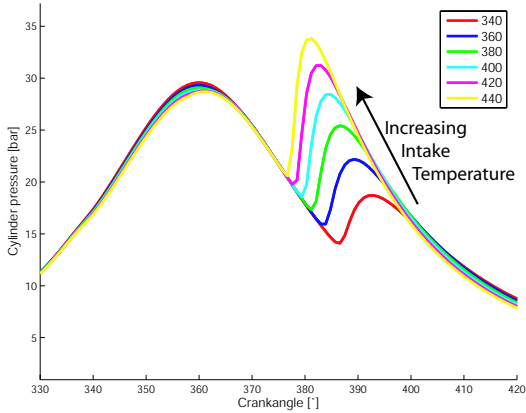


FIGURE 2.8. AMESim simulation. Variation on the intake temperature (K) on a fixed operating point in the HCCI combustion mode (2500 rpm, $M_{fuel} = 10.95$ mg/st, $P_{int} = 1.05$ bar, and $BGR = 37\%$): Effect on the cylinder pressure. T_{int} from 340 K to 440 K.

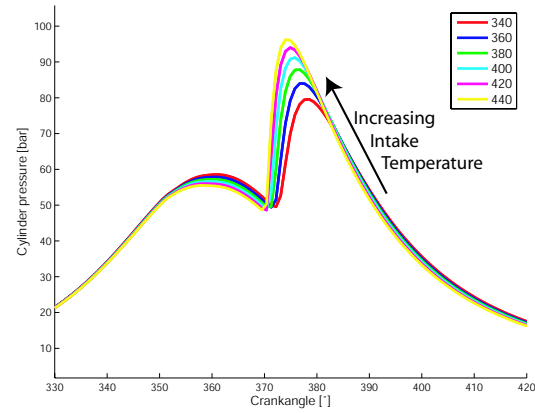


FIGURE 2.9. AMESim simulation. Variation on the intake temperature (K) on a fixed operating point in the conventional combustion mode (2500 rpm, $M_{fuel} = 23.44$ mg/st, $P_{int} = 1.9$ bar, and $BGR = 7\%$): Effect on the cylinder pressure. T_{int} from 340 K to 440 K.

2.4. Fuel path actuators impact on the combustion

In the previous subsection, we described the influence of the air path actuators on the mixture composition. Moreover, we detail the impact of the composition and the temperature on the resulting pressure. Now, we explain the influence of the injection management and the impact of the injection timing and quantity on the combustion?

2.4.1. Injection management. — The advent of the new electronically controlled common rail, unit injector and unit pump injections systems brought the possibility of multiple injections. Multiple injections give the possibility to control the combustion process. Initially, a combination of pilot and main injection is used and currently, post injections are added and some systems are capable of dividing the fuel supply into six injections. The main injection is mainly for the torque production. We now explain the contribution of a pilot injection (injection before the main injection) and of a post injection (injection after the main injection).

2.4.1.1. Pilot injection. — The advantage of injecting a small quantity of fuel ahead of the main injection is that the temperature at the start of the main injection is higher,

which reduces the ignition delay and thus the premixed combustion of the main injection. Reduction of the premixed combustion phase results in lower pressure peak and consequently lower temperature, lower mechanical losses, lower heat losses and less noise [95, 114, 18, 49]. A usual strategy to reduce NO_x emissions of Diesel engines is to retard the injection [114, 18, 106, 105]. A later phasing of the combustion reduces both peak pressure and average gas temperature, and thus NO_x formation. The retardation is limited, because the air temperature falls during expansion and the ignition delay becomes unacceptably long (even misfires may occur) if it is too long. Due to earlier combustion of the pilot fuel, the heat release phasing is better, improving fuel efficiency for a given level of NO_x emissions. The benefits of pilot injection are most pronounced in the low load operating range [95]. However, excessively minimizing the quantity and advancing the timing of pilot injection causes delay of main combustion ignition, resulting in greater combustion noise. Furthermore, HC and CO increase with the deterioration of the pilot combustion itself.

2.4.1.2. Post injection. — While the main purpose of the pilot injection is to lower NO_x emissions and noise, adding a post-injection after the main injection can result in significant reductions in soot emissions. The post injection extends the combustion process longer into the expansion stroke, which delays the temperature drop and increases turbulence in the combustion chamber [95], thereby enhancing soot oxidation. Moreover, for post treatment purpose, we use the post injection to raise the temperature at the end of the combustion and by the same way the temperature the exhaust pipe. It allows the regeneration of the post treatment elements.

2.4.2. Influence of the injection on the combustion. — The fuel loop controls injection quantity and timing. The injected fuel quantity is directly linked to the torque production. The start of the injection controls the start of the combustion. The effect of a variation of injection quantity and start of injection on a fixed operating condition is reported in Figures 2.10 and 2.11 respectively. The injection timing is fundamental in the HCCI combustion mode where the auto-ignition delay is not negligible. The increase in the delay with earlier or later injection timing occurs because the air temperature and pressure change significantly around the top center. If the injection starts earlier, the initial air temperature and pressure are lower so the delay will increase. If injection starts later than normal, the temperature is initially slightly higher, but, eventually, decreases as the delay proceeds.

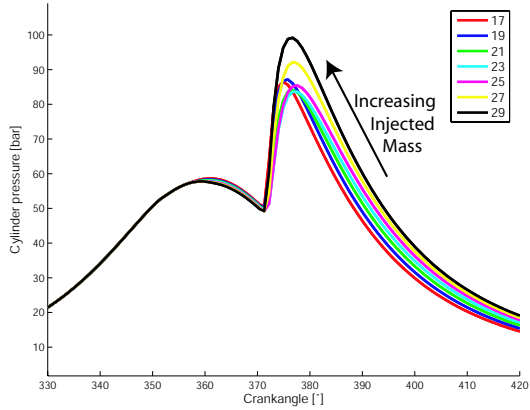


FIGURE 2.10. AMESim simulation. Variation on the injection duration on a fixed operating point in the conventional combustion mode (2500 rpm, $M_{fuel} = 23.44$ mg/st, $P_{int} = 1.9$ bar, and $BGR = 7\%$): Effect on the cylinder pressure.

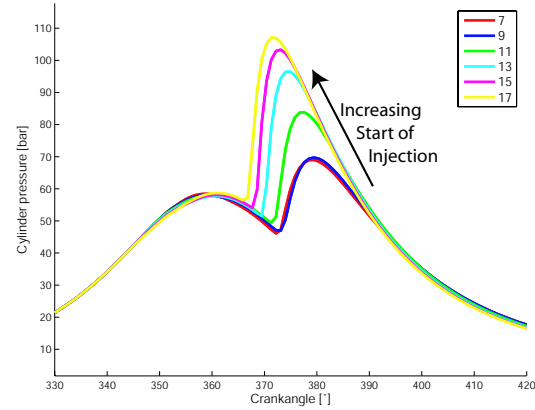


FIGURE 2.11. AMESim simulation. Variation on the start of injection on a fixed operating point in the conventional combustion mode (2500 rpm, $M_{fuel} = 23.44$ mg/st, $P_{int} = 1.9$ bar, and $BGR = 7\%$): Effect on the cylinder pressure.

CHAPTER 3

CONTROL PROBLEMS

Chapitre 3. — Problèmes de contrôle

Dans ce chapitre nous présentons les problèmes à résoudre pour que le moteur fonctionne correctement tant en régime stationnaire qu'en transitoire. Le mode de combustion HCCI rend le contrôle de la combustion très complexe. De très petites différences entre les caractéristiques du mélange de référence et celles du mélange air/gaz brûlés/essence contenu dans le cylindre peuvent avoir de graves conséquences. Nous avons montré que ces différences entraînent une augmentation du niveau de bruit et des émissions de polluants. Cela peut même aller jusqu'à des extinctions de cylindre. Comment contrôler la combustion? Nous proposons de répondre à cette question en résolvant les trois sous-problèmes suivant :

Le contrôle de la boucle d'air : *L'idée est de contrôler les masses aspirées dans le cylindre (air frais et gaz brûlés). La difficulté résulte de la complexité de la dynamique. En effet, il s'agit d'un système couplé à deux entrées/deux sorties non linéaire. De plus il présente un comportement à non minimum de phase. Nous proposons une solution dans la Section 3.2.*

Le contrôle cylindre à cylindre : *L'objectif est de garantir que tous les cylindres ont la même combustion. En effet, il ne suffit pas d'assigner le même point de consigne à chaque cylindre pour que leurs comportements soient identiques. Le déséquilibre observé engendre du bruit, des émissions polluantes et des extinctions de cylindre. Nous résolvons ce problème à la Section 3.3.*

Le contrôle de la boucle de fuel : *Pour que la combustion dans le cylindre ne produise ni trop de bruit, ni trop de polluants et surtout ait bien lieu, il faut que les*

caractéristiques du mélange de gaz et celles de l'injection d'essence respectent une certaine relation. Si cette relation est bien connue en statique elle l'est beaucoup moins en transitoire. De plus les temps caractéristiques des boucles en air et en fuel sont très différents. La première boucle est dix fois plus lente que la seconde. Lors d'un changement de demande en couple il est donc nécessaire de ralentir le transitoire de la boucle en fuel pour l'adapter à celui de la boucle en air. Nous proposons dans la Section 3.4 un exemple de solution à ce problème encore ouvert, et nous montrons les limitations de la stratégie proposée.

Un moteur ne pourra fonctionner si les deux premiers problèmes ne sont pas résolus. Il ne fonctionnera correctement, à un niveau de bruit et d'émissions polluantes compatible avec une utilisation industrielle, que si le troisième est également résolu.

3.1. Introduction

In this chapter, we present several control problems that need to be addressed to run the engine over a conventional operating range including steady-states and transients. In the HCCI combustion mode, it is very difficult to control the combustion. Small mismatches between the mixture in the cylinder (air-burned gas-fuel) and the reference mixture can have dramatic effects. We have seen that it could produce additional noises, additional pollutant emissions and possible stall.

We propose to decompose the general problem of combustion control into three control issues.

1. The air path control. In this problem, it is desired to control the masses (fresh air and burned gas of the mixture) in the cylinders. In Section 3.2, we describe two main bottlenecks: the dynamics is nonlinear and coupled (two actuators are considered to control two outputs). Moreover, it has a nonminimum phase behavior.
2. The cylinder balancing control problem. Here, it is desired to guarantee that all the cylinders have the same combustion. In Section 3.3, we explain that, even with the same set point, the cylinders do not behave similarly. This unbalance is always present and can lead to malicious noise, possible stall, and, higher pollutant emissions.
3. The fuel path control issues. The control problem is to adapt the fuel path to the air path dynamics. The air and fuel paths do not have the same timescale. The air path is typically 10 times slower. For a torque transient from \overline{IMEP} to \overline{IMEP} , the air path set points vary from $(\overline{P_{int}} = 1.02 \text{ bar}, \overline{F_{int}} = .45)$ to $(\overline{P_{int}} = 2 \text{ bar}, \overline{F_{int}} = .05)$ which is constrained to the air path dynamics. The final injection strategy will be $(\overline{M_{inj}}, \overline{t_{inj}})$,

but how do we manage the transient part? The problem is to adapt the fuel strategy with the air path variables. In Section 3.4, we describe the behavior when we directly apply $(\overline{M_{inj}}, \overline{t_{inj}})$. We describe the effect of such strategy and explain its limitation. The first two problems are essential to operate the engine. On the contrary, while it is possible to run the engine without solving the last problem, unacceptable noise and pollutant emissions in transient will prevent from reaching commercial specifications.

3.2. Air path control issues

In the HCCI combustion mode, the air path controls the composition and the temperature of the gas aspirated by the cylinder. BGR offsets may cause misfires (and decrease of torque production as can be seen on Figure 3.1 for large EGR valve opening) and unstable combustion⁽¹⁾ and malicious noises (as can be seen on Figure 3.1 for low EGR valve opening). In the HCCI combustion mode it is very high (40% or more). A close control of the masses of air and burned gas in the intake manifold is needed to run the HCCI combustion properly. Moreover, as studied in [78, 74], the air path system of a turbocharged Diesel engine features coupled dynamics. The EGR acts as a discharge valve for the turbocharger. All these studies stress the need and the relevance of a multivariable control.

3.2.1. Nonlinear coupled dynamics. — Both the EGR and the VGT are driven by the exhaust gas. This makes the control problem multivariable. To expose the nonlinearities and the coupling, we perform some tests on the engine testbed to generate the equilibrium points as functions of the VGT actuator position O_{vgt} (ranging from 0 to 1) and the EGR valve normalized effective area $O_{egr}(v_2)$ (ranging from 0 to 1) for a constant engine speed value $N_e = 1500$ rpm and constant fueling rate.

In Figures 3.2 and 3.3 we plot the steady-state values of the intake manifold pressure, P_{int} , and compressor mass air flow, D_{air} . The effect of O_{egr} on steady-state values of P_{int} and D_{air} is monotonic. Opening the EGR valve causes the intake pressure and the compressor air mass flow to decrease. For constant fuelling rate and engine speed, opening the VGT guide vanes causes a reduction in the intake manifold pressure. Hence, VGT can act as a wastegate and limit overboosting the engine at high fuelling rates. Opening the VGT for high fuelling rates may also improve fuel economy by reducing pumping losses associated with high exhaust manifold pressures. Closing the VGT for low fuelling rates

⁽¹⁾The combustion stability is the normalized variance of the cylinder pressure.

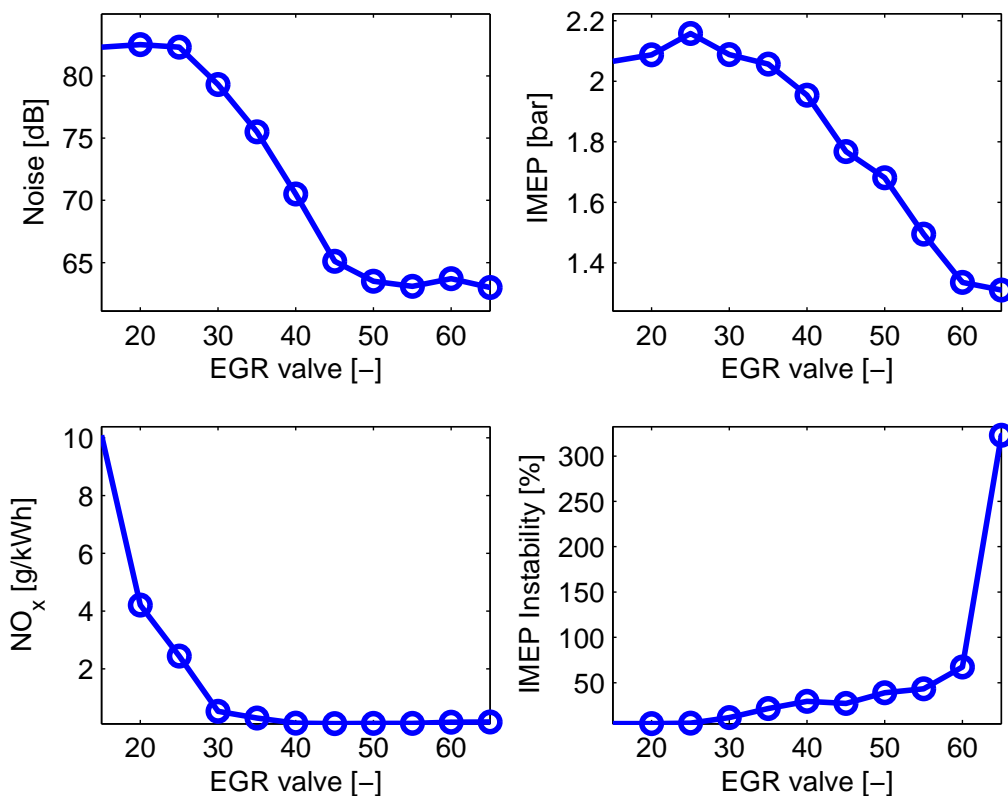


FIGURE 3.1. Experimental variation of the EGR valve with a fixed injection set point: Effects on noise (dB) (Top-Left), on the Indicated Mean Effective Pressure (IMEP in bar) (Top-Right), on the NO_x production (in g/kWh) (Bottom-Left), and on the combustion stability (Bottom-Right).

helps to maintain a larger pressure ratio across the EGR valve and thus increases the exhaust gas recirculation and reduces NO_x emissions. The effect of O_{vgt} on steady-state values of D_{air} is not monotonic when the EGR valve is wide open: when VGT is almost closed, an increase in O_{vgt} causes D_{air} to increase while, when VGT is almost completely open, an increase in O_{vgt} causes D_{air} to decrease. This shows the nonlinearities and the coupling dynamics of both actuators on the air path dynamics.

3.2.2. Nonminimum phase behavior. — As described in [78, 74], the coupled air path dynamics features nonminimum phase dynamics on some operating points.

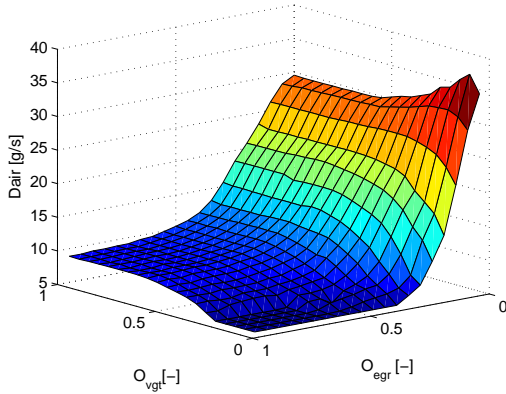


FIGURE 3.2. Experimental variation of EGR valve and VGT opening at fixed injection condition at 1500 rpm. Influence of the air flow D_{air} .

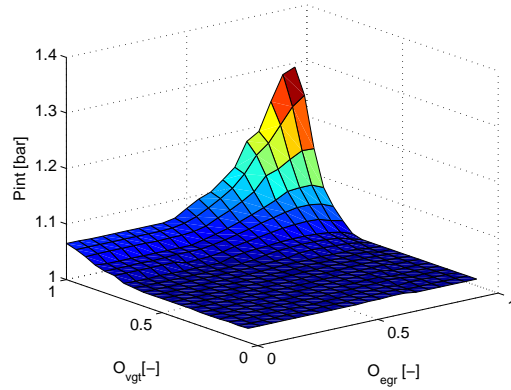


FIGURE 3.3. Experimental variation of EGR valve and VGT opening at fixed injection condition at 1500 rpm. Influence of the the intake pressure P_{int} .

3.2.2.1. Step of VGT position. — When applying a closing step in the VGT control signal, the exhaust manifold pressure rises. This results in a higher mass flow through the EGR and a higher intake manifold pressure. Closing the VGT also results in lower mass flows through both the turbine and the compressor. But, as a result of the increasing pressure in the exhaust manifold, these mass flows eventually increase and, after a while, reach a state where the mass flows are higher than before the step in the VGT position. This is a typical behavior for a nonminimum phase behavior. It results of zeros in the right half plane in the pole-zero map of the system. This nonminimum phase behavior (for step inputs) is represented in Figure 3.4.

3.2.2.2. Step in EGR position. — When the EGR valve opens, first the flow through the EGR valve increases thereby increasing the intake manifold pressure. However, since a relatively smaller portion of the exhaust gas is supplied to the turbocharger, and since the exhaust manifold is emptied at a higher rate when the EGR valve opens, eventually the intake manifold pressure decreases. The latter effect is, however, delayed because of the turbocharger dynamics. This nonminimum phase behavior is represented in Figure 3.5

Air loop control challenges. — The air path control problem can be summarized as follow:

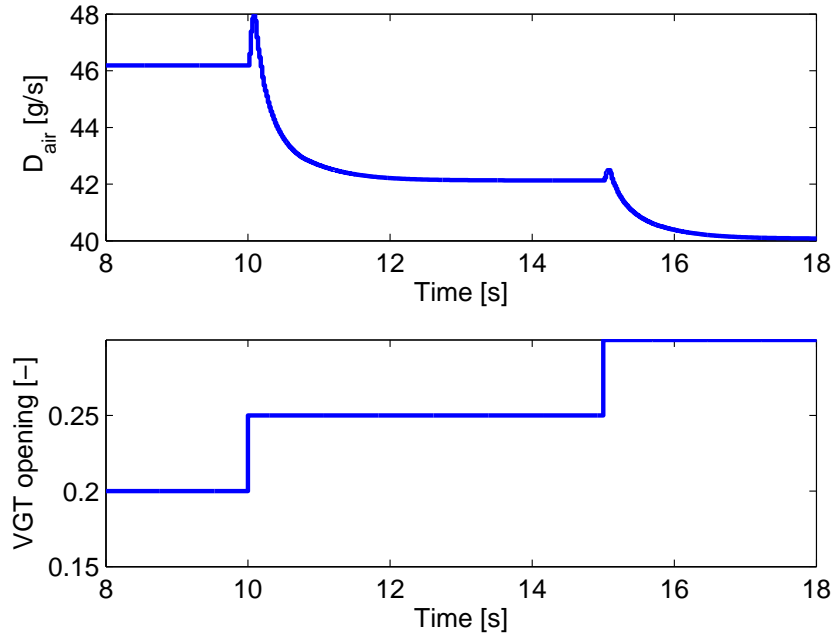


FIGURE 3.4. Variation of VGT opening for a fixed EGR valve and fixed injection condition at 1500 rpm. Influence of the intake mass air flow D_{air} : the mass air flow has a non minimum phase behavior.

- i) *Design an observer of the air and burned gas masses in the intake manifold.*
- ii) *Design a multivariable control (with the EGR valve and the Variable Geometry turbocharger) of these masses to reach the set points given by the torque controller.*

In Part II chapter 4, we propose a complete solution to this problem.

3.3. Cylinder balancing issues

Cylinder to cylinder torque imbalance in internal combustion engines can have many different causes. Fuel injectors may exhibit part to part variability, as they frequently do in high pressure fuel injection systems. Asymmetries in the intake system may cause different air charge and, therefore, different torque production among cylinders. Variability in the combustion systems of different cylinders may cause different combustion profiles.

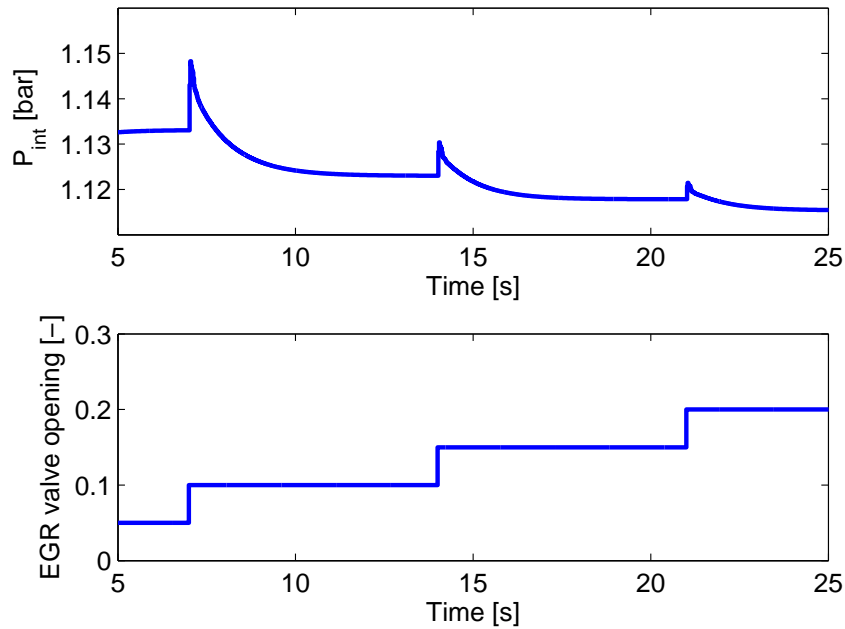


FIGURE 3.5. Variation of EGR valve for a fixed VGT opening and fixed injection condition at 1500 rpm. Influence of the intake pressure P_{man} : the pressure has a non minimum phase behavior.

While torque production is peak pressure limited, a balanced engine produces higher torque output than an unbalanced one, since the highest peak pressure of all cylinders sets the fueling level for the whole set of cylinders. Emissions for a given engine speed and load are also reduced for the same reason.

With a classical fuel path strategy, all cylinders share the same closed-loop input signal based on the engine measurements and the driver request. Ideally, all the cylinders should have the same behavior as they have the same injection set-point. Unfortunately, due to inherent flaws of the injection system (such as pressure waves as we can see in Figure 3.6 and mechanical tolerances) and the disparity of the injectors (as we can see in Figure 3.7), the total mass of fuel injected in each cylinder is very difficult to predict with a relative precision below 7%. Main of the unbalance comes from that difficulty. This lack of precision results in non optimal engine operating conditions. For HCCI engines and regeneration filters, even slight unbalance between the cylinders can in particular induce malicious noise,

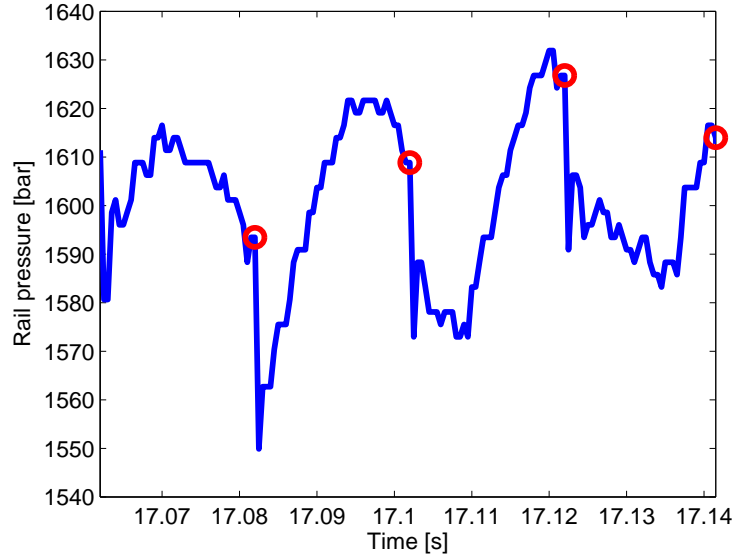


FIGURE 3.6. Experimental common rail pressure signal over an engine cycle. The circles correspond at the start of injection the cylinders. Oscillations in the Common Rail can introduce cylinder unbalance.

possible stall and increased emissions. A typical example of cylinder imbalance in HCCI and in conventional combustion mode is reported in Figures 3.8 and 3.9 respectively.

Cylinder number	1	2	3	4
IMEP (bar)	5.67	6.41	6.25	5.83
$P_{cyl,max}$ (bar)	43.0	54.4	49.5	49.7
Angle of $P_{cyl,max}$ ($^{\circ}$)	371.7	377.5	379.9	378.8
IMEP (bar)	8.93	9.00	9.14	9.22
$P_{cyl,max}$ (bar)	94.2	94.9	94.3	93.6
Angle of $P_{cyl,max}$ ($^{\circ}$)	367.7	367.6	367.6	367.4

TABLE 3.1. Experimental results. Summary of the cylinder unbalance at 1500 rpm and 6 bar of IMEP in HCCI combustion mode and 9 bar of IMEP in conventional combustion mode.

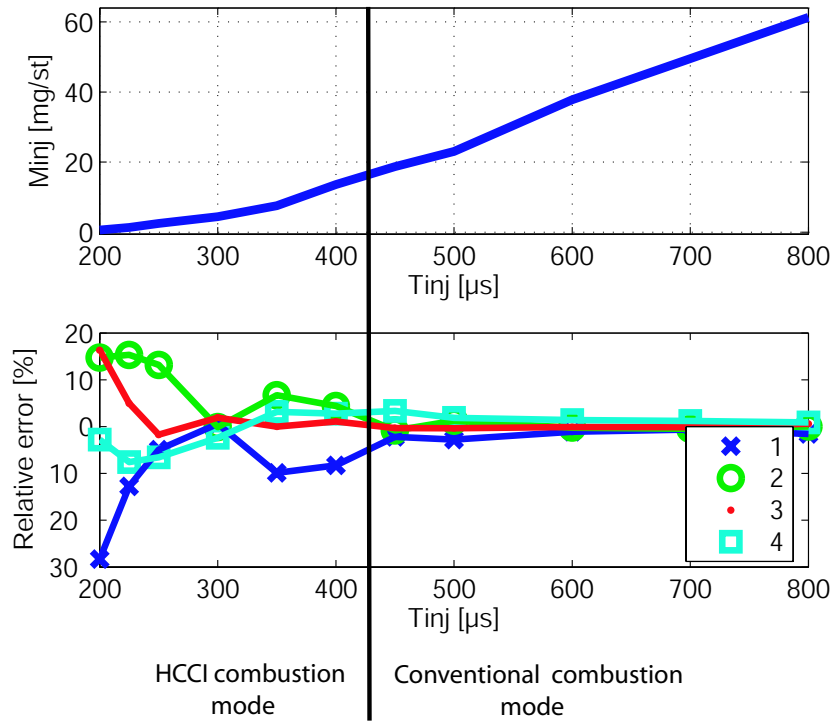


FIGURE 3.7. Variation of the injection time for the 4 injectors at a fixed common rail pressure ($P_{rail} = 1600$ bar). Top: Injected mass in mg/st . Bottom: relative error to the mean injection. The unbalance introduced by the injector is very important at low injection timing where the effects are the most important, mainly in the HCCI combustion mode.

Cylinder-individual control is needed to address the potential drawbacks in these planned technologies. In this context, *cylinder-individual* estimation and control may provide crucial information to assist the HCCI engine controller. To achieve this goal, we develop high frequency individual cylinder estimators. These serves as tools for real time control strategies.

First of all, the combustion torque characterizes the performance of the engine and is the result of various inputs such as injection quantity and timing, EGR rate Ideally, this torque could be measured using fast pressure sensors in each cylinder. Unfortunately, high cost and low reliability prevent these sensors from reaching commercial products. On-line estimation is necessary. Another way to control the combustion torque is to control

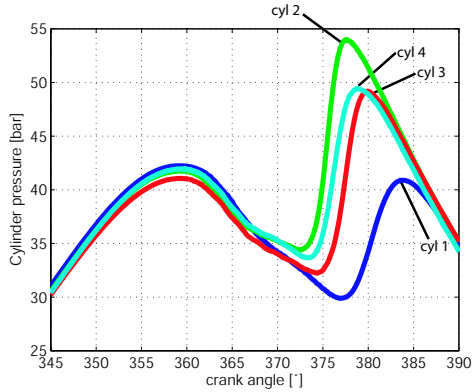


FIGURE 3.8. Cylinder pressures (bar) at 1500 rpm and 6 bar of IMEP in HCCI combustion mode: cylinder to cylinder variation.

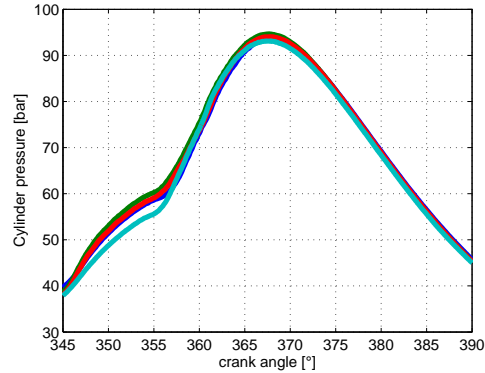


FIGURE 3.9. Cylinder pressures (bar) at 1500 rpm and 9 bar of IMEP in conventional combustion mode: cylinder to cylinder variation.

individual Air Fuel Ratios (AFR) which is a good representation of the torque balancing of a Diesel engine. Again, in theory, all the cylinders should have the same AFR since they have the same injection set-point. Not surprisingly, due to inherent flaws of the injection system (pressure waves, mechanical tolerances, ...), identical total mass of fuel injected in each cylinder is very difficult to achieve by design. Again, an estimator is a prerequisite to controlling the individual cylinder torque.

For both estimation problems we propose a physics-based approach. Using balance equations, crankshaft dynamics and exhaust manifold balance respectively, we underline the role of periodicity in the design of nonlinear observers. In the first case we use as the only sensor the crankshaft instantaneous speed sensor. In the other one we use the Air Fuel Ratio sensor placed downstream the turbine as the only sensor. These observers have common properties: their computational requirements are low, the tuning is made easy by using the periodicity of the corresponding equations, and estimation is performed at a high frequency (6° crankshaft).

Cylinder balancing challenges. —

- i) *Design a real time high frequency observer of the combustion torque with the use of the crankshaft instantaneous speed as only sensor.*
- ii) *Design a real time high frequency observer of the cylinder individual Air Fuel Ratio with the use of the oxygen sensor placed downstream the turbine.*

- iii) *Use both information for cylinder balancing (basically, removing offsets via integral action in a first step).*

3.4. Fuel path control issues

The fuel path is mainly defined by the fuel injection timing and quantity. Calibration is done around steady state to optimize the tedious tradeoff between the torque production, fuel consumption, noise, and pollutant formation. This means that for a torque set point, we have a set point of intake pressure, intake BGR for the air path and a injection timing and quantity for the fuel path. This calibration is done on some point of the operating range $(N_e, IMEP)$. Between these reference points, interpolation is made. This defines a map

$$SP: \begin{array}{l} \text{Torque Demand} \mapsto \text{Air path}^{sp} \times \text{Fuel path}^{sp} \\ (N_e, IMEP^{sp}) \mapsto (P_{int}^{sp}, F_{int}^{sp}) \times (M_{inj}^{sp}, t_{inj}^{sp}) \end{array}$$

The fuel loop control is instantaneous. You control it cycle to cycle. On the contrary, the air loop is not directly controlled, i.e. there is a dynamics to vary the intake pressure and the intake BGR. For a torque transient from \underline{IMEP} to \overline{IMEP} , the air path set points vary from $(\underline{P}_{int}, \underline{F}_{int})$ to $(\overline{P}_{int}, \overline{F}_{int})$ which is constrained to the air path dynamics. Nevertheless, during the air path transient, we are not in the map anymore. At the end of the transient, the injection set point is $(\overline{M}_{inj}, \overline{t}_{inj})$. However, we do not know how to manage the injection during transient.

Let us focus on a experimental examples. The first one is a tip-in, a large increase in the torque demand.

3.4.1. Tip-In. — Figure 3.10 shows experimental results of such a tip-in in two configurations. In the first case (solid plot), we instantaneously inject the fuel quantity corresponding to the IMEP set point (we apply directly $(\overline{M}_{inj}, \overline{t}_{inj})$). In second case (dotted plot), is the case where we inject a filtered amount. The torque response is faster in the first case but at the expense of higher pollutant emissions. Indeed, injecting instantaneously the whole fuel quantity leads to an excess of fuel in the cylinder. This results in a rich combustion and in a higher emission (smoke). Filtering the fuel quantity provides a lean combustion but slows down the torque production.

3.4.2. Control the start of injection w.r.t. BGR errors. — Figure 3.11 shows experimental transient with large transient of BGR. In this experiment, the BGR set point

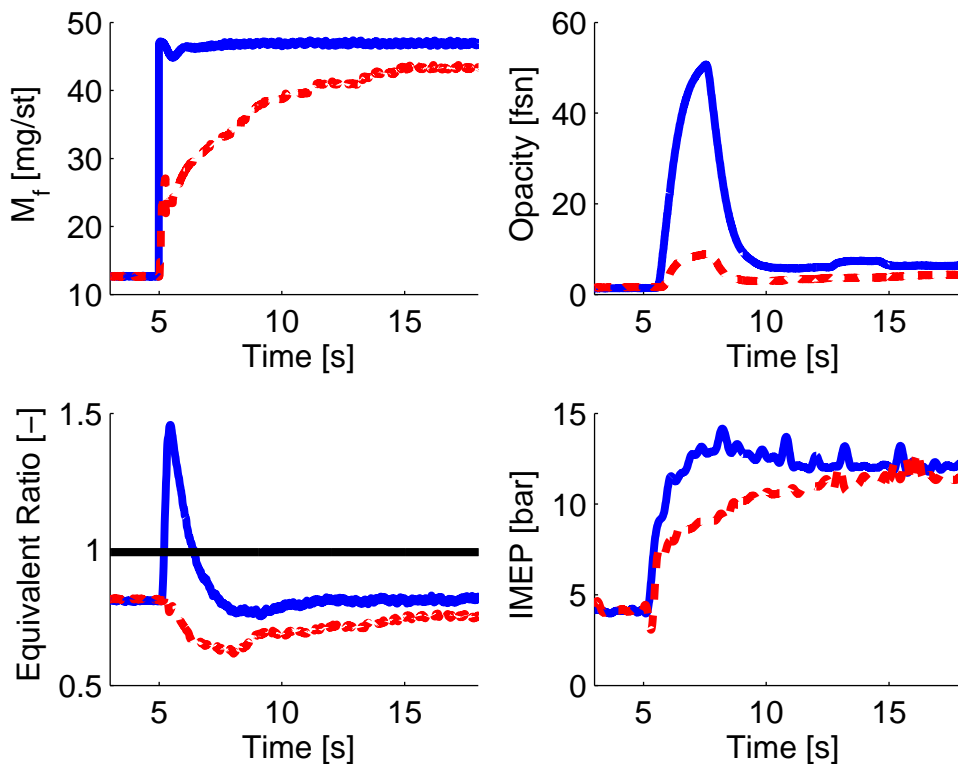


FIGURE 3.10. Experimental tip-in. IMEP demand from 4 to 13 bar of IMEP. The solid curves correspond to the injection of the final set point quantity. The dotted curve correspond to a filtered fuel injection. We look at the effects on the opacity (top-right), the equivalence ratio (bottom-left) and IMEP (bottom-right).

goes from $\overline{F_{int}} = .07$ to $\overline{F_{int}} = .32$. During the transient, we apply the fuel set point corresponding to the IMEP set point (we apply directly $(\overline{M_{inj}}, \overline{t_{inj}})$).

We look at the effects on the error between the BGR set point (dotted in top-left) and the BGR (solid in top-left) on the noise of each cylinder (top-right), the angle of maximum of $\frac{dP_{cyl}}{d\alpha}$ (bottom-left) and IMEP (bottom-right).

During this transient, we can see that the noise production and the combustion phasing (corresponding to the angle of maximum of $\frac{dP_{cyl}}{d\alpha}$) is very correlated to the BGR error. This variation of phasing leads to a higher pollutant emission. A way to improve the transient

is to take the BGR error in the management of the start of injection. This could lead to a stable phasing during the torque transient.

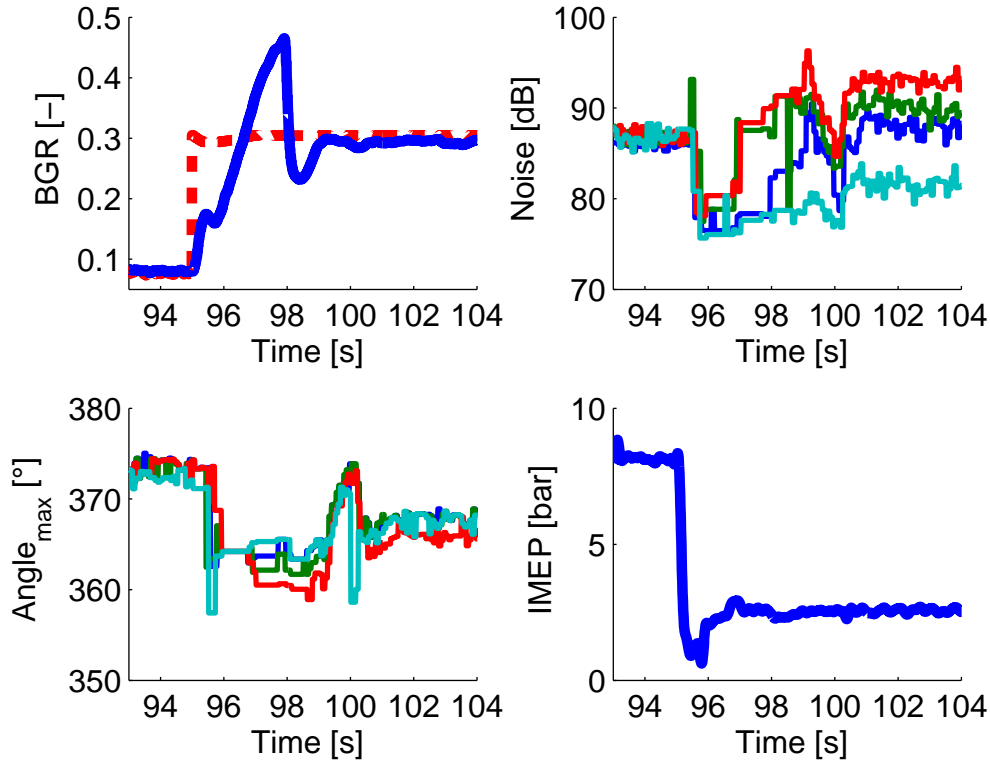


FIGURE 3.11. Experimental BGR transient. IMEP demand from 9 to 3 bar of IMEP. We look at the effects on the error between the BGR set point (dotted in top-left) and the BGR (solid in top-left) on the noise of each cylinder (top-right), the angle of maximum of $\frac{dP_{cyl}}{d\alpha}$ (bottom-left) and IMEP (bottom-right).

3.4.3. Combustion mode transient. — As described earlier the HCCI combustion mode has a specific fuel management, including early injection . . . This leads to several combustion mode for running the engine on the overall operating range. This means that the set point map is not continuous. The question is to deal with the injection management during this discontinuities. For example, when do we switch between a single main injection to a pilot-main injection?

PART II

AIR PATH CONTROL AND CYLINDER BALANCING

PRÉSENTATION DE LA PARTIE II

Cette partie présente des solutions aux deux premiers problèmes présentés dans la Partie I.

Dans le chapitre 4, nous nous plaçons dans le cas d'une modification de la demande en couple. Nous avons montré que pour garantir une combustion performante pendant le transitoire il était nécessaire de contrôler la boucle d'air. Grâce à une relation expérimentale statique nous traduisons l'évolution de la demande en couple en consigne sur les caractéristiques du mélange aspiré dans le cylindre. L'inversion d'un modèle dynamique de la boucle d'air permet de générer une trajectoire pour les commandes qui sont les débits d'air et d'EGR. Nous développons un observateur/contrôleur qui réalise le suivi des variables commandées autour de la trajectoire planifiée. Des résultats expérimentaux sont présentés. Ils démontrent la robustesse de la stratégie et son efficacité dans différentes configurations. Ce travail a été publié dans [31, 27].

Dans le chapitre 5, nous considérons le problème de l'estimation et du contrôle de la richesse cylindre à cylindre. Le terme de "richesse" désigne la composition des gaz dans le cylindre à la fin de la combustion. Les déséquilibres de richesse cylindre à cylindre reflètent les différences entre la combustion de chacun des cylindres. Ces différences peuvent être mesurées par un capteur placé derrière la turbine. Nous présentons deux stratégies dont nous comparons leurs efficacités. D'abord, nous proposons un observateur non linéaire dont les termes correctifs sont également non linéaires. Ensuite, nous présentons un filtre de Kalman étendu. Ces deux observateurs sont validés et comparés expérimentalement sur une large zone opératoire (Régime moteur de 1250 tr/min à 3500 tr/min et IMEP de 3 à 9). Nous présentons aussi des résultats en boucle fermée. Ce travail a été publié

dans [32, 34, 37, 33, 93, 36, 35].

Dans le chapitre 6, nous considérons le problème de l'estimation du couple de combustion. Ce couple caractérise les performances du moteur. Il dépend de diverses entrées comme le temps d'injection, le taux d'EGR... Il n'est pas directement mesuré. En revanche, la vitesse instantanée de l'arbre vilebrequin au bout de la transmission est bien mesurée. Cette vitesse instantanée est la sortie d'un système en cascade qui consiste en un système linéaire du premier ordre (dynamique bielle-manivelle) et d'un système linéaire du deuxième ordre (dynamique de la transmission) excité par le couple de combustion. Nous développons des observateurs haute fréquence pour estimer ce couple. Cet observateur est comparé à un filtre de Kalman. Nous prouvons la convergence des deux observateurs considérés et présentons des résultats expérimentaux. Ce travail a été publié dans [22, 23, 26, 24, 21].

PRESENTATION OF PART II

This part contains solutions to the first two control problems presented in Part I.

In Chapter 4, we present a control scheme for the air path of a turbocharged Diesel engine. The objective is to control the masses aspirated by the cylinder ($M_{asp,air}$ and $M_{asp,bg}$) with the two air path actuators (EGR valve and the Variable Geometry Turbocharger). In practical applications, the considered masses can not be measured. Yet, equivalent variables can be considered. Controlling those two masses is equivalent to controlling the intake pressure P_{int} (being an image of $M_{asp,air} + M_{asp,bg}$) and the burned gas rate F_{int} (representing to ratio $\frac{M_{asp,bg}}{M_{asp,air} + M_{asp,bg}}$). The contribution is twofold.

1. We design feedforward motion planning control strategy. It is based on the inversion of the fully actuated dynamics of the system under consideration (differential flat systems). Physical input constraints are explicitly taken into account in the feedforward control.
2. We propose an observer (linearization technique based on output injection and Lyapunov arguments for convergence)/controller to track the computed open loop trajectory. We first propose an observer to estimate the composition in the intake manifold and the EGR flow. Fast controllers are then used for tracking.

In this study, experimental results are reported on a 4 cylinder HCCI engine. We expose results for torque transient and also during driving phases of the eurocycle. This work has been published in [31, 27].

In Chapter 5, we address the cylinder individual Air Fuel Ratio estimation and control problem. The AFR is a representation of the composition of the gas in the cylinder at the end of the combustion. Cylinder individual AFR unbalances reflect a variability in the combustion. This variability can be measured on the single sensor located behind the turbine. We propose a nonlinear observer involving nonlinear correcting terms. Also, we present an extended Kalman filter. Comparisons and experimental results are reported with engine speed ranging from 1250 rpm to 3500 rpm and pressure from 3 to 9 bar of IMEP (Indicated Mean Effective Pressure). We study robustness issues and give some closed loop results. This work was published in [32, 34, 37, 33, 93, 36, 35].

In Chapter 6, we address the combustion torque estimation problem. The combustion torque characterizes the performance of the engine and is the result of various inputs such as injection quantity and timing, EGR rate... We do not have a direct measurement of this torque but of the instantaneous engine speed located at the end of the transmission. The instantaneous engine speed is the output of a cascade consisting of a first periodic linear system (crankshaft-connecting rod) and a second linear system (transmission dynamics) fed by a periodic combustion torque. We develop high frequency observers to estimate the instantaneous engine speed under the cylinders by inverting the transmission dynamics. Another high frequency observer is developed to estimate the combustion torque from this estimated instantaneous engine speed. This observer is compared against a Kalman filter. For all the considered observers and filters, convergence proof is given along with experimental results. This work has been published in [22, 23, 26, 24, 21].

CHAPTER 4

AIR PATH CONTROL

Chapitre 4. — Contrôle de la boucle d'air

Dans la partie I Section 3.2, nous avons vu que les caractéristiques du mélange aspiré dans le cylindre étaient les variables clés de dynamique d'air. De petites variations peuvent causer des ratés de combustion. Si la vanne d'EGR est grande ouverte, ces erreurs entraînent également la diminution du couple produit. Si elle a une ouverture faible, la combustion est plus bruyante.

Nous présentons une structure de contrôle pour la boucle d'air d'un moteur Diesel. L'objectif est donc de contrôler les masses aspirées par les cylindres (air frais $M_{asp,air}$ et gaz brûlés $M_{asp,bg}$) grâce à deux actionneurs (vanne EGR et turbine à géométrie variable). Ces masses ne sont pas mesurées expérimentalement. En revanche nous disposons d'une image de leur somme et de leur ratio. En effet la somme des masses ($M_{asp,air} + M_{asp,bg}$) s'exprime simplement en fonction de la pression dans le collecteur d'admission, P_{int} . En outre, leur ratio ($\frac{M_{asp,bg}}{M_{asp,air} + M_{asp,bg}}$) est directement lié au taux de gaz brûlés dans ce même collecteur. Nous choisissons de contrôler la pression et le taux de gaz brûlés dans le collecteur d'admission. Nous nous plaçons dans le cas d'une modification de la demande en couple, qui se traduit, grâce à une relation expérimentale statique en consignes de pression et de taux de gaz brûlés dans le collecteur d'admission. La contribution se divise en deux parties:

- 1. Nous filtrons les consignes et générons une trajectoire boucle ouverte, en utilisant le débit d'air frais D_{air} et le débit d'EGR D_{egr} comme commande, afin de suivre ces*

consignes. Pour ce faire, nous inversons la dynamique de la boucle d'air. Les contraintes sont explicitement intégrées dans la stratégie de contrôle à travers le filtrage des consignes.

2. *Nous développons un observateur/contrôleur pour suivre la trajectoire planifiée. Nous proposons tout d'abord un observateur qui estime la composition dans le collecteur d'admission et le débit d'EGR. Des contrôleurs sont ensuite utilisés pour suivre la trajectoire planifiée.*

Des résultats expérimentaux sont rapportés. Cette étude nous permet de conclure que la planification de trajectoire est une solution appropriée pour commander la dynamique d'air.

4.1. Introduction

In Part I Section 3.2, we have seen that the Burned Gas Rate (BGR) is the core variable for the air path dynamics. BGR offsets may cause misfires (and decrease of torque production for large EGR valve opening) and malicious noises (for low EGR valve opening). In the HCCI combustion mode, BGR setpoints are very high (40% or more). Accurate control of BGR can be achieved by controlling the whole air path system: intake and exhaust manifolds, EGR loop and fresh air loop. This is the subject of this chapter.

As studied in [78, 74], the air path system of a turbocharged Diesel engine features coupled dynamics. The EGR acts as a discharge for the turbocharger. Most studies consider the following control setup: both intake pressure and intake air flow are closely controlled using EGR valve and Variable Geometry Turbocharger (VGT) using gain scheduling PI controllers as in [109, 104, 108]. The PI gains are tuned with respect of engine speed and fueling rate. PI gains are generated by the inverted plant gain at each operating point. Linear Parameter-Varying (LPV) formulation is used in [70, 71]. A LPV Diesel air path model is derived from a simple nonlinear system and use H_∞ loopshaping control to regulate the intake pressure and the intake air flow. Controlling both intake and exhaust pressure has been exposed in [3]. In [65, 66], constructive Lyapunov technique is used to control the air-fuel ratio and EGR fraction to their respective set points determined by the operating conditions during quasi steady state operation. For that, they use the intake pressure, the intake mass air flow and the exhaust pressure for measurements and several change of coordinates for control purpose.

All these studies prove the relevance of a multivariable control. We use a motion planning strategy by expliciting a feedforward term. We cast the drivers's torque demand into

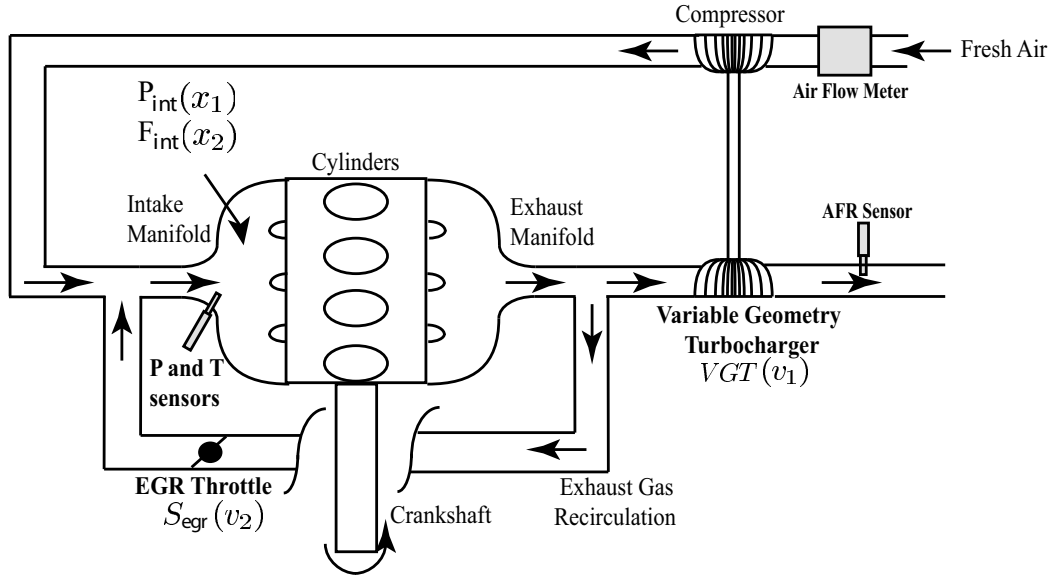


FIGURE 4.1. Air path problem. The sensors used are colored in grey. The inputs are the EGR valve and the Variable Geometry Turbocharger. The state variables are the intake pressure P_{int} and the BGR F_{int} .

in-cylinder masses set point, then into BGR and intake manifold pressure control problem. Then, an explicit unconstrained transient is computed. Hopefully, thanks to tuning parameters, it is consistent with physically important constraints on the inputs. If not, it is saturated, and, as is proven, eventually provides convergence anyway.

We design a hierarchical control strategy. The contribution is twofold :

1. Design of feedforward motion planning control strategy using the intake air flow D_{air} and the EGR flow D_{egr} as input. It is based on the inversion of the dynamics of the system using flatness based technique. Moreover, physical input constraints are explicitly taken into account in the feedforward control.
2. Design of an observer/controller to track the planned trajectory. We first propose an observer to estimate the composition in the intake manifold and the EGR flow. Fast controller are then used to track the planned trajectory.

Extensive experimental results are reported. At the light of this study, we can finally conclude, with supportive results, that motion planning is indeed an appropriate solution for controlling the air path dynamics.

The chapter is organized as follows. In Section 4.2, we detail the control problem. In Section 4.6, we decouple the air path fully actuated dynamics by a simple motion planning strategy. Physical input constraints are explicated in the motion planning strategy. It provides a tuning methodology. Experimental results are reported on a 4 cylinder HCCI engine in Section 4.8. Conclusions and future directions are given in Section 4.9.

4.2. Control problem

Our approach to combustion control is to manage the air and burned gas masses in the cylinder ($M_{asp,air}$ and $M_{asp,bg}$). In other words, we focus on the air path system. Figure 4.1 shows the flow sheet of the air path. Flows of fresh air and the Exhaust Gas Recirculation (EGR) mix into the intake manifold and are aspirated into the cylinders. In practical applications, the considered masses can not be measured. Yet, equivalent variables can be considered. Controlling those two masses is equivalent to controlling the intake pressure P_{int} (being an image of $M_{asp,air} + M_{asp,bg}$) and the burned gas rate F_{int} (representing to ratio $\frac{M_{asp,bg}}{M_{asp,air} + M_{asp,bg}}$). Set points are often chosen to maximize EGR in order to lower the NO_x emissions at low load. At high load, the EGR decreases the efficiency and imposes the use of low EGR. Typically, the set point at 1500 rpm and high load is ($P_{int,sp} = 2\text{bar}$, $F_{int,sp} = .05$) using low EGR, while at 1500 rpm and low load set points under consideration are close to ($P_{int,sp} = 1.013\text{bar}$, $F_{int,sp} = .45$) using high EGR.

In this context, the control problem we need to address is a large transient problem for a two outputs, two inputs system. The control inputs are the VGT actuator position S_{vgt} (ranging from 0 to 1) and the EGR valve normalized effective area S_{egr} (ranging from 0 to 1). Both are bounded. Other external inputs include the fueling rate M_{fuel} and the engine speed N_e . The underlying dynamics is also of dimension 2. The states are the outputs: P_{int} and F_{int} .

4.3. Intake manifold modelling

Figure 4.1 shows the flow sheet of the burned gas rate estimation problem. Flows from the fresh air (measured by the Manifold Air Flow) and the Exhaust Gas Recirculation (EGR) come into the intake manifold and are aspirated into the cylinders. In numerous references found in the literature [107, 73], mean value engine modelling approaches are considered. It uses temporal and spatial averages of relevant temperatures, pressures and mass flow rates. This leads to a seven state reference model. The states are the intake

and exhaust manifold pressure, temperature and composition and the turbocharger speed. Complexity of the model inspires the control design. Most authors consider a model reduction down to 3 states (see [109, 104], [71] or [66] for example). Further, we propose a reduction down to 2 states. Motivations are given in the following subsection.

4.3.1. Modelling assumptions. — First of all, as it is standard in modelling the intake manifolds in spark-ignited engines (e.g. [?] and [57]), we neglect the temperature fluctuations. Two states are thus eliminated. The usual model reduction (see [109, 104], [71] and [66]) consists of a three dimensional reference control model using the intake pressure, the exhaust pressure and the turbocharger speed as state. Composition dynamics are not taken into account because the corresponding two states (intake and exhaust composition) are difficult to measure and are only weakly observable from the remaining three states. In our case, we use the Air/Fuel Ratio sensor located downstream the turbine. It is an image of the composition in the exhaust manifold. This major difference with usually considered setups suggest to substitute the exhaust pressure dynamics by the intake composition dynamics. Finally, we neglect the turbocharger dynamics. The relevance of this last point is stressed by the following. The turbocharger speed dynamics is very slow compared to the pressure and composition dynamics. The turbocharger speed is modelled as a static function of the intake pressure P_{int} and the intake air flow D_{air} .

4.3.2. State space model. — We present a two states reference control model based on two conservation laws. A nomenclature is presented in Table 4.1.

4.3.2.1. Total mass balance in the intake manifold. — Ideal gas law in the intake manifold leads to

$$P_{int}V_{int} = M_{int}RT_{int}$$

Assuming that variations of temperature is small, the mass balance writes

$$\dot{P}_{int} = \frac{RT_{int}}{V_{int}}(D_{air} + D_{egr} - D_{asp}) \quad (4.1)$$

Classically (see [58] for exemple), we define the aspirated flow as

$$D_{asp} = \eta_{vol}(P_{int}, N_e) \frac{P_{int}}{RT_{int}} V_{cyl} \frac{N_e}{120}$$

where V_{cyl} is the cylinder volume. η_{vol} is the volumetric efficiency which is experimentally derived and, eventually, defined through a look-up table $\eta_{vol}(P_{int}, N_e)$ as presented in Figure 4.2.

Var.	Quantity	Unit	Symb.
P_{int}	Pressure in the i.m.	Pa	x_1
F_{int}	Fraction of burned gas in the i.m.	-	x_2
Θ_{egr}	Equivalent flow if EGR valve is full open	kg.s^{-1}	x_3
T_{int}	Temperature in the i.m.	-	x_4
$\delta\eta$	Volumetric efficiency error	-	x_5
D_{air}	Manifold air flow	kg.s^{-1}	u_1
D_{egr}	EGR flow	kg.s^{-1}	u_2
S_{VGT}	VGT normalized position	-	v_1
S_{egr}	EGR valve effective area	-	v_2
T_{int}	Temperature in the i.m.	K	
M_{int}	Total mass in the i.m.	kg	
$M_{int,air}$	Air mass in the i.m.	kg	
V_{int}	Volume of the i.m.	L	
N_e	Engine Speed	rpm	
D_{asp}	Aspirated flow into the cylinders	kg.s^{-1}	
V_{cyl}	Volume of the cylinders	L	
γ	Ratio of specific heats	-	
F_{exh}	Fraction of burned gas in the e.m.	-	
R	Gas constant	$\text{J.}(\text{kgK})^{-1}$	
η_{vol}	Volumetric efficiency	-	

TABLE 4.1. Nomenclature. i.m. refers to the intake manifold.

4.3.2.2. *Composition balance in the intake manifold.* — The burned gas ratio F_{int} is the fraction of burned gas in the intake manifold. It writes

$$F_{int} \triangleq 1 - \frac{M_{int,air}}{M_{int}}$$

The composition of the EGR (F_{egr}) is the composition in the exhaust manifold (F_{exh}) delayed by the transport through the EGR pipe. We consider that this delay is negligible, i.e. $F_{egr} = F_{exh}$. Mixing dynamics is modelled as

$$\dot{F}_{int} = \frac{RT_{int}}{P_{int}V_{int}}(D_{egr}(F_{exh} - F_{int}) - D_{air}F_{int}) \quad (4.2)$$

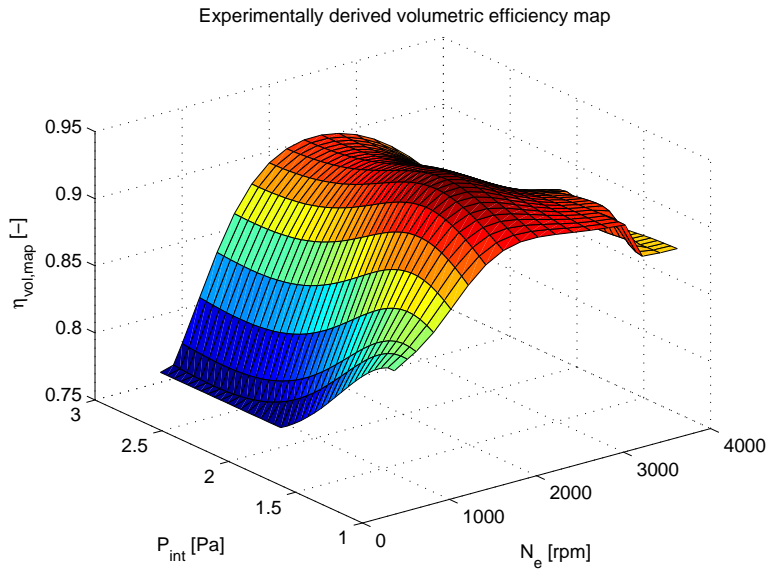


FIGURE 4.2. Experimentally derived volumetric efficiency map at steady state.

4.4. System properties

4.4.1. Reference model. — The air path is represented as the input output system (4.3) depicted in Figure 4.3. We note

$$\alpha_{int} \triangleq \frac{RT_{int}}{V_{int}} \quad \text{and} \quad \beta_{int} \triangleq \frac{1}{RT_{int}} V_{cyl} \frac{N_e}{120}$$

Using (4.1) and (4.2), the reference dynamics reads

$$\begin{cases} \dot{x}_1 = \alpha_{int} (u_1 + u_2 - \beta_{int} \eta_{vol}(x_1, N_e) x_1) \\ \dot{x}_2 = \frac{\alpha_{int}}{x_1} (F_{exh} u_2 - (u_1 + u_2) x_2) \end{cases} \quad (4.3)$$

This system is linearizable by non linear static feedback: (x_1, x_2) are linearizing output.

4.4.2. Input constraints. —

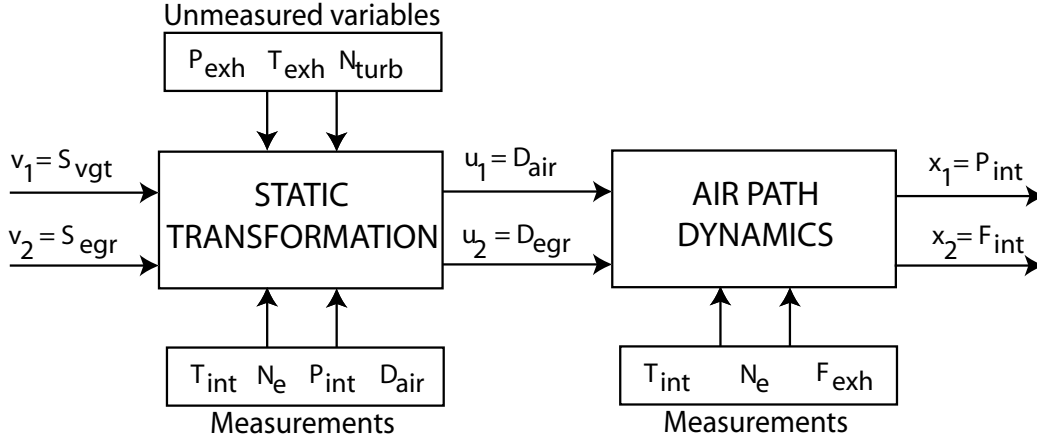


FIGURE 4.3. Input/Output scheme of the air path dynamics.

4.4.2.1. *Constraints on flow variables.* — For model constituency, input signals u_1 and u_2 must be positive. Moreover, to take physical limitation of the engine into account, the total input flow must be strictly positive and upper bounded. There exists $(u_{min}, u_{max}) \in (\mathbb{R}^+ \setminus \{0\})^2$ such that

$$0 < u_{min} \leq u_1 + u_2 \leq u_{max},$$

4.4.2.2. *Misfire avoidance.* — Our goal is to successfully pass the eurocycle. A necessary condition is to avoid misfires and the implied peaks in pollutant emissions. High EGR rates may cause these misfires. A simple strategy can address this issue. Conservatively, misfire avoidance can be guaranteed provided the following input constraints are satisfied

$$C(u) \triangleq F_{exh} \frac{u_2}{u_2 + u_1} \leq \bar{C} < 1$$

$C(u)$ is equivalent to the BGR at steady state.

4.4.2.3. *Feasible input set.* — Combining the previously discussed constraints, the set of feasible inputs is defined as

$$\mathcal{U} \triangleq \left\{ (u_1, u_2) \in (\mathbb{R})^2 / 0 < u_{min} \leq u_1 + u_2 \leq u_{max}, \right. \\ \left. u_2 \geq 0, \text{ and } F_{exh} \frac{u_2}{u_2 + u_1} \leq \bar{C} \right\}$$

and we note $\partial\mathcal{U}$ its boundary. A typical representation of the feasible set is given in Figure 4.4.

4.4.3. **Assumptions.** —

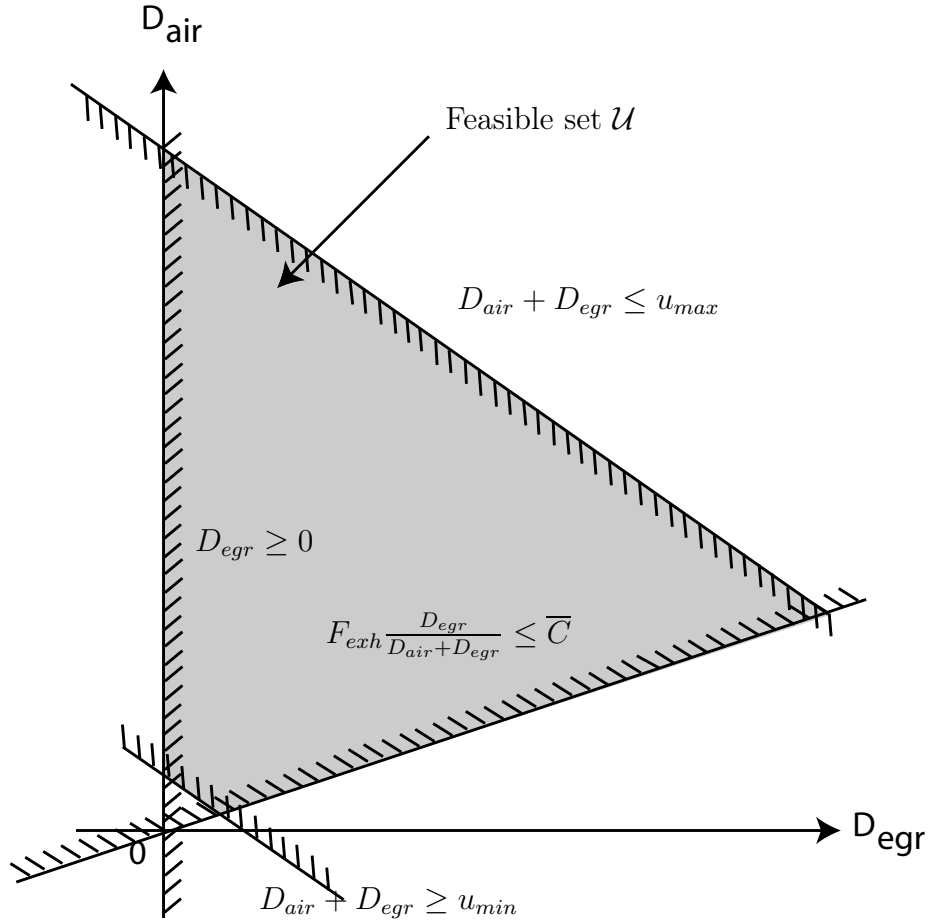


FIGURE 4.4. Input constraints in the plan $(u_1 = D_{air}, u_2 = D_{egr})$, the feasible set \mathcal{U} is represented in grey.

4.4.3.1. *Boundedness of α_{int} and β_{int} .* — We assume that there exists $(\alpha_m, \alpha_M, \beta_m, \beta_M) \in (\mathbb{R}^+ \setminus \{0\})^4$ such that

$$0 < \alpha_m \leq \alpha_{int} \leq \alpha_M \quad \text{and} \quad 0 < \beta_m \leq \beta_{int} \leq \beta_M$$

That means that T_{int} and N_e are strictly positive and upper bounded which is true experimentally.

4.4.3.2. *Characteristics of the volumetric efficiency.* — It is assumed that the volumetric efficiency slowly varies w.r.t. the intake pressure x_1 . We define the function h_{N_e}

$$\mathbb{R}^+ \ni x_1 \mapsto h_{N_e}(x_1) \triangleq \eta_{vol}(x_1, N_e)x_1 \quad (4.4)$$

we suppose that there exists a strictly positive constant $\underline{h} \in \mathbb{R}^+ \setminus \{0\}$ such that for all x_1 in \mathbb{R}^+ ,

$$\frac{\partial h_{N_e}}{\partial x_1}(x_1) \geq \underline{h} > 0$$

Experimentally, this assumption is actually easy to validate. We can now define

$$x_{1,m} \triangleq h_{N_e}^{-1}\left(\frac{u_{min}}{\beta_{int}}\right) \quad \text{and} \quad x_{1,M} \triangleq h_{N_e}^{-1}\left(\frac{u_{max}}{\beta_{int}}\right)$$

Notice that $x_{1,m} > 0$ because h is a strictly increasing function with $h(0) = 0$.

4.4.4. System properties. —

4.4.4.1. *The state x is bounded.* — Let $x_1 = x_{1,m}$ then we have

$$\begin{aligned} \dot{x}_1 &= \alpha_{int} (u_1 + u_2 - \beta_{int} h(x_{1,m})) \\ &= \alpha_{int} (u_1 + u_2 - u_{min}) \geq 0 \end{aligned}$$

By the same way, if $x_1 = x_{1,M}$ then $\dot{x}_1 \leq 0$. The following lemma hold

Lemma 4.1. — *For any initial condition such that $x_1(0) \in [x_{1,m}, x_{1,M}]$, then, for all $t \in \mathbb{R}^+$, the solution of (4.3) verifies $x_1(t) \in [x_{1,m}, x_{1,M}]$.*

Now, let us prove that $x_2 \in [0, \bar{C}]$. Let $x_2 = 0$, then, we have $\dot{x}_2 = \frac{\alpha_{int}}{x_1} F_{exh} u_2 \geq 0$. By the same way, if $x_2 = \bar{C}$,

$$\dot{x}_2 = \frac{\alpha_{int}}{x_1} (F_{exh} u_2 - (u_1 + u_2) \bar{C}) \leq 0$$

because $F_{exh} \frac{u_2}{u_2 + u_1} \leq \bar{C}$ as $u \in \mathcal{U}$. The following lemma holds

Lemma 4.2. — *For any initial condition such that $x_2(0) \in [0, \bar{C}]$, then, for all $t \in \mathbb{R}^+$, the solution of (4.3) verifies $x_2(t) \in [0, \bar{C}]$.*

We note $\mathcal{X} \triangleq [x_{1,m}, x_{1,M}] \times [0, \bar{C}]$, using Lemma 4.1 and 4.2 the following proposition holds

Proposition 4.1. — *For any initial condition $x(0) = (x_1(0), x_2(0)) \in \mathcal{X}$ and for any control input u such that $u(t) \in \mathcal{U}$ for all $t \in \mathbb{R}^+$, the solution $x(t)$ of (4.3) remains in \mathcal{X} for all $t \in \mathbb{R}^+$. The vector (x, u) is said to be a feasible trajectory.*

4.4.4.2. *System (4.3) is globally exponentially open loop stable.* — Let (x^r, u^r) be a feasible reference trajectory. Applying this open loop control law u^r to (4.3) with any initial condition $x(0) \in \mathcal{X}$, system (4.3) gives

$$\begin{cases} \dot{x}_1 = \alpha_{int} (u_1^r + u_2^r - \beta_{int} h_{N_e}(x_1)) \\ \dot{x}_2 = \frac{\alpha_{int}}{x_1} (F_{exh} u_2^r - (u_1^r + u_2^r) x_2) \end{cases} \quad (4.5)$$

Let $\tilde{x} = x^r - x$, the error between the reference state and the state (4.5). We get

$$\begin{cases} \dot{\tilde{x}}_1 = -\alpha_{int} \beta_{int} (h_{N_e}(x_1^r) - h_{N_e}(x_1)) \\ \dot{\tilde{x}}_2 = -\frac{\alpha_{int}}{x_1 x_1^r} (F_{exh} u_2^r - (u_1^r + u_2^r) x_2) \tilde{x}_1 - \alpha_{int} \frac{u_1^r + u_2^r}{x_1^r} \tilde{x}_2 \end{cases} \quad (4.6)$$

Exponential convergence of \tilde{x} toward 0 can be studied by exploiting the cascade structure of equations (4.6).

First, we focus on the \tilde{x}_1 -dynamics. The differentiation of the squared norm of \tilde{x}_1 leads to

$$\begin{aligned} \frac{d}{dt} (\tilde{x}_1^2) &= -2\alpha_{int} \beta_{int} (h_{N_e}(x_1) - h_{N_e}(x_1^r)) \tilde{x}_1 \\ &\leq -2\tau_m \tilde{x}_1^2 \end{aligned}$$

where $\tau_m \triangleq \alpha_m \beta_m \underline{h}$. Thus, we have

$$\forall t \in \mathbb{R}^+, \quad |\tilde{x}_1(t)| \leq e^{-\tau_m t} |\tilde{x}_1(0)| \quad (4.7)$$

Some easy rewriting of the \tilde{x}_2 -dynamics leads to

$$\dot{\tilde{x}}_2 = -\phi(t) \tilde{x}_2 + \psi(t) \quad (4.8)$$

where

$$\begin{cases} \psi(t) \triangleq -\frac{\alpha_{int}}{x_1 x_1^r} (F_{exh} u_2^r - (u_1^r + u_2^r) x_2) \tilde{x}_1 \\ \phi(t) \triangleq \alpha_{int} \frac{u_1^r + u_2^r}{x_1^r} \end{cases}$$

The analytic solution of (4.8) is

$$\tilde{x}_2(t) = e^{-\int_0^t \phi(s) ds} \tilde{x}_2(0) + \int_0^t e^{-\int_s^t \phi(\tau) d\tau} \psi(s) ds \quad (4.9)$$

From Proposition 4.1, x is bounded. Then, it follows that the function ψ is bounded because $u^r, x^r, \alpha_{int}, F_{exh}$ are. Yet, from (4.7), we have

$$\forall t \in \mathbb{R}^+ \quad |\psi(t)| \leq \Psi e^{-\tau_m t}$$

where $\Psi \triangleq 2 \frac{\alpha_M}{x_{1,M}^2} u_{max} \bar{C} |\tilde{x}_1(0)|$. The function ϕ is strictly positively bounded because α_{int} , x^r and u^r are, i.e.

$$\forall t \in \mathbb{R}^+ \quad 0 < \underline{\phi} \triangleq \min\left\{\frac{\tau_m}{2}, \alpha_m \frac{u_{min}}{x_{1,M}}\right\} \leq \phi(t)$$

These last two inequalities yield

$$|\tilde{x}_2(t)| \leq (|\tilde{x}_2(0)| + \frac{\Psi}{\tau_m - \underline{\phi}}) e^{-\phi t} + \frac{\Psi}{\tau_m - \underline{\phi}} e^{-\tau_m t}$$

Together with (4.7), this prove that the error \tilde{x} is globally exponentially stable. The following result holds.

Proposition 4.2. — *Consider a feasible reference trajectory (x^r, u^r) . Feed (4.3) with this control law. Then, the error state $x - x^r$ globally exponentially converges toward 0.*

This proposition is the key to understanding our approach. Provided chosen control values are feasible (i.e. belong to \mathcal{U}), it is sufficient to use them as inputs in the airpath system to exponentially reach a desired reference trajectory. For implementation, this strategy has to be complemented by an estimation technique to recover unmeasured variables.

4.5. Air path observer

As described in [58],

$$D_{egr} = S_{egr} \frac{P_{exh}}{\sqrt{RT_{exh}}} \sqrt{\frac{2\gamma}{\gamma-1} (p_r^{\frac{2}{\gamma}} - p_r^{\frac{\gamma-1}{\gamma}})}$$

where $p_r = \max\left\{\frac{P_{int}}{P_{exh}}, \left(\frac{2}{\gamma+1}\right)^{\frac{\gamma}{\gamma+1}}\right\}$. These two values describe both subsonic and choked EGR flow. In this model, numerous variables are not measured. The exhaust pressure and temperature for example are not easily available for a commercial engine. The effect of the EGR cooler is accounted for by considering

$$D_{egr} \triangleq S_{egr} \Theta_{egr}$$

where Θ_{egr} is a variable depending on the exhaust temperature, the pressure ratio between intake and exhaust manifold, and the behavior of the cooling system. This variable need

to be estimated to evaluate the EGR flow and the composition in the intake manifold, this is the purpose of this section.

In this section we design two observers to estimate both the EGR flow and the BGR. The first one is build on the assumption that the variation of temperature is small, i.e. $\dot{T}_{int} = 0$, the second one take this dynamics into consideration. Both observers are linearization technique based on output injection [79, 80]. Convergence is guaranteed with Lyapunov tools.

4.5.1. Isothermal Case. —

In this part, we assume that the volumetric efficiency error is null, i.e. $\delta\eta = 0$. Under these assumption, we now present the reference model dynamics and propose an observer. We assume that with a fixed distribution, the internal gas locked in the cylinder are negligible. Under these assumption, we now present the reference model dynamics and propose an observer. The observer design follows [27]. Exponential convergence of the observer is proven using Lyapunov arguments.

4.5.1.1. *Reference model.* — Let

$$x = [P_{int} \quad F_{int} \quad \Theta_{egr}]^T \in \mathbb{R}^3$$

be the state and $y = P_{int}$ the measurement. Using (4.1) and (4.2), the reference dynamics reads

$$\begin{cases} \dot{x}_1 = \alpha_{int} (u_1 + v_2 x_3 - \beta_{int} \eta_{vol}(x_1, N_e) x_1) \\ \dot{x}_2 = \frac{\alpha_{int}}{x_1} (F_{exh} v_2 x_3 - (u_1 + v_2 x_3) x_2) \\ \dot{x}_3 = 0 \\ y = x_1 \end{cases} \quad (4.10)$$

4.5.1.2. *Observer Design.* — The observer dynamics are

$$\begin{cases} \dot{\hat{x}}_1 = \alpha_{int} (u_1 + v_2 \hat{x}_3 - \eta_{vol}(y, N_e) \beta_{int} \hat{x}_1) - L_1 (\hat{x}_1 - y) \\ \dot{\hat{x}}_2 = \frac{\alpha_{int}}{y} (F_{exh} v_2 \hat{x}_3 - (u_1 + v_2 \hat{x}_3) \hat{x}_2) \\ \dot{\hat{x}}_3 = -L_3 (\hat{x}_1 - y) \end{cases} \quad (4.11)$$

with $(L_1, L_3) \in (\mathbb{R}^+ \setminus \{0\})^2$. One can notice that (4.11) is a copy of (4.10) with additive tracking terms. Unknowns are partially substituted with output measurement. Tuning parameters are chosen as follows

$$L_1 = (l_1 - \eta_{vol}(y, N_e)) \alpha_{int} \beta_{int} \quad \text{and} \quad L_3 = l_3 \alpha_{int} u$$

where l_1 and l_3 are positive constants. The state-error is $\tilde{x} \triangleq x - \hat{x}$. The error system writes under the triangular form (4.12)-(4.13)

$$\begin{cases} \dot{\tilde{x}}_1 = \alpha_{int} (v_2 \tilde{x}_3 - l_1 \beta_{int} \tilde{x}_1) \\ \dot{\tilde{x}}_3 = -l_3 \alpha_{int} \tilde{x}_1 v_2 \end{cases} \quad (4.12)$$

$$\dot{\tilde{x}}_2 = \frac{\alpha_{int}}{y} (F_{exh} v_2 \tilde{x}_3 - (u_1 + v_2 \hat{x}_3) \tilde{x}_2) + \frac{\alpha_{int}}{y} (F_{exh} - x_2) \tilde{x}_3 \quad (4.13)$$

4.5.1.3. Convergence analysis. — To investigate convergence of the proposed observer, we assume that $v_2 > 0$. This last assumption is not restrictive since v_2 equals 0 implies that the EGR valve is completely closed and that, consequently, the EGR flow equal to 0. The convergence proof is divided in two parts, exploiting the cascade structure of the error dynamics (4.12), (4.13).

(\tilde{x}_1, \tilde{x}_3)-dynamics. — The errors dynamics (4.12) is upper-triangular. Indeed, the $(\tilde{x}_1, \tilde{x}_3)$ -dynamics is independent of \tilde{x}_2 . The dynamics writes

$$\begin{bmatrix} \dot{\tilde{x}}_1 \\ \dot{\tilde{x}}_3 \end{bmatrix} = A_{int}(t) \begin{bmatrix} \tilde{x}_1 \\ \tilde{x}_3 \end{bmatrix}$$

where $A_{int}(t) \triangleq \begin{bmatrix} -l_1 \alpha_{int} \beta_{int} & \alpha_{int} v_2 \\ l_2 \alpha_{int} v_2 & 0 \end{bmatrix}$

A_{int} is a time varying matrix.

First, a Lyapunov function candidate is

$$V(\tilde{x}) = \frac{1}{2} \left(\tilde{x}_1^2 + \frac{1}{l_3} \tilde{x}_3^2 \right) \quad (4.14)$$

First of all, $V(0) = 0$, and $\forall \tilde{x} \in \mathbb{R}^2 \setminus \{0\} V(\tilde{x}) > 0$. Differentiation yields

$$\dot{V}(\tilde{x}) = \tilde{x}_1 \dot{\tilde{x}}_1 + \frac{1}{l_3} \tilde{x}_3 \dot{\tilde{x}}_3 = -\alpha_{int} \beta_{int} l_1 \tilde{x}_1^2$$

α_{int} and β_{int} are bounded. This leads to $\dot{V}(\tilde{x}) \leq -\alpha_m \beta_m l_1 \tilde{x}_1^2$. Since $\dot{V}(\tilde{x}) \leq 0$ in $\Omega_r = \{\tilde{x}_f = [\tilde{x}_{1,f} \ \tilde{x}_{3,f}]^T \in \mathbb{R}^2 / V(\tilde{x}_f) < r\} \subset \mathbb{R}^2$, $V(\tilde{x}(t))$ is a decreasing function in t . Since $V(\tilde{x})$ is continuous on the compact Ω_r , it is bounded from below on Ω_r . Therefore, $V(\tilde{x}(t))$ has a limit a as $t \rightarrow +\infty$. Moreover,

$$\begin{aligned} V(0) &\geq V(0) - V(\tilde{x}(t)) = - \int_0^t \dot{V}(\tilde{x}(\tau)) d\tau \\ &\geq \alpha_m \beta_m l_1 \int_0^t \tilde{x}_1^2(\tau) d\tau \end{aligned}$$

and so \tilde{x}_1 is square integrable. As \tilde{x}_1 is uniformly continuous, $\tilde{x}_1(t)$ tends to 0 as $t \rightarrow +\infty$. Moreover, \tilde{x}_1 and \tilde{x}_3 are uniformly continuous and bounded (because $V(\tilde{x}) \leq V(0)$) yielding $\dot{\tilde{x}}_1$ is uniformly continuous and bounded. Finally, $\dot{\tilde{x}}$ is a uniformly continuous and $\lim_{t \rightarrow +\infty} \tilde{x}_1(t) = 0$, then from Barbalat's lemma (see [76] Lemma 8.2)

$$\lim_{t \rightarrow +\infty} \dot{\tilde{x}}_1(t) = 0$$

Thus, $\lim_{t \rightarrow +\infty} \tilde{x}_3(t) = 0$ and the equilibrium point is uniformly asymptotically stable. However, the dynamics is linear. Thus this implies that \tilde{x}_1 and \tilde{x}_3 are exponentially stable (see [76] Theorem 4.11). In other words $\exists(\tau_{int}, \lambda_{int}) \in (\mathbb{R}^+ \setminus \{0\})^2$ s. t. $\forall t \in \mathbb{R}^+$

$$|\tilde{x}_1(t)| \leq \tau_{int} e^{-\lambda_{int} t} \quad \text{and} \quad |\tilde{x}_3(t)| \leq \tau_{int} e^{-\lambda_{int} t}$$

\tilde{x}_2 -dynamics. — On the other hand, the \tilde{x}_2 dynamics writes

$$\dot{\tilde{x}}_2 = -a_{int}(t)\tilde{x}_2 + b_{int}(t)$$

where

$$\begin{cases} a_{int}(t) \triangleq \frac{\alpha_{int}}{y}(u_1 + v_2 \hat{x}_3) \\ b_{int}(t) \triangleq \frac{\alpha_{int}}{y}(F_{exh} - x_2)v_2 \tilde{x}_3 \end{cases}$$

We compute the analytical solution

$$\tilde{x}_2(t) = e^{-\int_{t_0}^t a_{int}(s) ds} \tilde{x}_2(t_0) + \int_{t_0}^t e^{-\int_s^t a_{int}(\tau) d\tau} b_{int}(s) ds \quad (4.15)$$

The function b_{int} is bounded because v_2 , x , α_{int} , F_{exh} and \tilde{x}_3 are. We have

$$\forall t \in \mathbb{R}^+ \quad |b_{int}(t)| \leq B e^{-\lambda_{int} t}$$

where $B \triangleq \frac{\alpha_M}{x_{1,m}} \tau_{int}$. Moreover, as $|\tilde{x}_3(t)| \leq \tau_{int} e^{-\lambda_{int} t}$, there exists $t_0 \triangleq \max\{0, \frac{1}{\lambda_{int}} \ln(\frac{3|\tilde{x}_3(0)|}{2u_{min}})\}$ such that

$$\forall t \geq \tau_0, \quad a_{int}(t) \geq \underline{a} \triangleq \min\left\{\frac{\lambda_{int}}{2}, \frac{\alpha_M}{x_{1,m}} \frac{u_{min}}{3}\right\} > 0$$

Majorations in (4.15) lead to

$$|\tilde{x}_2(t)| \leq (|\tilde{x}_2(t_0)| + \frac{B}{\lambda_{int} - \underline{a}}) e^{-\underline{a}(t-t_0)} + \frac{B}{\lambda_{int} - \underline{a}} e^{-\lambda_{int}(t-t_0)}$$

The error is globally exponentially stable and the following result holds.

Proposition 4.3. — *Assuming that $v_2 > 0$, there exists $t_0 \triangleq \max\{0, \frac{1}{\lambda_{int}} \ln(\frac{3|\tilde{x}_3(0)|}{2u_{min}})\}$ such that, for $t \geq t_0$, the error states (4.12) and (4.13) exponentially converge towards 0.*

4.5.2. Adiabatic Case. — In this subsection, we do not assume that the variation of temperature is small, but rather that the energy balance yields

$$\dot{T}_{int} = \frac{RT_{int}}{V_{int}P_{int}}(D_{air}(\gamma T_{air} - T_{int}) - D_{asp}(\gamma - 1)T_{int} + D_{egr}(\gamma T_{egr} - T_{int})) \quad (4.16)$$

This case is of interest because for large variations of EGR, the temperature of the intake manifold can increase by 20° during the transient (this factor actually depends on the EGR cooling system). This rules out the isothermal assumption, and generates a tracking error and a nonzero volumetric efficiency offset $\delta\eta$ in the previously presented observer. Indeed, when the EGR valve is open, one cannot distinguish an error on the EGR flow from an error on the aspirated flow (which is based on experimental *steady state* values). Yet, using an EGR temperature sensor, one can reconstruct the volumetric efficiency error $\delta\eta$ and the EGR flow. This is the subject of the following section.

4.5.2.1. Reference Model. — Let

$$x = [P_{int} \quad F_{int} \quad \Theta_{egr} \quad T_{int} \quad \delta\eta]^T \in \mathbb{R}^5$$

be the state and $y = [P_{int}, T_{int}]^T \in \mathbb{R}^2$ devotes measurements. We note $\xi_{int} \triangleq \frac{R}{V_{int}}$ and $\rho_{int} \triangleq \frac{1}{R}V_{cyl}\frac{N_e}{120}$. The reference dynamics is

$$\left\{ \begin{array}{l} \dot{x}_1 = \xi_{int}(u_1 T_{air} + v_2 x_4 T_{egr} - (\eta_{vol, map}(x_1, N_e) + x_5)\rho_{int}x_1) \\ \dot{x}_2 = \xi_{int} \frac{x_4}{x_1} (F_{exh} v_2 x_3 - (D_{air} + v_2 x_3)x_2) \\ \dot{x}_3 = 0 \\ \dot{x}_4 = \xi_{int} \frac{x_4}{x_1} \left(u_1(\gamma T_{air} - x_4) + v_2 x_4(\gamma T_{egr} - x_4) \right. \\ \quad \left. - (\gamma - 1)(\eta_{vol, map}(x_1, N_e) + x_5)\rho_{int}x_1 \right) \\ \dot{x}_5 = 0 \\ y_1 = x_1 \\ y_2 = x_4 \end{array} \right. \quad (4.17)$$

Notations for this part is summarized in Table 4.2.

Var.	Symb.	Var.	Symb.
x_1	P_{int}	y_1	P_{int}
x_2	F_{int}	y_2	T_{int}
x_3	Θ_{egr}	ξ_{int}	$\frac{R}{V_{int}}$
x_4	T_{int}	ρ_{int}	$\frac{V_{cyl} N_e}{R \cdot 120}$
x_5	$\delta\eta$		

TABLE 4.2. Variables description for the adiabatic observer.

4.5.2.2. *Observer Design.* — The observer dynamics are

$$\left\{ \begin{array}{l} \dot{\hat{x}}_1 = \xi_{int}(u_1 T_{air} + v_2 \hat{x}_3 T_{egr} - (\eta_{vol, map}(y_1, N_e) + \hat{x}_5) \rho_{int} \hat{x}_1) \\ \quad - L_1(\hat{x}_1 - y_1) \\ \dot{\hat{x}}_2 = \xi_{int} \frac{y_4}{y_1} (F_{exh} v_2 \hat{x}_3 - (u_1 + v_2 \hat{x}_3) \hat{x}_2) \\ \dot{\hat{x}}_3 = -L_{3,1}(\hat{x}_1 - y_1) - L_{3,2}(\hat{x}_4 - y_2) \\ \dot{\hat{x}}_4 = \xi_{int} \frac{y_4}{y_1} (u_1(\gamma T_{air} - \hat{x}_4) + v_2 \hat{x}_3(\gamma T_{egr} - \hat{x}_4) \\ \quad - (\gamma - 1)(\eta_{vol, map}(y_1, N_e) + \hat{x}_5) \rho_{int} y_1) - L_4(\hat{x}_4 - y_2) \\ \dot{\hat{x}}_5 = L_{5,1}(\hat{x}_1 - y_1) + L_{5,2}(\hat{x}_4 - y_2) \end{array} \right. \quad (4.18)$$

with $(L_1, L_2, L_4, L_5) \in (\mathbb{R}^+ \setminus \{0\})^4$. Again, one can notice that (4.18) is a copy of (4.17) with additive tracking terms and where unknowns are partially substituted with output measurement injections. The state-error is $\tilde{x} \triangleq x - \hat{x}$. Classically, the error dynamics is

$$\left\{ \begin{array}{l} \dot{\tilde{x}}_1 = \xi_{int}(v_2 \tilde{x}_3 T_{egr} - \eta_{vol, map}(y_1, N_e) \rho_{int} \tilde{x}_1 - \rho_{int}(x_5 \tilde{x}_1 + \hat{x}_1 \tilde{x}_5)) \\ \quad - L_1 \tilde{x}_1 \\ \dot{\tilde{x}}_2 = \xi_{int} \frac{y_4}{y_1} (-(u_1 + v_2 \hat{x}_4) \tilde{x}_3 + (F_{exh} - v_2 x_3) \tilde{x}_3) \\ \dot{\tilde{x}}_3 = -L_{3,1} \tilde{x}_1 - L_{3,2} \tilde{x}_4 \\ \dot{\tilde{x}}_4 = \xi_{int} \frac{y_4}{y_1} (-u_1 \tilde{x}_4 + v_2 \tilde{x}_3(\gamma T_{egr} - \hat{x}_4) \\ \quad - v_2 x_3 \tilde{x}_4 - (\gamma - 1) \tilde{x}_5 \rho_{int} y_1) - L_4 \tilde{x}_4 \\ \dot{\tilde{x}}_5 = L_{5,1} \tilde{x}_1 + L_{5,2} \tilde{x}_4 \end{array} \right.$$

Tuning parameters are chosen as follows

$$\left\{ \begin{array}{l} L_1 = (l_1 - \eta_{vol, map}(y_1, N_e)) \xi_{int} \rho_{int} \\ L_{3,1} = l_3 \xi_{int} T_{egr} v_2 \\ L_{3,2} = l_3 \xi_{int} \frac{y_4}{y_1} v_2 (\gamma T_{egr} - \hat{x}_4) \\ L_4 = l_4 \xi_{int} \frac{y_4}{y_1} u_1 \\ L_{5,1} = l_5 \xi_{int} \rho_{int} \hat{x}_1 \\ L_{5,2} = l_5 \xi_{int} \frac{y_4}{y_1} (\gamma - 1) \rho_{int} y_1 \end{array} \right.$$

with $(l_1, l_2, l_4, l_5) \in (\mathbb{R}^+ \setminus \{0\})^4$, and $l_1 > 1$. With this choice, the error system writes under the following triangular form

$$\left\{ \begin{array}{l} \dot{\tilde{x}}_1 = \xi_{int} (v_2 \tilde{x}_3 T_{egr} - l_1 \rho_{int} \tilde{x}_1 - \rho_{int} (x_5 \tilde{x}_1 + \hat{x}_1 \tilde{x}_5)) \\ \dot{\tilde{x}}_3 = -l_3 \xi_{int} T_{egr} v_2 \tilde{x}_1 - l_3 \xi_{int} \frac{y_4}{y_1} v_2 (\gamma T_{egr} - \hat{x}_4) \tilde{x}_4 \\ \dot{\tilde{x}}_4 = \xi_{int} \frac{y_4}{y_1} (-(1 + l_2) u_1 \tilde{x}_4 + \tilde{x}_3 v_2 (\gamma T_{egr} - \hat{x}_4) - v_2 x_3 \tilde{x}_4 - (\gamma - 1) \tilde{x}_5 \rho_{int} y_1) \\ \dot{\tilde{x}}_5 = l_5 \xi_{int} \rho_{int} \hat{x}_1 \tilde{x}_1 + l_5 \xi_{int} \frac{y_4}{y_1} (\gamma - 1) \rho_{int} y_1 \tilde{x}_2 \end{array} \right. \quad (4.19)$$

$$\dot{\tilde{x}}_2 = \xi_{int} \frac{y_4}{y_1} (-(D_{air} + S_{egr} \hat{x}_4) \tilde{x}_3 + (F_{exh} - S_{egr} x_3) \tilde{x}_3) \quad (4.20)$$

4.5.2.3. Convergence analysis. —

Lyapunov function candidate. — Convergence of (4.19) towards $\{0\}$ can be proven through a Lyapunov stability analysis. A Lyapunov function candidate is

$$V(\tilde{x}) = \frac{1}{\xi_{int}} \left(\tilde{x}_1^2 + \frac{1}{l_3} \tilde{x}_3^2 + \tilde{x}_4^2 + \frac{1}{l_5} \tilde{x}_5^2 \right) \quad (4.21)$$

Differentiation yields

$$\begin{aligned} \dot{V}(\tilde{x}) &= \frac{1}{\alpha_{int}} (\tilde{x}_1 \dot{\tilde{x}}_1 + \frac{1}{\alpha_{int}} \tilde{x}_4 \dot{\tilde{x}}_4 + \frac{1}{\alpha_{int} l_3} \tilde{x}_3 \dot{\tilde{x}}_3 + \frac{1}{\alpha_{int} l_5} \tilde{x}_5 \dot{\tilde{x}}_5) \\ &= -(l_1 + x_5) \rho_{int} \tilde{x}_1^2 - \frac{y_4}{y_1} ((1 + l_2) u_1 + v_2 x_3) \tilde{x}_4^2 \end{aligned}$$

$(l_1 + x_5)\rho_{int}$ and $\frac{y_4}{y_1}((1 + l_2)u_1 + v_2x_3)$ are bounded. There exists $(\alpha_1, \alpha_4) \in (\mathbb{R}^+ \setminus \{0\})^2$ such that

$$0 < \alpha_1 \leq (l_1 + x_5)\rho_{int} \quad \text{and} \quad 0 < \alpha_4 \leq \frac{y_4}{y_1}((1 + l_2)u_1 + v_2x_3)$$

This leads to $\dot{V}(\tilde{x}) \leq -\alpha_1\tilde{x}_1^2 - \alpha_4\tilde{x}_4^2$. Since $\dot{V}(\tilde{x}) \leq 0$ in $\Omega_r = \{\tilde{x}_f = [\tilde{x}_{1,f} \ \tilde{x}_{3,f} \ \tilde{x}_{4,f} \ \tilde{x}_{5,f}]^T \in \mathbb{R}^4 / V(\tilde{x}_f) < r\} \subset \mathbb{R}^2$, $V(\tilde{x}(t))$ is a decreasing function in t . Since $V(\tilde{x})$ is continuous on the compact Ω_r , it is bounded from below on Ω_r . Therefore, $V(\tilde{x}(t))$ has a limit a as $t \rightarrow +\infty$. Moreover,

$$\begin{aligned} V(0) &\geq V(0) - V(\tilde{x}(t)) = - \int_0^t \dot{V}(\tilde{x}(\tau)) d\tau \\ &\geq \alpha_1 \int_0^t \tilde{x}_1^2(\tau) d\tau + \alpha_4 \int_0^t \tilde{x}_4^2(\tau) d\tau \end{aligned}$$

and so \tilde{x}_1 and \tilde{x}_4 are square integrable. As \tilde{x}_1 and \tilde{x}_4 are uniformly continuous, $\tilde{x}_1(t)$ and $\tilde{x}_4(t)$ tend to 0 as $t \rightarrow +\infty$. Moreover, $\tilde{x}_1, \tilde{x}_3, \tilde{x}_4$ and \tilde{x}_5 are uniformly continuous and bounded (because $V(\tilde{x}) \leq V(0)$) yielding $\dot{\tilde{x}}_1$ and $\dot{\tilde{x}}_4$ are uniformly continuous and bounded. Finally, \tilde{x}_1 and \tilde{x}_4 are a uniformly continuous and $\lim_{t \rightarrow +\infty} \tilde{x}_1(t) = \lim_{t \rightarrow +\infty} \tilde{x}_4(t) = 0$, then from Barbalat's lemma (see [76] Lemma 8.2)

$$\lim_{t \rightarrow +\infty} \dot{\tilde{x}}_1(t) = \lim_{t \rightarrow +\infty} \dot{\tilde{x}}_4(t) = 0$$

Thus,

$$\lim_{t \rightarrow +\infty} \mathcal{L}_{int}(t) \begin{bmatrix} \tilde{x}_{4,f} \\ \tilde{x}_{5,f} \end{bmatrix} = 0$$

where

$$\mathcal{L}_{int} \triangleq \begin{bmatrix} \xi_{int} T_{egr} v_2 & \xi_{int} \frac{y_4}{y_1} S_{egr} (\gamma T_{egr} - x_4) \\ \xi_{int} \rho_{int} x_1 & \xi_{int} \frac{y_4}{y_1} (\gamma - 1) \rho_{int} y_1 \end{bmatrix}$$

and the equilibrium point is uniformly asymptotically stable. However, the dynamics is linear. Thus this implies that $\tilde{x}_1, \tilde{x}_3, \tilde{x}_4$ and \tilde{x}_5 are exponentially stable (see [76] Theorem 4.11).

Convergence proof of \tilde{x}_2 is similar to the technique presented in the previous section.

In summary, the observation error is exponentially stable and the following result holds.

Proposition 4.4. — *Assuming that $v_2 > 0$, the state of observer (4.18) asymptotically converges towards the state of system (4.17).*

4.5.3. Simulation results. —

4.5.3.1. IMEP Trajectory. — We test our observer on a transient of EGR valve at 1500 rpm. The trajectories of the EGR valve, BGR, intake pressure and temperature are reported in Figure 4.5. The opening of the EGR valve implies a fall of the pressure and an increase of the temperature.

4.5.3.2. Observers Results. — We focus on 3 time zones of the observers responses.

- Time zone 1 : [6.5, 10] the EGR valve opens (Figure 4.6). Both observers have relevant slopes. Interestingly, the adiabatic observers catches the overshoot at the beginning.
- Time zone 2 : [12, 13] the EGR flow stabilizes (Figure 4.7). The adiabatic converges towards the reference BGR while the isothermal observer has a volumetric efficiency error $\delta\eta$ yielding an offset error in the BGR tracking.
- Time zone 3 : [13.5, 15] the EGR valve closes with one oscillation (Figure 4.8). Both observers have the same dynamic, they follow the BGR dynamics during the oscillation of the EGR valve.

4.5.3.3. Conclusion toward the relevance of the observers. — Simulation results stress the relevance of the proposed observers. Both seems appropriate for control purposes. The dynamical behavior of the system is well captured. Further, the adiabatic observer provides an estimation of the volumetric efficiency. This gives the exact total quantity of air aspirated into the cylinders. In that case, an accurate EGR and aspirated flows observation is done with two extra temperature sensors (fresh air and EGR temperatures). The static error on aspirated flow is eliminated and leads to convergence of both the EGR flow and the BGR. A summary is presented in Table 4.3. Moreover, we assume that with a fixed distribution, the internal recirculated gas locked in the cylinder are constant on a fixed operating point. This leads to an offset between the composition in the intake manifold and in the cylinder. For a fixed distribution, this offset is not problematic because this offset is already reflected in the BGR set point map. Nevertheless, with variable distribution engine (Variable Valve Actuation), this offset should be taken into account in order to control the exact composition in the cylinder. Robustness toward model error is discussed in the next subsection.

4.5.4. Robustness toward volumetric efficiency map errors. — The volumetric efficiency map depends on the engine speed (N_e) and the intake pressure (P_{int}). Nevertheless, the volumetric efficiency depends also (but at a low order) on other parameters (such as exhaust pressure for exemple). The static map can thus differ a little bit from the

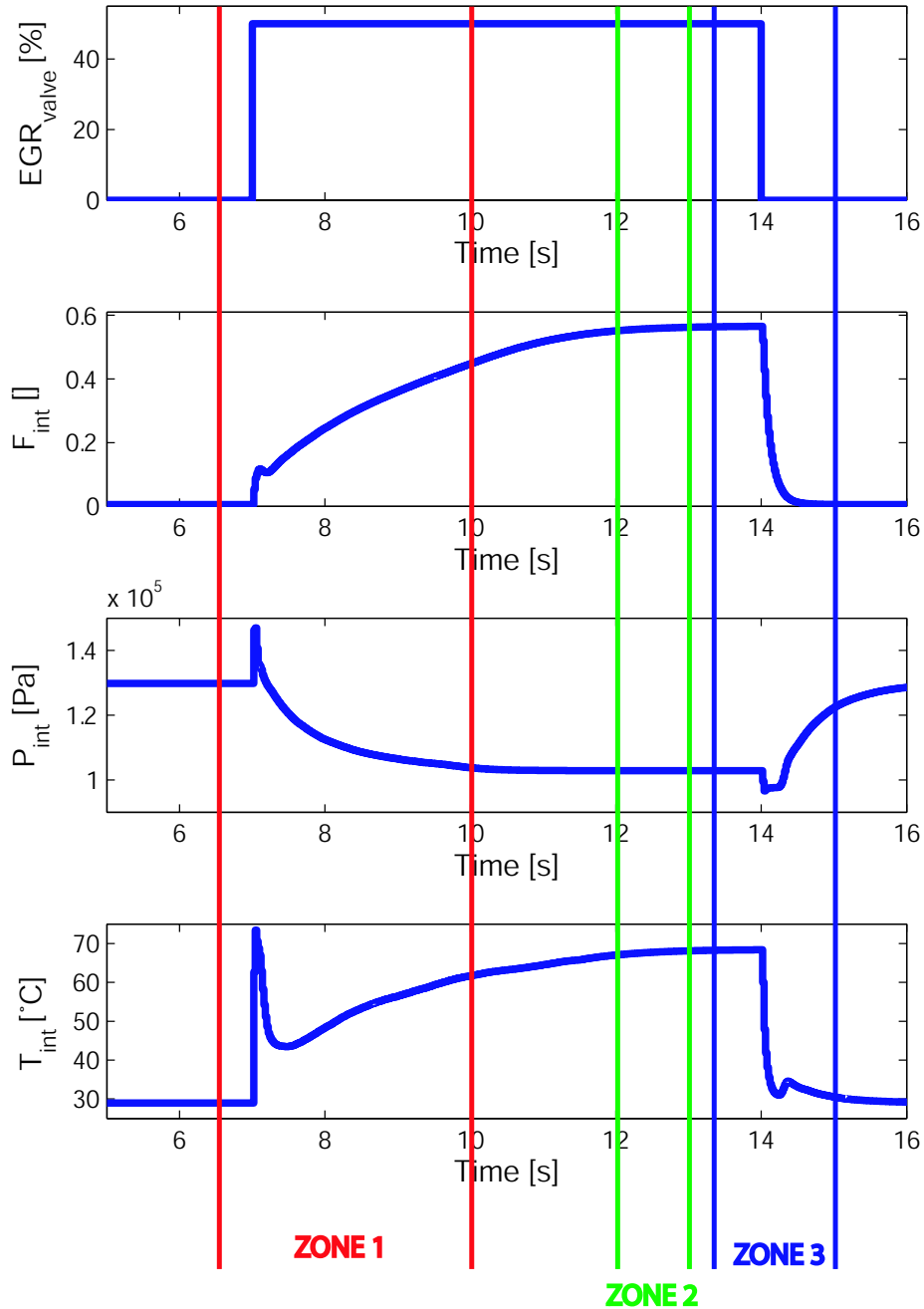


FIGURE 4.5. Transient at 1500 rpm, EGR valve variation. TFrom the top to the bottom: EGR valve position (%), BGR (-), intake pressure (Pa) and intake temperature (°C). Zone 1 corresponds to the opening of the EGR valve, Zone 1 corresponds to the settling of the EGR valve, and Zone 3 corresponds to the closing of the EGR valve.

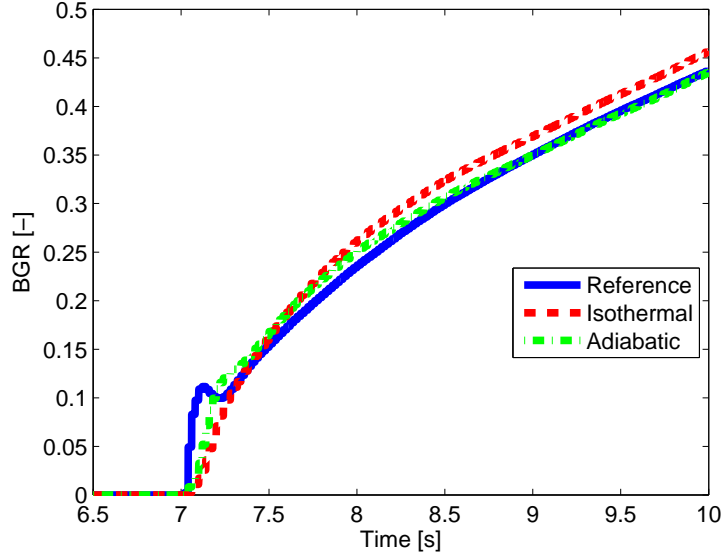


FIGURE 4.6. Observer results on a transient at 1500 rpm in HCCI combustion mode, EGR valve is opening. Blue: reference, red-dashed: isothermal observer, green-dotted: adiabatic observer. Both observers feature constant slopes. The adiabatic observer catches the overshoot at the beginning.

operating conditions $\delta\eta$. Assuming this error constant, we have at steady state

$$\begin{cases} D_{egr} = \eta_{vol}\beta_{int}P_{int} - D_{air} \\ F_{int} = F_{exh}\left(1 - \frac{D_{air}}{\eta_{vol}\beta_{int}P_{int} - D_{air}}\right) \end{cases}$$

We compute the relative error due to this offset $\delta\eta$. The relative errors reads

$$\begin{cases} \frac{\delta D_{egr}}{D_{egr}} = \delta\eta \frac{\rho_{int}}{(\eta_{map,vol} + \delta\eta)\rho_{int} - 1} \\ \frac{\delta F_{int}}{F_{int}} = -\frac{\delta\eta}{\eta_{vol}(\eta_{map,vol} + \delta\eta)\rho_{int} - 1} \end{cases}$$

where $\rho_{int} \triangleq \frac{\beta_{int}P_{int}}{D_{air}}$. The relative errors for a fixed operating points are represented in Figure 4.9.

The relative errors are almost linear in function of $\delta\eta$ and not negligible which means that we need a good volumetric efficiency map.

4.5.5. Evolution of Θ_{egr} when the EGR valve is closed. — When the EGR valve is closed, we are not able to estimate Θ_{egr} . This variable depends on the exhaust temperature, the pressure ratio between intake and exhaust manifold, and the behavior of the cooling

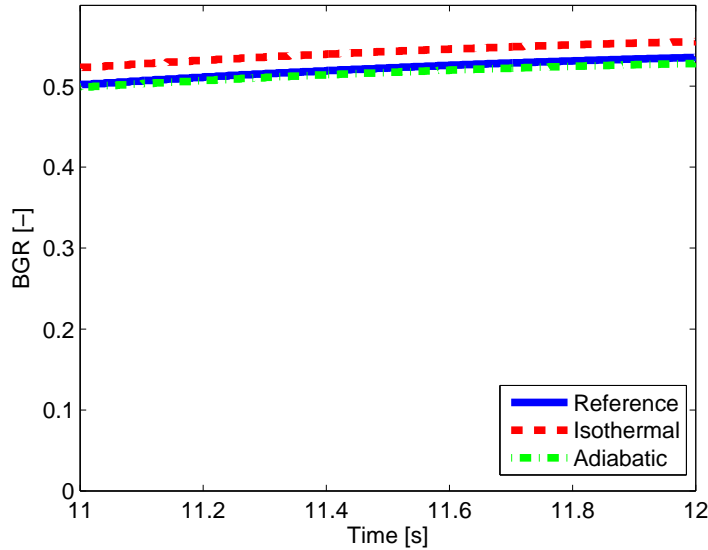


FIGURE 4.7. Observer results on a transient at 1500 rpm in HCCI combustion mode, EGR is settling. Blue: reference, red-dashed: isothermal observer, green-dotted: adiabatic observer. The adiabatic observer converges towards the reference BGR contrary to the isothermal observer that suffers from a non-zero volumetric efficiency error $\delta\eta$.

system. Results for different initial increasing initial value of $\hat{\Theta}_{egr}$ with the isothermal observer are presented in Figure 4.10. We see that the beginning of the transient part differs depending on the initial condition of $\hat{\Theta}_{egr}$. Changing the operating point without opening the EGR valve will have an impact on Θ_{egr} , i.e., increasing the load will increase Θ_{egr} . To have a better initial guess for $\hat{\Theta}_{egr}$ when the EGR valve will open again, we pose

$$\hat{\Theta}_{egr} = \hat{\Theta}_{egr,0} \frac{P_{int}}{P_{int,0}}$$

where $P_{int,0}$ and $\hat{\Theta}_{egr,0}$ are respectively the intake pressure and the estimated Θ_{egr} when the EGR valve has closed.

4.6. Air path feedforward control

Now, we have an estimation of the EGR flow and the BGR in the intake manifold. Thanks to that well defined change of variables, the control inputs are the EGR flow D_{egr}

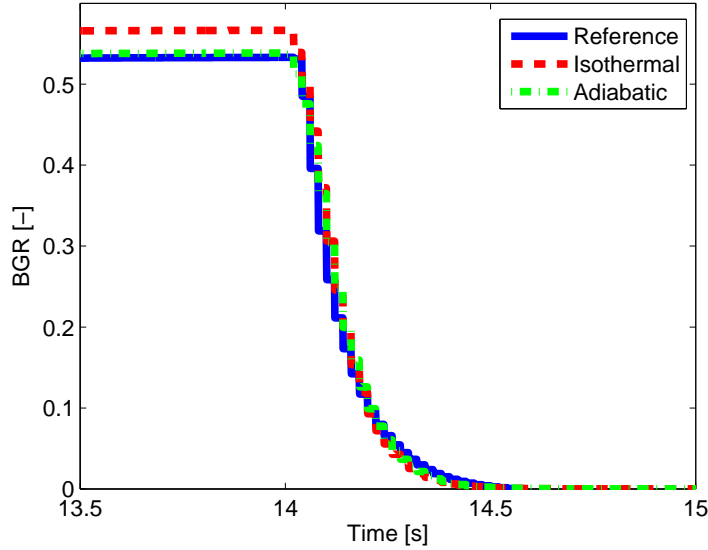


FIGURE 4.8. Observer results on a fast transient at 1500 rpm in HCCI combustion mode, EGR valve is closing with an oscillation. Blue: reference, red-dashed: isothermal observer, green-dotted: adiabatic observer. Both observers have the same dynamic, they follow the BGR dynamics during the oscillation of the EGR valve.

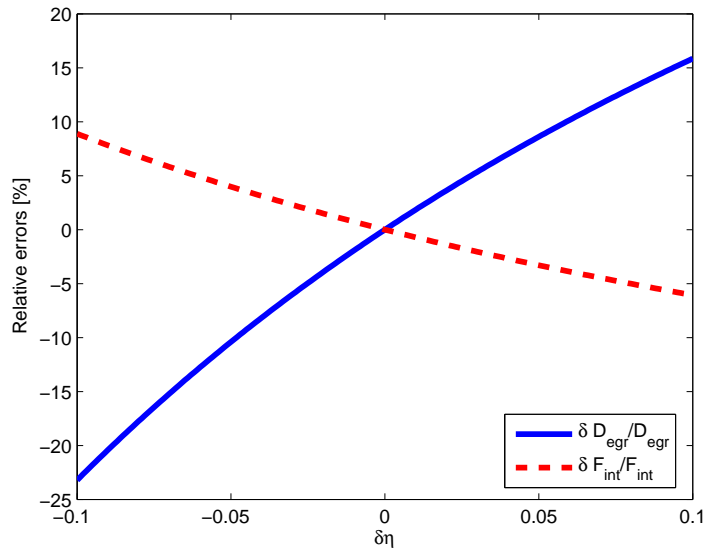
and the fresh air flow D_{air} . The reference model for the control writes

$$\begin{cases} \dot{x}_1 = \alpha_{int} (u_1 + u_2 - \eta_{vol}(x_1, N_e) \beta_{int} x_1) \\ \dot{x}_2 = \frac{\alpha_{int}}{x_1} (F_{exh} u_2 - (u_1 + u_2) x_2) \end{cases}$$

This system is linearizable by non linear static feedback: it is a differentially flat system with (x_1, x_2) as flat output. This standard non linear control techniques can be applied here (flatness based motion planing and tracking)[51]. To summarize, the air path is represented as the input output system (4.3) in depicted in Figure 4.3. We propose a motion planning control strategy which rely on the computation of transient trajectories for the air path dynamics (4.3). This strategy is detailed in Figure 4.11. It comprises 4 sub procedures: set point computations through static maps (first two blocks in Figure 4.11), trajectory generation, model inversion, and saturation of open-loop control values. We now detail these in the next subsection, we actually prove convergence of the air path system when using this strategy.

	Isothermal	Adiabatic
Sensors:		
P_{int}	Needed	Needed
T_{int}	Needed	Needed
D_{air}	Needed	Needed
AFR	Needed	Needed
T_{air}	Not Needed	Needed
T_{egr}	Not Needed	Needed
Volumetric efficiency:		
$\delta\eta$	0 by assumption	Estimated
D_{egr} estimation:		
	Offset due to $\delta\eta$	Convergence
BGR estimation:		
	Offset due to $\delta\eta$	Convergence

TABLE 4.3. Comparison of the two presented observers

FIGURE 4.9. Relative errors variation over $\delta\eta$ at a fixed operating point: $N_e = 1500\text{rpm}$, $IMEP = 4\text{bar}$, $F_{int} = .46$, and $D_{egr} = 0.0163\text{kg}\cdot\text{s}^{-1}$

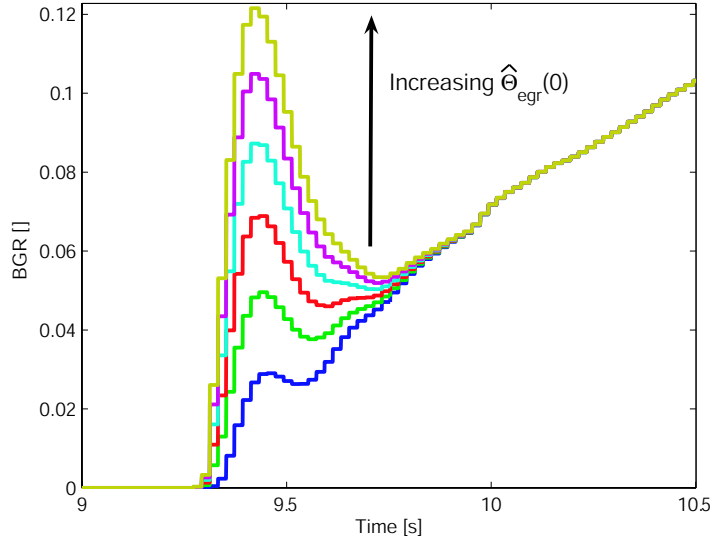


FIGURE 4.10. Observer results on a fast transient at 1500 rpm, IMEP from 10 to 4 bar, with increasing initial value of $\hat{\Theta}_{egr}$. $\hat{\Theta}_{egr}(0)$ from 0 to 50 by step of 10.

4.6.1. Set points. — The driver’s request considered here is the accelerator position. First, taking into account the gear box configuration, this request is turned into a torque control objective under the form of an IMEP (Indicated Mean Effective Pressure) set point. Then, the set points for the intake pressure and the BGR (noted x^{sp} in Figure 4.11) are inversely given by experimentally calibrated static maps on the $(\text{IMEP}^{\text{sp}}, N_e)$ operating range. The engine speed N_e is not modelled but directly measured. The $x^{\text{sp}} = (x_1^{\text{sp}}, x_2^{\text{sp}})$ vector is defined as

$$x_1^{\text{sp}} = f_{\text{pressure}}(\text{IMEP}^{\text{sp}}, N_e) \quad \text{and} \quad x_2^{\text{sp}} = f_{\text{bgr}}(\text{IMEP}^{\text{sp}}, N_e)$$

4.6.2. Motion planning. — Because IMEP^{sp} is arbitrarily specified by the driver, $t \mapsto x_1^{\text{sp}}(t)$ and $t \mapsto x_2^{\text{sp}}(t)$ may not be smooth nor monotonous. These signals must be filtered to correspond to feasible trajectories of (4.3). This can be done by many methods. Here, we propose the following approach that, besides other interesting properties, is easy to handle in the convergence analysis process. It addresses only the case of transients from one steady state to another. From a current steady state \underline{x} to a target \bar{x} we use an

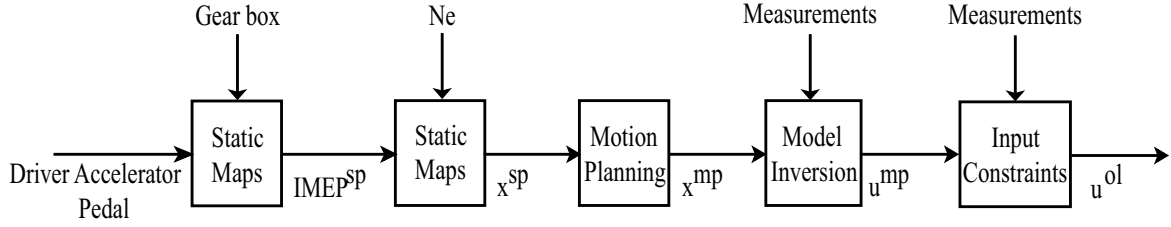


FIGURE 4.11. Motion planning scheme: from torque demand to feedforward control.

interpolation formula (4.23). Coordinate wise this defines x_1^{mp} and x_2^{mp} . Let

$$\phi(t, T) = \begin{cases} 0 & \text{for } 0 \leq t \\ (\frac{t}{T})^2(3 - 2\frac{t}{T}) & \text{for } 0 \leq t \leq T \\ 1 & \text{for } T \leq t \end{cases} \quad (4.22)$$

Note two positive constants T_1 and T_2 . The considered interpolation is

$$\begin{cases} x_1^{\text{mp}}(t) = \underline{x}_1 + (\bar{x}_1 - \underline{x}_1)\phi(t, T_1) \\ x_2^{\text{mp}}(t) = \underline{x}_2 + (\bar{x}_2 - \underline{x}_2)\phi(t, T_2) \end{cases} \quad (4.23)$$

4.6.3. Model inversion. — System (4.3) is fully actuated and invertible. Thus, an analytic expression of the input can be derived from the state variables and their first derivatives histories. In fact,

$$\begin{cases} u_1 + u_2 = \eta_{\text{vol}}(x_1, N_e)\beta_{\text{int}}x_1 + \frac{1}{\alpha_{\text{int}}}\dot{x}_1 \\ -x_2u_1 + (F_{\text{exh}} - x_2)u_2 = \frac{1}{\alpha_{\text{int}}}\dot{x}_2x_1 \end{cases} \quad (4.24)$$

This rewrites

$$\begin{cases} u_1 = f_1(x, \dot{x}) \\ u_2 = f_2(x, \dot{x}) \end{cases} \quad (4.25)$$

with

$$\begin{cases} f_1(x, \dot{x}) = \frac{1}{F_{\text{exh}}} \left(\frac{F_{\text{exh}} - x_2}{\alpha_{\text{int}}} \dot{x}_1 - \frac{1}{\alpha_{\text{int}}} \dot{x}_2 x_1 + (F_{\text{exh}} - x_2) \eta_{\text{vol}}(x_1, N_e) \beta_{\text{int}} x_1 \right) \\ f_2(x, \dot{x}) = \frac{1}{F_{\text{exh}}} \left(\frac{1}{\alpha_{\text{int}}} x_2 \dot{x}_1 + \eta_{\text{vol}}(x_1, N_e) \beta_{\text{int}} x_2 x_1 + \frac{1}{\alpha_{\text{int}}} \dot{x}_2 x_1 \right) \end{cases} \quad (4.26)$$

In these last expressions, F_{exh} , α_{int} , N_e , and β_{int} are all given by sensors measurements. The unique open-loop control law $(u_1^{\text{mp}}, u_2^{\text{mp}})$ corresponding to any desired $(x_1^{\text{mp}}, x_2^{\text{mp}})$ trajectory (defined by formulas (4.23)) is

$$\begin{cases} u_1^{\text{mp}} = f_1(x_1^{\text{mp}}, \dot{x}_1^{\text{mp}}, x_2^{\text{mp}}, \dot{x}_2^{\text{mp}}) \\ u_2^{\text{mp}} = f_2(x_1^{\text{mp}}, \dot{x}_1^{\text{mp}}, x_2^{\text{mp}}, \dot{x}_2^{\text{mp}}) \end{cases} \quad (4.27)$$

4.6.4. Input constraints. — Several input constraints are considered. We define the constrained control as

$$u^{\text{ol}}(t) \triangleq \arg(\min_{u \in \mathcal{U}} (u_1 - u_1^{\text{mp}}(t))^2 + (u_2 - u_2^{\text{mp}}(t))^2) \quad (4.28)$$

where $u_1^{\text{mp}}(t)$ and $u_2^{\text{mp}}(t)$ are defined by (4.27). A representation of the input constraints in the plane is given in Figure 4.4. In other words, for all $t \in \mathbb{R}^+$, $u^{\text{ol}}(t)$ is the projection of $u^{\text{mp}}(t) = (u_1^{\text{mp}}, u_2^{\text{mp}})(t)$ on to the set \mathcal{U} . In (4.28), both the cost function and the admissible set \mathcal{U} are convex. Thus, there always exists a uniquely defined solution x^{ol} . In fact, this solution can be analytically, computed in a straightforward way (by enumerating 8 possible solutions), which is compatible with our real-time control application requirements.

4.6.5. Convergence and tuning of the constrained motion planning. — We now prove that the proposed control strategy actually converges. The main focus is on the impact of input saturations as previously discussed.

4.6.5.1. Exponential stability. — Proposition ?? is the key to understanding our approach. Provided chosen control values are feasible (i.e. belong to \mathcal{U}), it is sufficient to use them as the step inputs in the airpath system to asymptotically reach the desired set point. Now, as we mentioned it in the Introduction, our goal is to provide more efficient transients. Ideally, we would like to have soft landing and fast transient. If the proposed control (4.27) are feasible, then $u^{\text{mp}}(t) = u^{\text{ol}}(t)$ for all $t \in \mathbb{R}^+$ and, neglecting possible perturbations, the transient is perfectly achieved. Yet, if the motion planning strategy is, at times, inconsistent with the input constraints, then $u^{\text{mp}}(t) \neq u^{\text{ol}}(t)$ during the transient. In any cases, for large values of t ($t \geq \max\{T_1, T_2\}$ as used in (4.22)), both coincide again and equal the feasible final input values. Ultimately, the system converges. The motion planning strategy can only improve transients when the computed input values are feasible, at least over some reasonably long period of the transient interval.

We now perform some analysis that allows us to guarantee this desired feasibility. From this, we can derive guidelines to tune parameters T_1 and T_2 .

4.6.5.2. Transient tuning. — Our open loop trajectories (4.23) are defined by two parameters: T_1 and T_2 . Certainly, this is a rather rough description of possible manoeuvres. Further developments could include the definition of the interpolation function ϕ by B-splines functions as in [90]. What motivates this restrictive choice is again the requirements of our real-time control system running at 100Hz at 1500rpm and the *relatively* heavy computational burden implied by this other approach.

We first show that for large enough values for T_1 and T_2 , the control values do not violate the constraints. Then, we explain why it is possible to reduce T_2 , once T_1 has been chosen.

For $t \in [0, T]$, the derivative of $\phi(\cdot, T)$ (defined in (4.22)) writes $\frac{d\phi}{dt}(t, T) = \frac{6}{T} \frac{t}{T} (1 - \frac{t}{T})$. Its maximum is reached at $t = \frac{T}{2}$ and its value is $\frac{3}{2T}$.

Consider a transient defined between the set points $(\underline{x}, \underline{u})$ and (\bar{x}, \bar{u}) . Assume that $(\underline{u}, \bar{u}) \in \mathcal{U}^2$. We will show that for large enough T_1 and T_2 , the motion planning control defined in (4.25) satisfies $u^{\text{mp}}(t) \in \mathcal{U}$ for all $t \in \mathbb{R}^+$.

The function (4.22) is monotonous. It gives a monotonous $t \mapsto x_1^{\text{mp}}(t)$. For $\epsilon > 0$, we denote

$$T_{M,1}(\epsilon) \triangleq \frac{2}{\epsilon} \frac{|\bar{x}_1 - \underline{x}_1|}{\alpha_{\text{int}}} \quad (4.29)$$

Then, we have for all $t \in \mathbb{R}^+$

$$\left| \frac{\dot{x}_1^{\text{mp}}(t)}{\alpha_{\text{int}}} \right| \leq \left| \frac{\dot{x}_1^{\text{mp}}(\frac{T_{M,1}}{2})}{\alpha_{\text{int}}} \right| \leq \frac{3|\bar{x}_1 - \underline{x}_1|}{2T_{M,1}\alpha_{\text{int}}} < \epsilon$$

and, from (4.27)

$$-\epsilon < (u_1^{\text{mp}} + u_2^{\text{mp}})(t) - \beta_{\text{int}} h(x_1^{\text{mp}}(t), N_e) < \epsilon$$

Further, h is monotonous w.r.t. x_1 . It follows that $t \mapsto h(x_1^{\text{mp}}(t), N_e)$ is monotonous w.r.t. t . Thus,

$$(u_1^{\text{mp}} + u_2^{\text{mp}})(t) \geq \min\{\underline{u}_1 + \underline{u}_2, \bar{u}_1 + \bar{u}_2\} - \epsilon > 0 \quad (4.30)$$

Let $\epsilon_1 \triangleq \min\{\underline{u}_1 + \underline{u}_2, \bar{u}_1 + \bar{u}_2\} - u_{\text{min}} \geq 0$. If $\epsilon_1 > 0$, i.e. $(\underline{u}, \bar{u}) \in (\mathcal{U} \setminus \partial\mathcal{U})^2$, then by choosing $T_1 > T_{M,1}(\frac{\epsilon_1}{2})$ we have for all $t \in \mathbb{R}^+$,

$$(u_1^{\text{mp}} + u_2^{\text{mp}})(t) > u_{\text{min}}$$

Under this assumption, $u_2 \geq 0$ is equivalent to $C(u) \geq 0$. Along the planned trajectory, using (4.27), the constraint C writes

$$C(u^{\text{mp}}(t)) = x_2^{\text{mp}}(t) + \frac{\dot{x}_2^{\text{mp}}(t)}{p_{T_1}(t)}$$

where

$$p_{T_1}(t) \triangleq \frac{\dot{x}_1^{\text{mp}}(t)}{x_1^{\text{mp}}(t)} + \Phi_{\text{int}} \eta_{\text{vol}}(x_1^{\text{mp}}(t), N_e)$$

and $\Phi_{\text{int}} \triangleq \alpha_{\text{int}} \beta_{\text{int}}$. Notice that the two steady states values satisfy

$$C(\underline{u}) = \underline{x}_2, \quad C(\bar{u}) = \bar{x}_2$$

Then, we have for all $t \in \mathbb{R}^+$

$$\Phi_{int\eta_{vol}} - \frac{3|\bar{x}_1 - \underline{x}_1|}{2T_1 \min\{\bar{x}_1, \underline{x}_1\}} \leq p_{T_1}(t) \leq \Phi_{int\eta_{vol}} + \frac{3|\bar{x}_1 - \underline{x}_1|}{2T_1 \min\{\bar{x}_1, \underline{x}_1\}}$$

For the other constraint ($0 \leq C(u) \leq \bar{C}$), we pose, for sufficiently large T_1 ,

$$T_{M,2}(T_1, \epsilon) \triangleq \frac{2}{\epsilon} \frac{|\bar{x}_2 - \underline{x}_2|}{\Phi_{int\eta_{vol}} - \frac{3|\bar{x}_1 - \underline{x}_1|}{2T_1 \min\{\bar{x}_1, \underline{x}_1\}}} \quad (4.31)$$

Thus, if we use $T_2 > T_{M,2}(T_1, \epsilon)$, then we have, for all $t \in \mathbb{R}^+$, $\left| \frac{\dot{x}_2^{\text{mp}}(t)}{p_{T_1}(t)} \right| \leq \epsilon$ and

$$|C(u^{\text{mp}}(t)) - x_2^{\text{mp}}(t)| \leq \epsilon$$

The motion planning strategy leads to a monotonous $t \mapsto x_2^{\text{mp}}(t)$. That imply that, $\forall t \in \mathbb{R}^+$

$$\begin{cases} C(u^{\text{mp}}(t)) \leq \max\{\underline{x}_2, \bar{x}_2\} + \epsilon \leq \max\{C(\underline{u}), C(\bar{u})\} + \epsilon \\ C(u^{\text{mp}}(t)) \geq \min\{\underline{x}_2, \bar{x}_2\} - \epsilon \geq \min\{C(\underline{u}), C(\bar{u})\} - \epsilon \end{cases}$$

Consider

$$\begin{cases} \epsilon_2^- \triangleq \min\{C(\underline{u}), C(\bar{u})\} \geq 0 \\ \epsilon_2^+ \triangleq \bar{C} - \max\{C(\underline{u}), C(\bar{u})\} \geq 0 \end{cases}$$

If $\epsilon_2^+ > 0$, i.e. $(\underline{u}, \bar{u}) \in (\mathcal{U} \setminus \partial\mathcal{U})^2$, then by choosing $T_2 > T_{M,2}(T_1, \frac{\epsilon_2^+}{2})$, we have for all $t \in \mathbb{R}^+$, $C(u^{\text{mp}}(t)) < \bar{C}$. Similarly, if $\epsilon_2^- > 0$, then by choosing $T_2 > T_{M,2}(T_1, \frac{\epsilon_2^-}{2})$, we have for all $t \in \mathbb{R}^+$, $C(u^{\text{mp}}(t)) > 0$ which is equivalent to $u_2^{\text{mp}}(t) > 0$. Thus, if $\epsilon_2 \triangleq \min\{\epsilon_2^-, \epsilon_2^+\} > 0$, for $T_2 > T_{M,2}(T_1, \frac{\epsilon_2}{2})$ we have for all $t \in \mathbb{R}^+$, $u^{\text{mp}}(t) \in \mathcal{U} \setminus \partial\mathcal{U}$ and the following result holds.

Proposition 4.5. — *Consider the motion planning strategy (4.27) aiming at steering the system from steady state $(\underline{x}, \underline{u})$ to (\bar{x}, \bar{u}) . If $(\underline{u}, \bar{u}) \in (\mathcal{U} \setminus \partial\mathcal{U})^2$, then by choosing large enough T_1 ($T_1 > T_{M,1}(\frac{\epsilon_1}{2})$) and T_2 ($T_2 > T_{M,2}(T_1, \frac{\epsilon_2}{2})$) as constructed above in equations (4.29) and (4.31), we have $u^{\text{mp}}(t) \in \mathcal{U} \setminus \partial\mathcal{U}$ for all $t \in \mathbb{R}^+$.*

Further, if $\bar{u} \in \partial\mathcal{U}$, then there exist $T_1 > 0$ and $T_2 > 0$ such that the constraints are violated by less than any prescribed ϵ , i.e. the distance $\text{dist}(u^{\text{mp}}(t), \mathcal{U}) < \epsilon$ for all $t \in \mathbb{R}^+$.

Now, for a fixed $T_1 \in \mathbb{R}^+$, let us try to reduce T_2 until we reach an infeasibility. Note

$$T_m(T_1) \triangleq \frac{|\bar{x}_2 - \underline{x}_2|}{\Phi_{int\eta_{vol}} + \frac{3|\bar{x}_1 - \underline{x}_1|}{2T_1 \max\{\bar{x}_1, \underline{x}_1\}}} \quad (4.32)$$

Then, we have

$$\left| \dot{x}_2^{\text{ol}}\left(\frac{T_m(T_1)}{2}\right) \right| = |\bar{x}_2 - \underline{x}_2| \frac{3}{2T_m} > \max_{t \in [0, T_1]} (p_{T_1}(t)) > p_{T_1}\left(\frac{T_m(T_1)}{2}\right)$$

Thus, for a sufficiently small time $T_2 = T_m(T_1)$, if $\bar{x}_2 > \underline{x}_2$ then $C(u^{\text{mp}}(\frac{T_m(T_1)}{2})) > \bar{C}$, and if $\bar{x}_2 < \underline{x}_2$ then $u_2^{\text{mp}}(\frac{T_m(T_1)}{2}) < 0$ leading to the violation of the constraints, i.e. $u^{\text{mp}}(\frac{T_m(T_1)}{2}) \notin \mathcal{U}$. On the contrary, if $\bar{x}_2 = \underline{x}_2$ we can not necessarily find a time T_1 such that the open-loop control strategy violates the constraints (a prime example is $\bar{x}_2 = \underline{x}_2 = 0$ and $\bar{x}_1 > \underline{x}_1$). finally, the following result holds.

Proposition 4.6. — *If $\bar{x}_2 \neq \underline{x}_2$, for all $T_1 \in \mathbb{R}^+ \setminus \{0\}$, then there exists a time $T_2 = T_m(T_1) > 0$ defined in (4.32) such that, at least one constraint is always violated by the planned input histories. In facts, $u^{\text{mp}}(\frac{T_m(T_1)}{2}) \notin \mathcal{U}$.*

From this performance analysis, we can propose the following tuning methodology for T_1 and T_2

1. We choose $\epsilon_1 > 0$ and pick $T_1 = \frac{2|\bar{x}_1 - \underline{x}_1|}{\epsilon_1 \alpha_{int}}$ in order to account for turbocharger inertia (which drives the air flow dynamics).
2. We choose $\epsilon_2 > 0$ and use

$$T_2 = \max\{T_2 \in [T_m(T_1), T_M(T_1, \epsilon_2)] / \forall t \in \mathbb{R}^+ \text{dist}(u^{\text{mp}}(t), \mathcal{U}) < \epsilon_2\}$$

where

$$\begin{cases} T_m(T_1) & \triangleq \frac{|\bar{x}_2 - \underline{x}_2|}{\Phi_{int} \bar{\eta}_{vol} + \frac{3|\bar{x}_1 - \underline{x}_1|}{2T_1 \max\{\bar{x}_1, \underline{x}_1\}}} \\ T_M(T_1, \epsilon_2) & \triangleq \frac{2}{\epsilon} \frac{|\bar{x}_2 - \underline{x}_2|}{\Phi_{int} \underline{\eta}_{vol} - \frac{3|\bar{x}_1 - \underline{x}_1|}{2T_1 \min\{\bar{x}_1, \underline{x}_1\}}} \end{cases}$$

These rules guarantee that the constraints are not violated by more than $\max\{\epsilon_1, \epsilon_2\}$.

4.7. Air Path Control Feedback

Fast PID controllers are added to the structure in order to provide further accuracy and robustness. The goal of the feedback is to control the EGR flow D_{egr} and the air flow D_{air} toward the reference set points D_{egr}^{ol} and D_{air}^{ol} . The main purpose of the feedforward is to give a feasible and continuous set point for the feedback action.

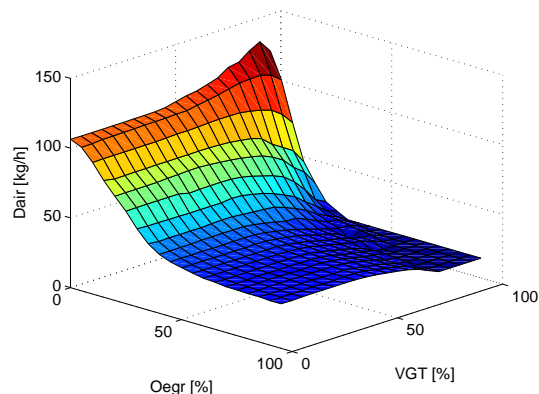


FIGURE 4.12. Experimental variation of EGR valve and VGT opening at fixed injection condition at $1500rpm$. Influence of the air flow D_{air} .

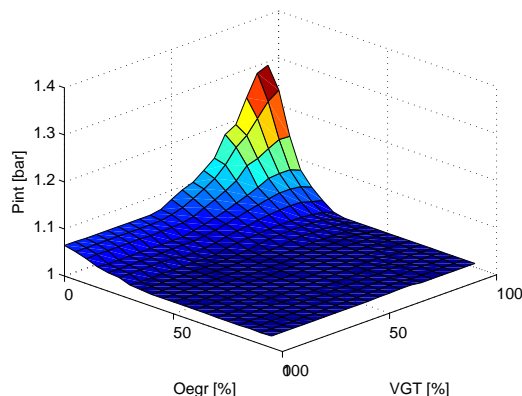


FIGURE 4.13. Experimental variation of EGR valve and VGT opening at fixed injection condition at $1500rpm$. Influence of the the intake pressure P_{int} .

4.7.1. EGR position to D_{egr} . — Increasing the EGR position corresponds to opening the EGR valve and, thereby, increasing the EGR flow D_{egr} . The flow response is almost instantaneous, the EGR valve opening controls the EGR flow D_{egr} . More precisely, a PI controller with an anti-wind up action on the normalized EGR flow ($\frac{D_{egr,sp} - \hat{D}_{egr}}{\hat{\Theta}_{egr}}$) is used on the EGR valve.

4.7.2. EGR/VGT to D_{air} . — Increasing the VGT position, i. e. opening the guide vanes, leads to a greater restriction of the exhaust gas flow and then to a decrease of the exhaust manifold pressure.

When the EGR valve is wide open (at low speed and low load e.g.), increasing the VGT results in a decreased EGR flow D_{egr} which in turn increases the air flow D_{air} as can be seen in Figure 4.12.

When the EGR valve is almost closed, most of the exhaust gas must pass through the turbine. Increasing the VGT decreases the compressor power and, then, increases the air flow. In this case, the VGT acts as a conventional wastegate, i.e. the VGT directly controls the turbocharger speed and the air flow D_{air} as can be seen in Figure 4.12. Therefore, the steady-state gain from VGT to D_{air} undergoes a sign change depending on the operating point. Since it is uncertain where the sign change occurs, the VGT should not be used to track D_{air} set points in a decentralized strategy. Rather, the strategy should use the

Low EGR	
Decreasing VGT	\Rightarrow High increasing D_{air}
	\Rightarrow Low increasing D_{egr}
High EGR	
Decreasing VGT	\Rightarrow Low decreasing D_{air}
	\Rightarrow Low increasing D_{egr}

TABLE 4.4. Variation of air/egr flows depending on VGT

EGR flow information. As one can see it in Figure 4.13, the variation of intake pressure is monotonic w.r.t. VGT. Depending on the opening of the EGR valve, i.e. depending on the EGR flow, the variation of pressure is very different. Indeed, in practice, with very high EGR rate, the variation of the VGT slightly impact the intake pressure. A tedious calibration work could yield a solution. Instead, we use the equivalent pressure

$$P_{int} \frac{1 - S_{egr}}{1 - r}$$

with r the EGR rate. It is equivalent to the following function of the flows D_{eq}

$$D_{eq} \triangleq \frac{(D_{air} + D_{egr})^2}{D_{air}} (1 - S_{egr})$$

With this variable, the calibration task is less complex.

4.8. Experimental results

4.8.1. Implementation. — The global control scheme is summarized in Figure 4.14. The air path observer block is the implementation of the observer described in Section 4.5. This block gives an estimation of the BGR and the EGR flow. The motion planning block is the implementation of the motion planning open loop control strategy described in Section 4.6. Fast PID controllers are added to the structure to provide further accuracy and robustness. Their implementation is described in Section 4.7.

4.8.2. Two experimental representative transients. — Figures 4.15, 4.16 and 4.17 report experimental closed-loop results. The scenario is a varying torque demand at constant engine speed (1500 rpm) in both HCCI combustion mode and conventional combustion mode. We now detail these experiments.

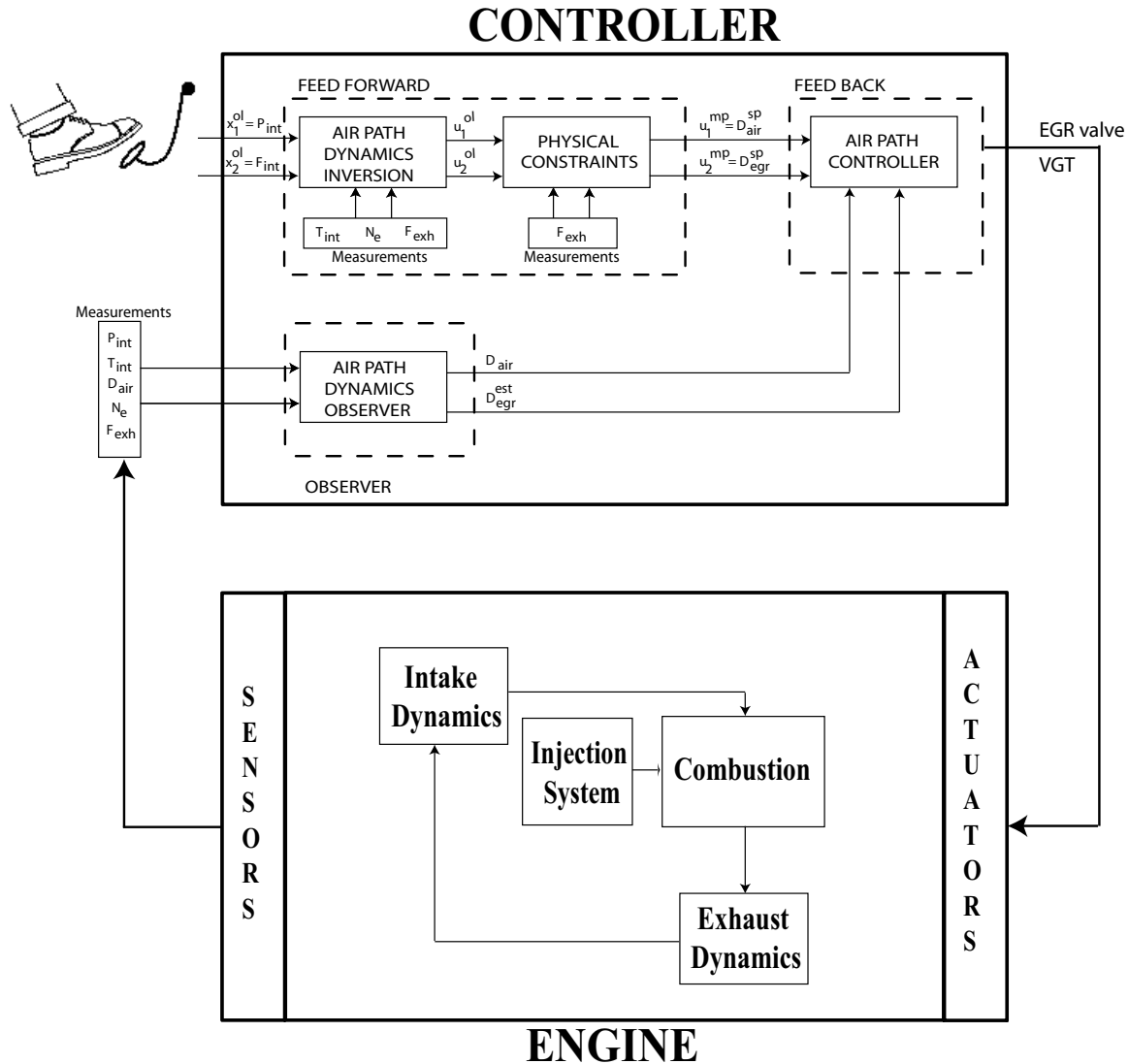


FIGURE 4.14. Control Scheme

4.8.2.1. From $t = 102s$ to $t = 112s$. — here, we have an IMEP transient at 1500 rpm in HCCI combustion mode. The IMEP of the system starts at 2 bar and eventually reaches 5 bar. This transient aims higher intake pressure and BGR set points. Starting and ending operating points are both in HCCI combustion mode. Let us focus on Figure 4.15. By contrast with all decentralized controllers, we notice on that our controller takes into

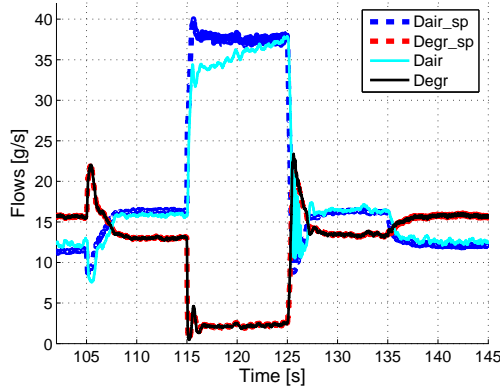


FIGURE 4.15. Experimental results: IMEP transient from 2 to 5 bar, to 9 bar, to 5 bar, and then to 4 bar at 1500 rpm. Flow histories. Dashed : set point (u^{sp}), solid: closed-loop trajectory.

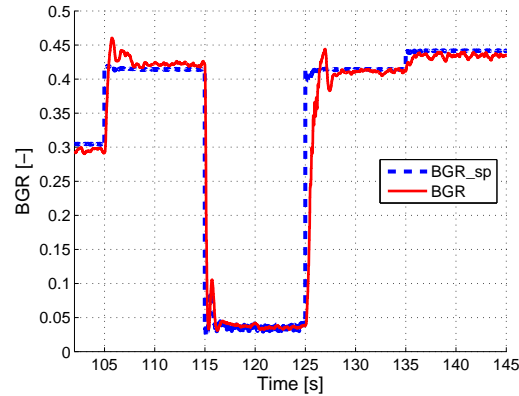


FIGURE 4.16. Experimental results: IMEP transient from 2 to 5 bar, to 9 bar, to 5 bar, and then to 4 bar at 1500 rpm. BGR histories. Dashed : set point, solid: closed-loop trajectory.

account the well known non minimum phase behavior of the system reported in [78]. More precisely, one can check that the main contribution to this is due to the open-loop controller (the closed loop control histories being very close to it). When the EGR valve opens, the flow increases leading to a pressure rise in the intake manifold. Meanwhile, the exhaust pipe acts as a discharge for the VGT. Its opening lowers the EGR supplied to the turbocharger yielding a significant drop of the exhaust manifold flow. The turbocharger slows down which eventually causes the decrease of the intake manifold pressure. This phenomenon is delayed and slowed down by the turbocharger inertia. Simple ramps and/or steps will fail to let the system reach the desired set point. With the proposed control strategy, the model takes into account this complex behavior. The motion planning efficiently drives the system to its set point.

4.8.2.2. *From $t = 112s$ to $t = 122s$.* — here, we have a tip-in (high increase of torque demand) at 1500 rpm. Implicitly, it is desired to steer the system from a low load point with high EGR to a high load point with much less BGR. The proposed open loop control strategy successively closes the EGR valve and then closes the VGT with an overshoot. One can notice the resulting decrease in EGR flow and simultaneous increase of the fresh air flow. As expected from a motion planning control strategy, this does provide a soft

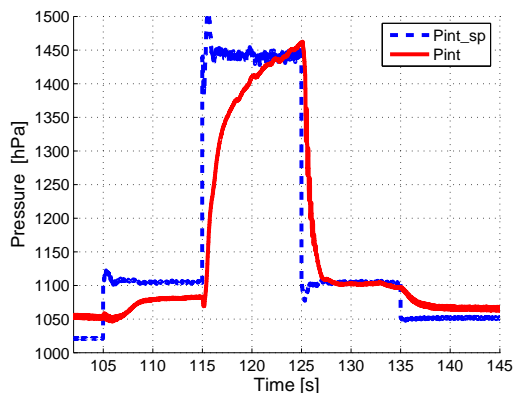


FIGURE 4.17. Experimental results: IMEP transient from 2 to 5 bar, to 9 bar, to 5 bar, and then to 4 bar at 1500 rpm. Intake pressure histories. Dashed : set point, solid: closed-loop trajectory.

landing for the state variables x_1 and x_2 onto their set points. During the transient, the open loop control laws are indeed saturated. This results in the temporary mismatch between the airflow and its set point. This effect is particularly noticeable on this very large pressure transient that we choose for sake of illustration.

Again, transients are smooth and present only small oscillations. It is instructive to note that, in this exact same setup, we failed to get a decentralized controller preventing both stall and noises. The main reason for this seems the undesired overshoot of the BGR.

4.8.3. Experimental results on a ECE driving cycle. — The control was tested on the driving cycle of the eurocycle which is very difficult to handle with high EGR rate. Indeed, 85% of the cycle is in the HCCI combustion mode. The same calibration was kept on all the driving cycle. The engine speed/ IMEP demand is given in Figure 4.18.

The BGR is well tracked as we can see on Figure 4.19. The dynamics is fast and the over/undershoot are very limited and with a short duration which limit the possible misfires and the malicious noise.

The air and EGR flows set points and closed-loop trajectory are presented on Figures 4.20 and 4.21. As in the following cases, the EGR flow is almost perfectly followed, the air flow tracking is good but a little bit slow in large transient parts due to the turbocharger inertia.

In summary, the results are good, even with a reasonably large transient. We are able to follow the planned trajectory. High pressure set point are more difficult to reach due to the turbocharger inertia and friction. However, it is not needed to accurately track the

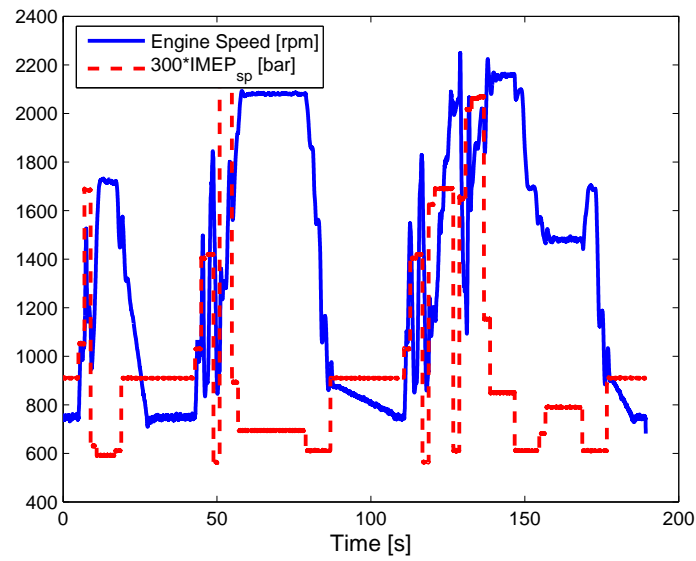


FIGURE 4.18. Engine speed/ Torque trajectory on the ECE cycle.

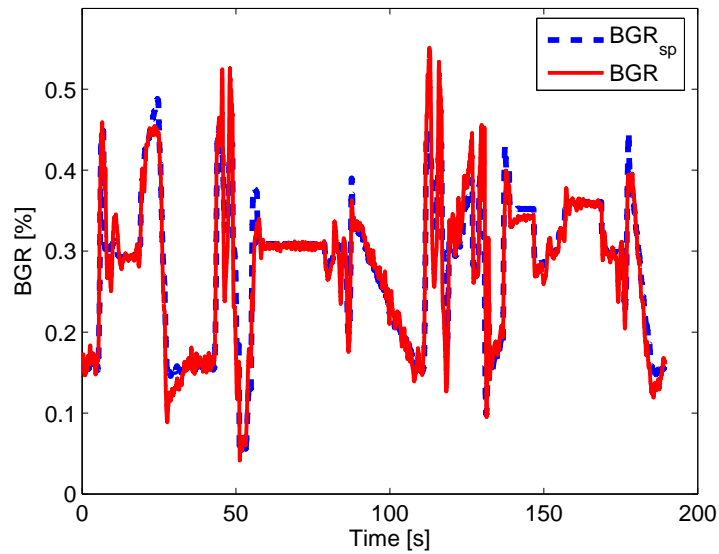


FIGURE 4.19. Experimental results on the ECE driving cycle: BGR histories. Dashed : set point, solid: closed-loop trajectory.

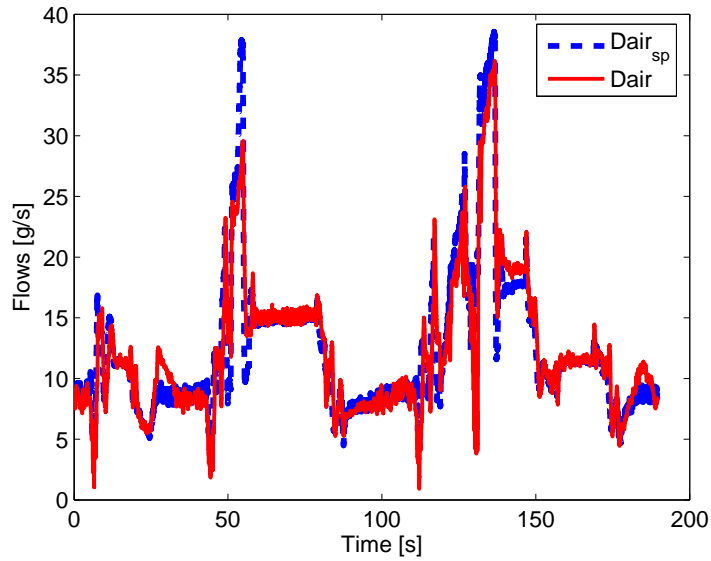


FIGURE 4.20. Experimental results on the ECE driving cycle: Air flow histories. Dashed : set point, solid: closed-loop trajectory.

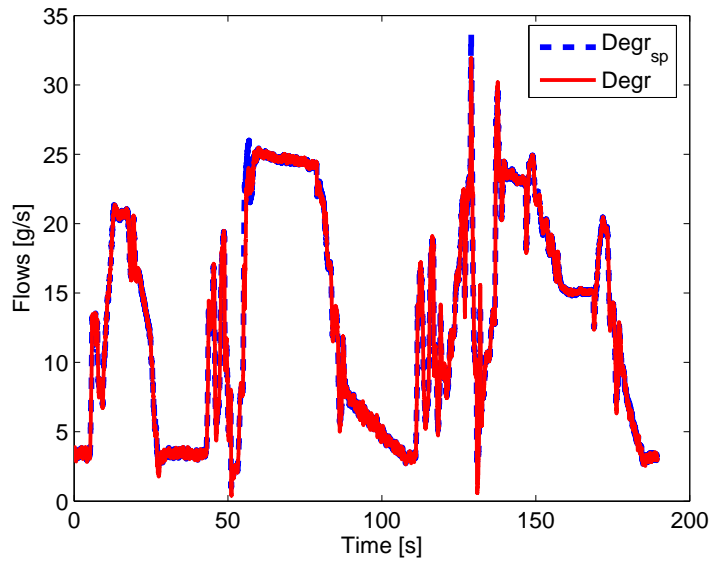


FIGURE 4.21. Experimental results on the ECE driving cycle: EGR flow histories. Dashed : set point, solid: closed-loop trajectory.

intake pressure because, for pollutant reduction purposes, only BGR needs to be closely controlled provided a limited Air-Fuel Ratio is guaranteed. The errors on the intake pressure will only lead to a very small error on the torque production. Nevertheless, on a vehicle, this problem will not appear because as the torque production increases, in response the engine speed and the turbocharger speed increases. This phenomenon is expected to be reduced in real-vehicle applications.

4.9. Conclusions and Future work

4.9.1. Conclusion. — The presented work demonstrates the relevance of motion planning in the control of the –coupled– air path dynamics of turbocharged Diesel engines using Exhaust Gas Recirculation. For the HCCI combustion mode, very large rates of burned gas need to be considered and we have proven on realistic test-bench cases that the proposed approach can handle such situations. Despite strong coupling and possible nonminimum phase dynamics, the air path dynamics has nice properties that make it easy to steer through our control strategy. Its triangular form yields exponential convergence over a wide range of set points. Moreover, we showed that input constraints can be added without jeopardizing convergence. The set points are maps based on static measurements. In a schematic point of view, the motion planning strategy can be considered as a dynamic mapping of the air path.

4.9.2. Toward general air path control. — The presented work is validated experimentally on a HCCI engine with a high pressure EGR circuit and a Variable Geometry Turbocharger. The next step is the extension of the control strategy to other engine configurations, e.g. considering low pressure EGR circuit, waste-gate, two-stage turbocharger, intake throttle . . . The control strategy can be kept. Indeed, whatever the configuration of the engine, the target will remain the same (aspirated mass of air and burned gas). The observer will be the same (in Figure 4.14), and so will the motion planning. The main modification will be to decentralize the control in order to use all the actuators for the control of the air flow D_{air} and the EGR flow D_{egr} .

CHAPTER 5

CYLINDER INDIVIDUAL AIR/FUEL RATIO ESTIMATION

Chapitre 5. — Estimation de la richesse cylindre à cylindre

Dans ce chapitre, nous considérons le problème de l'estimation et du contrôle de la richesse cylindre à cylindre. La richesse désigne la composition des gaz dans le cylindre à la fin de la combustion. Les déséquilibres de richesse cylindre à cylindre reflètent les différences entre la combustion de chacun des cylindres. Ces différences peuvent être mesurées par le capteur placé derrière la turbine. La dynamique du système fait intervenir un terme non linéaire, provenant de la non linéarité de la turbine, et est excitée par les débits sortant de chacun des cylindres. Nous présentons deux stratégies dont nous comparons les efficacités. D'abord, nous proposons un observateur non linéaire dont les termes correctifs sont également non linéaires. Les termes correctifs dépendent des débits à la sortie de chacun des cylindres ce qui permet de conclure à la convergence de l'observateur par des arguments de type Lyapunov. Ensuite, nous comparons les performances en terme de précision et de temps de calcul avec un filtre de Kalman étendu. Ces observateurs sont validés et comparés expérimentalement sur une large zone opératoire (Régime moteur de 1250 tr/min à 3500 tr/min et IMEP de 3 à 9 bar). Nous présentons aussi des résultats en boucle fermée.

5.1. Introduction

Another important step toward accurate combustion control is individual Air Fuel Ratio (AFR) control. $AFR = \frac{\dot{m}_{air}}{PCO\dot{m}_{fuel}}$ [58, chap. 3] employs various inputs such as injected quantities, Exhaust Gas Recirculation (EGR) rate and intake manifold pressure. Classically, in

spark ignition engines, overall AFR is directly controlled with the injection system. By this control strategy, all cylinders share the same closed-loop input signal based on the single equivalent ratio sensor ϕ (an oxygen sensor in the exhaust manifold $\phi \triangleq \frac{1}{AFR} \triangleq 1 - \frac{M_{exh,air}}{M_{exh}}$). Ideally, all the cylinders should have the same AFR as they have the same injection set-point. Unfortunately, due to inherent flaws of the injection system (such as pressure waves and mechanical tolerances), the total mass of fuel injected in each cylinder is very difficult to predict with a relative precision below 7%. Most of the source of unbalance comes from this difficulty. Consider now a class of planned Homogeneous Charge Compression Ignition (HCCI) engines (see [72, 60, 4, 111] for an overview of the technology, see [74, 78, 39] for more control oriented models, and [108, 66, 71, 3, 11] for control techniques). For these engines and regeneration filters (Particulate filters, DeNO_x [92, 8, 81], even slight unbalance between the cylinders can in particular induce malicious noise, possible stall and increased emissions. Cylinder-individual control is needed to address the potential drawbacks in these planned technologies. In this context, *cylinder-individual* AFR estimation may provide crucial information to assist the HCCI engine controller.

The contribution of this chapter is the design and experimental testing of two real-time observers for the cylinder-individual AFR, using only a equivalent ratio sensor placed downstream from the turbine as the source of measurement. In previous work, cylinder-individual control has been addressed using cylinder-individual equivalent ratio sensors in [12]. In practice, cost and reliability of multiple equivalent ratio sensors prevents this technology from reaching commercial products lines. Other approaches use a single equivalent ratio sensor. In [52, 19, 50], a method is proposed to reconstruct the AFR of each cylinder based on the permutation dynamics at the TDC (Top-Dead Center) time-scale. This method is well suited for SI engines where the normalized AFR is closely controlled to 1. However, for a HCCI engine, a wider operating region needs to be considered ($0.3 < \phi < 1$) and the available sensor measurements are noisy. To address this, we propose a high frequency model-based observer that considers the system as a gas mixing dynamic process fed with pulsative flows. In supportive detail, we claim it is possible to derive key information from the equivalent ratio sensor high frequency variations. Indeed, over an engine cycle time period, the measured signal is significantly varying, and typically a 5% fluctuation is often observed. Rather than considering average or downsampled values, as implicitly suggested by the previous approaches relying on the TDC dynamics, we notice that the AFR signal is correlated to output flows at the 6° resolution. By inverting the mixing dynamics, two high frequency filters (Extended Kalman Filter and Luenberger type) are synthesized. We demonstrate that the individual equivalent ratios are robustly

and efficiently reconstructed by using high frequency information, whereas the equivalent ratios are generally only poorly observable when relying on lower frequencies.

The chapter is organized as follows. In subsection 5.2, we state the AFR estimation problem under consideration. We propose a high frequency approach, using a 6° crankshaft angle model and update instead of a TDC-based model (180° for a 4-cylinder engine). The use of the various measurements and the mass balance model of the exhaust manifold dynamics is presented. In subsection 5.3, we define a nonlinear observer whose dynamics involve nonlinear tracking terms. In subsection 5.4, we present a Kalman filter. The same code and tuning parameters are kept and implemented in the control system in order to be tested on the true platform. Experimental results are reported in subsection 5.5, with test speed ranging from 1250 rpm to 3500 rpm and pressure from 3 to 9 bar of IMEP (Indicated Mean Effective Pressure). Accuracy of 10% or less of error is demonstrated. CPU power requirements are given and show that the nonlinear observer outperforms the Kalman filter. Robustness issues are studied in subsection 5.7. Conclusions and extensions of the proposed technique are then given in subsection 5.8.

5.2. Modelling

Figure 5.1 shows the flow sheet of individual FAR from the cylinders outlet down to the turbine. From the cylinders to the FAR sensor (located downstream the turbine), the gas travel through the exhaust pipes, the exhaust manifold, and the turbocharger. The EGR acts as a flow discharge for the turbocharger. Composition is preserved though. All these components have an influence on the gas pressure, the temperature, and the composition in the exhaust manifold. In a very naive model, the gas move at constant speed, without mixing. In practice, diffusion and mixing effects are present. We propose a nonlinear model to take these into account. Our approach focuses on macroscopic balances involving experimentally derived nonlinear functions.

5.2.1. Mass balance in the exhaust manifold. — Notations are given in Table 5.1. Mass balance in the exhaust manifold lead to

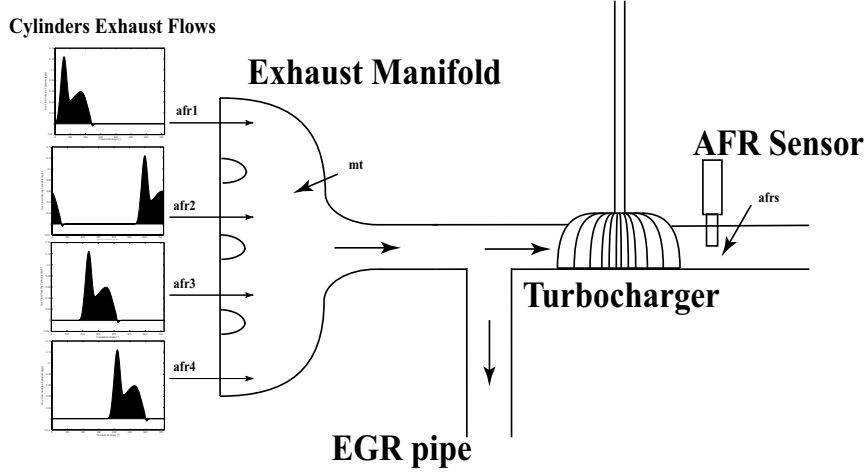


FIGURE 5.1. Flow sheet of individual AFR from the cylinders outlet down to the turbine.

$$\frac{dM_{exh}}{dt} = \sum_{i=1}^{n_{cyl}} D_i - D_{exh}$$

$$\frac{dM_{exh,air}}{dt} = \sum_{i=1}^{n_{cyl}} D_{i,air} - D_{exh,air}$$

Balance equations (5.1) and (5.2) and fixed operating conditions (5.3) yield

$$\frac{dM_{exh}}{d\alpha} = f_{1,\Xi}(M_{exh}, \alpha) \quad (5.1)$$

$$\frac{dM_{exh,air}}{d\alpha} = f_{2,\Xi}(M_{exh}, M_{exh,air}, \{\phi_i\}_{i \in [1, n_{cyl}]}, \alpha) \quad (5.2)$$

$$\frac{d\phi_i}{d\alpha} = 0, \quad \forall i \in [1, n_{cyl}] \quad (5.3)$$

where

$$\left\{ \begin{array}{l} f_{1,\Xi}(M_{exh}, \alpha) = -\frac{1}{N_e} D_{exh}(M_{exh}, \Xi) + \frac{1}{N_e} \sum_{i=1}^{n_{cyl}} D_i(\alpha, \Xi) \\ f_{2,\Xi}(M_{exh}, M_{exh,air}, \{\phi_i\}_{i \in [1, n_{cyl}]}, \alpha) = -\frac{1}{N_e} \frac{M_{exh,air}}{M_{exh}} D_{exh}(M_{exh}, \Xi) \\ \quad + \frac{1}{N_e} \sum_{i=1}^{n_{cyl}} (1 - \phi_i) D_i(\alpha, \Xi) \end{array} \right. \quad (5.4)$$

Symb.	Quantity	Unit
α	Crankshaft angle	
M_T	Total mass of gas in the exhaust manifold	kg
$M_{exh,air}$	Mass of air in the exhaust manifold	kg
N_e	Engine Speed	rpm
d_T	Gas flow rate through the exhaust manifold	kg.s ⁻¹
d_i	Gas flow rate from cylinder i	kg.s ⁻¹
Ξ	Operating conditions	
D_{asp}	Mean aspirated flow	kg.s ⁻¹
T_{exh}	Temperature in the exhaust manifold	K
N_{turbo}	Turbocharger speed	rpm
r	EGR rate	
ϕ_i	Normalized Fuel-Air Ratio of cylinder i	
ϕ	Oxygen sensor measurement	
P_{exh}	Pressure in the exhaust manifold	bar
M_0	Total mass in the exhaust manifold under atmospherical conditions	kg
n_{cyl}	Number of cylinders	
$\Delta\alpha \triangleq \frac{\pi}{30}$	Angular sample time	
$T_0 \triangleq 4\pi$	Period of the continuous-time dynamics	
$N_0 \triangleq 120$	Period of the discrete-time dynamics	
$\delta \triangleq \frac{\Delta\alpha}{N_e}$	Constant	rpm ⁻¹
γ_T, γ	Constants	

TABLE 5.1. Nomenclature for the cylinder-individual FAR estimation.

Operating conditions are defined by the Ξ parameters (mean aspirated flow D_{asp} , turbocharger speed N_{turb} , exhaust temperature T_{exh} , and the EGR rate r)

$$\Xi \triangleq (D_{asp}, N_{turb}, T_{exh}, r) \quad (5.5)$$

Due to the turbocharger inertia (resp. the thermal inertia), fluctuations over a cycle of the turbocharger speed N_{turb} (resp. the exhaust temperature T_{exh}) is small (less than 6% and 3% resp.) compared to exhaust pressure fluctuations (between 15% and 25%). Thus, T_{exh} and N_{turb} are assumed constant over an engine cycle. These variables are often non available on a commercial engine. Nevertheless, as presented in the previous chapter, the air path estimation module gives an estimation of the mean aspirated flow

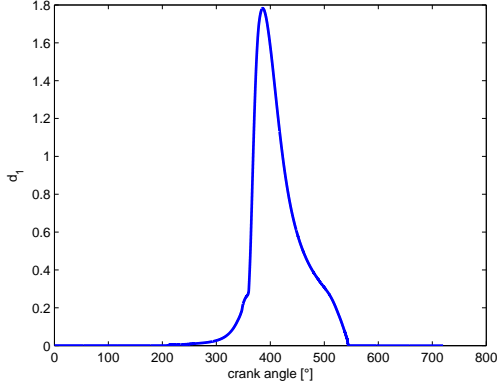


FIGURE 5.2. Experimental input flows from cylinder 1 at 1500 rpm and 11 bar of IMEP over one cycle.

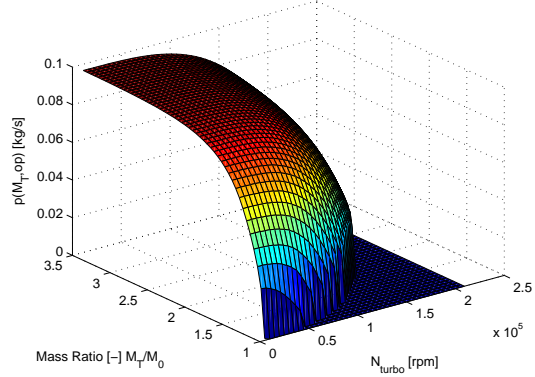


FIGURE 5.3. Flow rate through the turbine with $r = 0$ (no EGR) as a function of turbocharger speed and mass ratio.

D_{asp} and the EGR rate r . Moreover, the turbocharger speed N_{turb} is estimated by inverting the compressor map using the intake pressure and the intake air mass flow. Finally, the exhaust gas temperature T_{exh} estimation is given by a look-up table that has engine speed, intake pressure and AFR as inputs.

The T_0 -periodic $D_i(\cdot, \Xi)$ functions (i.e. $D_i(\alpha + T_0, \Xi) = D_i(\alpha, \Xi)$) are the flows from the cylinders. An experimentally derived model of d_1 is presented in Figure 5.2. We modelled it with a gauge. The dilatation factor is computed in order to have the conservation of the total mass that entered into the cylinder (given by the mean aspirated flow D_{asp}). The same gauge is kept on the overall operating range. The functions family $\{D_i\}_{i=1\dots n_{cyl}}$ is a linearly independent family of the set of continuous T_0 -periodic functions. D_1, \dots , and $D_{n_{cyl}}$ are phased-shifted by $\frac{4\pi}{n_{cyl}}$.

The flow rate D_{exh} comes out of the exhaust manifold. It is a function of the total mass M_{exh} , smooth away from 0, and can be factorized as

$$D_{exh}(M_{exh}, \Xi) = p(M_{exh}, \Xi)M_{exh}$$

Here, for a given operating condition Ξ , p is a positive increasing (concave) function with respect to the total mass M_{exh} , e.g.

$$p(z, \Xi) = p_0(\Xi) \sqrt{2 \frac{\gamma}{\gamma - 1} \left(\left(\frac{z}{M_0} \right)^{-\frac{2}{\gamma}} - \left(\frac{z}{M_0} \right)^{-\frac{\gamma+1}{\gamma}} \right)}$$

as proposed in [69] and [91]. This model gives values similar to those depicted in Figure 5.3. Composition of the flow through the turbine and in the exhaust manifold are equal.

5.2.2. Measurements. — At first, two sensors are considered for our observer design, although extra sensors are available on our prototype engine for performance analysis. The measurements are

- P_{exh} , the pressure in the exhaust manifold assumed to be related to the total mass by

$$P_{exh} = \gamma_T M_{exh} \quad (5.6)$$

This assumes that the ideal gas law holds and that T_{exh} is constant over a cycle. In this work, the exhaust pressure sensor is eventually substituted with an open loop model. The reason for this choice is to propose a versatile observer. It is able to work with or without an exhaust pressure sensor, usually not available on commercial engines.

- ϕ , the equivalent in the exhaust manifold $\phi \triangleq 1 - \frac{M_{exh,air}}{M_{exh}}$.

5.2.3. Reference system. — Consider the state $x = [M_{exh} \ M_{exh,air} \ \phi_1 \ \dots \ \phi_{n_{cyl}}]^T \in \mathbb{R}^{n_{cyl}+2}$ and measurements $y = [P_{exh} \ FAR]^T \in \mathbb{R}^2$. Gathering (5.1)-(5.2)-(5.3), the reference system reads

$$\left\{ \begin{array}{l} \frac{dx_1}{d\alpha} = f_{1,\Xi}(x_1, \alpha) \\ \frac{dx_2}{d\alpha} = f_{2,\Xi}(x_1, \dots, x_{n_{cyl}+2}, \alpha) \\ \frac{dx_{2+i}}{d\alpha} = 0, \quad \forall i \in [1, n_{cyl}] \\ y_1 = \gamma_T x_1 \\ y_2 = 1 - \frac{x_2}{x_1} \end{array} \right. \quad (5.7)$$

where $f_{1,\Xi}$ and $f_{2,\Xi}$ are defined in (5.4).

5.3. Cylinder-individual AFR nonlinear observer

The first observer we propose combines a copy of the nonlinear dynamics (5.7) and three weighted nonlinear tracking terms.

5.3.1. Observer definition. — The proposed observer is

$$\begin{cases} \frac{d\hat{x}_1}{d\alpha} = f_{1,\Xi} \left(\frac{1}{\gamma_T} y_1, \alpha \right) + \frac{L_1}{N_e} \left(\frac{y_1}{\gamma_T} - \hat{x}_1 \right) \\ \frac{d\hat{x}_2}{d\alpha} = f_{2,\Xi} \left(\frac{1}{\gamma_T} y_1, (1-y_2) \frac{1}{\gamma_T} y_1, \hat{x}_3, \dots, \hat{x}_{n_{cyl}+2}, \alpha \right) + \frac{L_2}{N_e} \left((1-y_2) \frac{1}{\gamma_T} y_1 - \hat{x}_2 \right) \\ \frac{d\hat{x}_{2+i}}{d\alpha} = -\frac{L_\phi}{N_e} D_i(\alpha) \left((1-y_2) \frac{1}{\gamma_T} y_1 - \hat{x}_2 \right) \end{cases} \quad (5.8)$$

where the last equation holds for all $i \in [1, n_{cyl}]$, and where $(L_1, L_2, L_\phi) \in (\mathbb{R}^+ \setminus \{0\})^3$. Let $\tilde{x} = x - \hat{x}$. The error dynamics reads

$$\begin{cases} \frac{d\tilde{x}_1}{d\alpha} = -\frac{1}{N_e} L_1 \tilde{x}_1 \\ \frac{d\tilde{x}_2}{d\alpha} = -\frac{1}{N_e} \left(\sum_{i=1}^{n_{cyl}} \tilde{x}_{2+i} D_i(\alpha) + L_2 \tilde{x}_2 \right) \\ \frac{d\tilde{x}_{2+i}}{d\alpha} = \frac{1}{N_e} L_\phi D_i(\alpha) \tilde{x}_2, \quad \forall i \in [1, n_{cyl}] \end{cases} \quad (5.9)$$

To prove convergence of the observer rate \hat{x} , described by System (5.8), to the state x of the reference System (5.7), we exhibit a Lyapounov function and use LaSalle's theorem to conclude to the convergence of the observer.

5.3.2. Lyapounov function candidate. — We consider the following Lyapounov function candidate

$$V(\tilde{x}) = \frac{N_e}{2} \left(\frac{1}{L_1} \tilde{x}_1^2 + \frac{1}{L_2} \tilde{x}_2^2 + \frac{1}{L_2 L_\phi} \sum_{i=1}^{n_{cyl}} \tilde{x}_{2+i}^2 \right) \quad (5.10)$$

On the one hand, $V(\tilde{x}) > 0$ for $\tilde{x} \in \mathbb{R}^{n_{cyl}+2} \setminus \{0\}$ and $V(0) = 0$. Then the following computation yield next lemma.

$$\begin{aligned} \frac{dV}{d\alpha}(\tilde{x}) &= -\tilde{x}_1^2 - \frac{1}{L_2} \sum_{i=1}^{n_{cyl}} \tilde{x}_{2+i} D_i(\alpha) \tilde{x}_2 - \tilde{x}_2^2 + \frac{1}{L_2} \sum_{i=1}^{n_{cyl}} D_i(\alpha) \tilde{x}_2 \tilde{x}_{2+i} \\ &= -\tilde{x}_1^2 - \tilde{x}_2^2 \leq 0 \end{aligned}$$

Lemma 5.1. — *The function V defined by (5.10) is a Lyapounov function for the error-state System (5.9).*

5.3.3. Application of LaSalle's theorem. — Let $\Omega_r = \{\tilde{x}_f \in \mathbb{R}^{n_{cyl}+2} / V(\tilde{x}_f) < r\} \subset \mathbb{R}^{n_{cyl}+2}$. Ω_r is a compact set positively invariant with respect to the error dynamics because $\frac{dV}{d\alpha} \leq 0$. Therefore V is a continuously differentiable function such that $\frac{dV}{d\alpha}(\tilde{x}_f) \leq 0$ in Ω_r . Let I_f be the largest invariant set in $\{\tilde{x}_f \in \Omega_r / \frac{dV}{d\alpha}(\tilde{x}_f) = 0\}$. From LaSalle's theorem (see [76] Theorem 4.4), every solution starting in Ω_r approaches I_f as $\alpha \rightarrow \infty$.

5.3.4. Characterization of the invariant set I_f . — We first characterize $\{\tilde{x}_f \in \Omega_r / \frac{dV}{d\alpha}(\tilde{x}_f) = 0\}$ and then I_f .

$$x_0 \in \{\tilde{x}_f \in \Omega_r / \frac{dV}{d\alpha}(\tilde{x}_f) = 0\} \Leftrightarrow -\tilde{x}_{1_f}^2 - \tilde{x}_{2_f}^2 = 0 \Leftrightarrow \begin{cases} \tilde{x}_{1_f} = 0 \\ \tilde{x}_{2_f} = 0 \end{cases}$$

Thus

$$\{\tilde{x}_f \in \Omega_r / \frac{dV}{d\alpha}(\tilde{x}_f) = 0\} = \{[0 \ 0 \ \tilde{\phi}_{1,0} \ \dots \ \tilde{\phi}_{n_{cyl},0}]^T \in \mathbb{R}^{n_{cyl}+2}\}$$

From LaSalle's theorem, I_f is the largest invariant set in $\{\tilde{x}_f \in \Omega_r / \frac{dV}{d\alpha}(\tilde{x}_f) = 0\}$. I_f writes

$$I_f = \{[0 \ 0 \ \tilde{\phi}_{1,0} \ \dots \ \tilde{\phi}_{n_{cyl},0}]^T \in \mathbb{R}^{n_{cyl}+2} / \forall \alpha \in [0, 4\pi] \sum_{i=1}^{n_{cyl}} \tilde{\phi}_{i,0} D_i(\alpha) = 0\}$$

The functions family $\{D_i\}_{i=1 \dots n_{cyl}}$ is a linearly independent family of the set $\mathcal{C}^0([0, 4\pi], \mathbb{R})$. Therefore the set I_f is reduced to $\{0\}$. The observation error is asymptotically stable and the following results hold.

Lemma 5.2. — *The largest set in*

$$\Omega_r = \{\tilde{x}_f \in \mathbb{R}^{n_{cyl}+2} / V(\tilde{x}_f) < r\} \subset \mathbb{R}^{n_{cyl}+2}$$

invariant by the dynamics of the system (5.9) where the function V is defined in (5.10) is the null space.

Proposition 5.1. — *The observer defined in equation (5.8) converges toward the reference model (5.7).*

5.4. Cylinder-individual AFR Kalman filter

In this section, we propose a Kalman filter. A linear (linearized) system is required. First, we notice that the masses dynamics converge toward a limit cycle. Then we use an Euler explicit discretization and compute the linearized system around this limit cycle. Finally we prove convergence of a periodic Kalman filter using the uniform observability of the system. Then, we extend it for implementation purpose.

5.4.1. The masses dynamics converge toward a limit cycle. — First, we prove that the exhaust dynamics are a periodically driven contracting system. Then, analysis of convergence can be performed in the vicinity of the limit cycle. The first part of the exhaust dynamics (total and air masses balance equations) described by (5.7) writes

$$\frac{dz}{d\alpha} = g(\alpha) - f_{\Xi}(z) \quad (5.11)$$

where $z = [M_{exh} \ M_{exh,air}]^T$, $f_{\Xi}(z) = \frac{1}{N_e} [z_1 p(z_1, \Xi) \ z_2 p(z_2, \Xi)]^T$ and $g(\alpha) = \frac{1}{N_e} \sum_{i=1}^{n_{cyl}} D_i(\alpha, \Xi) [1 \ (1 - \phi_i)]^T$. Let

$$\mathcal{D} \triangleq \{(z_1, z_2) \in (\mathbb{R}^+)^2 \mid z_1 \geq z_2 \text{ and } z_1 > (1 + \epsilon)M_0 \ \epsilon > 0\}$$

For all $(z_1, z_2) \in \mathcal{D}$,

$$N_e \frac{d(z_1 - z_2)}{d\alpha} = (z_1 - z_2)p(z_1, \Xi) + \sum_{i=1}^{n_{cyl}} \phi_i D_i(\alpha, \Xi) \geq 0,$$

and $\frac{dz_1}{d\alpha} \geq 0$ because, $\forall \alpha$, $\sum_{i=1}^{n_{cyl}} D_i(\alpha, \Xi) > (1 + \epsilon)M_0 p((1 + \epsilon)M_0, \Xi)$. It follows that \mathcal{D} is positively invariant by the exhaust dynamics (5.11). The symmetric part of the Jacobian of f is

$$J_{f_{\Xi}}^+(z) = \frac{1}{N_e} \begin{bmatrix} p(z_1, \Xi) + z_1 p'(z_1, \Xi) & \frac{1}{2} z_2 p'(z_1, \Xi) \\ \frac{1}{2} z_2 p'(z_1, \Xi) & p(z_2) \end{bmatrix}$$

Computation of its eigenvalues leads to

$$\text{eig}(J_{f_{\Xi}}^+(z)) = \frac{1}{N_e} \left\{ p(z_1, \Xi) + \frac{1}{2} p'(z_1, \Xi) (z_1 \pm \sqrt{z_1^2 + z_2^2}) \right\}$$

For all $(z_1, z_2) \in \mathcal{D}$,

$$\frac{1 - \sqrt{2}}{2} z_1 \leq z_1 - \sqrt{z_1^2 + z_2^2} \leq 0$$

As p is increasing,

$$\mathcal{D} \ni z \mapsto p(z_1, \Xi) + \frac{1}{2} p'(z_1, \Xi) \left(z_1 + \frac{1 - \sqrt{2}}{2} z_1 \right)$$

is a strictly positive increasing function. Thus,

$$\exists J_0 \in \mathbb{R}^+ \setminus \{0\}, \quad \text{s.t. } \forall z \in \mathcal{D}, \quad J_{f_{\Xi}}^+(z) \geq J_0 I$$

We note $\phi(\alpha, \alpha_0, M_0)$ the solution of system (5.11) at time α with initial condition

$\phi(\alpha_0, \alpha_0, M_0) = M_0$, and define the Poincaré application

$$P_{\alpha_0} : \mathcal{D} \ni M_0 \mapsto \phi(\alpha_0 + T_0, \alpha_0, M_0) \in D$$

From [56, 87], we get that the strict positiveness of J_f^+ leads to the contracting property of P_{α_0} , i.e.

$$\forall (Z_1, Z_2) \in \mathcal{D}^2, \quad \|P_{\alpha_0}(Z_1) - P_{\alpha_0}(Z_2)\| \leq e^{-J_0 T_0} \|Z_1 - Z_2\|$$

Then, from the global inversion theorem, P_{α_0} has a unique fixed point, $\bar{\phi}(\alpha_0)$ and

$$\forall (t_0, M_0) \in \mathbb{R}^+ \times \mathcal{D} \quad \lim_{k \rightarrow \infty} (\phi(t_0 + kT_0, 0, M_0)) = \bar{\phi}(t_0)$$

$\bar{\phi}$ is solution of (5.11) and $\bar{\phi}(T_0) = \bar{\phi}(0)$.

Proposition 5.2. — *For every initial condition in D , system (5.11) converges towards a unique limit cycle of period T_0 .*

System (5.7) consists in system (5.11) with added linear equations

$$N_e \frac{d\phi_i}{d\alpha} = 0 \quad \forall i \in [1, n_{cyl}]$$

Trivially, the ϕ_i are constant and the following proposition holds

Proposition 5.3. — *For every initial condition in $\mathcal{D} \times [0, 1]^{n_{cyl}+1}$, system (5.7) converges toward a limit cycle of period T_0 . This limit cycle depends only on $\phi_1(0), \dots, \phi_{n_{cyl}}(0)$.*

In the following, we note the obtained limit cycle

$$\alpha \ni [0, T_0] \mapsto x_{\text{per}}(\alpha) \in D \times [0, 1]^{n_{cyl}+1}$$

with $x_{\text{per}}(\alpha) = [M_{T,\text{per}}(\alpha) \quad M_{\text{air},\text{per}}(\alpha) \quad \phi_{1,\text{per}}(\alpha) \quad \dots \quad \phi_{n_{cyl},\text{per}}(\alpha)]^T$

5.4.2. Discrete-time reference system. — The discrete-time reference system is the discrete approximation of system (5.7) around the limit cycle obtained through an Euler explicit scheme around the previously defined limit cycle x_{per} . The sample angle is $\Delta\alpha = 6^\circ$ and, for sake of conciseness, we note $x_d(k) = x_{\text{per}}(k\Delta\alpha)$ and $\delta \triangleq \frac{\Delta\alpha}{N_e}$. We define A_k , D_k and C_k as

$$A_k = \begin{bmatrix} \alpha_k & \beta_k \\ 0 & I_{n_{cyl}} \end{bmatrix} \in \mathcal{M}_{n_{cyl}+2, n_{cyl}+2}(\mathbb{R})$$

where $I_{n_{cyl}}$ is the n_{cyl} -Identity matrix, $\mathcal{M}_{k_1, k_2}(\mathbb{R})$ is the set of real matrices of dimension $k_1 \times k_2$, and, finally,

$$\alpha_k \triangleq \begin{bmatrix} 1 - \delta d'_T(x_{d,1}(k), \Xi) & 0 \\ -\delta x_{d,2}(k) p'(x_{d,1}(k), \Xi) & 1 - \delta p(x_{d,1}(k), \Xi) \end{bmatrix} \in \mathcal{M}_{2,2}(\mathbb{R}) \quad (5.12)$$

$$\beta_k \triangleq -\delta \begin{bmatrix} 0 & \dots & 0 \\ d_1(k\Delta\alpha, \Xi) & \dots & d_{n_{cyl}}(k\Delta\alpha, \Xi) \end{bmatrix} \in \mathcal{M}_{2, n_{cyl}}(\mathbb{R})$$

$$U_k \triangleq \delta \sum_{i=1}^{n_{cyl}} D_i(k\Delta\alpha, \Xi) [1 \ 1 \ 0 \ \dots \ 0]^T \in \mathcal{M}_{n_{cyl}+2, 1}(\mathbb{R})$$

$$C_k \triangleq \begin{bmatrix} \gamma_T & 0 & 0 & \dots & 0 \\ \frac{x_{d,2}(k)}{x_{d,1}(k)^2} & -\frac{1}{x_{d,1}(k)} & 0 & \dots & 0 \end{bmatrix} \in \mathcal{M}_{2, 2+n_{cyl}}(\mathbb{R})$$

We define the discrete-time reference system as

$$\begin{cases} x_{k+1} &= A_k x_k + U_k + v_k \\ y_k &= C_k x_k + w_k \end{cases} \quad (5.13)$$

where $(v, w) \in \mathbb{R}^{2+n_{cyl}} \times \mathbb{R}^2$ are added white noise. Notice that A_k, U_k and C_k are $N_0 \triangleq \frac{T_0}{\Delta\alpha}$ -periodic (here $N_0 = 120$ as $T_0 = 4\pi$ and $\Delta\alpha = \frac{\pi}{30}$). We note $A_* = \{A_k\}_{k \in [1, N_0]}$, $C_* = \{C_k\}_{k \in [1, N_0]}$ and $D_* = \{D_k\}_{k \in [1, N_0]}$. Clearly, $A_{k+N_0} = A_k$, $C_{k+N_0} = C_k$ and $U_{k+N_0} = U_k$.

5.4.3. Periodic Kalman filter. — We use a time-varying Kalman predictor for the AFR estimation. For this purpose, we introduce the system

$$\hat{x}_{k+1} = A_k \hat{x}_k + U_k + L_k (y_k - C_k \hat{x}_k) \quad (5.14)$$

with chosen arbitrary initial condition \hat{x}_0 , where L_k is the Kalman gain matrix

$$L_k = A_k P_k C_k^T (C_k P_k C_k^T + R_k)^{-1} \quad (5.15)$$

In this last expression, the covariance error P_k is recursively computed through the discrete periodic Riccati equation (DPRE)

$$P_{k+1} = A_k P_k A_k^T + Q_k - A_k P_k C_k^T (C_k P_k C_k^T + R_k)^{-1} C_k P_k A_k^T \quad (5.16)$$

with P_0 a freely chosen initial condition (positive definite). At last, Q_k and R_k are weighting matrices, to be chosen in $\mathcal{M}_{n_{cyl}+2, n_{cyl}+2}(\mathbb{R})$ and $\mathcal{M}_{2,2}(\mathbb{R})$ respectively.

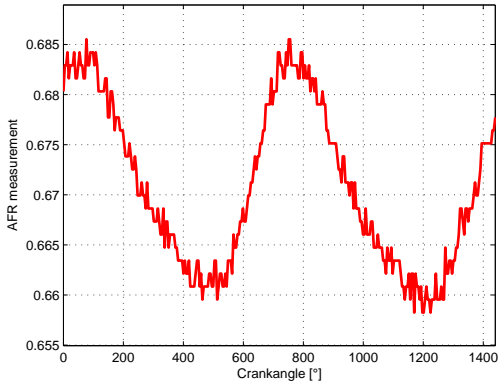


FIGURE 5.4. AFR measurement oscillations over 2 engine cycles with a +20% injection offset on cylinder 1.

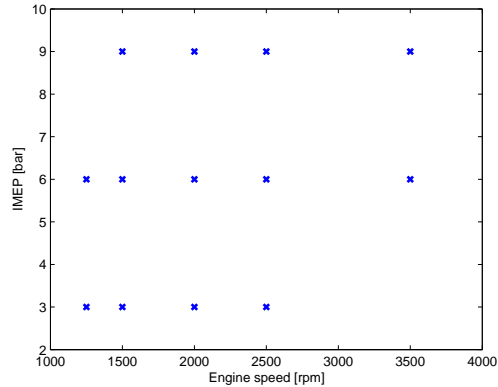


FIGURE 5.5. Operating points under consideration for the tests campaign.

5.4.4. Convergence. —

Convergence of this observer is detailed in Appendix D.2 leading to the follow proposition

Proposition 5.4. — *With R_k and Q_k constant symmetric positive definite matrices, the state of the Kalman filter defined by equations (5.14),(5.15),(5.16) converges towards the discrete time reference model state (5.13).*

5.5. Experimental Results

5.5.1. AFR imbalance. — To introduce unbalance on the experimental testbed, we apply an injection duration timing trajectory. It produces offsets in injected masses leading to AFR disturbances. More precisely, the injection steps have an effect on the average level of the measured AFR and introduce oscillations as represented in Figure 5.4. These oscillations are the direct consequences of the individual AFR unbalance.

During cylinder 1 exhaust phase, the AFR increases in the manifold, and then decreases while the other cylinders exhaust phases occur. The magnitude of the oscillations is related to the amount of the AFR difference between the cylinders and the gas mass in the manifold (and thus to its volume). The oscillation is then propagated to the turbine, and to the UEGO sensor, where it is filtered.

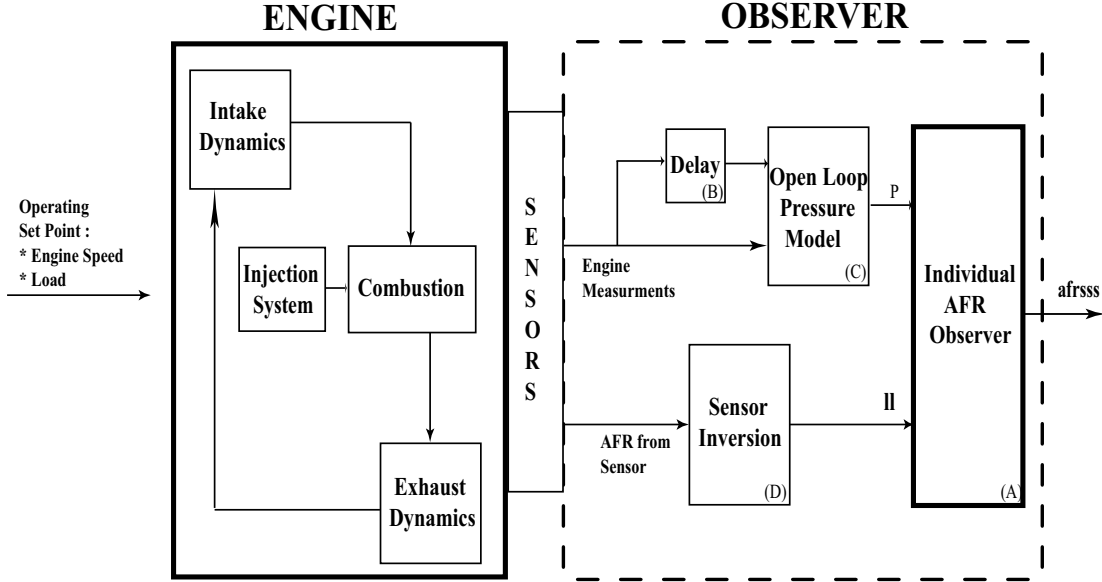


FIGURE 5.6. Engine and observer connection.

5.6. Observers implementation

On the test bench, we use both proposed observers according to the scheme in Figure 5.6. Block (A) contains the observer. Several practical issues need to be considered. We now detail these.

5.6.1. Nonlinear observer implementation. — The implementation of the observer described in subsection 5.3 is achieved by an explicit Euler approximation

$$\left\{ \begin{array}{l} \hat{x}_1(k+1) = \hat{x}_1(k) + \Delta\alpha \left(f_1 \left(\frac{1}{\gamma_T} y_1, \alpha \right) + \frac{L_1}{N_e} \left(\frac{y_1}{\gamma_T} - \hat{x}_1 \right) \right) \\ \hat{x}_2(k+1) = \hat{x}_2(k) + \Delta\alpha \left(f_2 \left(\frac{1}{\gamma_T} y_1, (1-y_2) \frac{1}{\gamma_T} y_1, \hat{x}_3, \dots, \hat{x}_{n_{cyl}+2}, \alpha \right) \right. \\ \quad \left. + \Delta\alpha \frac{L_2}{N_e} \left((1-y_2) \frac{1}{\gamma_T} y_1 - \hat{x}_2 \right) \right) \\ \hat{x}_{2+i}(k+1) = \hat{x}_{2+i}(k) - \Delta\alpha \frac{L_\phi}{N_e} D_i(\alpha) \left((1-y_2) \frac{1}{\gamma_T} y_1 - \hat{x}_2 \right) \quad \forall i \in [1, n_{cyl}] \end{array} \right.$$

The parameters are chosen to normalize the equations. Indeed, L_1 is unitary, L_2 is homogeneous to a flow rate and L_ϕ homogeneous to the inverse of a flow rate. Eventually, a single set of parameters (L_1, L_2, L_ϕ) is used for all operating points.

5.6.2. Kalman filter implementation. — The Kalman filter described by (5.14), (5.15) and (5.16) is extended to take into account variations of x_{per} along the overall operating range.

$$\hat{x}_{k+1} = f_{\Xi}(\hat{x}_k) + D_k + L_k(y_k - C_k\hat{x}_k)$$

where D_k , C_k , and L_k are given in subsection 5.4 and α_k is, in this implementation,

$$\alpha_{k,imp} \triangleq \begin{bmatrix} 1 - \delta d'_T(\hat{x}_{k,1}, \Xi) & 0 \\ -\delta \hat{x}_{k,2}(k) p'(\hat{x}_{k,1}, \Xi) & 1 - \delta p(\hat{x}_{k,1}, \Xi) \end{bmatrix}$$

Initial conditions and (diagonal) weighting matrices (R_k and Q_k) are chosen according to preliminary simulations based on the Kalman filter presented in Section 5.4. Eventually, a single set of parameters (R, Q) is used for all operating points.

5.6.3. Gas transport delay. — Lags due to gas transport along the engine exhaust (pipes and dead volumes), and the dead time of the sensor are not represented by the model described in System(5.7). Delays can be lumped into a single delay for the complete exhaust system. This delay can be identified and kept as a constant for a given set point on the (engine speed, aspirated flow) map. This estimation is implemented in Block (B) in Figure 5.6.

5.6.4. Open loop pressure model. — Exhaust pressure sensor can be expected for forthcoming HCCI vehicles only. In experimentation, we consider not having this sensor and give to the estimator an open loop value. This value is given by the open loop balance with the input flows (D_i) and output flow (D_{exh}) as described previously in Section 5.2. The crank angle α is shifted of α_0 to take the delay into account. This model is implemented in Block (C) in Figure 5.6.

5.6.5. AFR sensor inversion. — The AFR sensor has a low-pass transfer function. Sampling noise is cut-off by a high frequency low-pass filter. The sensor dynamics can be approximated by a second order filter. In order to robustly invert dynamics of the sensor, we apply an observer based on an adaptive Fourier decomposition (Block (D) in Figure 5.6).

5.6.6. Experimental results of the nonlinear observer. — In the following, we aim at evaluating both observers performance around several operating points (Engine Speed, IMEP) reported in Figure 5.5. The same tuning parameters are kept from simulation

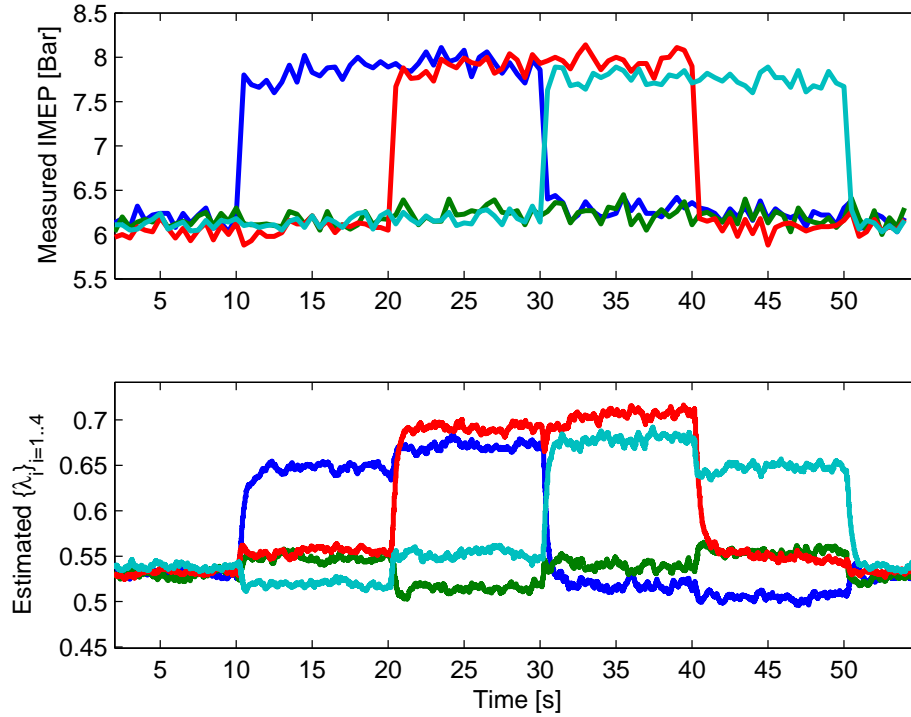


FIGURE 5.7. Test bench nonlinear observer results (engine speed 2000 rpm, IMEP 6 bar). 15% injection time offset. Top: Measured IMEP [bar]. Bottom: cylinder-individual estimated $\{\phi_i\}_{i=1..4}$.

to experimentation. Further, a single set of tuning parameters is kept over all operating points.

Actual AFR are not directly available but can be correlated on the experimental engine to the torque produced by each cylinder (reconstructed from the experimental individual in-cylinder pressure sensors). These correlated values, noted ϕ_{ref} , serve as reference for comparisons. To numerically evaluate performance, we define two norms which represent the maximum and the mean value of the relative absolute errors around steady states.

$$\|\phi_*\|_{\infty} \triangleq \max_{i,\alpha} \left| \frac{\hat{\phi}_i - \phi_{i,ref}}{\phi_{i,ref}} \right| \quad \text{and} \quad \|\phi_*\|_{\text{mean}} \triangleq \text{mean}_{i,\alpha} \left| \frac{\hat{\phi}_i - \phi_{i,ref}}{\phi_{i,ref}} \right|$$

This subsection summarizes the experimental results of the nonlinear observer presented in Section 5.3. Typical results are given in Figure 5.7. Extensive test campaign range

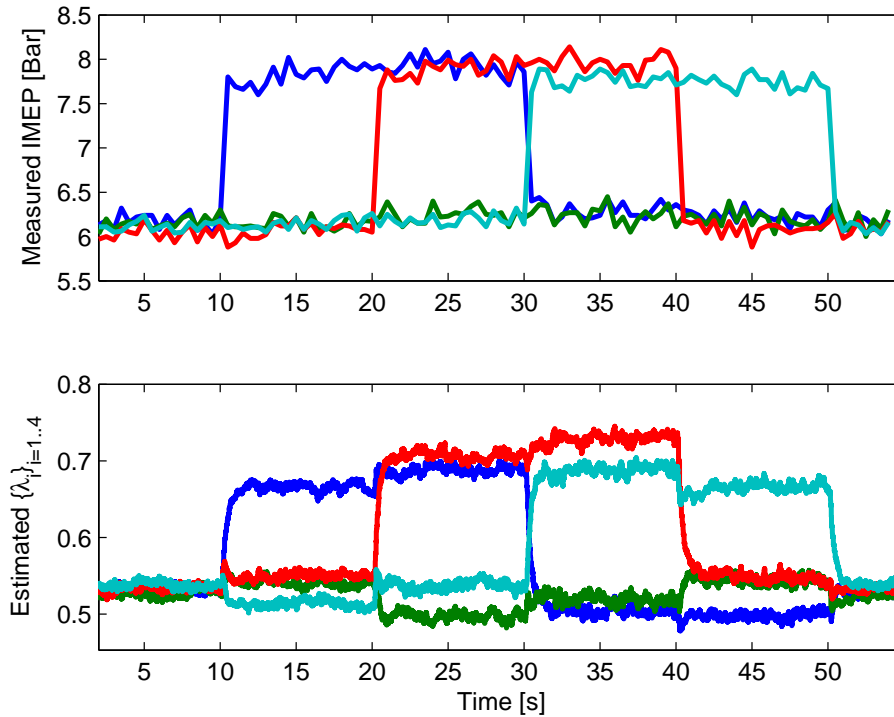


FIGURE 5.8. Test bench extended Kalman filter results (engine speed 2000 rpm, IMEP 6 bar). 15% injection time offset. Top: Measured IMEP [bar]. Bottom: cylinder-individual estimated $\{\phi_i\}_{i=1..4}$.

from 1250 rpm to 3500 rpm and from 3 to 9 bar of IMEP. Tests results are reported in Table 5.2. Results are quantitatively and qualitatively accurate. We reproduce well the evolution of the AFR. In practice, convergence is achieved within 4 engine cycles. In all test bench cases, we were able to predict the cylinder-individual AFR well. Further, we can easily detect the AFR unbalance and have a good estimation of the peaks of the AFR disturbances. The magnitude of the individual AFR offsets are satisfactory. Results are better at mid-high load (over 6 bar of IMEP). This comes from the model of the variable geometry turbocharger. Indeed, at low load, the turbocharger is almost not deactivated ($N_{turbo} < 25000$ rpm) and our model is not accurate under these operating conditions due to friction on the turbocharger (errors around high slopes points yield important model mismatch, see Figure 5.3). At higher load, the turbocharger is in action and the model of

N_e	IMEP	Non linear		Kalman	
		$100 \ \phi_*\ _\infty$	$100 \ \phi_*\ _{\text{mean}}$	$100 \ \phi_*\ _\infty$	$100 \ \phi_*\ _{\text{mean}}$
1250	3	23.5	8.0	19.5	7.4
1250	6	6.8	2.8	3.9	1.0
1500	3	17.4	6.1	15.9	6.4
1500	6	3.3	1.5	7.6	2.1
1500	9	5.1	2.1	11.2	3.7
2000	3	19.2	5.0	20.8	6.2
2000	6	7.6	2.8	9.6	2.6
2000	9	7.7	2.4	10.1	2.4
2500	3	24.5	8.0	25.8	9.4
2500	6	10.5	3.0	11.4	3.2
2500	9	12.0	4.0	16.1	4.5
3500	6	35.9	12.0	35.9	9.6
3500	9	20.7	6.7	20.3	5.5

TABLE 5.2. Experimental results: normed values of estimation errors.

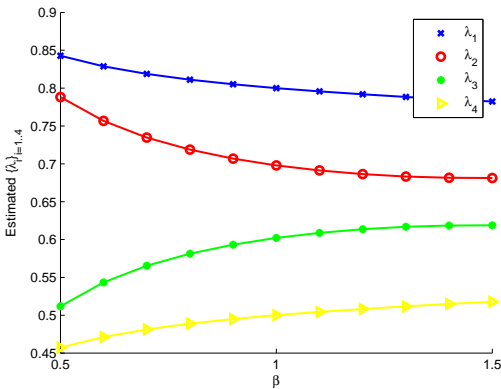
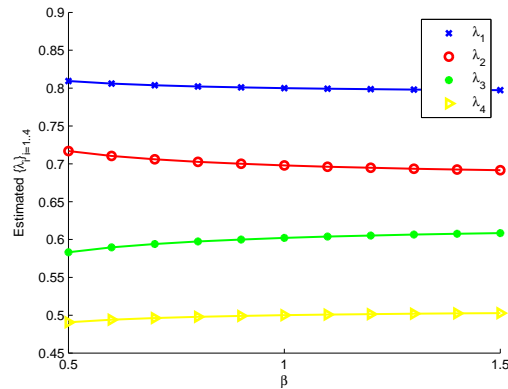
flow through the turbine is a lot more accurate and leads to very good results. Measurement noise is not set point independent, in fact sampling errors impact the results for high rpm.

5.6.7. Experimental results of the extended Kalman filter. — This subsection summarizes the experimental results of the extended Kalman filter presented in Section 5.4. Typical results are given in Figure 5.8. Extensive test campaign ranges from 1250 rpm to 3500 rpm and from 3 to 9 bar of IMEP. Results (see Table 5.2) are quantitatively and qualitatively accurate, and closed to the one obtained with the nonlinear observer. As expected, low turbocharger speed and high rpm have a negative impact on accuracy.

5.6.7.1. Computation times. — Computation times of each element in Figure 5.6 required for observer implementation are reported in Table 5.3. Relatively to the nonlinear observer, the Extended Kalman filter is computationally intensive. The nonlinear observer outperforms the Kalman filter by an approximate ratio of 30. Recalling that CPU availability is a requirement for other tasks of engine control, this is a strong advantage in favor of the nonlinear observer.

Block A: Individual AFR Estimation	
Nonlinear observer	$2.70\mu s$
Kalman observer	$85.65\mu s$
Block B: Exhaust dynamics model	$6.70\mu s$
Block C: Delay	$< 0.05\mu s$
Block D: AFR sensor dynamics inversion	$6.35\mu s$

TABLE 5.3. Typical computation times of sub-blocks on a 2GHz pentium PC.

FIGURE 5.9. Robustness to modelling errors of the input flows $\{\beta D_i\}_{i=1..4}$ with the nonlinear observer.FIGURE 5.10. Robustness to modelling errors of the flow through the exhaust manifold βd_T with the nonlinear observer.

5.7. Robustness toward parametric errors

5.7.1. Robustness to model errors. — We investigate robustness of our observers to model errors. The estimation is expected to depend on flow models, namely $\{D_i\}_{i=1..4}$ and d_T . To investigate robustness, we introduce a multiplicative error gain β on these and evaluate the induced steady state errors. Initially, the injection system is arbitrarily unbalanced with the following values: $\phi_1 = 0.8$, $\phi_2 = 0.7$, $\phi_3 = 0.6$, and $\phi_4 = 0.5$. Results for an error gain on the input flows are presented in Figure 5.9. While results for an error gain on the flow through the exhaust manifold are presented in Figure 5.10. Figure 5.9 shows that the absolute value of the steady state significantly depends on the multiplicative

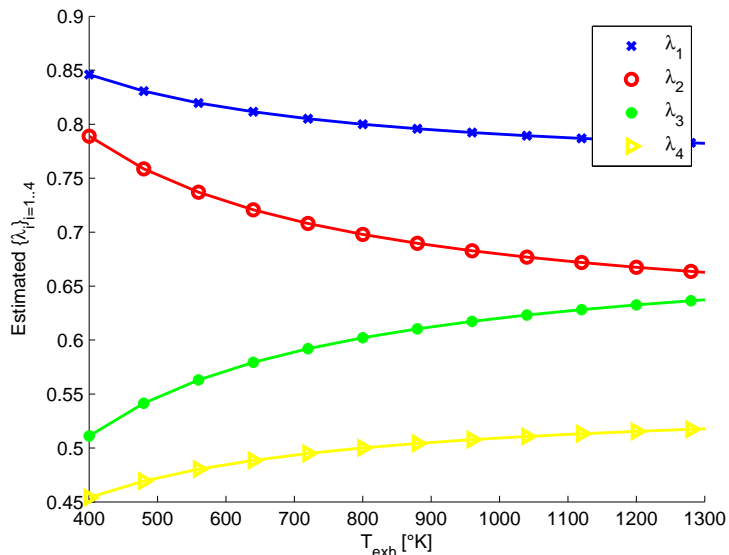


FIGURE 5.11. Robustness to errors on T_{exh} of the nonlinear observer. The nominal exhaust temperature is 800°K.

gain β but that the relative error is very small. Even a large multiplicative gain does not jeopardize the unbalance diagnosis. Further, Figure 5.10 suggests that our observer is robust with respect to multiplicative error on the turbocharger model.

5.7.2. Robustness to operating conditions errors. — The flow rate through the turbine $D_{exh}(\cdot, \Xi)$ model (see Section 5.2) explicitly depends on operating conditions: exhaust temperature and turbocharger speed. These are measured on the testbench but, more generally, are not available on commercial engines. In our approach, both exhaust temperature and turbocharger speed values are estimated through table lookups. The temperature look up table has engine speed, intake pressure and AFR as inputs, on the other hand, the turbocharger speed has intake pressure and intake air flow as input.

We investigate robustness of our observers to errors in these estimations. for that purpose, we introduce offsets in the turbocharger speed and in the exhaust temperature. Not surprisingly, both observers have similar responses as they share the turbocharger model. For that reason, we only reproduce here results of experiments conducted on the nonlinear observer. Figure 5.11 gives a sensitivity analysis with respect to the exhaust temperature.

5.8. Experimental closed-loop validation

The work presented in this chapter reports the development and implementation of two cylinder-individual AFR estimators. Both proposed observers reconstruct the AFR of each cylinder from a measurement made by a *single* sensor located downstream the turbine. While both approaches provide equally robust observers and similar performances, comparisons in terms of ease of tuning (3 parameters against 8 for diagonal weighting of the Kalman filter) and CPU load suggest the superiority of the nonlinear individual AFR observer. The availability of such an estimator giving reliable information can lead to improvements on Diesel engines in terms of combustion control, noise, and pollutant emissions. Simple issues such as control of AFR imbalance between the cylinders can be addressed by controlling the individual injection quantities (which is the relevant control strategy for such unbalance) with a PI controller. Figure 5.12 presents the results of such a control strategy relying on the individual AFR estimation. On the testbench, we turn off the control at 7.5s which leads to the natural imbalance of the engine. We introduce an injection offset on cylinder 2 at 19s and finally turn the controller back on at 35s. We see that the control is efficient and that we are able to balance the torque produced by each cylinder.

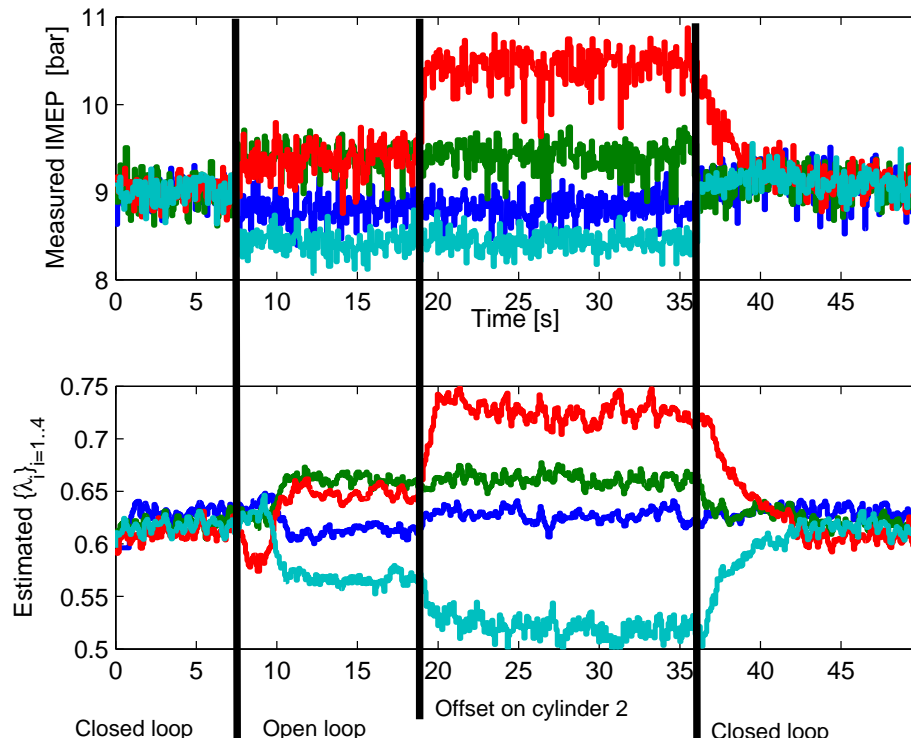


FIGURE 5.12. Results of AFR balancing control strategy based on cylinder-individual AFR estimation: test bench results (Engine Speed 1500rpm, IMEP 9bar). The control is turned off at 7.5s, an injection offset on cylinder 2 is introduced at 19s, and, finally, the controller is turned back on at 35s. Top: IMEP from cylinder pressure sensors. Bottom: cylinder-individual AFR estimated with the nonlinear observer

CHAPTER 6

INDICATED TORQUE ESTIMATION

Chapitre 6. — Estimation du couple de combustion

Dans ce chapitre, nous regardons le problème de l'estimation du couple de combustion. nous considérons le problème de l'estimation du couple de combustion. Le couple de combustion caractérise les performances du moteur. Il dépend de diverses entrées comme le temps d'injection, le taux d'EGR... Il n'est pas directement mesuré. En revanche, la vitesse instantanée de l'arbre vilebrequin au bout de la transmission est mesurée. Nous décomposons le problème en deux étapes. Nous commençons par réaliser un observateur qui reconstruit la vitesse instantanée du vilebrequin sous les cylindres à partir du régime instantané mesuré au bout de la transmission. Il s'agit d'un observateur de Luenberger périodique. Le modèle de la dynamique de la transmission est un système linéaire du deuxième ordre. Ensuite, nous utilisons cette estimation pour reconstruire le couple de combustion. Pour ce faire, nous développons des observateurs périodiques dont nous comparons les performances en terme de précision et de temps de calcul. Nous prouvons la convergence des deux observateurs considérés et présentons des résultats expérimentaux.

6.1. Introduction

The combustion torque characterizes the performance of the engine and is the result of various inputs such as injection quantity and timing, EGR rate In the previous chapter, we describe how to balance the AFR, i.e. the composition of the cylinders at the end of the combustion. Nevertheless, it is not sufficient to provide the same combustion for all the cylinders.

Conventionally, the in-cylinder pressure has been directly measured using in-cylinder pressure transducers in a experimental testbed. Then the indicated torque is calculated from the measured in-cylinder pressure based on the engine geometry. Unfortunately, high cost and low reliability prevent these sensors from reaching commercial products. Therefore, instead of employing this expensive and not yet reliable conventional approach, the research study investigates different approaches of obtaining such performances variables while utilizing existing sensors and easily accessible engine state variables such as the instantaneous angular position and velocity of the crankshaft.

As described in [99], the crankshaft of a Diesel engine is subjected to complex forces and torque excitations created by the combustion process from each cylinder. These torque excitations cause the engine crankshaft to rotate at a varying angular velocity. The resulting angular speed consists of slowly varying mean component and fast varying component caused by the combustion process in each cylinder. As a consequence, we need to design real-time observers for the combustion torque using the reliable and available instantaneous engine speed as the only measurement.

Over the past years, the combustion torque determination by the measurement of the instantaneous engine speed has been investigated previously explicitly or implicitly, inverting an engine dynamic model of various complexity. A proposed solution by Rizzoni *et al.* was introduced in [99, 98] focusing on reconstructing the instantaneous as well as average engine torque based on the frequency domain deconvolution method. However, this method requires pre-computation of the frequency response functions relating crankshaft speed to indicated torque in the frequency domain and storing their inverses in a mapping format, which has difficulties of determining the frequency functions experimentally. An approach bypassing this difficulty was proposed by Srinivasan *et al.* using repetitive estimators [103]. Further studies of the speed-based torque estimation was continued by Drakunov *et al.* in [48] through the use of nonlinear observers. Other torque estimation efforts involving an observer were based on the use of the unknown input by Rizzoni *et al.* [100]. Other work based on the stochastic approach was developed by Guezennec *et al.* for torque estimation in [54, 55]. Solving this first problem opens the door to more exciting applications such as misfiring detection ([9] and [112]) and combustion analysis. Here we propose a real time torque observer taking into account the transmission dynamics.

The chapter is organized as follows. In section 6.2, we look at the estimation of the instantaneous engine speed under the cylinders with the measurement of the engine speed at the end of the transmission by inverting the transmission dynamics. Then, we propose

where $\bar{\xi}$ is a damping coefficient and $\bar{\omega}$ the natural frequency of the transmission. Let

$$w \triangleq \bar{\omega}^2 x_2$$

as x_2 is mechanically periodic so does w_0 . Some rewriting yields

$$\begin{cases} \frac{d^2 x_1}{d\alpha^2} = -2\bar{\xi}\bar{\omega} \frac{dx_1}{d\alpha} - \bar{\omega}^2 x_1 + w_0 \\ y = x_1 \end{cases}$$

6.2.2. Reference model. — The state is $x = [x_1 \quad \frac{dx_1}{d\alpha}]^\dagger$. The dynamics writes

$$\begin{cases} \frac{dx}{d\alpha} = Ax + A_0 w_0 \\ y = Cx \end{cases} \quad (6.1)$$

with $A = \begin{bmatrix} 0 & 1 \\ -\bar{\omega}^2 & -2\bar{\xi}\bar{\omega} \end{bmatrix}$, $A_0 = [0 \quad 1]^\dagger$, and $C = [1 \quad 0]$. The system is a linear with a periodic unknown input w_0 . The goal is to estimate of the π -periodic continuous input signal $w(t) \in \mathbb{R}$, through its Fourier decomposition over a finite number 2 of harmonics

$$w(t) \triangleq \sum_{k \in [-2, 2]} c_k e^{ik\omega_0 t}, \quad \omega_0 \triangleq 2$$

with $c_{-k} = c_k^\dagger$. The measurement is $y = x_1$, a partial measurement of the state of the system.

6.2.3. Observer design. — Corresponding to state-space model (6.1), we define a time-varying Luenberger type observer following chapter 7

$$\begin{cases} \frac{d\hat{x}}{d\alpha} = A\hat{x} + A_0(\sum_{k \in [-2, 2]} \hat{c}_k e^{2ik\alpha}) - L(t)(C(t)\hat{x} - y) \\ \frac{d\hat{c}_k}{d\alpha} = -e^{-2ik\alpha} L_k(t)(C(t)\hat{x} - y), \quad \forall k \in [0, 2] \end{cases} \quad (6.2)$$

with the gains defined by Equation (7.10) in chapter 7. We take $L = [2\bar{\xi}\bar{\omega} \quad 2\bar{\omega}^2]^\dagger$, and $L_k(t) = -\epsilon\beta_k((ik\omega_0 - (A - LC))^{-1}A_0)^\dagger C^T$. We choose $\epsilon = 0.1$ and $\beta_k = \frac{1}{k^2+1}$.

6.2.4. Convergence. — Using Proposition 7.3, convergence of the observer designed according to (6.2) is guaranteed if Hypothesis H 7.1 and H 7.2 hold, i.e. that for all t , $\ker A_0(t) = \{0\}$, and $\ker C^\dagger(t) = \{0\}$, and that the only solution $t \mapsto (x(t), \{c_k(t)\}_{k \in \mathcal{I}_h^+})$ of Equation (6.1) for which the output $y(t) = C(t)x(t)$ is identically zero over $[0, T_0]$, is the zero solution. Clearly, the first assumption is true. Let $(x, \{c_k\}_{k \in [0, 2]})$ be a nontrivial solution of (6.1): $y(t) \equiv 0$ implies $x_1 = 0$ and $\dot{x}_1 = 0$, and then $x_2 = 0$. Moreover $\frac{dc_k}{d\alpha} = 0, \quad \forall k \in [0, 2]$ implies $c_k(t) = \bar{c}_k, \quad \forall k \in [0, 2]$. By substitution in (6.1) we get $\sum_{k \in [-2, 2]} \bar{c}_k e^{2ik\alpha} = 0$. Then, $(x, \{c_k\}_{k \in [0, 2]}) = 0$ and the second hypothesis hold.

6.2.5. From w to x_2 . — The coefficients of the decomposition of x_2 are obtained from the coefficients of w . x_2 is also periodic and writes

$$x_2(t) \triangleq \sum_{k \in [-2, 2]} d_k e^{2ik\alpha}$$

The coefficients $\{d_k\}_{k \in [-2, 2]}$ are obtained from the coefficients $\{c_k\}_{k \in [-2, 2]}$ by multiplication, i.e.

$$d_k = \frac{1}{\bar{\omega}^2} c_k$$

6.2.6. Testbench results. — The implementation is achieved in discrete time with a sample angle of 6° deg crank angle. The observer described is evaluated on a 4 cylinder engine testbench described in Appendix. The observer design yields the reconstruction of the engine speed next to the cylinder with the measurement of the engine speed and the end of the transmission. Experimental results are given in Figure 6.2.

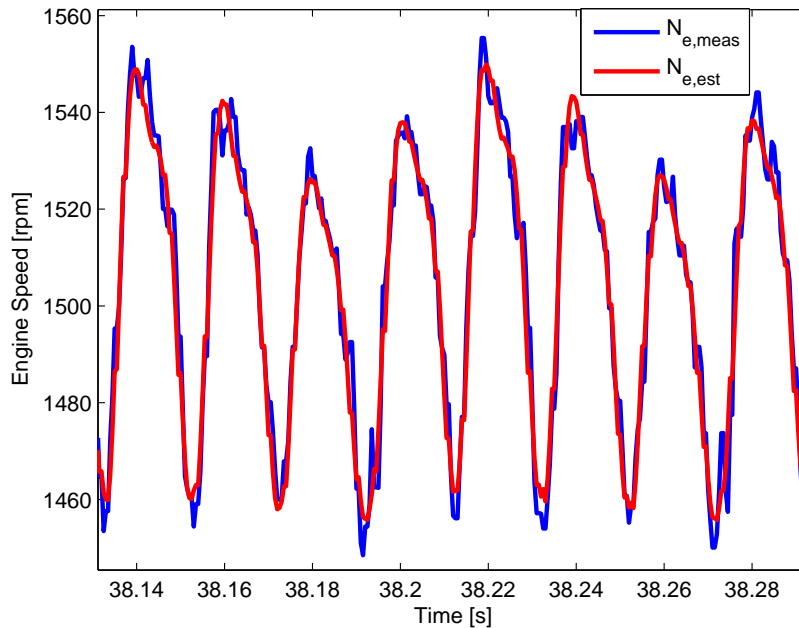


FIGURE 6.2. Testbench results. Engine speed reconstruction over 2 cycles at 1500 rpm and 8 bar of IMEP: Blue : measured engine speed $N_{e,meas}$, reconstructed engine speed red : $N_{e,est}$

6.3. Indicated torque estimation

The previous section gives an estimation of the engine speed under the cylinders. Then, we estimate the indicated torque produced by the cylinders. First of all, we detail the crankshaft modelling in subsection 6.3.1. We propose two observers for the estimation of the engine torque. We propose an extended Kalman filter based on a periodic limit cycle in subsection 6.3.2. An observer using adaptive Fourier based decomposition is designed in subsection 6.3.3. Experimental comparison of the observers is reported in subsection 6.3.4.

6.3.1. Crankshaft Modelling. — In this part, we briefly describe the dynamics of the system stressing out the role of the combustion torque, T_{comb} , also referred as the indicated torque. Following [77], the torque balance on the crankshaft can be written

$$T_{comb} - T_{mass} - T_{load}^* = 0 \quad (6.3)$$

where $T_{load}^* = T_{load} + T_{fric}$ is referred to “the extended load torque” and T_{load} and T_{fric} are known. The mass torque T_{mass} is the derivative of the kinetic energy E_{mass} of the moving masses in the engine as described in Figure 6.3.

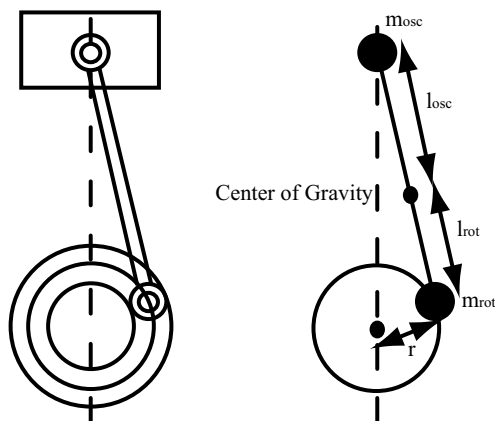


FIGURE 6.3. Mass Model.

$$E_{mass} = \int_0^{2\pi} T_{mass} d\alpha = \frac{1}{2} J(\alpha) \dot{\alpha}^2$$

The mass torque T_{mass} can be expressed as $\frac{dE_{mass}}{dt} = T_{mass} \dot{\alpha}$. The computation of the various elements of J are usually perfectly known for a particular engine. $J(\alpha)$ is a periodic function in α over an engine cycle.

6.3.2. Kalman torque observer. —

6.3.2.1. *Discrete Time-varying Linear Approximation.* — The torque balance writes

$$J(\alpha)\ddot{\alpha} = T_{comb}(\alpha) - T_{load}^*(\alpha) - \frac{1}{2} \frac{dJ}{d\alpha}(\alpha)\dot{\alpha}^2$$

We can reformulate this equation as

$$\dot{\alpha} \frac{d\dot{\alpha}}{d\alpha} = \frac{1}{J(\alpha)} (T_{comb}(\alpha) - T_{load}^*(\alpha) - f(\alpha)\dot{\alpha}^2) \quad (6.4)$$

Using a first order approximation on the left hand-side of the previous equation, we can break the dependence on time and on the crankshaft angle and only save a dependence on the square of the crankshaft angle speed.

$$\dot{\alpha}^2(n+1) - \dot{\alpha}^2(n) \approx \frac{2\Delta\alpha}{J(n)} (T_{comb}(n) - T_{load}^*(n) - f(n)\dot{\alpha}^2(n))$$

In practice an angular path $\Delta\alpha = 6^\circ$ is used. Using the square of the crankshaft angle speed $\dot{\alpha}^2$ as the first state variable x_1 , we get the linear equation

$$x_1(n+1) = \left(1 - \frac{2\Delta\alpha}{J(n)} f(n)\right) x_1(n) + \frac{2\Delta\alpha}{J(n)} x_2(n) \quad (6.5)$$

where

$$\begin{cases} x_1(n) = \dot{\alpha}^2(n) \\ x_2(n) = T_{comb}(n) - T_{load}^*(n) \end{cases}$$

This formulation of the problem as a two dimensional linear time-varying system suggests that classical methods for combustion torque estimation (x_2) can be used.

6.3.2.2. *Mass torque as a filter.* — The combustion torque generates the movement of the crankshaft. The oscillations of the combustion torque and of the load torque decrease when the engine is accelerating. This oscillation can be described by a low-pass $h(z)$ (the transfert function) filter excited by a white noise $u(z)$.

$$x_2(z) = h(z)u(z) \quad (6.6)$$

6.3.2.3. *Combustion Torque estimation using Kalman filtering.* — As stated in Equation (6.5), the crankshaft is subject to torque excitations created by the combustion process in each cylinder (T_{comb}) which is a highly varying signal (due to combustion cycles and their imperfections). The resulting angular speed has a slowly varying component and a fast varying one resulting from the combustion process.

A colored white noise can be a good representation for the combustion torque. x_2 can be modelled in the z -transform domain as the product of a filter $h(z)$ and a white noise $u(z)$

$$x_2(z) = h(z)u(z)$$

where $h(z)$ is :

$$h(z) = \frac{b_0 + b_1 z^{-1} + \dots + b_p z^{-p}}{1 + a_1 z^{-1} + \dots + a_q z^{-q}} \quad (6.7)$$

This filter is chosen stable.

6.3.2.4. Reference model. — Gathering past values of x_2 over $[k - q + 1, k]$, we obtain a time-varying linear system.

$$\begin{cases} x_{k+1} &= A_k x_k + B_k u_k \\ y_k &= C_k x_k + w_k \end{cases} \quad (6.8)$$

with the state

$$x_k = \begin{pmatrix} \dot{\alpha}^2(k) \\ T_{comb}(k) - T_{load}^*(k) \\ \dots \\ T_{comb}(k - q + 1) - T_{load}^*(k - q + 1) \end{pmatrix} \in \mathbb{R}^{q+1}$$

The matrices A_k , B_k and C_k are

$$A_k = \begin{bmatrix} 1 - \frac{2\Delta\alpha}{J(k)} f(k) & v_k \\ 0 & M \end{bmatrix} \in \mathcal{M}_{q+1, q+1}(\mathbb{R}) \quad (6.9)$$

$$B_k = \begin{bmatrix} 0 & 0 & 0 \\ b_0 & \dots & b_p \\ 0 & 0 & 0 \\ \dots & \dots & \dots \\ 0 & 0 & 0 \end{bmatrix} \in \mathcal{M}_{q+1, p+1}(\mathbb{R}) \quad (6.10)$$

$$C_k = [1 \ 0 \ \dots \ 0] \in \mathcal{M}_{1, q+1}(\mathbb{R}) \quad (6.11)$$

with

$$v_k = \begin{bmatrix} \frac{2\Delta\alpha}{J(k)} & 0 & \dots & 0 \end{bmatrix} \in \mathcal{M}_{1, q}(\mathbb{R}) \quad (6.12)$$

and

$$M = \begin{bmatrix} -a_1 & -a_2 & -a_3 & \dots & -a_q \\ 1 & 0 & 0 & 0 & 0 \\ 0 & 1 & 0 & 0 & 0 \\ \dots & \dots & \dots & \dots & \dots \\ 0 & 0 & 0 & 1 & 0 \end{bmatrix} \in \mathcal{M}_{q,q}(\mathbb{R})$$

Finally, u_k is a white noise. This system is $N = 120$ -periodic (since the angle dynamics (6.4) is 4π periodic and the angle sample is $\pi/30$).

6.3.2.5. Time-varying prediction algorithm. — We use a time-varying Kalman predictor for the combustion torque. For purpose we introduce the system

$$\hat{x}_{k+1/k} = A_k \hat{x}_{k/k-1} + L_k (y_k - C_k \hat{x}_{k/k-1}) \quad (6.13)$$

with the initial condition

$$x_{0/-1} = m_0$$

where L_k is the Kalman gain matrix

$$L_k = A_k P_k C_k^T (C_k P_k C_k^T + R_k)^{-1} \quad (6.14)$$

In this last expression, the covariance error $P_k = \text{cov}(x_k - \hat{x}_{k/k-1})$ is recursively computed through

$$P_{k+1} = A_k P_k A_k^T + B_k Q_k B_k^T - A_k P_k C_k^T (C_k P_k C_k^T + R_k)^{-1} C_k P_k A_k^T \quad (6.15)$$

with $P_0 = \text{cov}(x_0)$. At last Q_k and R_k are matrices to be chosen.

6.3.2.6. Conclusion on time-varying Kalman filter convergence. —

In the general time-varying case, there is no proof of the convergence of the Kalman observer algorithm. Nevertheless linear periodic systems have received a lot of attention for the last twenty years. The Discrete Periodic Riccati Equation (DPRE) properties are used to extend the Kalman filter to periodic systems. A key challenge is to prove the existence and uniqueness of a Symmetric Periodic Positive Solution (SPPS). In short, Bittanti *et al.* exposes sufficient conditions to prove convergence of the estimator. Theses properties are the detectability of the system. To check theses, the Gramian is a handy tool. Since C_* (i.e. the set of all C_k for $k \in \mathbb{N}$) are constant matrices, the criteria of detectability is equivalent to the observability criteria. In Appendix D.1, we check this last property, through observability Gramian.

Convergence of this observer is detailed in leading to the follow proposition

Proposition 6.1. — *With R_k and Q_k constant symmetric definite positive matrices, the Kalman filter state defined in Equations (6.13,6.14,6.15) converges towards the reference model state (6.8) whatever the choice of the combustion model (6.7).*

6.3.2.7. *Testbench results.* — The implementation is achieved in discrete time with a sample angle of 6° deg crank angle. The observer described is evaluated on a 4 cylinder engine testbench described in Appendix D. Experimental results are presented in 6.4

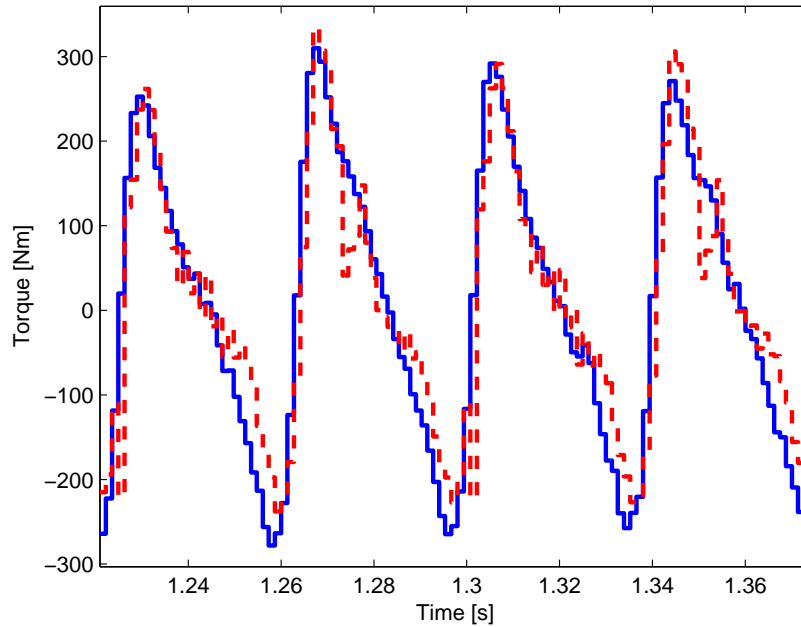


FIGURE 6.4. Testbench results. Torque reconstruction with the Kalman filter at (800 rpm, 2 bar). Measurement (blue-solid) : estimated (red-dotted).

6.3.3. Adaptive Fourier Basis decomposition. — In this subsection, we decompose the periodic mass torque (π -periodic with zero mean on a fixed operating point) over its Fourier basis.

$$T_{mass}(\alpha) \simeq \sum_{k \in \mathcal{I}_h} c_k e^{2ik\alpha}$$

where $\mathcal{I}_h \triangleq [-n_h, n_h] \setminus \{0\}$.

6.3.3.1. *Reference model.* — The state is The dynamics of the system writes

$$\begin{cases} \frac{d\phi}{d\alpha} = \sum_{k \in \mathcal{I}_h} c_k e^{2ik\alpha} \\ \frac{dc_k}{d\alpha} = 0, \quad \forall k \in \mathcal{I}_h \\ y = \dot{\alpha}^2 \end{cases}$$

where $\phi(\alpha) = E_{mass} = \frac{1}{2}J(\alpha)\dot{\alpha}^2$ is the kinetic energy of the system. This is again a periodic linear system with a unknown periodic input T_{mass} . In the notations of chapter 7, the dynamics write

$$\begin{cases} \frac{dx}{d\alpha} = Ax + A_0 w_0 \\ \frac{dc_k}{d\alpha} = 0, \quad \forall k \in \mathcal{I}_h^+ \end{cases}$$

where $A = 0$, $A_0 = 1$, and $C(\alpha) = \frac{2}{J(\alpha)}$.

6.3.3.2. *Observer design.* — Corresponding to state-space model, we define a time-varying Luenberger type observer following chapter 7

$$\begin{cases} \frac{d\hat{x}}{d\alpha} = \left(\sum_{k \in \mathcal{I}_h} \hat{c}_k e^{2ik\alpha} \right) - L_{ec}(C(\alpha)\hat{x} - y) \\ \frac{d\hat{c}_k}{d\alpha} = -\frac{L_T}{k^2 + 1} e^{-2ik\alpha} (C(\alpha)\hat{x} - y), \quad \forall k \in \mathcal{I}_h^+ \end{cases} \quad (6.16)$$

with L_{ec} and L_T two positive gains. Using Proposition 7.3, convergence of the observer designed according to (6.2) is guaranteed.

6.3.3.3. *Testbench results.* — The implementation is achieved in discrete time with a sample angle of 6°deg crank angle.

6.3.4. Comparison of the two observers. —

6.3.4.1. *Choice of the number of harmonics.* — In the previous section, we use n_h as the number of harmonics to reconstruct the signal. The number of harmonics must be large enough to estimate the signal, but on the other hand the more harmonics we have, the more tedious the tuning phase is. One of the main advantage of the filter is that the structure of the filter gives a natural tuning of the gains. Moreover, the tuning is valid whatever the number of harmonics you finally use. The experimental tuning is made with

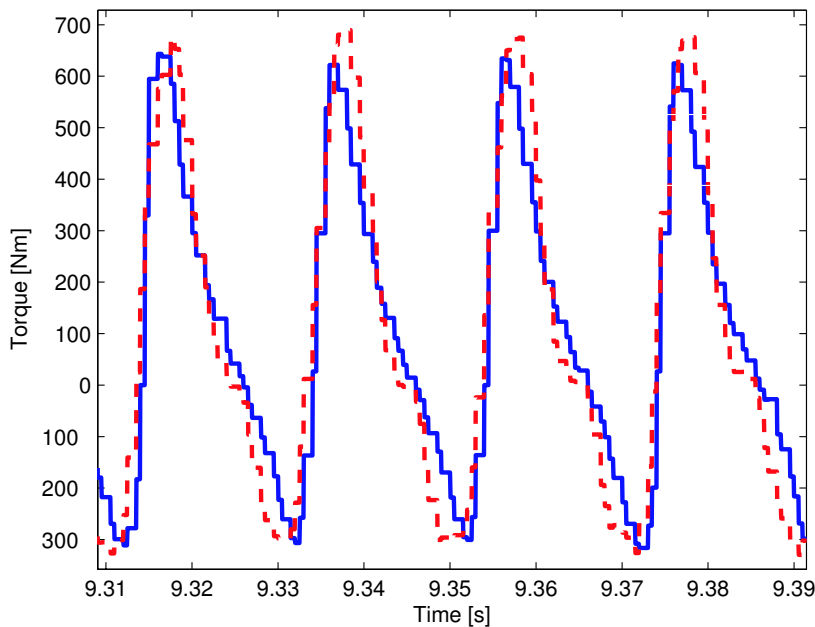


FIGURE 6.5. Testbench results. Torque estimation with the Kalman filter at (800 rpm, 2 bar). Measurement (blue-solid) : estimated (red-dotted).

n_h	1	2	3	4	5	6	7	8	9	10
Error %	87.6	20.9	11.8	11.2	10.5	8.2	7.3	5.9	4.5	3.2

TABLE 6.1. Estimation errors w.r.t. the number of harmonics used in the Fourier expansion with the H_1 -norm.

a few number of harmonics (usually 2), and then naturally extended to a high number of harmonics without re-tuning.

Figure 6.6 is an exemple of such a combustion torque. Lot of harmonics are needed in order to reconstruct the signal (at least 7). Table 6.1 summarize the estimation errors w.r.t. the number of harmonics used in the Fourier expansion.

6.3.4.2. Computation time. — The main advantage of the periodic Fourier filter is to be able to choose as many harmonics as needed with a limited increase of the computation time. Figure 6.7 reports the variation of computation time with respect to the number of harmonics used for the reconstruction. Compared to the periodic Kalman filter, whose

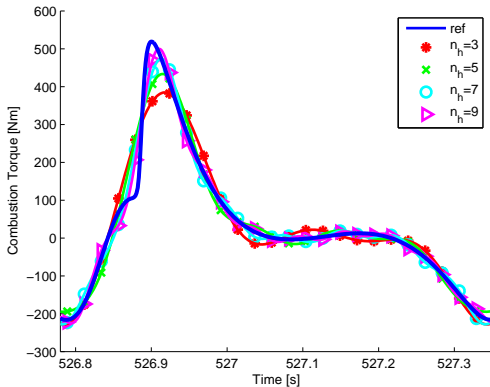


FIGURE 6.6. Testbench results. Decomposition of the combustion torque (1500 rpm, 2 bar of Indicated Mean Effective Pressure), comparisons between the reference signal (blue) and its reconstructed version through harmonic expansion with $n_h = 7$.

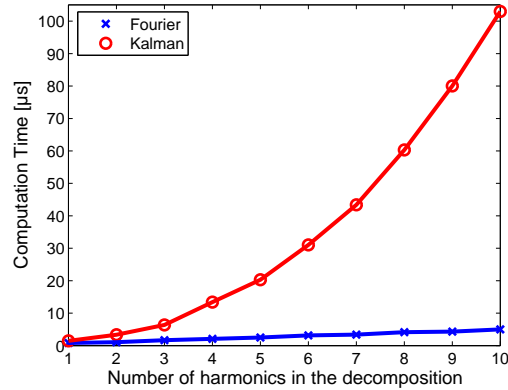


FIGURE 6.7. Testbench Results. CPU time with respect to the harmonic expansion. Comparison between a Kalman filter and the Fourier filter.

computation time increase quadratically w.r.t. the number of harmonics, our filter's computation time increase linearly which allow the use of a lot of harmonics.

6.4. Conclusions

The work presented in this chapter reports the development and implementation of two kind of observers. First, we design an observer to deconvolute the transmission dynamics. The proposed observer reconstruct the instantaneous engine speed under the cylinders from the instantaneous engine speed sensor located at the end of the transmission. Then, we propose the design of two indicated torque estimators from the estimation of the instantaneous engine speed under the cylinders. While both approaches provide equally robust observers and similar performances, comparisons in terms of ease of tuning and CPU load suggest the superiority of the nonlinear torque observer.

PART III

ESTIMATION FOR LINEAR-TIME PERIODIC SYSTEMS

PRÉSENTATION DE LA PARTIE III

Comme vu au chapitre 6, l'estimation des systèmes périodiques excités par une perturbation périodique inconnue est très utile dans les problèmes d'observateurs dans le domaine du contrôle moteur. Comme décrit dans 6.3.4, les filtres de Kalman donnent une estimation de cette excitation au prix d'un temps de calcul très élevé. C'est pourquoi, nous proposons des observateurs linéaires périodiques pour résoudre ce problème.

Dans le chapitre 7, nous considérons le système $\dot{x} = A(t)x + A_0(t)w(t)$, $y = C(t)x$, $x \in \mathbb{R}^n$, $w \in \mathbb{R}^m$, $y \in \mathbb{R}^p$, ($m \leq p \leq n$) où $A(t)$, $A_0(t)$, et $C(t)$ sont des matrices T_0 -périodiques. Le signal d'entrée inconnu $w(t)$ est T_0 -périodique mais nous supposons qu'il admet une décomposition de Fourier ayant un nombre fini d'harmonique. Nous proposons une technique, inspiré des techniques de moyennisation [53], permettant d'estimer w à partir de la mesure y . Dans les cas d'une mesure partielle ou totale, nous proposons un observateur pour les coefficients de Fourier de la décomposition de $w(t)$. Cette technique est particulièrement attractive pour les applications automobiles où la fréquence d'échantillonnage est très grande. A la différence des filtres de Kalman, limités par leurs grands temps de calcul, la technique proposée est bien adaptée aux applications temps réel. Ce travail a été publié dans [30, 29].

Dans le chapitre précédent, nous avons regardé les filtres de dimension finie pour les systèmes linéaires périodiques excités par une entrée périodique inconnue. Dans ce chapitre, nous regardons son extension naturelle: le cas des filtres de dimensions infinies. L'extension de la théorie aux filtres de dimension infinies permet d'obtenir une formule asymptotique qui, une fois restreinte à un nombre fini de termes, sert de méthodologie de calibration.

Nous expliquons sous quelles conditions un choix approprié de gains garantit la convergence dans l'espace des fonctions de Sobolev de type H^1 .

PRESENTATION OF PART III

As seen in Chapter 6, estimation of periodic systems driven by periodic unknown inputs is very useful in automotive engine estimation problems. As described in 6.3.4, Kalman filters provide an estimation of this excitation but at the expense of a high computation burden. As an alternative, we propose linear periodic observers to solve this problem.

In Chapter 7, we consider $\dot{x} = A(t)x + A_0(t)w(t)$, $y = C(t)x$, $x \in \mathbb{R}^n$, $w \in \mathbb{R}^m$, $y \in \mathbb{R}^p$, ($m \leq p \leq n$) where $A(t)$, $A_0(t)$, and $C(t)$ are T_0 -periodic matrices. The T_0 -periodic input signal $w(t)$ is unknown but is assumed to admit a finite dimensional Fourier decomposition. We propose a technique, based on averaging ideas [53], to estimate w from the measurements y . In both full state and partial state measurement cases, we propose an efficient observer for the coefficients of the Fourier decomposition of $w(t)$. This technique is particularly attractive for automotive engine applications where sampling time is very short. In this situation, standard estimation techniques based on Kalman filters are sometimes discarded because of their relative high computational burden. By contrast, the proposed technique is well suited to such real-time system requirements. This work appears in [30, 29].

In Chapter 8, we address the case of an infinite number of harmonics (w his a series) in the case $n = p$. Convergence is guaranteed under some hypothesis. The extension of the theory to the infinite dimensional case provide a simple asymptotic formula that, when truncated, can successfully serve as a tuning methodology. We explain under which conditions an appropriate choice of gains guarantees convergence in Sobolev functional space of H^1 type.

CHAPTER 7

PERIODIC INPUT ESTIMATION FOR LINEAR PERIODIC SYSTEMS

Chapitre 7. — Idéalement, les pressions, températures, et les débits devraient être mesurés en différents endroits du moteur, permettant des stratégies de contrôle très fines. Malheureusement, leur coût et leur fiabilité, empêchent ces capteurs d'être utilisés sur les véhicules de série. C'est pourquoi l'étude des observateurs, aussi appelés capteurs logiciels, se révèle de plus en plus importants dans l'ingénierie automobile. Les problématiques du contrôle moteur ont certains points communs. En effet, beaucoup des problèmes d'observations peuvent être vus comme des problèmes de filtrage inverse pour des systèmes périodiques excités par des entrées périodiques inconnues (voir chapitres 5 et 6 par exemple). La périodicité est une propriété fondamentale des moteurs. À différents niveaux de modélisation, les dynamiques présentes dans le moteur peuvent être considérées comme des systèmes linéaires périodiques synchronisés mécaniquement par la rotation du vilebrequin.

Dans ce chapitre, nous reformulons le problème de la reconstruction d'une entrée périodique dans le cadre général des systèmes linéaires périodiques excités par un signal T_0 -périodique. Nous considérons $\dot{x} = A(t)x + A_0(t)w(t)$, $y = C(t)x$, $x \in \mathbb{R}^n$, $w \in \mathbb{R}^m$, $y \in \mathbb{R}^p$, ($m \leq p \leq n$) où $A(t)$, $A_0(t)$, et $C(t)$ sont des matrices T_0 -périodiques. Le signal d'entrée $w(t)$ est inconnu mais nous supposons que sa décomposition de Fourier n'admet qu'un nombre fini d'éléments. Notre contribution est une technique d'observation qui estime w à partir de la mesure y . Cette technique est particulièrement intéressante pour les applications du contrôle moteur où la fréquence d'échantillonnage est très grande. Dans la même situation, un filtre de Kalman aurait une précision équivalente mais au prix de temps de calcul beaucoup trop élevés.

Nous présentons la technique d'observation dans trois cas distincts. Dans chaque cas, nous proposons une méthode de réglage des gains de l'observateur. La majeure partie de ce chapitre est dédiée à l'analyse de la convergence. Nous prouvons la convergence asymptotique de l'observateur sous des conditions standards d'observabilités.

7.1. Introduction

Ideally, pressures, temperatures, and flows would be measured at numerous places in the engine, enabling accurate control strategies. Unfortunately, their cost and reliability often prevent these sensors from reaching commercial products. As a result, observer design has been garnering increasing attention in recent years. In this context, several common threads can be found. In particular, many observation problems may be seen as inverse filtering problems for periodic systems driven by periodic inputs (see chapters 5 and 6 for example). This periodicity stems from a fundamental property of the engines. At various levels of modelling, as seen in chapter 6, automotive engine dynamics can be considered as a linear periodic system being mechanically coordinated and synchronized by the revolution of the crankshaft. Let us now present some observation topics in more details. A first example is the sensor dynamics inversion problem (used in Chapter 5 for the inversion of the AFR sensor dynamics). A usual model for such sensors is a first order linear system driven by a periodic signal which can be, depending on the application, the intake pressure, the intake temperature, the exhaust pressure, or the mass air flow. A second example is the estimation of the combustion torque, using as only sensor the instantaneous crankshaft angle speed (used in Chapter 6). More advanced topics are the estimation of the flow from the intake manifold to the cylinders (see [15, 58, 57, 38] for more details) or the transmission dynamics inversion (used in Chapter 6).

Online estimation of the frequencies of a signal which is the sum of a finite number of sinusoids with unknown magnitudes, frequencies, and phases has been addressed by numerous authors (one can refer to [59, 89, 113] for instance). The problem we address is different. First, the signal we wish to estimate is not directly measured. This signal, which is also assumed to admit a finite dimensional Fourier decomposition, is filtered through a linear periodic system. The output of this system represents the only available data. Secondly (and very importantly), its periodicity is precisely known. This particularity suggests a dedicated observation technique could be worth developing.

In this chapter, we formulate the reconstruction of periodic inputs into the general framework of time-periodic linear systems driven by T_0 -periodic signals. We consider

$\dot{x} = A(t)x + A_0(t)w(t)$, $y = C(t)x$, $x \in \mathbb{R}^n$, $w \in \mathbb{R}^m$, $y \in \mathbb{R}^p$, ($m \leq p \leq n$) where $A(t)$, $A_0(t)$, and $C(t)$ are T_0 -periodic matrices. The T_0 -periodic input signal $w(t)$ is unknown but is assumed to admit a finite dimensional Fourier decomposition. Our contribution is a technique to estimate w from the measurements y . In both full state and partial state measurement cases, we propose an efficient observer for the coefficients of the Fourier decomposition of $w(t)$. This technique is particularly attractive for automotive engine applications where sampling time is very short. In this situation, standard estimation techniques based on Kalman filters are sometimes discarded because of their relative high computational burden. By contrast, the proposed technique is well suited to such real-time system requirements.

The chapter is organized as follows. In Section 7.2, we detail the problem statement and notations. Then, we present the observers in three distinct cases. In the various situations under consideration, we propose specific sets of gains. They require only a very small number of tuning parameters to be chosen. Finally, the major part of the chapter is dedicated to convergence analysis. Under standard observability conditions, we prove asymptotic convergence, when the tuning parameters are chosen sufficiently small. In details, convergence in the full state measurement case is proven in Section 7.3 with Proposition 7.1. Then, we prove convergence in the case of partial state measurement. Time-invariant systems are treated in Section 7.4, while time-periodic systems are addressed in Section 7.5. Convergence proof is achieved by computing a monodromy matrix and investigating its stability. Several cascaded changes of coordinates and an averaging reduction of the dynamics are used. The main result of these two sections are Propositions 7.2 and 7.3.

7.2. Problem statement and observer design

7.2.1. Notations and problem statement. — Consider the periodic system driven by an unknown periodic input signal $w(t)$

$$\dot{x} = A(t)x + A_0(t)w(t), \quad y = C(t)x \quad (7.1)$$

where $x(t) \in \mathbb{R}^n$ is the state and $A(t)$, $A_0(t)$, $C(t)$ are T_0 -periodic matrices ($T_0 > 0$ assumed to be known) in $\mathcal{M}_{n,n}(\mathbb{R})$, $\mathcal{M}_{n,m}(\mathbb{R})$ and $\mathcal{M}_{p,n}(\mathbb{R})$ respectively. The goal of our study is the estimation of the T_0 -periodic continuous input signal $w(t) \in \mathbb{R}^m$, with

$m = \dim(w) \leq p = \dim(y) \leq n = \dim(x)$, through its Fourier decomposition over a finite number h of harmonics

$$w(t) \triangleq \sum_{k \in \mathcal{I}_h} c_k e^{ik\omega_0 t}, \quad \omega_0 \triangleq \frac{2\pi}{T_0}$$

where $\mathcal{I}_h \triangleq \bigcup_{\sigma=1}^h \{\rho(\sigma), -\rho(\sigma)\}$ indexes the h modes, and $\rho : \mathbb{N} \setminus \{0\} \rightarrow \mathbb{N}$ is strictly increasing. We note $\mathcal{I}_h^+ \triangleq \{k \in \mathcal{I}_h, k \geq 0\}$, $d_h \triangleq \text{card}(\mathcal{I}_h)$. With these notations, (7.1) can be rewritten as

$$\begin{cases} \dot{x} = A(t)x + A_0(t) \left(\sum_{k \in \mathcal{I}_h} c_k e^{ik\omega_0 t} \right), & y = C(t)x \\ \dot{c}_k = 0, \quad \forall k \in \mathcal{I}_h^+, \quad c_{-k} = c_k^\dagger \end{cases} \quad (7.2)$$

where each vector c_k admits m complex entries. We denote by \dagger the Hermitian transpose.

All along the chapter, we assume that the two following assumptions hold

H 7.1. — For all t , $\ker A_0(t) = \{0\}$, and $\ker C^\dagger(t) = \{0\}$.

H 7.2. — The only solution $t \mapsto (x(t), \{c_k(t)\}_{k \in \mathcal{I}_h^+})$ of Equation (7.2) for which the output $y(t) = C(t)x(t)$ is identically zero over $[0, T_0]$, is the zero solution.

7.2.2. Observer structure. — Corresponding to state-space model (7.2), we define a time-varying Luenberger type observer

$$\begin{cases} \dot{\hat{x}} = A(t)\hat{x} + A_0(t) \left(\sum_{k \in \mathcal{I}_h} \hat{c}_k e^{ik\omega_0 t} \right) \\ \quad - L(t)(C(t)\hat{x} - y) \\ \dot{\hat{c}}_k = -e^{-ik\omega_0 t} L_k(t)(C(t)\hat{x} - y(t)), \quad \forall k \in \mathcal{I}_h^+ \end{cases} \quad (7.3)$$

To construct a real signal \hat{w} , we define $\hat{c}_{-k} \triangleq \hat{c}_k^\dagger$ for all $k \in \mathcal{I}_h^+$. The gain matrices $L(t)$ (with real entries) and $\{L_k\}_{k \in \mathcal{I}_h^+}$ (with complex entries) are T_0 -periodic functions defined in the following sub-section. The errors $\tilde{x} = x - \hat{x}$ and $\tilde{c}_k = c_k - \hat{c}_k$ satisfy

$$\begin{cases} \dot{\tilde{x}} = (A(t) - L(t)C(t))\tilde{x} + A_0(t) \left(\sum_{k \in \mathcal{I}_h} \tilde{c}_k e^{ik\omega_0 t} \right) \\ \dot{\tilde{c}}_k = -e^{-ik\omega_0 t} L_k(t)C(t)\tilde{x}, \quad \forall k \in \mathcal{I}_h^+ \end{cases} \quad (7.4)$$

7.2.3. Overview of main practical results: observer gains design guidelines. —

7.2.3.1. *Full state measurement case.* — We assume here that $m \leq p = n$. Thus, for all t , $C(t)$ is invertible. In this case, we choose

$$L(t) \triangleq (A(t) - \bar{A})C^{-1}(t) \quad (7.5)$$

where \bar{A} is any asymptotically stable matrix in $\mathcal{M}_{n,n}(\mathbb{R})$ and for all $k \in \mathcal{I}_h^+$, we choose the gains $L_k(t)$ as

$$L_k(t) \triangleq \beta_k A_0^\dagger(t) P C^{-1}(t) \quad (7.6)$$

where P is the symmetric positive definite solution of the Lyapunov equation (which is uniquely defined because \bar{A} is stable)

$$P\bar{A} + \bar{A}^\dagger P = -I_n \quad (7.7)$$

and $\{\beta_k\}_{k \in \mathcal{I}_h^+}$ are strictly positive reals. Asymptotic convergence with such gains is proven in Section 7.3.

7.2.3.2. *Time invariant partial measurement case.* — We consider here that $m \leq p < n$ and that A , A_0 , and C do not depend on t . In this case, hypothesis H 2 implies that (A, C) is observable. A gain L can be chosen such that $A - LC$ is asymptotically stable. Then, for all $k \in \mathcal{I}_h^+$, one can choose the gains $L_k(t)$ under the form

$$L_k(t) \triangleq \epsilon \beta_k [(ik\omega_0 - (A - LC))^{-1} A_0]^\dagger C^\dagger \quad (7.8)$$

where $\{\beta_k\}_{k \in \mathcal{I}_h^+}$ are strictly positive reals. For small enough $\epsilon > 0$, convergence is proven in Section 7.4.

7.2.3.3. *Time periodic partial measurement case.* — In this part, we consider that $m \leq p < n$ and assume that we have at our disposal a periodic gain $L(t)$ such that the time-periodic system $\dot{\xi} = (A(t) - L(t)C(t))\xi$ is asymptotically stable. As will appear in the proof in Section 7.5, this assumption is valid provided H 1 and H 2 hold. This means that we have already solved the real-time estimation of x from y measurements when $w = 0$. We propose here an observer design, based on perturbation theory.

For $k \in \mathcal{I}_h^+$, denote by $W_k(t)$, a $n \times m$ matrix with complex entries, solution of

$$\begin{cases} \dot{W}_k(t) &= (A(t) - L(t)C(t))W_k(t) + e^{ik\omega_0 t} A_0(t) \\ W_k(0) &= W_k(T_0). \end{cases} \quad (7.9)$$

Existence of W_k is proven in Section 7.5. For implementation purposes, one can remark that, since $\dot{\xi}(t) = (A(t) - L(t)C(t))\xi(t)$ is asymptotically stable, the initial conditions on W_k are exponentially forgotten. Thus, a numerical approximation of $W_k(t)$ can be derived

from the asymptotic solution of (7.9) from a zero initial condition. For any $k \in \mathcal{I}_h^+$, we set

$$L_k(t) \triangleq \epsilon \beta_k W_k^\dagger(t) C^\dagger(t) \quad (7.10)$$

where $\{\beta_k\}_{k \in \mathcal{I}_h^+}$ are strictly positive reals. We prove in Proposition 7.3 that, for small enough $\epsilon > 0$, the state of the observer (7.3) converges asymptotically toward the state of reference system (7.2). Notice that when $(A - LC)$ and A_0 are constant matrices, $W_k = (ik\omega_0 - (A - LC))^{-1} A_0$ and we recover the gain designed for the previously considered time-invariant case.

7.3. Convergence results in the case of full state measurement

We now present convergence proofs. In the first case under consideration $p = n$, and C is a square invertible matrix. To prove convergence toward 0 of the error dynamics (7.4) for the gain design in sub-section 7.2.3.1, we exhibit a Lyapunov function and use LaSalle's invariance principle.

7.3.1. Lyapunov function candidate. — Let A be an asymptotic stable matrix in $\mathcal{M}_{n,n}(\mathbb{R})$, we set $L(t) = (A(t) - \bar{A})C^{-1}(t)$ and P the symmetric definite solution of the Lyapunov equation $P\bar{A} + \bar{A}^\dagger P = -I_n$. Consider strictly positive real numbers $\{\beta_k\}_{k \in \mathcal{I}_h^+}$. For $k < 0$, we define $\beta_k = \beta_{-k}$. A Lyapunov function candidate for (7.4) is

$$V(\tilde{x}, \{\tilde{c}_k\}_{k \in \mathcal{I}_h^+}) = \tilde{x}^T P \tilde{x} + \sum_{k \in \mathcal{I}_h} \frac{1}{\beta_k} \tilde{c}_k^\dagger \tilde{c}_k \quad (7.11)$$

By differentiation w.r.t. t , we have

$$\dot{V} = -\tilde{x}^T \tilde{x} + \sum_{k \in \mathcal{I}_h} (\tilde{x}^T M_k(t) \tilde{c}_k + \tilde{c}_k^\dagger M_k^\dagger(t) \tilde{x})$$

where

$$M_k(t) \triangleq (PA_0(t) - \frac{1}{\beta_k} C^\dagger(t) L_k(t)^\dagger) e^{ik\omega_0 t} \quad (7.12)$$

According to (7.6), for all $k \in \mathcal{I}_h^+$, we use $L_k(t) \triangleq \beta_k A_0^\dagger(t) PC(t)^{-1}$. Thus, for all $k \in \mathcal{I}_h$, $M_k = 0$ and

$$\dot{V} = -\tilde{x}^\dagger \tilde{x} \quad (7.13)$$

In summary, V is continuously differentiable and satisfies

- $V(0) = 0$.
- $V(\tilde{x}, \{\tilde{c}_k\}_{k \in \mathcal{I}_h^+}) > 0$ for $(\tilde{x}, \{\tilde{c}_k\}_{k \in \mathcal{I}_h^+}) \neq 0$.
- $\dot{V}(\tilde{x}, \{\tilde{c}_k\}_{k \in \mathcal{I}_h^+}) \leq 0$.

Thus, V is a Lyapunov function for system (7.4).

7.3.2. Application of LaSalle's theorem. — To conclude, we now use LaSalle's invariance principle. It is usually exposed for time invariant systems (see for instance [76] Theorem 4.4). Nevertheless, the result can be extended to periodic systems where the notion of invariance set is easily transposed (see, e.g. [110]). Let I_c be the largest invariant set in $\{(\tilde{x}, \{\tilde{c}_k\}_{k \in \mathcal{I}_h^+}) \mid \dot{V}(\tilde{x}, \{\tilde{c}_k\}_{k \in \mathcal{I}_h^+}) = 0\}$. From [110] §5.2, if I_c does not contain any trajectory but the trivial trajectory, then the equilibrium 0 is uniformly asymptotically stable. We now characterize I_c . From (7.13)

$$\left\{ (\tilde{x}, \{\tilde{c}_k\}_{k \in \mathcal{I}_h^+}) \mid \dot{V}(\tilde{x}, \{\tilde{c}_k\}_{k \in \mathcal{I}_h^+}) = 0 \right\} = \left\{ (\tilde{x}, \{\tilde{c}_k\}_{k \in \mathcal{I}_h^+}) \mid \tilde{x} = 0 \right\}$$

We apply the error dynamics (7.4) to an element of this last set. To remain in I_c , the variation of the first coordinate of the dynamics must equal zero. This implies

$$\forall t \in \mathbb{R}, \quad A_0(t) \left(\sum_{k \in \mathcal{I}_h} e^{ik\omega t} \tilde{c}_k \right) = 0$$

Yet, from H 1, $A_0(t)$ is injective for all t . Thus, for all t , $\sum_{k \in \mathcal{I}_h} e^{ik\omega t} \tilde{c}_k = 0$. The functions $\{e^{ik\omega t}\}_{k \in \mathcal{I}_h}$ are linearly independent. Then, the previous equation implies $\tilde{c}_k = 0$, for all $k \in \mathcal{I}_h$. Therefore, the set I_c is reduced to $\{0\}$. The observation error is asymptotically stable. We have proven the following result.

Proposition 7.1. — *Consider (7.2). Assume that $m \leq p = n$, and that H 7.1 and H 7.2 hold. Consider the observer (7.3) with gains L and L_k as defined in Equations (7.5) and (7.6), then the error dynamics (7.4) asymptotically converge to 0.*

7.4. Convergence results in the case of time invariant partial state measurement

In this part, we consider that $m \leq p < n$. By contrast with Section 7.3, it is not always possible to find L_k and P_k yielding $M_k = 0$ in (7.12). Further investigations are required. The key idea is to assume that the tuning parameters $\{L_k\}_{k \in \mathcal{I}_h}$ are small, so that the dynamics of \tilde{x} in (7.4) converge much faster than the $(\tilde{c}_k)_{k \in \mathcal{I}_h^+}$ dynamics. We note

$$\forall k \in \mathcal{I}_h^+, \quad L_k \triangleq \epsilon l_k, \quad 0 < \epsilon \ll 1$$

In this section, we perform a perturbation analysis and conclude toward convergence of the proposed observer (7.3) with the gains defined in subsection 7.2.3.2 when $\epsilon > 0$ is

sufficiently small (Proposition 7.2). The proof is based on several changes of coordinates represented in Figure 7.1. We now sketch what are the benefits of these cascaded transformations.

In the original coordinates, the error dynamics involve a matrix of the form $\begin{bmatrix} (A - LC) + \mathcal{O}(\epsilon) & f(A - LC, A_0) \\ 0 & \mathcal{O}(\epsilon) \end{bmatrix}$. It is impossible to infer the stability property when $\epsilon \rightarrow 0$. But, with carefully chosen coordinates changes, a new matrix of the form $\begin{bmatrix} (A - LC) + \mathcal{O}(\epsilon) & \mathcal{O}(\epsilon) \\ \mathcal{O}(\epsilon^2) & \epsilon E + \mathcal{O}(\epsilon^2) \end{bmatrix}$ appears. For ϵ small enough, this matrix is asymptotically stable if the time-invariant matrices $A - LC$ and E are.

7.4.1. A first change of coordinates: $(\bar{z}, z_k) \mapsto (\bar{\bar{z}}, z_k)$.—

Since (A, C) is observable, we can find L such that $A - LC$ is asymptotically stable. Let $\bar{z} = z = \tilde{x}$, $z_k = \tilde{c}_k$, and $P = A - LC$. The error dynamics (7.4) rewrite

$$\begin{cases} \dot{\bar{z}} = P\bar{z} + \sum_{k \in \mathcal{I}_h} A_0 e^{ik\omega_0 t} z_k \\ \dot{z}_k = -\epsilon e^{-ik\omega_0 t} l_k C z, \quad \forall k \in \mathcal{I}_h^+ \end{cases} \quad (7.14)$$

At zero order ($\epsilon = 0$), the matrix of system (7.14) is $\begin{bmatrix} P & f(P, A_0) \\ 0 & 0 \end{bmatrix}$ which does not allow us to conclude toward convergence. This first change of variables aims at cancelling the term $f(P, A_0)$ and replace it by an $\mathcal{O}(\epsilon)$ -term. As P is asymptotically stable, $\forall k \in \mathcal{I}_h$, $\det(P - ik\omega_0 I_n) \neq 0$. We set $\bar{A}_k \triangleq (ik\omega_0 - P)^{-1} A_0$ and, then, $ik\omega_0 \bar{A}_k = A_0 + P\bar{A}_k$. We define

$$\bar{\bar{z}} \triangleq \bar{z} - \sum_{k \in \mathcal{I}_h} e^{ik\omega_0 t} \bar{A}_k z_k \quad (7.15)$$

Some computations yield

$$\dot{\bar{\bar{z}}} = (P + \epsilon Q)\bar{\bar{z}} + \epsilon \sum_{k \in \mathcal{I}_h} e^{ik\omega_0 t} Q \bar{A}_k z_k$$

where $Q \triangleq \sum_{k \in \mathcal{I}_h} \bar{A}_k l_k C$. In the $(\bar{\bar{z}}, \{z_k\}_{k \in \mathcal{I}_h^+})$ coordinates, system (7.14) reads

$$\begin{cases} \dot{\bar{\bar{z}}} = (P + \epsilon Q)\bar{\bar{z}} + \epsilon \sum_{k \in \mathcal{I}_h} e^{ik\omega_0 t} Q \bar{A}_k z_k \\ \dot{z}_k = -\epsilon e^{-ik\omega_0 t} l_k C \bar{\bar{z}} - \epsilon \sum_{l \in \mathcal{I}_h} e^{i(l-k)\omega_0 t} R_{k,l} z_l, \quad \forall k \in \mathcal{I}_h^+ \end{cases} \quad (7.16)$$

where $R_{k,l} \triangleq l_k C \bar{A}_l$. This change of coordinates stresses the first part of the dynamics as an asymptotically linear stable system with an $\mathcal{O}(\epsilon)$ perturbation.

7.4.2. Second change of coordinates: $(\bar{z}, z_k) \mapsto (\bar{z}, \bar{z}_k)$.—

The purpose of this second change of variables, bearing on the $\{z_k\}_{k \in \mathcal{I}_h^+}$ variables only, is to make a $\mathcal{O}(\epsilon^2)$ coupling term appear through which \bar{z} impacts on z_k . Let $\forall k \in \mathcal{I}_h$, $F_k \triangleq l_k C (\imath k \omega_0 - P)^{-1}$. This gives $F_k \imath k \omega_0 = l_k C + F_k P$. Then, with

$$\forall k \in \mathcal{I}_h \quad \bar{z}_k \triangleq z_k - \epsilon e^{-\imath k \omega_0 t} F_k \bar{z}$$

we have, after some calculus, that for all $k \in \mathcal{I}_h$

$$\dot{\bar{z}}_k = -\epsilon \sum_{l \in \mathcal{I}_h} e^{\imath(l-k)\omega_0 t} R_{k,l} \bar{z}_l + \epsilon^2 (f_{k,\bar{z}}(t) \bar{z} + \sum_{l \in \mathcal{I}_h} f_{k,l}(t) \bar{z}_l) + \epsilon^3 f_{\epsilon,k,\bar{z}}(t) \bar{z} \quad (7.17)$$

where the functions $\{f_{k,\bar{z}}, f_{k,l}, f_{\epsilon,k,\bar{z}}\}_{(k,l) \in \mathcal{I}_h^2}$ are regular, and T_0 -periodic in t .

7.4.3. Final change of coordinates: $(\bar{z}, \bar{z}_k) \mapsto (\bar{z}, \bar{\phi})$.—

Gathering $\{\bar{z}_k\}_{k \in \mathcal{I}_h^+}$ in $\phi \triangleq [\bar{z}_{-h} \ \dots \ \bar{z}_h]^T$, we can finally regroup system (7.16) and (7.17) under the form

$$\begin{cases} \dot{\bar{z}} &= (P + \epsilon Q) \bar{z} + \epsilon \sum_{k \in \mathcal{I}_h} e^{\imath k \omega_0 t} Q \bar{A}_k \bar{z}_k - \epsilon^2 f_{\bar{z}}(t) \bar{z} \\ \dot{\phi} &= -\epsilon E(t) \phi + \epsilon^2 ((f_{\phi,\bar{z}}(t) + \epsilon f_{\epsilon,\phi,\bar{z}}(t)) \bar{z} + f_{\phi}(t) \phi) \end{cases} \quad (7.18)$$

where the functions $f_{\phi,\bar{z}}$, $f_{\epsilon,\phi,\bar{z}}$ and f_{ϕ} are computed from (7.17). These are regular, and T_0 -periodic in t . Finally, $E(t) = (E_{\mu,\nu})$ is a $d_h \times d_h$ matrix. Its coefficients are of the form

$$E_{\mu,\nu}(t) \triangleq e^{\imath(\rho(\nu) - \rho(\mu))\omega_0 t} l_{\rho(\mu)} C (\imath \rho(\nu) \omega_0 - P)^{-1} A_0 \quad (7.19)$$

Theorem 7.1 (Averaging theorem [53]). — *There exists a C^r change of coordinates $\phi = \bar{\phi} + \epsilon w(\bar{\phi}, t, \epsilon)$ such that $\dot{\phi} = \epsilon f(\phi, t, \epsilon)$, where f is a C^r , $r > 1$ bounded function of period $T_0 > 0$ w.r.t. t , becomes*

$$\dot{\bar{\phi}} = \epsilon \bar{f}(\bar{\phi}) + \epsilon^2 f_1(\bar{\phi}, t, \epsilon)$$

where f_1 is of period T_0 w.r.t. t , $\bar{f}(\bar{\phi}) \triangleq \frac{1}{T_0} \int_0^{T_0} f(\bar{\phi}, t, 0) dt$, and $w(\bar{\phi}, t, \epsilon) = \int_0^t f(\bar{\phi}, s, \epsilon) - \bar{f}(\bar{\phi}) ds$.

In our case, $f(\phi, t, 0) = -E(t)\phi$, then $\bar{f}(\bar{\phi}) = -\bar{E}\bar{\phi}$ where

$$\bar{E} \triangleq \frac{1}{T_0} \int_0^{T_0} E(t) dt = \text{diag}(E_{-\rho(h), -\rho(h)}, \dots, E_{\rho(h), \rho(h)})$$

We set $\bar{\phi}(I - \epsilon \int_0^t (E(s) - \bar{E}) ds) \triangleq \phi$, then we have

$$\dot{\bar{\phi}} = -\epsilon \bar{E} \bar{\phi} + \epsilon^2 (g_{\bar{\phi}, \bar{z}}(\bar{\phi}, \epsilon, t) \bar{z} + g_{\bar{\phi}}(\bar{\phi}, t, \epsilon))$$

where the functions $g_{\bar{\phi}, \bar{z}}$ and $g_{\bar{\phi}}$ are regular, bounded, and T_0 -periodic w.r.t. t .

7.4.4. Conclusion toward convergence. — In the obtained $(\bar{z}, \bar{\phi})$ -coordinates, system (7.18) reads

$$\begin{cases} \dot{\bar{z}} &= (P + \epsilon Q)\bar{z} + \epsilon g_{\bar{z}, \bar{\phi}}(t)\bar{\phi} - \epsilon^2(f_{\bar{z}}(t)\bar{z} + f_{\bar{z}, \bar{\phi}}(t)\bar{\phi}) \\ \dot{\bar{\phi}} &= -\epsilon \bar{E}\bar{\phi} + \epsilon^2(g_{\bar{\phi}, \bar{z}}(\bar{\phi}, \epsilon, t)\bar{z} + g_{\bar{\phi}}(\bar{\phi}, t, \epsilon)) \end{cases} \quad (7.20)$$

To check convergence of the observer, we investigate the hyperbolic stability of the monodromy matrix of (7.20). Since this system is triangular up to second order terms, there exists $(M_{1,1}, M_{1,2}) \in \mathcal{M}_n(\mathbb{R}) \times \mathcal{M}_{n,md_h}(\mathbb{C})$ such that the considered monodromy matrix writes

$$\Phi_{\bar{z}, \bar{\phi}, \epsilon} = \begin{bmatrix} P - \epsilon M_{1,1} & -\epsilon M_{1,2} \\ 0 & -\epsilon \bar{E} \end{bmatrix} + \mathcal{O}(\epsilon^2)$$

Further, this expression is (up to second order terms in ϵ) time-invariant. Because P is asymptotically stable, (7.20) is asymptotically stable for $0 < \epsilon \ll 1$ if and only if the system

$$\dot{\bar{\phi}} = -\epsilon \bar{E}\bar{\phi} \quad (7.21)$$

is hyperbolically stable. All the changes of coordinates are linear, time-periodic and smooth, and thus uniformly continuous. Therefore, convergence toward 0 of $(\bar{z}, \bar{\phi})$ leads to the convergence toward 0 of $(z, \{z_k\}_{k \in \mathcal{I}_h^+})$. To impose hyperbolic stability of system (7.21), we set, for $k \in \mathcal{I}_h^+$

$$l_k(t) \triangleq \beta_k((\imath k \omega_0 - P)^{-1} A_0)^\dagger C^\dagger \quad (7.22)$$

In this case, we have $E_{\mu, \mu} = \beta_{\rho(\mu)} P_{\rho(\mu)}^\dagger P_{\rho(\mu)}$ where $P_{\rho(\mu)} \triangleq C(\imath \rho(\mu) \omega_0 - P)^{-1} A_0$, and $\mu \in \mathcal{I}_h$. But, for all $k \in \mathcal{I}_h$, $P_k \triangleq C(\imath k \omega_0 - P)^{-1} A_0$ has full rank, i.e., $\ker P_k = \{0\}$ ($m \leq p$). This holds because otherwise H 2 would be violated. For any $\Gamma_k \in \ker P_k$, $x = e^{\imath k \omega_0 t} (\imath k \omega_0 - P)^{-1} A_0 \Gamma_k$ and $c_l = \delta_{l,k} \Gamma_k$, is solution of (7.2) with $y = Cx \equiv 0$. Thus, system (7.21) is asymptotically stable. We have proven the following proposition.

Proposition 7.2. — *Consider (7.2) with $m \leq p < n$. Assume that the matrices A , A_0 and C are constant and that H 7.1 and H 7.2 hold. Consider the observer (7.3) with gain L and L_k as defined in subsection 7.2.3.2. Then, for small enough $\epsilon > 0$, the error dynamics (7.4) asymptotically converge to 0.*

7.5. Convergence results in the case of time periodic partial state measurement

In this last part, we assume that $m \leq p < n$ and we consider time-periodic matrices $A(t)$, $A_0(t)$, $C(t)$ with the gain design of sub-section 7.2.3.3. The proof has similarities with

the time-invariant case treated in the previous Section. A sequence of changes of variables is used, and additionally, Floquet's theorem and averaging provide rescaling under a time invariant form. Again, Figure 7.1 summarizes the organization of the proof.

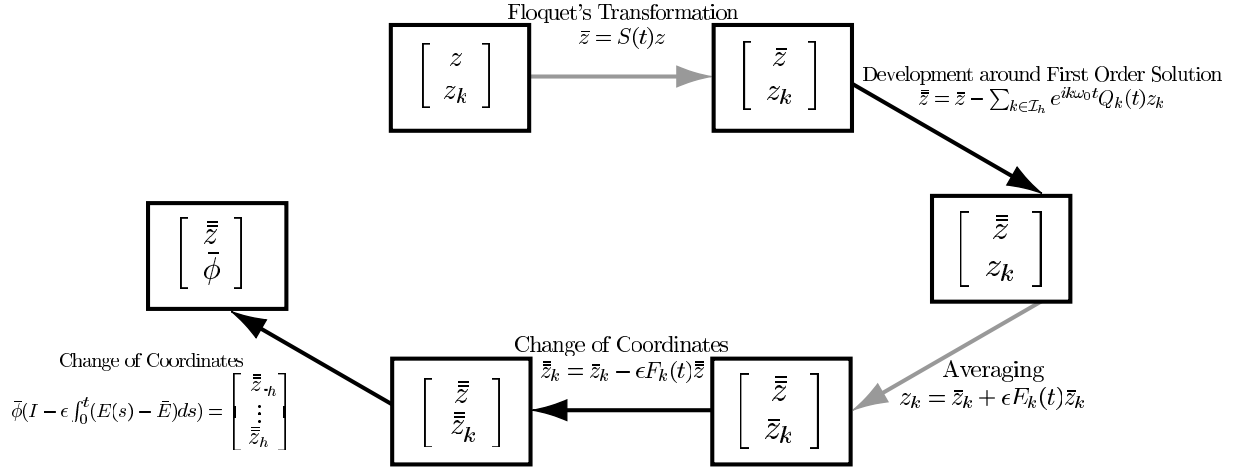


FIGURE 7.1. Proof of Propositions 7.2 and 7.3 organization. Proposition 7.3 is an extension of Proposition 7.2 to the periodic matrices. Grey arrows represent changes of coordinates that are used only in the time periodic case. They reduce to identity in the time invariant case.

By H 2, the observability Gramian on $[0, T_0]$ is definite positive. Thus, we can find a T_0 -periodic matrix $L(t)$ such that $A - LC$ is asymptotically stable (see [5] §14.2 and [62] for example). A constructive choice is given, for example, by the Kalman filter. In the case under consideration here, the error dynamics (7.4) can be formulated under the familiar expression

$$\begin{cases} \dot{z} = P(t)z + \sum_{k \in \mathcal{I}_h} A_0(t) e^{ik\omega_0 t} z_k \\ \dot{z}_k = -\epsilon e^{-ik\omega_0 t} l_k(t) C(t) z, \quad \forall k \in \mathcal{I}_h^+ \end{cases} \quad (7.23)$$

with $P(t) = A(t) - L(t)C(t)$. The matrices P , A_0 , and $l_k C$ are T_0 -periodic. Further, P is asymptotically stable. We note Φ the transition matrix of P , i.e. the nonsingular matrix solution of $\dot{\Phi}(t) = P(t)\Phi(t)$, $\Phi(0) = I_n$. Analysis of linear time periodic systems can be performed by the following result (see [42] and [16] for example).

Theorem 7.2 (Floquet's Theorem). — Consider the state space model $\dot{z} = P(t)z$ with T_0 -periodic matrix P . There exists a matrix $J \in \mathcal{M}_{n,n}(\mathbb{R})$ such that $S(t) \triangleq e^{Jt} \Phi^{-1}(t)$

is a periodic nonsingular T_0 -periodic matrix with $S(0) = I_n$. Generally, J is noted $J \triangleq \frac{1}{T_0} \log(\Phi(T_0))$. The following results hold

- The state transformation $\bar{z} = S(t)z$ yields a linear time invariant system $\dot{\bar{z}} = J\bar{z}$.
- A necessary and sufficient condition for asymptotic stability is that all the eigenvalues of the monodromy matrix ($\Phi(T_0) = e^{JT_0}$) lie in the open unitary disk, i.e. J is asymptotically stable.

Our convergence analysis heavily relies on this last result. We use periodic changes of variables to find conditions on asymptotic stability of system (7.23).

7.5.1. First change of coordinates: $(z, z_k) \mapsto (\bar{z}, z_k)$.— Following Theorem 7.2 with $P(t) = A(t) - L(t)C(t)$, we set $\bar{z} \triangleq S(t)z$. By construction, $S(t)$ is invertible and T_0 periodic. Since P is asymptotically stable, J is asymptotically stable. In the $(\bar{z}, \{z_k\}_{k \in \mathcal{I}_h^+})$ coordinates, the dynamics rewrite

$$\begin{cases} \dot{\bar{z}} = J\bar{z} + \sum_{k \in \mathcal{I}_h} e^{ik\omega_0 t} \bar{A}(t) z_k \\ \dot{z}_k = -\epsilon e^{-ik\omega_0 t} R_k(t) \bar{z}, \quad \forall k \in \mathcal{I}_h^+ \end{cases} \quad (7.24)$$

with $\bar{A}(t) = S(t)A_0(t) \in \mathcal{M}_{n,m}(\mathbb{R})$, and $R_k(t) = l_k(t)C(t)S^{-1}(t) \in \mathcal{M}_{p,n}(\mathbb{R})$. Both \bar{A} and R_k are T_0 -periodic, and they can be rewritten as Fourier series

$$\bar{A}(t) = \sum_{l \in \mathbb{Z}} e^{il\omega_0 t} \mathcal{F}_l(\bar{A}), \quad R_k(t) = \sum_{l \in \mathbb{Z}} e^{il\omega_0 t} \mathcal{F}_l(R_k)$$

where, for all $l \in \mathbb{Z}$, $\mathcal{F}_l(\cdot) = \frac{1}{T_0} \int_0^{T_0} \cdot(s) e^{-il\omega_0 s} ds$. Comparing (7.23) and (7.24), we notice that some progress has been made by stressing time invariant terms. We now investigate the effects of coupling through the ϵ -terms.

7.5.2. Second change of coordinates: $(\bar{z}, z_k) \mapsto (\bar{\bar{z}}, z_k)$.— Following [67] and [68], we now perform a series expansion w.r.t. ϵ on (7.24). Since J is asymptotically stable, then $\forall k \in \mathcal{I}_h$, $(ik\omega_0 - J)^{-1}$ is non singular. Consider

$$Q_k(t) \triangleq \sum_{l \in \mathbb{Z}} e^{il\omega_0 t} (l(l+k)\omega_0 - J)^{-1} \mathcal{F}_l(\bar{A}) \quad (7.25)$$

This series is well defined because $\{(l(l+k)\omega_0 - J)^{-1} \mathcal{F}_l(\bar{A})\}_{l \in \mathbb{Z}}$ belongs to $\ell_m^1 \triangleq \{\{u_l\}_{l \in \mathbb{Z}} \in (\mathbb{R}^m)^{\mathbb{Z}} / \sum_{l \in \mathbb{Z}} \|u_l\| < +\infty\}$. This can be proven by noticing that its general term is the product of the general terms of two ℓ_m^2 series. Moreover, it is periodic, and differentiable: $\forall k \in \mathcal{I}_h$,

$$\frac{d(e^{ik\omega_0 t} Q_k(t))}{dt} = J e^{ik\omega_0 t} Q_k(t) + e^{ik\omega_0 t} \bar{A}(t)$$

Notice that, by construction, $W_k(t) \triangleq S^{-1}(t)Q_k(t)$ is a periodic solution of

$$\dot{W}_k(t) = (A(t) - L(t)C(t))W_k(t) + e^{ik\omega_0 t}A_0(t)$$

and satisfies $W_k(0) = W_k(T_0)$. Then, we define $\bar{z} \triangleq \bar{z} - \sum_{k \in \mathcal{I}_h} e^{ik\omega_0 t}Q_k(t)z_k$. In the $(\bar{z}, \{z_k\}_{k \in \mathcal{I}_h^+})$ coordinates, system (7.24) rewrites

$$\begin{cases} \dot{\bar{z}} &= (J + \epsilon Q(t))\bar{z} + \epsilon \sum_{k \in \mathcal{I}_h} Q(t)Q_k(t)z_k \\ \dot{z}_k &= -\epsilon e^{-ik\omega_0 t}R_k(t)\bar{z} - \epsilon \sum_{l \in \mathcal{I}_h} R_{k,l}(t)e^{i(l-k)\omega_0 t}z_l, \quad \forall k \in \mathcal{I}_h^+ \end{cases} \quad (7.26)$$

where $Q(t) \triangleq \sum_{k \in \mathcal{I}_h} Q_k(t)R_k(t)$ and

$$R_{k,l}(t) \triangleq R_k(t)Q_l(t) \quad (7.27)$$

This change of coordinates stresses the first part of the dynamics as an asymptotically stable system with a perturbation in ϵ . We obtain the right structure for analysis of the first equation of (7.26), but the second equation is still time-varying. In the next subsection, we explicit a change of coordinates such that the whole dynamics become linear time-invariant.

7.5.3. Third change of coordinates: $(\bar{z}, z_k) \mapsto (\bar{z}, \bar{z}_k)$.— The second part of (7.26) is factorized as ϵ times a periodic function. Averaging Theorem 7.1 will give insights here. We note for all $k \in \mathcal{I}_h$, $f_k(z_k, t, \epsilon) = -R_{k,k}(t)z_k$ and

$$\bar{f}_k(z_k) = -\frac{1}{T_0} \left(\int_0^{T_0} R_{k,k}(t)dt \right) z_k \triangleq -\bar{R}_k z_k$$

From (7.25) and (7.27), we have, for all $k \in \mathcal{I}_h$

$$\bar{R}_k = \sum_{l \in \mathbb{Z}} \mathcal{F}_{-l}(R_k)(i(l+k)\omega_0 - J)^{-1} \mathcal{F}_l(\bar{A}) \quad (7.28)$$

We note $E_k(t) \triangleq -\int_0^t (R_{k,k}(\tau) - \bar{R}_k) d\tau$. By Theorem 7.1, for all $k \in \mathcal{I}_h^+$ the new coordinate \bar{z}_k satisfies $z_k = \bar{z}_k + \epsilon E_k(t)\bar{z}_k$. This yields, $\forall k \in \mathcal{I}_h^+$,

$$\dot{\bar{z}}_k = -\epsilon e^{-ik\omega_0 t}R_k(t)\bar{z} + \epsilon^2 \sum_{l \in \mathcal{I}_h} f_{k,l}(\bar{z}_k, \bar{z}_l, t, \epsilon) - \epsilon \sum_{l \in \mathcal{I}_h, l \neq k} R_{k,l}(t)e^{i(l-k)\omega_0 t}\bar{z}_l - \epsilon \bar{R}_k \bar{z}_k$$

where $\{f_{k,l}\}_{(k,l) \in \mathcal{I}_h^2}$ are bounded regular functions, T_0 -periodic w.r.t. t . In the $(\bar{z}, \{\bar{z}_k\}_{k \in \mathcal{I}_h^+})$ coordinates, system (7.26) rewrites

$$\begin{cases} \dot{\bar{z}} &= (J + \epsilon Q(t))\bar{z} + \epsilon \sum_{k \in \mathcal{I}_h} Q(t)Q_k(t)(1 + \epsilon E_k(t))\bar{z}_k \\ \dot{\bar{z}}_k &= -\epsilon e^{-ik\omega_0 t}R_k(t)\bar{z} - \epsilon \bar{R}_k \bar{z}_k - \epsilon \sum_{l \in \mathcal{I}_h, l \neq k} R_{k,l}(t)e^{i(l-k)\omega_0 t}\bar{z}_l \\ &\quad + \epsilon^2 \sum_{l \in \mathcal{I}_h} f_{k,l}(\bar{z}_k, \bar{z}_l, t, \epsilon), \quad \forall k \in \mathcal{I}_h^+ \end{cases} \quad (7.29)$$

Now, the $\{\bar{z}_k\}_{k \in \mathcal{I}_h^+}$ dynamics have a time invariant self-excitation. Unfortunately, the monodromy matrix can not be easily derived and stability remains to be proven. Yet, the constant stable matrix J in the dynamics of \bar{z} has a positive impact on convergence toward 0 and compensates the ϵ -perturbation. The next subsection exhibits a change of coordinates which triangulates the system, i.e. the excitation in the new variable on the \bar{z} -dynamics will be a ϵ^2 -term.

7.5.4. Fourth change of coordinates: $(\bar{z}, \bar{z}_k) \mapsto (\bar{z}, \bar{z}_k)$.— A final change of coordinates leads to consider a new variable $\{\bar{z}_k\}_{k \in \mathcal{I}_h}$ whose dynamics dependance on \bar{z} is a term in ϵ^2 . We set for all $k \in \mathcal{I}_h$ $F_k(t) \triangleq \sum_{l \in \mathbb{Z}} e^{-il\omega_0 t} \mathcal{F}_{-l}(R_k)(i(l+k)\omega_0 - J)^{-1}$. Then, for all $k \in \mathcal{I}_h$,

$$\frac{d(e^{-ik\omega_0 t} F_k(t))}{dt} = -e^{-ik\omega_0 t} F_k(t) J - e^{-ik\omega_0 t} R_k(t)$$

Consider, for all $k \in \mathcal{I}_h$, $\bar{z}_k \triangleq \bar{z}_k - \epsilon e^{-ik\omega_0 t} F_k(t) \bar{z}$. Following the computation presented in subsection 7.4.2, we easily conclude that, in the $(\bar{z}, \{\bar{z}_k\}_{k \in \mathcal{I}_h^+})$ coordinates, system (7.29) rewrites

$$\begin{cases} \dot{\bar{z}} &= (J + \epsilon \mathcal{Q}(t)) \bar{z} + \epsilon \sum_{k \in \mathcal{I}_h} \mathcal{Q}(t) Q_k(t) \bar{z}_k \\ &\quad + \epsilon^2 h_{\bar{z}, k}(t, \epsilon) \bar{z} + \epsilon^2 \mathcal{Q}(t) \sum_{k \in \mathcal{I}_h} Q_k(t) E_k(t) \bar{z}_k \\ \dot{\bar{z}}_k &= -\epsilon \bar{R}_k \bar{z}_k - \epsilon \sum_{l \in \mathcal{I}_h, l \neq k} R_{k,l}(t) e^{i(l-k)\omega_0 t} \bar{z}_l \\ &\quad + \epsilon^2 h_k(\bar{z}, \{\bar{z}_l\}_{l \in \mathcal{I}_h^+}, t, \epsilon) \end{cases} \quad (7.30)$$

where the functions $\{h_k, h_{\epsilon, k, \bar{z}}\}_{k \in \mathcal{I}_h}$ are regular, bounded, and T_0 -periodic w.r.t. t .

7.5.5. Final change of coordinates: $(\bar{z}, \bar{z}_k) \mapsto (\bar{z}, \bar{\phi})$.— Gathering $\phi = [\bar{z}_{-h} \ \dots \ \bar{z}_h]^T$, the $\{\bar{z}_k\}_{k \in \mathcal{I}_h}$ dynamics of system (7.30) write

$$\dot{\phi} = -\epsilon E(t) \phi + \epsilon^2 \mathcal{K}(\phi, \bar{z}, t, \epsilon) \quad (7.31)$$

where \mathcal{K} is regular, and T_0 -periodic w.r.t. t .

$$E_{k,l}(t) \triangleq e^{i(l-k)\omega_0 t} R_{k,l} \quad (7.32)$$

We use the averaging theorem 7.1. In our case, $f(\phi) = -E(t)\phi$, then $\bar{f}(\bar{\phi}) = -\bar{E}\bar{\phi}$ where $\bar{E} = \frac{1}{T_0} \int_0^{T_0} E(t) dt$. We set $\bar{\phi}(I - \epsilon \int_0^t (E(s) - \bar{E}) ds) \triangleq \phi$, then we have

$$\dot{\bar{\phi}} = -\epsilon \bar{E} \bar{\phi} + \epsilon^2 \bar{\mathcal{K}}(\phi, \bar{z}, t, \epsilon)$$

where $\bar{\mathcal{K}}$ is regular, and T_0 -periodic w.r.t. t .

7.5.6. Conclusion toward the convergence of the observer. — To check convergence of the observer, we check hyperbolic stability of the monodromy matrix of system (7.30). Gathering terms yields that there exists $(\tilde{M}_{1,1}, \tilde{M}_{1,2}) \in \mathcal{M}_{n,n}(\mathbb{R}) \times \mathcal{M}_{n,md_h}(\mathbb{C})$ such that the sought-after monodromy matrix is

$$\Phi_{\bar{z}, \{\bar{z}_k\}_{k \in \mathcal{I}_h}, \epsilon} = \begin{bmatrix} J - \epsilon \tilde{M}_{1,1} & -\epsilon T_0 \tilde{M}_{1,2} \\ 0 & -\epsilon \bar{E} \end{bmatrix} + \mathcal{O}(\epsilon^2) \quad (7.33)$$

which is (up to second order terms in ϵ) time-invariant. Because J is asymptotically stable, (7.33) is asymptotically stable for $0 < \epsilon \ll 1$ if and only if the system

$$\dot{\bar{\phi}} = -\epsilon \bar{E} \bar{\phi} \quad (7.34)$$

is hyperbolically stable. All the changes of coordinates are linear, time-periodic and smooth, and thus uniformly continuous. Therefore, convergence toward 0 of $(\bar{z}, \bar{\phi})$ leads to the convergence toward 0 of $(z, \{z_k\}_{k \in \mathcal{I}_h})$. To ensure hyperbolic stability of system (7.34), we set $\beta_k \neq 0$ and

$$l_k(t) \triangleq \beta_k (C(t)W_k(t))^\dagger \quad (7.35)$$

where J and $S(t)$ are defined from Theorem 7.2, and $W_k = S^{-1}Q_k$, where Q_k is defined in Equation (7.25). With this choice, we have for all $(k, l) \in \mathcal{I}_h^2$

$$R_{l,k} = (C(t)W_l(t))^\dagger C(t)W_k(t)$$

Then, $E(t) \geq 0$ and so is \bar{E} . Therefore, hyperbolic stability of $-\bar{E}$ is equivalent to $\ker \bar{E} = \{0\}$. Yet, necessarily, $\ker \bar{E} = \{0\}$ otherwise H 2 would be violated: for any $\Gamma = [\Gamma_{-h}, \dots, \Gamma_h]^T \in \ker \bar{E}$, $x = \sum_k e^{ik\omega_0 t} W_k(t) \Gamma_k$ and $c_l = \delta_{l,k} \Gamma_k$, is solution of (7.2) with $y = Cx \equiv 0$. Thus system (7.34) is asymptotically stable. We have proven the following proposition.

Proposition 7.3. — Consider (7.2) with $m \leq p < n$. Assume that the matrices A , A_0 and C are T_0 -periodic and that hypothesis H 7.1 and H 7.2 hold. Consider the observer (7.3) with gains L and L_k as defined in subsection 7.2.3.3. Then, for small enough $\epsilon > 0$, the error dynamics (7.4) asymptotically converge to 0.

7.6. Other applications

In the second part of the thesis, we have seen several applications of the estimation of periodic input for linear periodic systems in the context of Diesel HCCI control. In

this Section, we describe other applications of this technique in both automotive engine industry.

7.6.1. Sensor dynamics inversion. — The first example is the inversion of sensor dynamics. A classical way of modelling such a sensor is a linear system (often a first or second order dynamics) with periodic excitations which can be, depending on the application, the intake pressure, the intake temperature, the exhaust pressure, the Air Fuel Ratio, or the Mass Air Flow.

For a first order system with a time constant τ , the system is similar to system (7.2):

$$\begin{cases} \dot{x} &= Ax + A_0 w(t) \\ y &= Cx \end{cases}$$

with $A = -\frac{1}{\tau}$, $A_0 = \frac{1}{\tau}$, $C = 1$.

7.6.1.1. Example of the AFR sensor. — The sensor can be considered as a cascade of two first order systems with time constant $\tau_1 = 25\text{ms}$ and $\tau_2 = 20\text{ms}$. w is the input signal driving a cascade of two first order dynamics. First the intermediate variable x_1 is reconstructed under the form of a periodic signal. Second, this estimation feeds another observer. The structure is explained in Figure 7.2. The observer is designed according

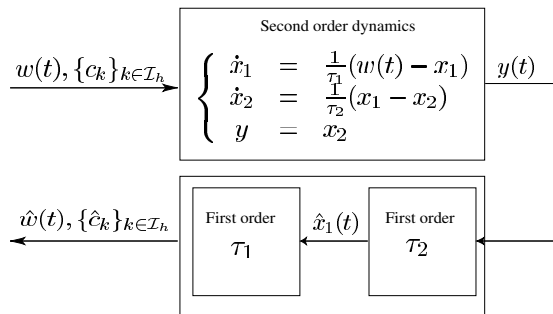


FIGURE 7.2. Top: w is the input signal driving a cascade of two first order dynamics. Bottom: the sensor is used to reconstruct in two steps w . First the intermediate variable x_1 is reconstructed under the form of a periodic signal. Second, this estimation feeds another observer.

to (7.3) with the gains defined by Equations (7.5) and (7.6). We use $\tilde{L} = -\frac{4}{\tau}$ and $\alpha_k^2 = \frac{4}{k^2+1}$.

7.6.1.2. AFR oscillations. — To introduce imbalance on the experimental testbed, we apply an injection duration timing trajectory. It produces offsets in injected masses leading

to AFR disturbances. More precisely, the injection steps have an effect on the average level of the measured AFR and introduce oscillations.

These oscillations are the direct consequences of the individual AFR imbalance. During cylinder 1 exhaust phase, the AFR increases in the manifold, and then decreases while the other cylinders exhaust phases occur. The magnitude of the oscillations is related to the amount of the AFR difference between the cylinders and the gas mass in the manifold (and thus to its volume). The oscillation is then propagated to the turbine, and to the UEGO sensor, where it is filtered. The implementation is achieved in discrete time with a sample angle of 6° deg crank angle. At $t = 4.5$ s, we introduce an imbalance on cylinder 1 (+25% of IMEP). This produces the expected oscillation of the AFR signal. The proposed technique is used and provides the results reported in Figure 7.3.

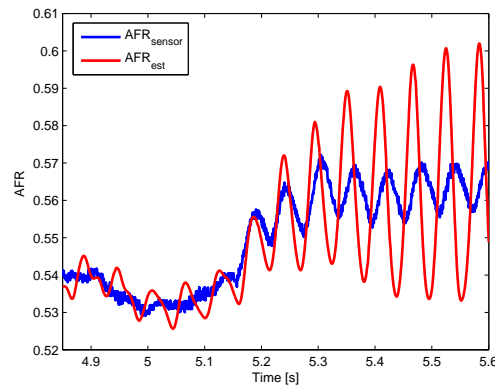


FIGURE 7.3. Testbench results. AFR reconstruction. Measured AFR by the sensor located downstream the turbine (blue), reconstructed AFR in exhaust manifold (red)

7.6.2. The Mathieu equation. — The first example had time invariant dynamics. Here, the time periodic dynamics of the Mathieu equation are considered

$$\begin{cases} \ddot{x} + (\alpha + \beta \cos(\omega_0 t))x = w(t) \\ w(t) = \sum_{i=1}^4 (a_i \cos(i\omega_0 t) + b_i \sin(i\omega_0 t)) \end{cases} \quad (7.36)$$

with the measurement $y = x$. The parameter values selected for this example are $\omega_0 = 2$, $\alpha = 1$, $\beta = .1$, and

$$\begin{aligned} a_1 = 3, \quad a_2 = 0, \quad a_3 = 2, \quad a_4 = 1 \\ b_1 = 0, \quad b_2 = 1, \quad b_3 = 0, \quad b_4 = -.5 \end{aligned}$$

Let $z \triangleq [x \ \dot{x}]^T \in \mathbb{R}^2$, the dynamics writes

$$\begin{cases} \dot{z} &= A(t)z + A_0 w(t) \\ y &= Cz \end{cases}$$

where

$$A(t) = \begin{bmatrix} 0 & 1 \\ -(\alpha + \beta \cos(\omega_0 t)) & 0 \end{bmatrix}, \quad A_0 = \begin{bmatrix} 0 \\ 1 \end{bmatrix}$$

and

$$C = [1 \ 0]$$

7.6.2.1. Verification of the hypothesis. — First of all, H 7.1 is trivially verified. Let us focus on H 7.2. Consider that $y = x \equiv 0$ over $[0, T_0]$. Then $\dot{x} \equiv \ddot{x} \equiv 0$ over $[0, T_0]$ leading to $w_0 \equiv 0$ over $[0, T_0]$. H 7.2 is then verified.

7.6.2.2. Observer design. — The observer is designed according to (7.3) with the gains defined by Equations (7.9) and (7.10). Simulations are presented in Figures 7.4, 7.5,

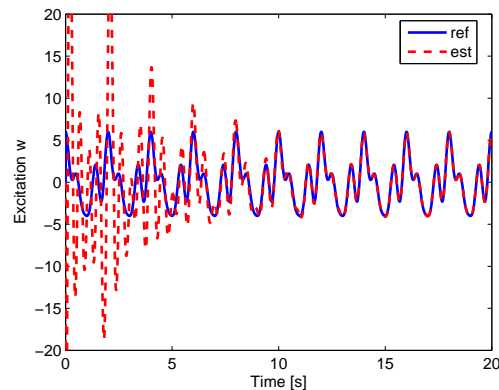


FIGURE 7.4. Simulation results. Excitation reconstruction. Reference excitation w (solid-blue), reconstructed excitation \hat{w} (dashed-red)

and 7.6. With this observer, we are able to reconstruct the unknown periodic input w and the state in a few cycle. Moreover, we have an estimation of the periodic excitation through the Fourier decomposition. We have, in addition, a frequential information on the excitation.

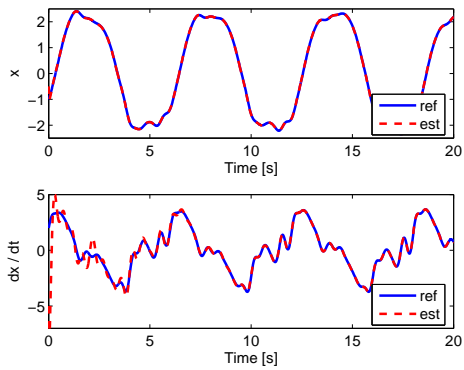


FIGURE 7.5. Simulation results. State reconstruction. Reference state (solid-blue), reconstructed state (dashed-red)

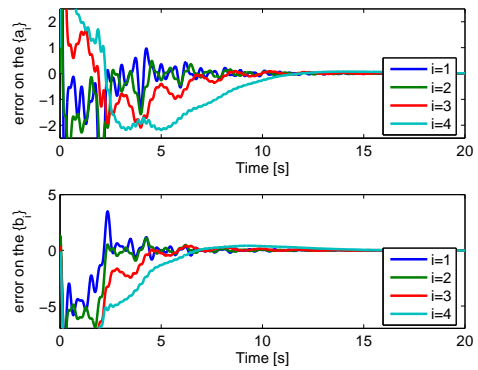


FIGURE 7.6. Simulation results. Coefficient estimation. Top: error $\{a_i - \hat{a}_i\}_{i=1\dots 4}$, Bottom: error $\{b_i - \hat{b}_i\}_{i=1\dots 4}$

CHAPTER 8

H^1 PERIODIC INPUT ESTIMATION FOR LINEAR BOUNDED SYSTEMS WITH FULL MEASUREMENT

Chapitre 8. — Dans le chapitre précédent, nous avons regardé les filtres de dimension finie pour les systèmes linéaire périodique excité par une entrée périodique inconnu. Dans ce chapitre, nous regardons son extension naturelle: le cas de filtres de dimension infinis. L'extension de la théorie aux filtres de dimension infinis permet d'obtenir une formule asymptotique qui, une fois tronquée, sert de méthodologie de calibration. Nous expliquons sous quelles conditions un choix approprié de gains garantie la convergence dans l'espace des fonction de Sobolev de type H^1 .

8.1. Introduction

In the previous chapter, we addressed the case of finite dimensional filters for linear time periodic systems driven by periodic unknown inputs. As a natural extension, we address the infinite dimensional filter design case in this chapter. The case of an infinite number of harmonics is considered. The extension of the theories to the infinite dimensional case provide a simple asymptotic formula that, when truncated, can successfully serve as a tuning methodology. We explain under which conditions an appropriate choice of gains guarantees convergence in Sobolev functional space of H^1 type.

The chapter is organized as follows. In Section 8.2, we detail the problem statement and the observer structure with an explicit design of its gains. Convergence proof is given in Section 8.3. The main result of this section is Proposition 8.3. This results also gives insight to observer design through the number of harmonics selection.

Notations. — In the following $\|\cdot\|_n$ refers to the Euclidian norm of \mathbb{R}^n , $\|\cdot\|_{nm}$ refers to the H_∞ -norm of $\mathcal{M}_{n,m}(\mathbb{R})$, $\ell_n^j \triangleq \{\{x_k\}_{k \in \mathbb{Z}} \in (\mathbb{R}^n)^{\mathbb{Z}} / \sum_{k \in \mathbb{Z}} \|x_k\|_n^j < +\infty\}$, and $H_n^1 \triangleq \{\{x_k\}_{k \in \mathbb{Z}} \in (\mathbb{R}^n)^{\mathbb{Z}} / \sum_{k \in \mathbb{Z}} (k^2 + 1) \|x_k\|_n^2 < +\infty\}$. Both ℓ_n^2 and H_n^1 are Hilbert spaces. We pose $\Omega \triangleq \mathbb{R}^n \times H_m^1$ and note its elements $\mathcal{X} = (x, c)$. The norm on Ω is $\|\mathcal{X}\|_\Omega^2 = \|x\|_n^2 + \|c\|_{H_m^1}^2$. We note $L_n^2 \triangleq \{t \mapsto x(t) \in \mathcal{C}^0([0, +\infty[, \mathbb{R}) / \int_0^{+\infty} \|x(t)\|_n^2 dt < +\infty\}$, and $L_{n, \text{Loc}}^2([t - T_0, t]) \triangleq \{t \mapsto x(t) \in \mathcal{C}^0([t - T_0, t], \mathbb{R}) / \int_{t-T_0}^t \|x(s)\|_n^2 ds < +\infty\}$. Finally, we denote by \dagger the Hermitian transpose.

8.2. Problem statement and observer design

8.2.1. Problem statement. — Consider the periodic system driven by an unknown periodic input signal $w(t)$

$$\begin{cases} \dot{x} = A(t)x + A_0(t)w(t) \\ y = C(t)x \end{cases} \quad (8.1)$$

where $x(t) \in \mathbb{R}^n$ is the state and $A(t)$, $A_0(t)$, $C(t)$ are bounded matrices in $\mathcal{M}_{n,n}(\mathbb{R})$, $\mathcal{M}_{n,m}(\mathbb{R})$ and $\mathcal{M}_{n,n}(\mathbb{R})$ respectively. The theme of our study is the estimation of the T_0 -periodic continuous input signal $t \mapsto w(t) \in \mathbb{R}^m$, with $m = \dim(w) \leq n = \dim(y) = \dim(x)$, through its Fourier decomposition

$$w(t) \triangleq \sum_{k \in \mathbb{Z}} c_k e^{ik\omega_0 t}, \quad \omega_0 = \frac{2\pi}{T_0}$$

As w is continuous, the $\{c_k\}_{k \in \mathbb{Z}}$ are in ℓ_m^2 (as implied by Parseval equality). Throughout the paper, we assume that $\{c_k\}_{k \in \mathbb{Z}} \in H_m^1$. We denote $\mathbb{Z}^+ = \{k \in \mathbb{Z}, k \geq 0\}$. Model (8.1) writes

$$\begin{cases} \dot{x} &= A(t)x + A_0(t)(\sum_{k \in \mathbb{Z}} c_k e^{ik\omega_0 t}) \\ \dot{c}_k &= 0, \quad \forall k \in \mathbb{Z}^+ \\ y &= C(t)x \end{cases} \quad (8.2)$$

where each vector c_k is a m dimensional complex vector. As w is a real quantity, for any $k \in \mathbb{Z}$, we have $c_{-k} = c_k^\dagger$. The state is noted $\mathcal{X} = (x, c) \in \Omega$.

The main technical assumption is H (8.3). We restrict our study to systems (8.1) such that there exist two positive real numbers (c_m, c_M) such that :

$$\mathbf{H\ 8.3.} \quad \forall t \geq 0, \quad \begin{cases} A^\dagger(t)A(t) & \leq c_M^2 I_n \\ c_m^2 I_m & \leq A_0^\dagger(t)A_0(t) \leq c_M^2 I_m \\ c_m^2 I_n & \leq C^\dagger(t)C(t) \leq c_M^2 I_n \end{cases}$$

8.2.2. Observer definition. — Corresponding to state-space model (8.2), we define a time-varying Luenberger type observer

$$\begin{cases} \dot{\hat{x}} & = A(t)\hat{x} + A_0(t)(\sum_{k \in \mathbb{Z}} \hat{c}_k e^{ik\omega_0 t}) - L(t)(C(t)\hat{x} - y) \\ \dot{\hat{c}}_k & = -e^{-ik\omega_0 t} L_k(t)(C(t)\hat{x} - y(t)), \quad \forall k \in \mathbb{Z} \\ (\hat{x}(0), \hat{c}(0)) & \in \Omega \quad \text{with} \quad \hat{c}_{-k}(0) = \hat{c}_k^\dagger(0) \quad \forall k \in \mathbb{Z}^+ \end{cases} \quad (8.3)$$

The gain matrices $L(t)$ (with real entries) and $\{L_k\}_{k \in \mathbb{Z}}$ (with complex entries) are defined in the following sub-section.

8.2.3. Design of L and $\{L_k\}_{k \in \mathbb{Z}^+}$. —

As $C^\dagger(t)C(t) \geq c_m^2 I_n$, then C is a square invertible matrix. Let \tilde{L} be any asymptotic stable matrix in $\mathcal{M}_{n,n}(\mathbb{R})$, we set

$$L(t) = (A(t) - \tilde{L})C^{-1}(t)$$

and P the unique symmetric definite solution of the Lyapounov equation

$$P\tilde{L} + \tilde{L}^\dagger P = -I_{n,n}$$

We set

$$L_k(t) \triangleq \frac{\alpha}{k^2 + 1} A_0^\dagger(t) P C(t)^{-1} \quad (8.4)$$

with α a strictly positive constant. Let $\tilde{\mathcal{X}} \triangleq \mathcal{X} - \hat{\mathcal{X}}$. Then, the error dynamics read

$$\begin{cases} \dot{\tilde{x}} & = \tilde{L}\tilde{x} + A_0(t)(\sum_{k \in \mathbb{Z}} \tilde{c}_k e^{ik\omega_0 t}) \\ \dot{\tilde{c}}_k & = -\frac{\alpha}{k^2 + 1} e^{-ik\omega_0 t} A_0^\dagger(t) P \tilde{x}, \quad \forall k \in \mathbb{Z}^+ \end{cases} \quad (8.5a)$$

$$(\tilde{x}(0), \tilde{c}(0)) \in \Omega \quad \text{with} \quad \tilde{c}_{-k}(0) = \tilde{c}_k^\dagger(0) \quad \forall k \in \mathbb{Z}^+ \quad (8.5b)$$

The adaptation law of the Fourier parameters are proportional to $\frac{1}{k^2+1}$ for the k^{th} harmonics. The main idea of this observation technique is to reconstruct w by observing its Fourier decomposition coefficients. By construction, these coefficients belong to H_m^1 . Besides some mathematical properties that, as will appear next, are useful to prove convergence of our observer, H_m^1 is an appropriate choice for engineering applications because it contains useful signals such as the continuous signals.

8.3. Convergence proof

Proof follows along standard lines, except that we use the Parseval equality to prove convergence of the observer. By contrast with finite dimensional analysis, existence, uniqueness and precompactness of trajectories needs to be proven (such an approach was used in [88], [47], [88], or [46]).

The proof is organized as follows. First, we prove that system (8.5) defines a unique solution in Ω over the time range $[0, +\infty[$. Then, we use the Parseval equality to prove that $\tilde{\mathcal{X}}$ is a Cauchy series in Ω . This leads to the convergence of $\tilde{\mathcal{X}}$ on Ω toward $\bar{\mathcal{X}}$ with respect to time. Finally, we conclude by proving that the error dynamics converges toward $\{0\}_\Omega$.

8.3.1. Observer Trajectories are well defined. —

Existence and uniqueness of the reference system trajectories. — Because the coefficient c is constant with respect to time, existence and uniqueness of the trajectories of the reference system (8.2) can be proven by showing that the function $\mathbb{R} \times \mathbb{R}^n \ni (t, x) \mapsto f(t, x) = A(t)x + A_0(t)w(t) \in \mathbb{R}^n$ is uniformly Lipschitz over \mathbb{R}^n using the Cauchy Lipschitz theorem on \mathbb{R}^n as explained in [43]. From hypothesis (8.3), this is trivially verified because f is uniformly c_M -Lipschitz over \mathbb{R}^n and the following lemma hold.

Lemma 8.1. — *Consider system (8.2) with $\mathcal{X}(0) = \mathcal{X}_0 \in \Omega$. It has a unique solution over $[0, +\infty[$. Moreover, this solution is continuously depending on initial values \mathcal{X}_0 , and uniformly continuous over $[0, +\infty[$.*

Existence and uniqueness of the error system trajectories. — Existence and uniqueness of trajectories can be proven by showing that the right hand-side of (8.5) is Lipschitz over Ω . For that purpose, we note

$$\Omega \ni (t, \mathcal{X} = (x, c)) \mapsto f_x(t, \mathcal{X}) = \tilde{L}x + A_0(t) \left(\sum_{k \in \mathbb{Z}} c_k e^{ik\omega_0 t} \right) \in \mathbb{R}^n \quad (8.6)$$

and

$$\Omega \ni (t, \mathcal{X} = (x, c)) \mapsto f_c(t, \mathcal{X}) = \left\{ -\frac{\alpha}{k^2 + 1} e^{-ik\omega_0 t} A_0^\dagger(t) P x \right\}_{k \in \mathbb{Z}} \in H_m^1 \quad (8.7)$$

First of all, let us focus on f_x . For all $(\mathcal{X}_1, \mathcal{X}_2) \in \Omega^2$ and all $t \in \mathbb{R}$

$$\|f_x(t, \mathcal{X}_1) - f_x(t, \mathcal{X}_2)\|_n^2 \leq 2 \left\| \tilde{L} \right\|_{nn}^2 \|x_1 - x_2\|_n^2 + 2 \|A_0(t)\|_{nm}^2 \sum_{k \in \mathbb{Z}} (k^2 + 1) \|c_{1,k} - c_{2,k}\|_m^2$$

On the other hand, $A_0(t)$ is bounded. Therefore, consider $c_x \triangleq 2 \max\{\|\tilde{L}\|_{nn}, c_M\}$, we then have $\|f_x(t, \mathcal{X}_1) - f_x(t, \mathcal{X}_2)\|_n \leq c_x \|\mathcal{X}_1 - \mathcal{X}_2\|_\Omega$ and the following result holds.

Lemma 8.2. — *The function f_x defined by (8.6) is uniformly c_x -Lipschitz over Ω .*

Now, let us focus on f_c . For all $(\mathcal{X}_1, \mathcal{X}_2) \in \Omega^2$ and all $t \in \mathbb{R}$

$$\|f_c(t, \mathcal{X}_1) - f_c(t, \mathcal{X}_2)\|_{H_m^1}^2 \leq \alpha^2 \left\| A_0^\dagger(t)P \right\|_{mn}^2 \sum_{k \in \mathbb{Z}} \frac{1}{k^2 + 1} \|x_1 - x_2\|_n^2$$

Define $c_c \triangleq \alpha c_M \|P\|_{mn} \sqrt{\sum_{k \in \mathbb{Z}} \frac{1}{k^2 + 1}}$. Finally, we have $\|f_c(t, \mathcal{X}_1) - f_c(t, \mathcal{X}_2)\|_{H_m^1} \leq c_c \|\mathcal{X}_1 - \mathcal{X}_2\|_\Omega$ and the following result holds.

Lemma 8.3. — *The function G defined by (8.7) is uniformly c_c -Lipschitz over Ω .*

Proposition 8.1. — *Consider system (8.5) with $\tilde{\mathcal{X}}(0) = \tilde{\mathcal{X}}_0 \in \Omega$. It has a unique solution over $[0, +\infty[$. Moreover, this solution is continuously depending on initial values $\tilde{\mathcal{X}}_0$, and uniformly continuous over $[0, +\infty[$.*

proof : Ω is a Banach space, f_x and f_c are uniformly Lipschitz over Ω (by Lemma 8.2 and 8.3). We can conclude on the existence and the uniqueness of the solution of (8.5) by [17, Theorem VII.3] (one can also refer to [7]). The regularity mentioned in the proposition follows the same result. Thus, system (8.3), the difference between the reference system (8.2) and the error system (8.5), share the same properties.

8.3.2. Definition of a Lyapunov function. — Define

$$V(\tilde{\mathcal{X}}) \triangleq \tilde{x}^\dagger P \tilde{x} + \frac{1}{\alpha} \|\tilde{c}\|_{H_m^1}^2 \quad (8.8)$$

By derivation of V with respect to t , we have

$$\begin{aligned} \dot{V} &= \dot{\tilde{x}}^\dagger P \tilde{x} + \tilde{x}^\dagger P \dot{\tilde{x}} + \frac{1}{\alpha} \sum_{k \in \mathbb{Z}} (k^2 + 1) (\dot{\tilde{c}}_k^\dagger \tilde{c}_k + \tilde{c}_k^\dagger \dot{\tilde{c}}_k) \\ &= -\|\dot{\tilde{x}}\|_n^2 + \sum_{k \in \mathbb{Z}} (\tilde{c}_k^\dagger M_k^\dagger(t) \dot{\tilde{x}} + \dot{\tilde{x}}^\dagger M_k(t) \tilde{c}_k) \end{aligned}$$

where

$$M_k^\dagger(t) \triangleq \left(P(t)A_0(t) - C^\dagger(t)L_k(t) \right)^\dagger \frac{k^2 + 1}{\alpha} e^{ik\omega_0 t} \quad (8.9)$$

By definition of L_k in Equation (8.4), we have for all $k \in \mathbb{Z}$, $M_k = 0$ and $\dot{V} = -\|\dot{\tilde{x}}\|_n^2$.

V is a Lyapunov function since it is continuously differentiable and satisfies

- i) $V(0) = 0$ and $V(\tilde{\mathcal{X}}) > 0$ for $\tilde{\mathcal{X}} \in \Omega \setminus \{0\}$,
- ii) $\frac{dV}{dt}(\tilde{\mathcal{X}}) \leq 0$ in Ω

This results in the following lemma.

Lemma 8.4. — *The function V defined by (8.8) is a Lyapounov function for the error-state system (8.5).*

Further, V is decreasing and bounded by below by 0. Then, V has a limit when t approaches $+\infty$. Moreover, by Barbalat's Lemma [96]

$$\lim_{t \rightarrow \infty} \dot{V}(t) = \lim_{t \rightarrow \infty} \|\tilde{x}(t)\|_n^2 = 0 \quad (8.10)$$

because V and \dot{V} are uniformly continuous from the uniform continuity of $\tilde{\mathcal{X}}$ (see Prop. 8.1). Finally, $t \mapsto \tilde{x}(t)$ is a L_n^2 function because $V(0)$ is bounded and V converges to a limit. We can state the following result.

Lemma 8.5. — *Consider $\tilde{\mathcal{X}} = (\tilde{x}, \tilde{c})$ the state of the error dynamics (8.5), $t \mapsto \tilde{x}(t)$ is a L_n^2 function, and $\lim_{t \rightarrow +\infty} \dot{\tilde{x}}(t) = \lim_{t \rightarrow +\infty} \tilde{x}(t) = 0$.*

8.3.3. Global State Convergence. — In this part, we show that the orbit is precompact. Ω is complete because it is the product of two complete spaces. Therefore, our task reduces to proving that the orbit is compact. On the one hand, we already know that $\tilde{x}(t) \rightarrow 0$ as $t \rightarrow +\infty$. Further, we now prove that $\{\tilde{c}_k\}_{k \in \mathbb{Z}}$ converges as well. For $t > T_0$, we have

$$\tilde{c}_k(t) = \tilde{c}_k(t - T_0) - \frac{\alpha}{k^2 + 1} \int_{t-T_0}^t e^{-ik\omega_0 s} (A_0^\dagger P \tilde{x})(s) ds$$

We note $\tilde{x}_{k,t} \triangleq \int_{t-T_0}^t e^{-ik\omega_0 s} (A_0^\dagger P \tilde{x})(s) ds$. We get

$$(k^2 + 1)^2 \|\tilde{c}_k(t) - \tilde{c}_k(t - T_0)\|_m^2 = \alpha^2 \|\tilde{x}_{k,t}\|_m^2$$

Since $t \mapsto \tilde{x}(t)$ is a L_2 function, $[t - T_0, t] \ni s \mapsto \tilde{x}(s)$ is a $L_{2,\text{Loc}}([t - T_0, t])$ function. Moreover by Parseval inequality, we have

$$\sum_{k \in \mathbb{Z}} \|\tilde{x}_{k,t}\|_m^2 = \frac{1}{T_0} \int_{t-T_0}^t \left\| (A_0^\dagger P \tilde{x})(s) \right\|_m^2 ds$$

Thus for $p_1 > p_2$

$$\begin{aligned}
\|\tilde{c}(p_1 T_0) - \tilde{c}(p_2 T_0)\|_{H_m^1}^2 &= \sum_{k \in \mathbb{Z}} (k^2 + 1) \|\tilde{c}_k(p_1 T_0) - \tilde{c}_k(p_2 T_0)\|^2 \\
&\leq \sum_{k \in \mathbb{Z}} (k^2 + 1)^2 \|\tilde{c}_k(p_1 T_0) - \tilde{c}_k(p_2 T_0)\|_m^2 \\
&\leq \sum_{j=p_2+1}^{p_1} \sum_{k \in \mathbb{Z}} (k^2 + 1)^2 \|\tilde{c}_k((j+1)T_0) - \tilde{c}_k(jT_0)\|_m^2 \\
&\leq \alpha^2 \sum_{j=p_2+1}^{p_1} \sum_{k \in \mathbb{Z}} \|\tilde{x}_{k,jT_0}\|_m^2 \\
&\leq \alpha^2 \frac{1}{T_0} \int_{p_2 T_0}^{p_1 T_0} \left\| (A_0^\dagger P \tilde{x})(s) \right\|_m^2 ds
\end{aligned}$$

Since $t \mapsto \tilde{x}(t)$ is a L_2 function, $t \mapsto (A_0^\dagger P \tilde{x})(t)$ is a L_2 function too. Therefore $\tilde{c}(nT_0)_{n \in \mathbb{N}}$ is a Cauchy series in ℓ_2^m which is complete. Finally

$$\exists \bar{c} \in H_m^1, \text{ s.t. } \|\tilde{c}(pT_0) - \bar{c}\|_{H_m^1} \rightarrow 0 \text{ as } t \rightarrow +\infty$$

and the following result holds

Proposition 8.2. — Consider $\tilde{\mathcal{X}} = (\tilde{x}, \tilde{c})$ the state of the error dynamics (8.5), $\tilde{\mathcal{X}}$ converges asymptotically toward $\bar{\mathcal{X}} = (0, \bar{c})$ in Ω .

8.3.4. Characterization of the limit. — We get the limit of (8.5)

This implies that,

$$\lim_{t \rightarrow +\infty} A_0(t) \sum_{k \in \mathbb{Z}} \tilde{c}_k(t) e^{ik\omega_0 t} = 0$$

Then, $\lim_{t \rightarrow +\infty} \|A_0(t) \sum_{k \in \mathbb{Z}} \tilde{c}_k e^{ik\omega_0 t}\|^2 = 0$. As for all $t \in \mathbb{R}$ $A_0^\dagger(t)A_0(t) \geq c_m^2 I_m$ by H 8.3, the previous equality is equivalent to the fact that, for all $t \in \mathbb{R}$, $\sum_{k \in \mathbb{Z}} \tilde{c}_k e^{ik\omega_0 t} = 0$. Since the Fourier transform is injective from $L_{m, \text{Loc}}^2([t - T_0, t])$ to ℓ_m^2 , and since $\bar{c} \in H_m^1 \subset \ell_m^2$, one can conclude that for all $k \in \mathbb{Z}$, $\bar{c}_k = 0$.

We can now formulate our main result.

Proposition 8.3. — Consider system (8.2). Assume that H 8.3 holds. Consider the observer (8.3) with L and $\{L_k\}_{k \in \mathbb{Z}}$ defined in subsection 8.2.3. Then, the error dynamics (8.5) asymptotically converges toward 0_Ω .

If we look at the frequent case where A , A_0 and C are time invariant, we obtain the following corollary.

Corrolary 1. — Consider (8.2). Assume that C is invertible and A_0 injective. Consider the observer (8.3) with L and $\{L_k\}_{k \in \mathbb{Z}}$ defined in subsection 8.2.3. Then, the error dynamics (8.5) asymptotically converges toward 0_Ω .

APPENDIX A

PERSONAL PUBLICATIONS AND PATENTS

PUBLICATIONS

- [1] A. Albrecht, J. Chauvin, F. Lafossas, S. Potteau, and G. Corde, “Development of highly premixed combustion diesel engine model : From simulation to control design,” in *Proc. of the SAE Conference*, no. 2006-01-1072, 2006.
- [2] A. Albrecht, J. Chauvin, S. Potteau, and G. Corde, “Design of real-time torque balancing control for highly premixed combustion engine using a 1d Diesel engine model,” in *Proc. of the IAV Conference "Engine process simulation and supercharging"*, 2005.
- [21] J. Chauvin, G. Corde, P. Moulin, M. Castagné, N. Petit, and P. Rouchon, “Observer design for torque balancing on a DI engine,” in *Proc. of the SAE Conference*, 2004.
- [22] —, “Real-time combustion torque estimation on a Diesel engine test bench using an adaptive Fourier basis decomposition,” in *Proc. of the the 43rd IEEE Conf. Decision and Control*, 2004.
- [23] —, “Real-time combustion torque estimation on a Diesel engine test bench using time-varying Kalman filtering,” in *Proc. of the the 43rd IEEE Conf. Decision and Control*, 2004.
- [24] —, “Time-varying linear observer for torque balancing on a DI engine,” in *IFAC Symp. Advances in Automotive Control (AAC04)*, 2004.

- [25] J. Chauvin, G. Corde, and N. Petit, "Constrained motion planning for the airpath of a diesel HCCI engine," in *Proc. of the Conf. Decision and Control*, 2006.
- [27] J. Chauvin, G. Corde, N. Petit, and P. Rouchon, "Experimental motion planning in airpath control for HCCI engine," in *Proc. of the American Control Conference*, 2006.
- [28] —, "High frequency individual cylinder estimation for control of Diesel engines," *Oil & Gas Science and Technology, special issue "Development and Control of Combustion Systems"*, vol. 61, no. 1, pp. 57–72, 2006.
- [29] —, "Periodic input observer design: Application for unbalance diagnosis," in *Proc. of the SAE Conference*, no. 2006-01-0181, 2006.
- [30] —, "Real-time estimation of periodic systems: automotive engine applications," *Automatica (revision under review)*, 2006.
- [31] J. Chauvin, G. Corde, C. Vigild, N. Petit, and P. Rouchon, "Air path estimation on HCCI engine," in *Proc. of the SAE Conference*, 2006.
- [32] J. Chauvin, P. Moulin, G. Corde, N. Petit, and P. Rouchon, "High frequency real-time individual cylinder Air Fuel Ratio observer on a Diesel engine," *Control Engineering Practice (submitted)*, 2005.
- [33] —, "Real-time nonlinear individual cylinder Air Fuel Ratio observer on a Diesel engine test bench," in *Proc. of the IFAC World Congress*, 2005.
- [34] —, "Kalman filtering for real-time individual cylinder air fuel ratio observer on a Diesel engine test bench," in *Proc. of the American Control Conference*, 2006.
- [37] —, "Six degrees crankshaft individual air fuel ratio estimation of Diesel engines for cylinder balancing purpose," in *Proc. of the SAE Conference*, no. 2006-01-0013, 2006.

[93] P. Moulin, G. Corde, J. Chauvin, and M. Castagné, “Cylinder individual AFR estimation based on a physical model and using Kalman filters,” in *Proc. of the FISITA World Automotive Congress*, no. F2004V279, 2004.

[94] O. Nilsson, A. Rantzer, and J. Chauvin, “A model reduction case study: Automotive engine air path,” in *Proc. of the Conference on Control Applications*, 2006.

PATENTS

[20] J. Chauvin, Y. Bentolila, and O. Grondin, “Méthode d’estimation en temps réel de paramètres de combustion moteur à partir de signaux vibratoires,” French Patent, 2006.

[26] J. Chauvin, G. Corde, N. Petit, and P. Rouchon, “Méthode d’estimation du régime instantané produit par chacun des cylindres d’un moteur à combustion interne,” French Patent, September 2005.

[35] J. Chauvin, P. Moulin, G. Corde, N. Petit, and P. Rouchon, “Méthode d’estimation par un filtre de kalman étendu de la richesse dans un cylindre d’un moteur à combustion,” European Patent, April 2006.

[36] —, “Méthode d’estimation par un filtre non-linéaire adaptatif de la richesse dans un cylindre d’un moteur à combustion,” European Patent, April 2006.

APPENDIX B

EXPERIMENTAL SETUP

To overcome limitations in power output, a “dual mode” engine was developed, using highly premixed combustion (HPC) at low and medium loads and conventional Diesel combustion at high loads (with injection close to TDC). This means that the combustion system should be able to run in both conventional and HCCI combustion mode.

B.1. NADITM engine configuration

The NADITM (Narrow Angle Direct Injection) application presented here is an engine equipped with only one turbo-charger. The turbocharger technology is conventional but the compressor and the turbine efficiency have been slightly improved compared to a production turbo-charger. However, a turbocharger somewhat larger was chosen at full load in order to reach the power target fixed at about 60 kW/l. The air circuit includes an air cooler to maintain the temperature at 50°C in the intake manifold at full load. A High Pressure EGR circuit was chosen for this application because of its short response time in transient operation for further engine management development. This type of EGR circuit takes burnt gas in the exhaust manifold upstream of the turbine. The introduction of the exhaust gas is made downstream of the compressor, just upstream of the intake manifold, by means of a venturi to improve burnt gas with fresh air mixing. The EGR circuit includes a cooler which is supplied by a special low temperature water circuit. The EGR cooler can be by-passed, which allows an increase of the intake temperature favorable to HC and CO emissions at very low engine loads. A well-adapted valve allows the EGR rate to be controlled. The high EGR mass flows required by the NADITM concept, particularly at low engine load, necessitated careful designing of the EGR circuit in order to maintain low level of pressure losses.

At full load, the output torque and power specifications impose the air mass flow required by the engine according to the geometric compression ratio. At part load, the HPC mode needs high EGR mass flow. At medium loads, the demand of air and EGR increases and the compressor must supply sufficient air flow to ensure engine load with lambda value above 1.1, while high burned gas mass flow is needed for combustion control. We use a conventional single stage turbocharger with variable geometry turbine (VGT). When engine load increases in the HPC mode, intake EGR/ fresh air mixture mass flow increases and requires high intake pressure which can make the compressor operate near the surge line at low engine speed. Small compressor size has therefore to be preferred. But future target standards for the maximum output power impose an adapted air mass flow leading to larger compressor size. So the compressor has to be compatible with high and low engine speeds. Compressor choice is helped by turbocharger development progress which leads to enlarged compressor maps. On the other hand, the weak exhaust gas energy available at the turbine inlet at low engine speed, which is further reduced by a high EGR rate, makes turbine efficiency a very important parameter to consider for the turbocharger choice. Because the EGR rate used in highly premixed combustion is significantly higher than in conventional combustion, advanced development of a specific cooler and valve is required both for the circuit permeability and for the fouling resistance optimization. EGR cooling system effectiveness is also an important parameter to be considered because of the high temperature burned gas mass flow used. Control of the burned gas temperature leads to better pollutant emission levels. By-passing partly the EGR cooler is in fact a simple way to modulate the burned gas temperature, already used on the production engine.

B.2. Experimental set up

This section aims to describe the engine hardware used in terms of combustion chamber parts, compression ratio, turbocharger and type of EGR circuit. The multi-cylinder application is based on a production engine : As mentioned previously, the components of the combustion chamber were defined using single cylinder tests. The piston bowl was designed with the NADITM bowl drawing specifications and the bowl volume was adapted to obtain a compression ratio of 14 : 1. The intake ducts of the cylinder head were modified in order to adapt the swirl motion to the required swirl number of 1.3 at BDC. All the results shown in this paper, including full load conditions, were obtained with the same swirl number, without any inlet duct closure. The injection system is with a maximum injection pressure of 1600 bar. The features of the injectors used are as follows :

Bore x Stroke	87.0 x 92.0 mm
Number of cylinders	4
Displacement	2.2 Liters
Injection device	Solenoid
Maximum injection pressure	1600 bar
Turbocharger	Variable Nozzle Turbine

TABLE B.1. Engine main characteristics.

- Spray cone angle : 60°
- Number of holes : 6
- Flow rate : 500 ml / 30 seconds / 100 bar.

The NADITM application presented here is an engine equipped with only one turbocharger. The turbocharger was chosen in order to reach the power target fixed at full load. The turbocharger technology is conventional but the compressor and the turbine efficiency have been slightly improved compared to a production turbocharger. The air circuit includes an air cooler to maintain the temperature at 50° C in the intake manifold at full load.

A standard commercial gasoil with less than 50 ppm sulphur content has been used.

APPENDIX C

FROM SIMULATION TO CONTROL

For development and tuning of the numerous controller, reference engine models are essential. They provide a helpful tool during each step of design, from understanding the control problem and the dynamics involved, to using reference model for off-line design, to testing control strategies off-line and on real time engine model. The aim of this chapter is to present the engine simulation technique involved in our control design.

C.1. Engine Simulator Design

The engine system simulation tool used for this study is the IFP-ENGINE library (Figure C.1). It has been developed in the IMAGINE's numerical platform AMESim which is an open numerical environment for the modelling and the simulation of dynamic systems inspired by Bond Graph approach [75]. The numerical solver automatically and dynamically selects the best-adapted calculation method among 17 available algorithms. In this library version, the computed gas consists of 3 species : fresh air, vaporized fuel and burned gas. Such a thermodynamic assumption has been identified as sufficient for engine performance results. The combustion dual mode model previously described has been introduced in the library as an additional development in order to have a best accuracy of combustion process which is a crucial item in this study.

C.1.1. Reference Engine Model Description. — The goal of engine system simulation is to supply the relevant model for the specific application. User expectations have to

independent temperatures for the cylinder head, the piston and the liner. The combustion heat release model has already been presented in the dedicated part.

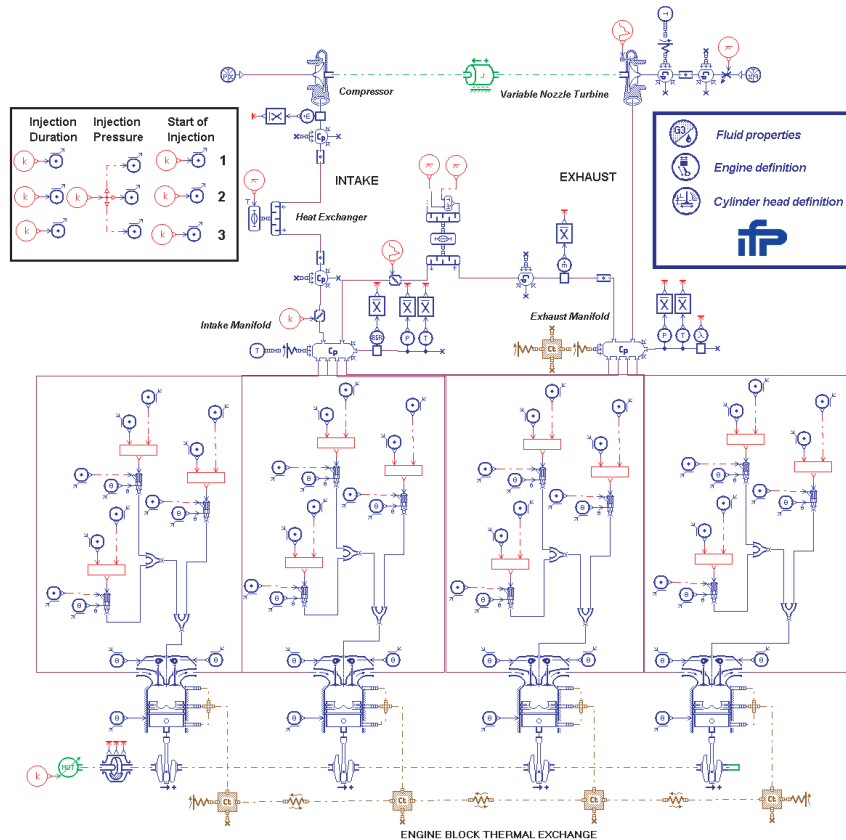


FIGURE C.2. HPC Diesel engine model diagram.

C.1.2. Engine Module Calibration. — Once all the geometrical specifications of the engine module have been defined in the model such as bore, stroke or compression ratio, main aspects of the engine block model have to be calibrated :

- The cylinder head permeability : In this study, aerodynamic testbed results are used.
- The injection model : The instantaneous mass fuel rate has been fitted on injection testbed results and depends of pulse width and rail pressure.
- The in-cylinder heat transfer parameters : The Woschni's parameters have been calibrated using a cylinder pressure acquired at the bench during a without combustion cycle (turning off the fuel injection on one cylinder).

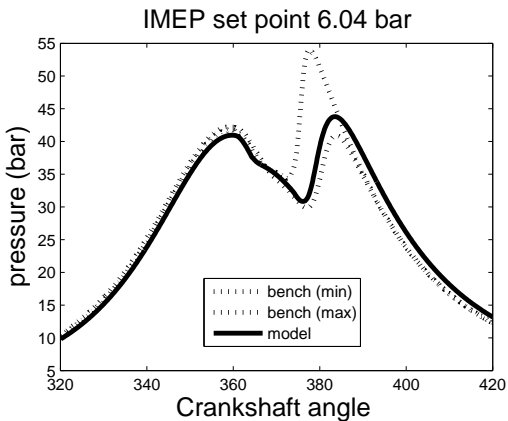


FIGURE C.3. Model/Bench cylinder pressure comparison at 1500 rpm: 6 bar of IMEP.

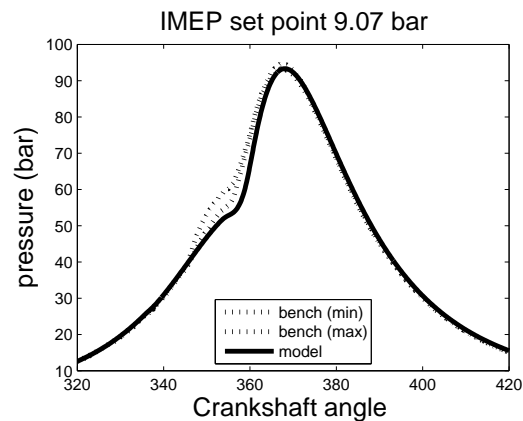


FIGURE C.4. Model/Bench cylinder pressure comparison at 1500 rpm: 9 bar of IMEP.

- The combustion dual mode model : This is a crucial calibration for the engine model. The parameters have been calibrated on experimental cylinder pressures obtained at the bench with a load variation at 1500 rpm.

Bench/model comparisons for some load set points are presented on Figures C.3 and C.4. The results highlights the cylinder-to-cylinder pressure deviation for such a combustion mode engine and shows that the combustion model gives a good agreement with experiment after being calibrated.

C.1.3. Air Path Calibration. — From the gas dynamic point of view, the air path calibration mainly consists in the tuning of the friction in the air path duct but above all in the characterization of the actuators : air throttle, variable nozzle turbine distributor and EGR valve. From the thermal point of view, material heat exchanges such as manifold thermal losses or engine block thermal behavior have to be adapted to reproduce experimental results and the cooling systems used in the air path such as the supercharging air cooler or the EGR cooler have also to be calibrated in order to obtain a good predictive capability of the engine simulator on gas temperature which is a crucial item for exhaust gas recirculation.

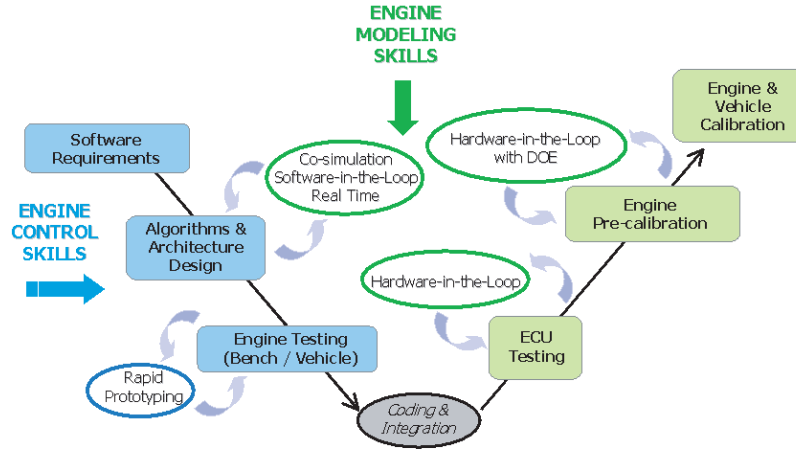


FIGURE C.5. Model-based engine control development cycle.

C.2. From Reference Simulator to Real Time Simulator

C.2.1. Engine Simulator: Support Tool for Engine Control Design. — As presented on Figure C.5, during the model-based engine control development cycle, the engine model goals for control issues, change. In fact, three main versions of the engine simulators are required with associated software platforms to be able to support as well as possible the control conception:

- the reference engine simulator used in the co-simulation platform.
- the fixed-step engine simulator used in the complete export platform.
- the real time engine simulator used in the software-in-the-loop or hardware-in-the-loop real time platform.

In order to be able to deliver with efficiency the different engine simulator versions, the coherent and real-time compatible AMESim's environment allows us to perform a continuous engine model development with an integrated conception platform.

C.2.2. Reference Simulator & Co-simulation Platform. — The main goal for this simulator is to perform a model with a high representative ability of the real engine. This simulator is crucial for the following steps because it fixes the starting accuracy level for the other simulator versions used in the cycle. The co-simulation environment allows us to run two separate models with two different softwares at the same time. Both

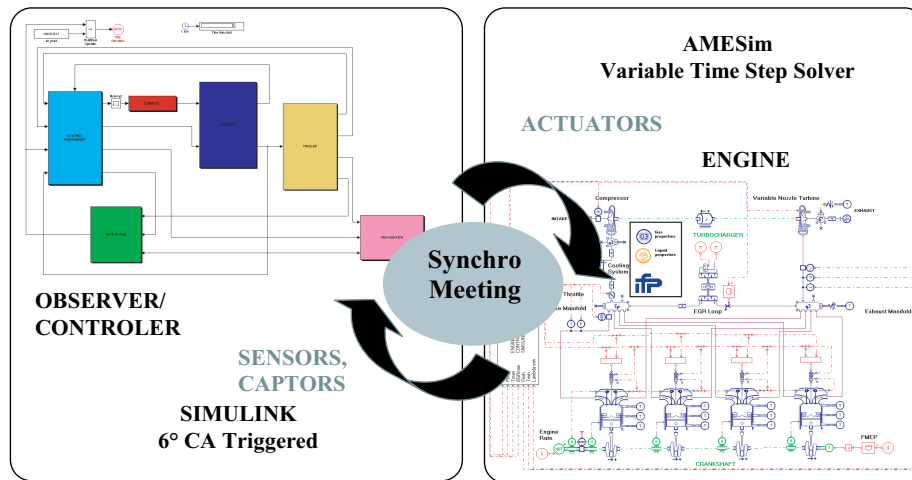


FIGURE C.6. AMESim/SIMULINK co-simulation platform.

solvers compute independently their respective systems and exchange information with a fixed communication step interval. Since Matlab SIMULINK is the cornerstone tool for current engine control designers, the co-simulation platform may be used in order to run the engine model on AMESim's side and the control model on SIMULINK's side. At each synchronised meeting time, the engine model send sensor data to SIMULINK and the engine control send back actuator positions to AMESim. The engine model may be computed with the AMESim's variable timestep solver and the control model with the SIMULINK's 6° CA triggered management. Figure C.6 presents a schematic representation of the AMESim/SIMULINK co-simulation environment. This platform is a helpful and efficient tool in order to understand engine behavior and to develop the engine observers and controllers. It allows us to validate the control design developments with the most accurate engine model available.

C.2.3. Fixed-step Simulator & Complete Export Platform. — Once one or various control algorithms are defined, an engine simulator is needed to achieve further tests and to validate the control under wide range of operating conditions. This simulator version is the fixed-step engine simulator which is supposed to have increased CPU performance while preserving the relevant physical behavior obtained with the reference simulator. The complete export platform is a convenient way to perform this stage. It consists in encapsulating the engine model in an S-function and in exporting it to SIMULINK. So, the same engine model may continue to be used for the control, computed by the SIMULINK's

solver. The engine simulator has therefore to be adapted to fixed-step conditions, especially for the cylinder model which requires a specific approach to preserve the accuracy of the combustion process.

C.2.4. RT Simulator & SiL/HiL RT Platform. — The last step for the engine control before testing on the engine bench is to validate it under real time conditions. Therefore, the real time engine simulator is required. Thanks to specific adaptation, the engine model may run in real time and support the control development up to real time targets such as xPC Target or dSPACE. This simulator version allows us to use the engine model until the very last stages of the control design and to transfer to the bench a more robust controller at low cost by reducing the conception time and the risks of damaging on prototype hardware.

APPENDIX D

CONVERGENCE OF THE PERIODIC KALMAN FILTER

Let us first recall the following classic result

Theorem D.1 (Bittanti et al. [14].) — *[Predictor Convergence]*

With the above notations, consider the optimal Kalman gain

$$L_k = A_k P_k \hat{C}_k^T (\hat{C}_k P_k \hat{C}_k^T + I)^{-1}$$

associated with any semi-definite solution P of

$$P_{k+1} = A_k P_k A_k^T + \hat{B}_k \hat{B}_k^T - A_k P_k \hat{C}_k^T (\hat{C}_k P_k \hat{C}_k^T + I)^{-1} \hat{C}_k P_k A_k^T$$

If (A_, \hat{B}_*) is stabilizable and (A_*, \hat{C}_*) detectable, then the corresponding closed-loop matrix $\hat{A}_* = A_* - L_* \hat{C}_*$ is exponentially stable*

D.1. Combustion Torque estimation using Kalman filtering

D.1.1. Reference model. — First of all, we redefine the reference model

$$\begin{cases} x_{k+1} &= A_k x_k + B_k u_k \\ y_k &= C_k x_k + w_k \end{cases} \quad (\text{D.11})$$

with the state

$$x_k = \begin{pmatrix} \dot{\alpha}^2(k) \\ T_{comb}(k) - T_{load}^*(k) \\ \dots \\ T_{comb}(k - q + 1) - T_{load}^*(k - q + 1) \end{pmatrix} \in \mathbb{R}^{q+1}$$

The matrices A_k , B_k and C_k are

$$A_k = \begin{bmatrix} 1 - \frac{2\Delta\alpha}{J(k)}f(k) & v_k \\ 0 & M \end{bmatrix} \in \mathcal{M}_{q+1,q+1}(\mathbb{R}) \quad (\text{D.12})$$

$$B_k = \begin{bmatrix} 0 & 0 & 0 \\ b_0 & \dots & b_p \\ 0 & 0 & 0 \\ \dots & \dots & \dots \\ 0 & 0 & 0 \end{bmatrix} \in \mathcal{M}_{q+1,p+1}(\mathbb{R}) \quad (\text{D.13})$$

$$C_k = [1 \ 0 \ \dots \ 0] \in \mathcal{M}_{1,q+1}(\mathbb{R}) \quad (\text{D.14})$$

with

$$v_k = \begin{bmatrix} \frac{2\Delta\alpha}{J(k)} & 0 & \dots & 0 \end{bmatrix} \in \mathcal{M}_{1,q}(\mathbb{R}) \quad (\text{D.15})$$

and

$$M = \begin{bmatrix} -a_1 & -a_2 & -a_3 & \dots & -a_q \\ 1 & 0 & 0 & 0 & 0 \\ 0 & 1 & 0 & 0 & 0 \\ \dots & \dots & \dots & \dots & \dots \\ 0 & 0 & 0 & 1 & 0 \end{bmatrix} \in \mathcal{M}_{q,q}(\mathbb{R})$$

Finally, u_k is a white noise.

D.1.2. Time-varying prediction algorithm. — We use a time-varying Kalman predictor for the combustion torque. For purpose we introduce the system

$$\hat{x}_{k+1/k} = A_k \hat{x}_{k/k-1} + L_k (y_k - C_k \hat{x}_{k/k-1}) \quad (\text{D.16})$$

with the initial condition

$$x_{0/-1} = m_0$$

where L_k is the Kalman gain matrix

$$L_k = A_k P_k C_k^T (C_k P_k C_k^T + R_k)^{-1} \quad (\text{D.17})$$

In this last expression, the covariance error $P_k = \text{cov}(x_k - \hat{x}_{k/k-1})$ is recursively computed through

$$P_{k+1} = A_k P_k A_k^T + B_k Q_k B_k^T - A_k P_k C_k^T (C_k P_k C_k^T + R_k)^{-1} C_k P_k A_k^T \quad (\text{D.18})$$

with $P_0 = \text{cov}(x_0)$. At last Q_k and R_k are matrices to be chosen.

D.1.3. Reference model properties. —

D.1.3.1. A_k 's eigenvalues. —

To check stability, we investigate A_k 's eigenvalues. All the A_k matrices are block upper-triangular, so

$$\text{eig}(A_k) = \left\{ 1 - \frac{2\Delta\alpha}{J(k)}f(k), \lambda_1, \dots, \lambda_p \right\}$$

Both J and $f(k) = \frac{1}{2} \frac{dJ}{d\alpha}(k)$ are periodic while $\frac{2}{J(k)}f(k) = \frac{d \log(J)}{d\alpha}(k)$ is periodic with a 0 mean value. The system is thus unstable when $f(k) > 0$ which occurs half of the time along the engine cycle.

D.1.3.2. Stability of A_ .* —

The properties of each A_k do not allow us to conclude stability of $A_* = \{A_k\}_{k \in \mathbb{N}}$ as a set. It is a common result that A_* is asymptotically stable if and only if the characteristic multipliers are included in the unitary circle (see [13]). To compute these multipliers we compute by induction the transition matrices

$$\forall (k_1, k_2) \in \mathbb{N}^2 \quad k_2 \geq k_1$$

$$\Phi(k_2, k_1) = \begin{bmatrix} \pi_{k_2, k_1} & \phi_{k_2, k_1} \\ 0 & M^{k_2 - k_1} \end{bmatrix}$$

with

$$\phi_{k_2, k_1} = \begin{cases} 0 & \text{if } k_2 = k_1 \\ \sum_{j=k_1}^{k_2-1} (\pi_{k_2, j+1} v_j M^{j-k_1}) & \text{if } k_2 > k_1 \end{cases} \quad (\text{D.19})$$

and

$$\pi_{k_2, k_1} = \begin{cases} 1 & \text{if } k_2 = k_1 \\ \prod_{i=k_1}^{k_2-1} \left(1 - \frac{2\Delta\alpha}{J(i)}f(i) \right) & \text{if } k_2 > k_1 \end{cases}$$

We finally have

$$\text{eig}(\Phi(N+1, 1)) = \{ \pi_{N+1, 1}, \lambda_1^N, \dots, \lambda_p^N \}$$

The analytical expression of $J(n)$ allows us to state the $\frac{N}{2}$ -periodicity of $J(n)$ and $\frac{d}{d\alpha}(\frac{1}{J})(n)$. Note that this last expression is also symmetric with respect of the $n \mapsto -n$ mapping. Thus

$$\forall k \in \left\{ 1, \frac{N}{2} \right\} \quad \frac{2\Delta\alpha}{J(k)}f(k) + \frac{2\Delta\alpha}{J(N-k)}f(N-k) = 0$$

thus

$$\prod_{i=1}^N \left(1 - \frac{2\Delta\alpha}{J(i)}f(i) \right) = \prod_{i=1}^{\frac{N}{2}} \left(1 - \left(\frac{2\Delta\alpha}{J(i)}f(i) \right)^2 \right) < 1$$

finally $\text{eig}(\Phi(N+1, 1)) \subset \mathcal{D}_{0,1}$. Stability of the system is proven. The following result holds

Lemma D.6. — *The system $x_k = A_k x_k + B_k u_k$, $y_k = C_k x_k + w_k$ where A_k , B_k and C_k are given by Equations (D.12), (D.13) and (D.14) is asymptotically stable.*

D.1.3.3. Observability. —

We now compute the observability Gramian W_o over an interval $[k_0, k_0 + k]$ and check its uniform positiveness over k . Again, since the system is periodic, we just have to check positiveness of W_o over $k \in [1, N]$. The observability Gramian over $[k_0, k_f]$ is defined by

$$W_o(k_f, k_0) = \sum_{i=k_0}^{k_f} \Phi_{k_f, i}^T C_i^T C_i \Phi_{k_f, i}$$

To check wether $W_o(k_0 + nN, k_0)$ is positive definite, we pose

$$V_o(k, i) = C_i \Phi_{k, i} = \begin{bmatrix} \pi_{k_f, i} & \phi_{k_f, i} \end{bmatrix}$$

We have

$$W_o(k_0 + nN, k_0) > 0 \Leftrightarrow \bigcap_{i=k_0}^{k_0+nN} \text{Ker}(V_o(k_0 + nN, i)) = \{0\}$$

As before, we pose

$$\mathcal{V}_o(k_2) = \begin{bmatrix} V_o(k_2, k_2) \\ V_o(k_2, k_2 - 1) \\ \dots \\ V_o(k_2, k_2 - (q-1)) \end{bmatrix}$$

We note $L_1^{(j)}$ the first line of M^j . Due to the analytic expression of v_j as defined in (D.15) we notice that ϕ_{k_2, k_1} is a linear combination of the elements of $\{L_1^{(j)}\}_{j=0, \dots, k_2 - k_1}$. This yields

$$\text{rank} \left(\begin{bmatrix} \phi_{k_2, k_2} \\ \phi_{k_2, k_2 - 1} \\ \dots \\ \phi_{k_2, k_2 - (q-1)} \end{bmatrix} \right) = \text{rank}(\mathbf{L})$$

with

$$\mathbf{L} = \begin{bmatrix} L_1^{(0)} \\ L_1^{(1)} \\ \dots \\ L_1^{(q-1)} \end{bmatrix}$$

Yet $|\det(\mathbf{L})| = |\det(M)|^{q-1}$. So \mathbf{L} is a full rank matrix and so is $\mathcal{V}_o(k_2)$.

$$\bigcap_{i=k_0}^{k_0+nN} \text{Ker}(V_o(k_0 + nN, i)) \subset \text{Ker}(\mathcal{V}_o(k_0 + nN)) = \{0\}$$

Observability is proven and the following result holds

Lemma D.7. — *The system $x_k = A_k x_k + B_k u_k$, $y_k = C_k x_k + w_k$ where A_k , B_k and C_k are given by Equations (D.12), (D.13) and (D.14) is observable.*

D.1.3.4. Riccati equation for discrete-time periodic systems. —

We now focus on the properties of the DPRE described by (D.18) adapting the results of Theorem 1. The weight matrices R_k and Q_k previously defined are supposed to be constant symmetric definite positive matrices. We have

$$R_k = \tilde{R}\tilde{R}^T \quad \text{and} \quad Q_k = \tilde{Q}\tilde{Q}^T$$

where \tilde{R} and \tilde{Q} are symmetric definite positive matrices. Let

$$\hat{B}_k = B_k \tilde{Q}_k \quad \text{and} \quad \hat{C}_k = \tilde{R}_k^{-1} C_k$$

Equation (D.18) becomes

$$P_{k+1} = A_k P_k A_k^T + \hat{B}_k \hat{B}_k^T - A_k P_k \hat{C}_k^T (\hat{C}_k P_k \hat{C}_k^T + I)^{-1} \hat{C}_k P_k A_k^T \quad (\text{D.20})$$

As a result, the previous simple change of coordinates yields Theorem D.1 formulation.

D.1.3.5. Conclusion on time-varying Kalman filter convergence. —

First of all, we proved that the system is stable while each matrix A_k is not. Moreover, we proved the controllability and the observability of the reference system. We finally get on Bittanti et al's conditions (the observability (resp. controllability) condition is invariant by multiplication of C_* (resp. B_*) by a definite positive matrix) with more general weighting matrices R_k and Q_k as used in Equation (D.18). All these steps lead to the convergence of the observer.

Proposition D.4. — *With R_k and Q_k constant symmetric definite positive matrices, the Kalman filter state defined in Equations (D.16, D.17, D.18) converges towards the reference model state (D.11).*

D.2. Individual AFR estimation convergence proof

In 5.4.1, we proved that masses converge toward a limit cycle. First of all, we remind the discrete time reference system. Then, we define the periodic Kalman filter and, finally, we look at the convergence of the observer.

D.2.1. Discrete-time reference system. — The discrete-time reference system is the discrete approximation of system (5.7) around the limit cycle obtained through an Euler explicit scheme around the previously defined limit cycle x_{per} . The sample angle is $\Delta\alpha = 6^\circ$ and, for sake of conciseness, we note $x_d(k) = x_{\text{per}}(k\Delta\alpha)$ and $\delta \triangleq \frac{\Delta\alpha}{N_e}$. We define A_k , D_k and C_k as

$$A_k = \begin{bmatrix} \alpha_k & \beta_k \\ 0 & I_{n_{\text{cyl}}} \end{bmatrix} \in \mathcal{M}_{n_{\text{cyl}}+2, n_{\text{cyl}}+2}(\mathbb{R})$$

where $I_{n_{\text{cyl}}}$ is the n_{cyl} -Identity matrix, $\mathcal{M}_{k_1, k_2}(\mathbb{R})$ is the set of real matrices of dimension $k_1 \times k_2$, and, finally,

$$\alpha_k \triangleq \begin{bmatrix} 1 - \delta d'_T(x_{d,1}(k), \Xi) & 0 \\ -\delta x_{d,2}(k) p'(x_{d,1}(k), \Xi) & 1 - \delta p(x_{d,1}(k), \Xi) \end{bmatrix} \in \mathcal{M}_{2,2}(\mathbb{R}) \quad (\text{D.21})$$

$$\beta_k \triangleq -\delta \begin{bmatrix} 0 & \dots & 0 \\ d_1(k\Delta\alpha, \Xi) & \dots & d_{n_{\text{cyl}}}(k\Delta\alpha, \Xi) \end{bmatrix} \in \mathcal{M}_{2, n_{\text{cyl}}}(\mathbb{R})$$

$$D_k \triangleq \delta \sum_{i=1}^{n_{\text{cyl}}} d_i(k\Delta\alpha, \Xi) [1 \ 1 \ 0 \ \dots \ 0]^T \in \mathcal{M}_{n_{\text{cyl}}+2, 1}(\mathbb{R})$$

$$C_k \triangleq \begin{bmatrix} \gamma_T & 0 & 0 & \dots & 0 \\ \frac{x_{d,2}(k)}{x_{d,1}(k)^2} & -\frac{1}{x_{d,1}(k)} & 0 & \dots & 0 \end{bmatrix} \in \mathcal{M}_{2, 2+n_{\text{cyl}}}(\mathbb{R})$$

We define the discrete-time reference system as

$$\begin{cases} x_{k+1} &= A_k x_k + D_k + v_k \\ y_k &= C_k x_k + w_k \end{cases} \quad (\text{D.22})$$

where $(v, w) \in \mathbb{R}^{2+n_{\text{cyl}}} \times \mathbb{R}^2$ are added white noise. Notice that A_k , D_k and C_k are $N_0 \triangleq \frac{T_0}{\Delta\alpha}$ -periodic (here $N_0 = 120$). We note $A_* = \{A_k\}_{k \in [1, N_0]}$, $C_* = \{C_k\}_{k \in [1, N_0]}$ and $D_* = \{D_k\}_{k \in [1, N_0]}$. Clearly, $A_{k+N_0} = A_k$, $C_{k+N_0} = C_k$ and $D_{k+N_0} = D_k$.

D.2.2. Periodic Kalman filter. — We use a time-varying Kalman predictor for the AFR estimation. For this purpose, we introduce the system

$$\hat{x}_{k+1} = A_k \hat{x}_k + D_k + L_k(y_k - C_k \hat{x}_k) \quad (\text{D.23})$$

with chosen arbitrary initial condition \hat{x}_0 , where L_k is the Kalman gain matrix

$$L_k = A_k P_k C_k^T (C_k P_k C_k^T + R_k)^{-1} \quad (\text{D.24})$$

In this last expression, the covariance error P_k is recursively computed through the discrete periodic Riccati equation (DPRE)

$$P_{k+1} = A_k P_k A_k^T + Q_k - A_k P_k C_k^T (C_k P_k C_k^T + R_k)^{-1} C_k P_k A_k^T \quad (\text{D.25})$$

with P_0 a freely chosen initial condition (positive definite). At last, Q_k and R_k are weighting matrices, to be chosen in $\mathcal{M}_{n_{cyl}+2, n_{cyl}+2}(\mathbb{R})$ and $\mathcal{M}_{2,2}(\mathbb{R})$ respectively.

D.2.3. Convergence. —

D.2.3.1. Stability of the discrete time reference system over a period. — We compute by induction the transition matrices $\Phi(k_2, k_1) \triangleq \prod_{k=k_1}^{k_2-1} A_k$ and get

$$\forall (k_1, k_2) \in \mathbb{N}^2 \quad k_2 \geq k_1 \quad \Phi(k_2, k_1) = \begin{bmatrix} \pi_{k_2, k_1} & \phi_{k_2, k_1} \\ 0 & I_{n_{cyl}} \end{bmatrix}$$

with

$$\phi_{k_2, k_1} = \begin{cases} 0 & \text{if } k_2 = k_1 \\ \sum_{j=k_1}^{k_2-1} \pi_{k_2, j+1} \beta_j & \text{if } k_2 > k_1 \end{cases} \quad (\text{D.26})$$

and

$$\pi_{k_2, k_1} = \begin{cases} I_2 & \text{if } k_2 = k_1 \\ \prod_{i=k_1}^{k_2-1} \alpha_i & \text{if } k_2 > k_1 \end{cases}$$

The transition matrix is upper triangular with an identity term on the diagonal, as $\pi_{N_0+1, 1}$ is asymptotically stable, the discrete time reference system (D.22) is stable.

D.2.4. Observability. — We now compute the observability Gramian W_o over an interval $[k_0, k_0 + k]$ and check its uniform positiveness over k . Again, since the system is periodic, we just have to check positiveness of W_o over $k \in [1, N]$. The observability Gramian over $[k_0, k_f]$ is defined by

$$W_o(k_f, k_0) = \sum_{i=k_0}^{k_f} \Phi_{k_f, i}^T C_i^T C_i \Phi_{k_f, i}$$

To check whether $W_o(k_0 + N, k_0)$ is positive definite, we note

$$\varpi_{k_2, k_1} \triangleq \delta\pi_{k_2, k_1}(2, 2)$$

By induction, we can easily show negativeness of ϖ_{k_2, k_1} . Let

$$\varrho_i(k_2, k_1) \triangleq \sum_{j=k_1, k_2-1} \varpi_{k_2, j+1} d_i(j) \quad (\text{D.27})$$

Moreover, we note $V_0(k, i)$ the first two lines of $C_i\Phi_{k,i}$. Then,

$$V_0(k_2, k_1) = \begin{bmatrix} \gamma_T^2 + \frac{1}{x_{d,1}(k_1)^2} & -\frac{x_{d,2}(k_1)}{x_{d,1}(k_1)^3} & 0 & \cdots & 0 \\ -\frac{x_{d,2}(k_1)}{x_{d,1}(k_1)^3} & 0 & 0 & \cdots & 0 \end{bmatrix} \text{ if } k_2 = k_1 \quad (\text{D.28})$$

or

$$V_0(k_2, k_1) = \begin{bmatrix} V_{1,1}(k_2, k_1) & V_{1,2}(k_2, k_1) & \rho(k_2, k_1) \\ V_{1,2}(k_2, k_1) & 0 & \rho(k_2, k_1) \end{bmatrix} \text{ if } k_2 > k_1 \quad (\text{D.29})$$

where

$$\rho(k_2, k_1) = \begin{bmatrix} 0 & \cdots & 0 \\ \varrho_1(k_2, k_1) & \cdots & \varrho_{n_{cyl}}(k_2, k_1) \end{bmatrix}$$

Propositions *i*) and *ii*) are equivalent

$$\begin{aligned} & i) W_o(k_0 + N_0, k_0) > 0 \\ & ii) \bigcap_{i=k_0}^{k_0+N_0} \text{Ker}(V_o(k_0 + N_0, i)) = 0 \end{aligned}$$

Let

$$\mathcal{V}_o(k_2) = \begin{bmatrix} V_o(k_2, k_2) \\ V_o(k_2, k_2 - 1) \\ \cdots \\ V_o(k_2, k_2 - N_0) \end{bmatrix} \in \mathcal{M}_{2(N_0+1), 2+n_{cyl}}(\mathbb{R})$$

Then proposition *ii*) is equivalent to the injectivity of $\mathcal{V}_o(k_2)$. Let us show the injectivity of $\mathcal{V}_o(k_2)$. Assume that there exists $X = (X_T, X_{air}, X_1, \dots, X_{n_{cyl}})$ s.t. $\mathcal{V}_o(k_2)X = 0$, by (D.28) we have $X_T = X_{air} = 0$. Moreover, by using the n_{cyl} last columns of $\mathcal{V}_o(k_2)$, a straightforward expansion of $\mathcal{V}_o(k_2)$ using the expressions of $\rho_i(k_2, k_1)$ in (D.27) yields that propositions *ii*) and *iii*) are equivalent

$$\begin{aligned} & ii) \mathcal{V}_o(k_2) \text{ has full rank} \\ & iii) \begin{bmatrix} d_1(k_2) & \cdots & d_{n_{cyl}}(k_2) \\ \vdots & \vdots & \vdots \\ d_1(k_2 - N_0) & \cdots & d_{n_{cyl}}(k_2 - N_0) \end{bmatrix} \text{ has full rank} \end{aligned}$$

This last condition is true because the functions family $\{d_i\}_{i=1\dots n_{cyl}}$ is a linearly independent family of the set $\mathcal{C}^0([0, T_0], \mathbb{R})$ of the continuous functions $[0, T_0] \mapsto \mathbb{R}$. The *iii*) holds and so does *ii*). This proves

$$\bigcap_{i=k_0}^{k_0+N_0} \text{Ker}(V_0(k_0 + N_0, i)) \subset \text{Ker}(\mathcal{V}_0(k_0 + N_0)) = \{0\}$$

Uniform positiveness of the observability Gramian over $[k_0, k_0 + N_0]$ proposition *i*) is then proven and the following result holds

Proposition D.5. — *System (D.22) is uniformly observable.*

Using Theorem D.1 in [14], we have

Proposition D.6. — *With R_k and Q_k constant symmetric positive definite matrices, the state of the Kalman filter defined by equations (D.23),(D.24),(D.25) converges towards the discrete time reference model state (D.22).*

BIBLIOGRAPHY

- [1] A. Albrecht, J. Chauvin, F. Lafossas, S. Potteau, and G. Corde, "Development of highly premixed combustion diesel engine model : From simulation to control design," in *Proc. of the SAE Conference*, no. 2006-01-1072, 2006.
- [2] A. Albrecht, J. Chauvin, S. Potteau, and G. Corde, "Design of real-time torque balancing control for highly premixed combustion engine using a 1d Diesel engine model," in *Proc. of the IAV Conference "Engine process simulation and supercharging"*, 2005.
- [3] M. Ammann, N. Fekete, L. Guzzella, and A. Glattfelder, "Model-based control of the VGT and EGR in a turbocharged common-rail Diesel engine: theory and passenger car implementation," in *Proc. of the SAE Conference*, no. 2003-01-0357, 2003.
- [4] P. Amnéus, D. Nilsson, F. Mauss, M. Christensen, and B. Johansson, "Homogeneous Charge Compression Ignition engine: experiments and detailed kinetic calculations," in *4th International Symposium on Diagnostic and Modeling in Internal Combustion Engines*, 1998.
- [5] B. Anderson and J. Moore, *Linear optimal control*. Prentice-Hall, 1971.
- [6] I. Arsie, F. Di Genova, C. Pianese, M. Sorrentino, G. Rizzo, A. Caraceni, P. Cioffi, and G. Flauti, "Development and identification of phenomenological models for combustion and emissions of common-rail multi-jet Diesel engines," in *Proc. of the SAE Conference*, no. 2004-01-1877, 2004.
- [7] J.-P. Aubin, *Applied Functional Analysis*. Wiley, 2000.
- [8] T. Auckenthaler, C. Onder, and H. Geering, "Aspects of dynamic three-way catalyst behaviour including oxygen storage," in *IFAC Symp. Advances in Automotive Control (AAC04)*, 2004.

- [9] J. Ball, J. Bowe, C. Stone, and P. McFadden, "Torque estimation and misfire detection using block angular acceleration," in *Proc. of the SAE Conference*, 2000.
- [10] C. Barba, C. Burkhardt, K. Boulouchos, and B. M., "A phenomenological combustion model for heat release rate prediction in high-speed DI Diesel engines with common-rail injection," in *Proc. of the SAE Conference*, no. 2000-01-2933, 2000.
- [11] J. Bengtsson, P. Strandh, R. Johansson, P. Tunestål, and B. Johansson, "Control of Homogeneous Charge Compression Ignition HCCI engine dynamics," in *IEEE Proc. of 2004 American Control Conference*, 2004.
- [12] P. Berggren and A. Perkovic, "Cylinder individual lambda feedback control in an SI engine," Master's thesis, Linköpings Universitet, 1996.
- [13] S. Bittanti, *Time Series and Linear Systems*. Springer-Verlag, 1986.
- [14] S. Bittanti, P. Colaneri, and G. De Nicolao, "The difference periodic Riccati equation for the periodic prediction problem," *Proc. of the IEEE Transactions on Automatic Control*, vol. 33, no. 8, Aug. 1988.
- [15] —, "Application of input estimation techniques to charge estimation and control in automotive engines," *Control Engineering Practice*, vol. 10, pp. 1371–1383, 2002.
- [16] F. Brauer and J. Nohel, *The Qualitative Theory of Ordinary Differential Equations: An Introduction*. Dover Publications, 1989.
- [17] H. Brezis, *Analyse Fonctionnelle, Théorie et Applications*. Masson, 1983.
- [18] P. Carlucci, A. Ficarella, and D. Laforgia, "Effects of pilot injection parameters on combustion for common rail Diesel engines," in *Proc. of the SAE Conference*, no. 2003-01-0700, 2003.
- [19] C. Carnevale and M. Hadji, "Cylinder to cylinder AFR control with an asymmetrical exhaust manifold in a GDI system," in *Proc. of the SAE Conference*, no. 981064, 1998.
- [20] J. Chauvin, Y. Bentolila, and O. Grondin, "Méthode d'estimation en temps réel de paramètres de combustion moteur à partir de signaux vibratoires," French Patent, 2006.
- [21] J. Chauvin, G. Corde, P. Moulin, M. Castagné, N. Petit, and P. Rouchon, "Observer design for torque balancing on a DI engine," in *Proc. of the SAE Conference*, 2004.

- [22] —, “Real-time combustion torque estimation on a Diesel engine test bench using an adaptive Fourier basis decomposition,” in *Proc. of the the 43rd IEEE Conf. Decision and Control*, 2004.
- [23] —, “Real-time combustion torque estimation on a Diesel engine test bench using time-varying Kalman filtering,” in *Proc. of the the 43rd IEEE Conf. Decision and Control*, 2004.
- [24] —, “Time-varying linear observer for torque balancing on a DI engine,” in *IFAC Symp. Advances in Automotive Control (AAC04)*, 2004.
- [25] J. Chauvin, G. Corde, and N. Petit, “Constrained motion planning for the airpath of a diesel HCCI engine,” in *Proc. of the Conf. Decision and Control*, 2006.
- [26] J. Chauvin, G. Corde, N. Petit, and P. Rouchon, “Méthode d’estimation du régime instantané produit par chacun des cylindres d’un moteur à combustion interne,” French Patent, September 2005.
- [27] —, “Experimental motion planning in airpath control for HCCI engine,” in *Proc. of the American Control Conference*, 2006.
- [28] —, “High frequency individual cylinder estimation for control of Diesel engines,” *Oil & Gas Science and Technology, special issue "Development and Control of Combustion Systems"*, vol. 61, no. 1, pp. 57–72, 2006.
- [29] —, “Periodic input observer design: Application for unbalance diagnosis,” in *Proc. of the SAE Conference*, no. 2006-01-0181, 2006.
- [30] —, “Real-time estimation of periodic systems: automotive engine applications,” *Automatica (revision under review)*, 2006.
- [31] J. Chauvin, G. Corde, C. Vigild, N. Petit, and P. Rouchon, “Air path estimation on HCCI engine,” in *Proc. of the SAE Conference*, 2006.
- [32] J. Chauvin, P. Moulin, G. Corde, N. Petit, and P. Rouchon, “High frequency real-time individual cylinder Air Fuel Ratio observer on a Diesel engine,” *Control Engineering Practice (submitted)*, 2005.
- [33] —, “Real-time nonlinear individual cylinder Air Fuel Ratio observer on a Diesel engine test bench,” in *Proc. of the IFAC World Congress*, 2005.
- [34] —, “Kalman filtering for real-time individual cylinder air fuel ratio observer on a Diesel engine test bench,” in *Proc. of the American Control Conference*, 2006.

- [35] —, “Méthode d’estimation par un filtre de kalman étendu de la richesse dans un cylindre d’un moteur à combustion,” European Patent, April 2006.
- [36] —, “Méthode d’estimation par un filtre non-linéaire adaptatif de la richesse dans un cylindre d’un moteur à combustion,” European Patent, April 2006.
- [37] —, “Six degrees crankshaft individual air fuel ratio estimation of Diesel engines for cylinder balancing purpose,” in *Proc. of the SAE Conference*, no. 2006-01-0013, 2006.
- [38] A. Chevalier, C. Vigild, and E. Hendricks, “Predicting the port air mass flow of SI engine in Air/Fuel ratio control applications,” in *Proc. of the SAE Conference*, 2000.
- [39] C. Chiang and A. Stefanopoulou, “Steady-state multiplicity and stability of thermal equilibria in Homogeneous Charge Compression Ignition (HCCI) engines,” in *IEEE Proc. of 2004 Conference in Decision and Control*, 2004.
- [40] F. Chmela, M. Engelmayer, G. Pirker, and A. Wimmer, “Prediction of turbulence controlled combustion in Diesel engines,” in *Thiesel*, 2004.
- [41] F. Chmela and G. Orthaber, “Rate of heat release prediction for direct injection Diesel engines based on purely mixing controlled combustion,” in *Proc. of the SAE Conference*, no. 1999-01-0186, 1999.
- [42] E. Coddington and N. Levinson, *Theory of Ordinary Differential Equations*. New York: McGraw-Hill, 1955.
- [43] —, *Theory of Ordinary Differential Equations*. McGraw-Hill, 1955.
- [44] B. Compagny, “www.bosch.de.”
- [45] G. Compagny, “www.turbobygarrett.com.”
- [46] J.-M. Coron and d’Andréa Novel B., “Stabilization of a rotating body beam without damping,” *Proc. of the IEEE Transactions on Automatic Control*, vol. 43, no. 5, pp. 608–618, 1998.
- [47] C. Dafermos and M. Slemrod, “Asymptotic behavior of nonlinear contraction semi-groups,” *J. Funct. Anal.*, vol. 13, pp. 437–442, 1973.
- [48] S. Drakunov, G. Rizzoni, and Y. Wang, “Estimation of engine torque using nonlinear observers in the crank angle domain,” in *Proc. of the 5th ASME symposium on Advanced Automotive Technologies*, 1995.

- [49] M. Durnholz, H. Endres, and P. Frisse, "Preinjection: a measure to optimize emission behavior of DI Diesel engine," in *Proc. of the SAE Conference*, no. 940674, 1994.
- [50] J. Fantini and J.-F. Burq, "Exhaust-intake manifold model for estimation of individual cylinder air fuel ratio and diagnostic of sensor-injector," in *Proc. of the SAE Conference*, no. 2003-01-1059, 2003.
- [51] M. Fliess, J. Lévine, P. Martin, and P. Rouchon, "Flatness and defect of nonlinear systems: introductory theory and examples," *International Journal of Control*, vol. 61, no. 6, pp. 1327–1361, 1995.
- [52] J. Grizzle, K. Dobbins, and J. Cook, "Individual cylinder air-fuel ratio control with a single EGO sensor," *Proc. of the IEEE Transactions on Vehicular Technology*, vol. 40, no. 1, pp. 357–381, Feb. 1991.
- [53] J. Guckenheimer and P. Holmes, *Nonlinear Oscillations, Dynamical Systems and Bifurcation of Vector Fields*. Springer, 1983.
- [54] Y. Guezennec and P. Gyan, "A novel approach to real-time estimation of the individual cylinder pressure for SI engine control," in *Proc. of the SAE Conference*, 1999.
- [55] P. Gyan, S. Ginoux, J. Champoussin, and Y. Guezennec, "Crankangle based torque estimation: mechanistic/stochastic," in *Proc. of the SAE Conference*, 2000.
- [56] P. Hartman, *Ordinary Differential Equations, Second Edition*. Birkhäuser Boston, 1982.
- [57] E. Hendricks, A. Chevalier, M. Jensen, S. Sorenson, D. Trumpy, and J. Asik, "Modelling of the intake manifold filling dynamics," in *Proc. of the SAE Conference*, 1996.
- [58] J. Heywood, *Internal Combustion Engine Fundamentals*. McGraw-Hill, Inc, 1988.
- [59] L. Hsu, R. Ortega, and G. Damn, "A globally convergent frequency estimator," *Proc. of the IEEE Transactions on Automatic Control*, vol. 44, no. 4, p. 698–713, Apr. 1999.
- [60] A. Hultqvist, U. Engdar, B. Johansson, and J. Klingmann, "Reacting boundary layers in a homogeneous charge compression ignition (HCCI) engine," in *Proc. of the SAE Conference*, no. 2001-01-1032, 2001.
- [61] J. Hwang, J. Park, M. Kim, and J. Chae, "Multizone model for DI Diesel engine combustion and emissions," in *Proc. of the SAE Conference*, no. 1999-01-2926, 1999.

- [62] M. Ikeda, H. Maeda, and S. Kodama, “Stabilization of linear systems,” *SIAM J. Control*, vol. 13, pp. 304–326, 1975.
- [63] IMAGINE, *AMESim user manual*, <http://www.amesim.com>, 2004.
- [64] T. Jaïne, A. Benkenida, P. Menegazzi, and P. Higelin, “Zero dimensional computation of Diesel spray - comparison with experiments and 3D model,” in *Proc. of the SAE-NA congress*, no. 2003-01-82, 2003.
- [65] M. Janković and I. Kolmanovsky, “Robust nonlinear controller for turbocharged Diesel engine,” in *Proc. of the American Control Conference*, 1998.
- [66] —, “Constructive Lyapounov control design for turbocharged Diesel engines,” *IEEE Transactions on Control Systems Technology*, vol. 8, pp. 288–299, 2000.
- [67] H. Javid, “Observing the slow states of singularly perturbed system,” *Proc. of the IEEE Transactions on Automatic Control*, vol. 25, no. 5, pp. 277–280, 1980.
- [68] —, “Stabilization of time-varying singularly perturbed systems by observer-based slow-state feedback,” *Proc. of the IEEE Transactions on Automatic Control*, vol. 27, no. 3, pp. 702–704, 1982.
- [69] J. Jensen, A. Kristensen, S. Sorensen, N. Houbak, and E. Hendricks, “Mean value modeling of a small turbocharged Diesel engine,” in *Proc. of the SAE Conference*, no. 910070, 1991.
- [70] M. Jung and K. Glover, “Control-oriented linear parameter-varying modelling of a turbocharged Diesel engine,” 2003.
- [71] —, “Comparison of uncertainty parameterisations for H-infinity robust control of turbocharged Diesel engines,” vol. 13, pp. 15–25, 2005.
- [72] J. Kahrstedt, K. Behnk, A. Sommer, and T. Wormbs, “Combustion processes to meet future emission standards,” in *Motortechnische Zeitschrift*, 2003, pp. 1417–1423.
- [73] M. Kao and J. Moskwa, “Turbocharged Diesel engine modeling for nonlinear engine control and estimation,” vol. 117, 1995.
- [74] —, “Turbocharged Diesel engine modelling for nonlinear engine control and estimation,” *ASME Journal of Dynamic Systems, Measurements and Control*, vol. 117, 1995.
- [75] D. Karnopp, D. Margolis, and R. Rosenberg, *Systems Dynamics : a Unified Approach*. John Wiley & Sons, New-York, USA, 1990.

- [76] H. Khalil, *Nonlinear Systems*. Prentice-Hall, Inc., 1992.
- [77] U. Kiencke and L. Nielsen, *Automotive Control Systems For Engine, Driveline, and Vehicle*, Springer, Ed. SAE Internationnal, 2000.
- [78] I. Kolmanovsky, A. Stefanopoulou, P. Moraal, and M. van Nieuwstadt, “Issues in modelling and control of intake flow in variable geometry turbocharged engines,” in *Proc of the 18th IFIP Conference on System Modelling and Optimization*, 1997.
- [79] A. Krener and A. Isidori, “Linearization by output injection and nonlinear observers,” *Syst. Contr. Letters*, vol. 3, pp. 47–52, 1983.
- [80] A. Krener and W. Respondek, “Nonlinear observers with linearizable error dynamics,” *SIAM J. Control Optim.*, vol. 23, pp. 197–216, 1985.
- [81] T. Kreuzer, E. Lox, D. Lindner, and L. J., “Advanced exhaust gas aftertreatment systems for gasoline and Diesel fuelled vehicles,” *Catalysis Today*, vol. 29, pp. 17–27, 1996.
- [82] X.-C. Lü, W. Chen, and Z. Huang, “A fundamental study on the control of the HCCI combustion and emissions by fuel design concept combined with controllable EGR. Part 1: The basic characteristics of HCCI combustion,” *Fuel*, vol. 84, pp. 1074–1083, 2005.
- [83] N. Ladommatos, S. Abdelhalim, H. Zhao, and Z. Hu, “The dilution, chemical, and thermal effects of exhaust gas recirculation on Diesel engine emissions – part 1: Effect of reducing inlet charge oxygen,” in *Proc. of the SAE Conference*, no. 961165, 1996.
- [84] —, “The dilution, chemical, and thermal effects of exhaust gas recirculation on Diesel engine emissions – part 2: Effects of carbon dioxide,” in *Proc. of the SAE Conference*, no. 961167, 1996.
- [85] —, “The dilution, chemical, and thermal effects of exhaust gas recirculation on Diesel engine emissions – part 4: Effects of carbon dioxide and water vapour,” in *Proc. of the SAE Conference*, no. 971660, 1996.
- [86] —, “The dilution, chemical, and thermal effects of exhaust gas recirculation on Diesel engine emissions – part 3: Effects of water vapour,” in *Proc. of the SAE Conference*, no. 971659, 1997.
- [87] W. Lohmiller and J.-J. Slotine, “On contracting analysis for nonlinear systems,” *Automatica*, vol. 34(6), pp. 683–696, 1998.

- [88] Z. Luo, B. Guo, and O. Morgül, *Stability and stabilization of infinite dimensional systems with applications*. Springer Verlag, 1999.
- [89] R. Marino and P. Tomei, “Global estimation of n unknown frequencies,” in *Proc. of the 39th IEEE Conf. Decision and Control*, 2000.
- [90] M. B. Milam, “Real-time optimal trajectory generation for constrained systems,” Ph.D. dissertation, California Institute of Technology, 2003.
- [91] P. Moraal and I. Kolmanovsky, “Turbocharger modeling for automotive control applications,” in *Proc. of the SAE Conference*, no. 1999-01-0908, 1999.
- [92] P. Moraal, Y. Yacoub, U. Christen, B. Carberry, and G. S., “Diesel particulate filter regeneration: control or calibration?” in *IFAC Symp. Advances in Automotive Control (AAC04)*, 2004.
- [93] P. Moulin, G. Corde, J. Chauvin, and M. Castagné, “Cylinder individual AFR estimation based on a physical model and using Kalman filters,” in *Proc. of the FISITA World Automotive Congress*, no. F2004V279, 2004.
- [94] O. Nilsson, A. Rantzer, and J. Chauvin, “A model reduction case study: Automotive engine air path,” in *Proc. of the Conference on Control Applications*, 2006.
- [95] D. Pierpont, D. Montgomery, and R. Reitz, “Reducing particulate and NO_x using multiple injections and EGR in a DI Diesel,” in *Proc. of the SAE Conference*, no. 950217, 1995.
- [96] V. Popov, *Hyperstability of automatic control systems*,. Springer Verlag, 1973.
- [97] B. Reveille, M. Miche, S. Jay, and S. Henriot, “Contribution of 3D CFD tools to the development and understanding of Diesel engines,” in *Proc. of the SIA Congress*, 2004.
- [98] G. Rizzoni, “Estimate of indicated torque from crankshaft speed fluctuations: A model for the dynamics of the IC engine,” *Proc. of the IEEE Transactions on Vehicular Technology*, vol. 38, pp. 169–179, 1989.
- [99] G. Rizzoni and F. Connolly, “Estimate of IC engine torque from measurement of crankshaft angular position,” in *Proc. of the SAE Conference*, 1993.
- [100] G. Rizzoni, Y. Kim, and Y. Wang, “Design of an IC engine torque estimator using unknown input observer,” *ASME Journal of Dynamic Systems, Measurement, and Control*, vol. 121, 1999.

- [101] L. Shi, Y. Cui, K. Deng, H. Peng, and C. Y., "Study of low emission homogeneous charge compression ignition (HCCI) engine using combined internal and external exhaust gas recirculation (EGR)," *Energy*, vol. 84, pp. 1084–1092, 2006.
- [102] K. Song-Chang, A. Patel, and R. Reitz, "Development and application of detailed chemistry based CFD models for Diesel PCCI engine simulations," in *Proc. of the SAE Conference*, no. 2004-30-0030, 2004.
- [103] K. Srinivasan, G. Rizzoni, V. Trigui, and G. Luh, "On-line estimation of net torque from crankshaft angular velocity measurement using repetitive estimations," in *Proc. of the American Control Conference*, 1992.
- [104] A. Stefanopoulou, I. Kolmanovsky, and J. Freudenberg, "Control of variable geometry turbocharged Diesel engines for reduced emissions," *IEEE Transactions on Control Systems Technology*, vol. 8, pp. 733–745, 2000.
- [105] T. C. Tow, D. A. Pierpont, and R. D. Reitz, "Measurement of the effect of injection rate and split injections on Diesel engine soot and NO_x emissions," in *Proc. of the SAE Conference*, no. 940668, 1994.
- [106] —, "Reducing particulate and NO_x emissions by using multiple injections in a heavy duty DI Diesel engine," in *Proc. of the SAE Conference*, no. 940897, 1994.
- [107] S.-C. Tsai and M. Goyal, "Dynamic turbocharged Diesel engine model for control analysis and design," in *Proc. of the SAE Conference*, 1986.
- [108] M. van Nieuwstadt, I. Kolmanovsky, P. Moraal, A. Stefanopoulou, and M. Janković, "Experimental comparison of EGR-VGT control schemes for a high speed Diesel engine," *Control System Magazine*, vol. 20, pp. 63–79, 2000.
- [109] M. van Nieuwstadt, P. Moraal, I. Kolmanovsky, A. Stefanopoulou, P. Wood, and M. Criddle, "Decentralized and multivariable designs for EGR-VGT control of Diesel engine," in *Proc of the 2nd IFAC Workshop on Advances in Automotive Control*, 1998.
- [110] M. Vidyasagar, *Nonlinear systems analysis (2nd ed.)*. Upper Saddle River, NJ, USA: Prentice-Hall, Inc., 1992.
- [111] B. Walter and B. Gatellier, "Near zero NO_x emissions and high fuel efficiency diesel engine: the NADITM concept using dual mode combustion," vol. 58, no. 1, pp. 101–114, 2003.
- [112] J. Williams, "An overview of misfiring cylinder engine diagnostic techniques based on crankshaft angular velocity measurements," in *Proc. of the SAE Conference*, 1996.

- [113] X. Xia, "Global frequency estimation using adaptive identifiers," *Proc. of the IEEE Transactions on Automatic Control*, vol. 47, no. 7, pp. 1188–1193, July 2002.
- [114] L. Zhang, "A study of pilot injection in a DI Diesel engine," in *Proc. of the SAE Conference*, no. 1999-01-3493, 1999.